THE UNIVERSITY OF QUEENSLAND

AUSTRALIA

LARGE-EDDY SIMULATION OF COMPRESSIBLE TURBULENT BOUNDARY LAYERS WITH HEAT ADDITION

By

Andrew Denman

B.E. (Mechanical and Space)

A THESIS SUBMITTED FOR THE DEGREE OF

DOCTOR OF PHILOSOPHY

Principal Supervisor: Dr Peter Jacobs

Associate Supervisor: Associate Professor David Mee

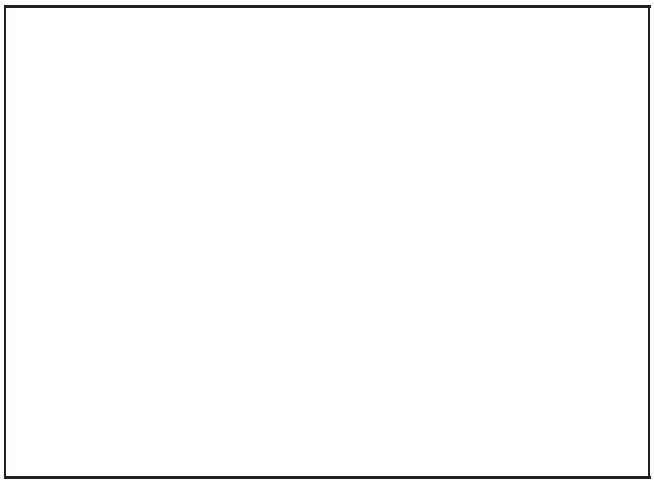

Division of Mechanical Engineering,

School of Engineering

January, 2007

The work presented in this thesis is, to the best of my knowledge and belief, original and my own work, except as acknowledged in the text. This material has not been submitted, either in whole or in part, for a degree at this or any other university.

Andrew Denman

Dr Peter Jacobs

Abstract

Turbulent wall shear stress has a significant impact on high speed vehicle performance. Its large magnitude, relative to the thrust that can be produced by propulsion systems such as Scramjets, means that it is worthwhile to attempt to control the wall shear stress levels. Experimental and numerical investigations have revealed that combustion of hydrogen in the boundary layer provides a means for such control. When combustion occurs, changes in mean flow property profiles across the boundary layer have already been identified. These changes in mean flow properties have been used to hypothesize about changes occurring to the turbulent mechanisms of momentum transfer. The purpose of this thesis is to examine the changes that occur to the turbulent momentum transfer mechanisms for boundary layers that experience a wall shear stress reduction through chemical heat evolution from hydrogen combustion.

The comparisons are made using large eddy simulation (LES) to simulate the turbulent transport processes within a fully developed turbulent boundary layer. With the advent of dynamic subgrid scale LES models that require no *a priori* specification of model coefficients, LES presents itself as a high fidelity means of studying turbulent processes without the computational expense of direct numerical simulation (DNS). Comparisons were made between two types of subgrid scale models, the eddy-viscosity/eddy-diffusivity model and the approximate deconvolution model (ADM). While the differences were minimal in most instances, the dynamically adjusting ADM procedure yielded better agreement with DNS and experimental datasets. The ADM subgrid scale model was able to clearly demonstrate the presence of the turbulent coherent structures found within boundary layers.

The evolution of heat from the combustion of hydrogen within the boundary layer is included through two methods. Firstly, finite rate chemical kinetics are used to model the combustion reactions of hydrogen pre-mixed with the boundary layer flow. Secondly, the finite rate chemical kinetics approach is used to develop an energy source term to represent the heat evolution without

the additional computational overheads of advancing the chemical reactions through time. The results from the numerical simulations with and without heat addition to turbulent boundary layers are presented and both methods of heat addition indicated reductions in wall shear stress. The analysis of the mechanisms of wall shear stress reduction used mean flow profiles, velocity fluctuation statistics, two-point spatial correlations, energy spectra, Reynolds stress transport budgets and instantaneous flow field visualizations.

Changes to the processes of turbulent momentum transport were observed. The contribution of the Reynolds shear stress ($\rho u'w'$) to the transport of momentum across the boundary layer was computed to be reduced by 40% when compared to the levels computed with no heat addition. Investigation of the Reynolds shear stress without density scaling ($u'w'$) revealed that not all of the reduction is tied up in the reduced mean density profile. The observation of changes to the turbulent velocity field was confirmed by lower levels of the RMS of wall normal velocity fluctuations. An explanation for the reduced wall normal velocity fluctuation levels was provided by the heat addition process reducing the pressure-strain velocity fluctuation redistribution from the streamwise to wall normal direction. This redistribution process is the dominant mechanism responsible for the supply of the wall normal velocity fluctuations and hence momentum transport to the wall. The turbulent structures were observed to be altered significantly with the near wall streaks increasing their coherence length in the streamwise and spanwise directions. The increasing streamwise coherence revealed a possible mechanism of wall shear stress reduction with the streak termination event, near wall ejections, demonstrating a significantly reduced contribution to the Reynolds shear stress which it normally dominates.

This work has shown that the changes that occur within the turbulent boundary layer can be captured using the LES technique. Additionaly, these changes that occur during the combustion process can be represented efficiently using a heat source approach. The hypothesis that the addition of heat to the boundary layer would not only induce a reduction in wall shear stress through mean property changes but also alter the turbulent coherent structures has been demonstrated.

Acknowledgements

There has been a great many people that have played a part in the completion of this work. Each has contributed in different but equally important ways that must be acknowledged.

I would like to first and foremost thank my finacé, Amber, for her tireless support and for maintaining my sanity. Thanks must also go to my parents Allen and Veronica and my brother Nicholas and sister Christina. Without their help and encouragement none of my achievements would have been possible.

My supervisor, Dr. Peter Jacobs has played a large role and must be thanked for his guidance and invaluable help throughout the period of this work. Often questions that would plague me for weeks could be cleared up in a manner of minutes. Similarly, I must thank Emeritus Professor Ray Stalker and Associate Professor David Mee for the many important discussions on this topic. The help of Dr. Steffen Stolz (ETHZ) was also important in implementing a part of the numerical scheme in my early candidature stages and must be acknowledged. Many colleagues have played a large role in my life over the past years. Special thanks must go to Rowan Gollan and Anthony Reid for all the coffee breaks, laughs and advice and to Tony Keating and Matthew Bilson for sparking my interest in computational fluid dynamics.

I would finally like to acknowledge the Australian Postgraduate Award Scheme, the Division of Mechanical Engineering and the University of Queensland Graduate School for financial support over the duration of this work. The Center for Hypersonics in conjunction with the Smart State Scheme of the Queensland Government also deserve thanks for the provision of the significant computing resources required.

Contents

List of Tables

List of Figures

Nomenclature

Symbols

α	filtering weights, sampling period
β	average structure angle, recycling method scaling parameter
C_f	skin friction coefficient, activation energy
C_h	heat transfer coefficient
$\mathcal{C}_{ij}$	turbulent convection
χ	relaxation regularization parameter
Δ^*	integral velocity defect thickness (m)
$\overline{\Delta}$	grid spacing (m)
δ	boundary layer thickness (m), Dirac delta
δ_2, θ	boundary layer momentum thickness (m)
δ_3	kinetic energy defect thickness (m)
d	hot-wire filament diameter (m)
D^t_{ijk}	turbulent diffusion
D^v_{ijk}	viscous diffusion
$\mathcal{D}_j$	subgrid scale viscous work
E	total energy per unit mass (J/kg), error estimator
$E_{\alpha\alpha}$	turbulent energy content
ε_{ij}	turbulent dissipation, grid convergence error
ϵ	internal energy per unit mass (J/kg)
ϵ_v	subgrid scale viscous dissipation
η	recycling to inflow station scaling parameter
f_i	mass fraction of species i
F_s	safety factor
$\mathcal{F}$	subgrid scale species turbulent transport
l	hot-wire filament length, mixing length (m)
L	domain length (m)
λ	wave speeds, representative length scale

G	filter function
γ	ratio of friction velocity at recycling station to inflow
H_{12}	shape factor, δ/δ_2
H_{32}	shape factor, δ_3/δ_2
H	enthalpy (J)
k	conductivity, wavenumber
k_f	forward reaction rate
k_b	backward reaction rate
M	freestream Mach number
μ	dynamic viscosity (Pa $\cdot$ s)
ν	kinematic viscosity (m^2/s)
ν_i	stoichiometric coefficients
P	pressure (Pa)
P_{ij}	turbulent production
Π_{ij}^d	presure strain
Π_{ij}^{dl}	pressure dilatation
Π_{dil}	subgrid scale pressure dilatation
Pr	Prandtl number
Q	source term
Q_j	subgrid scale heat flux
Q_N	deconvolution operator
r	refinement factor
Re_{δ_2}	$\rho_\delta \tilde{u}_\delta \delta_2/\mu_w$
Re_θ	$\rho_\delta \tilde{u}_\delta \delta_2/\mu_\delta$
ρ	density (kg/m^3)
τ	shear stress, subgrid scale stress (Pa)
R	gas constant
$\mathrm{R}_{\alpha\alpha}$	two-point correlation function
σ	viscous stress
s	Reynolds analogy factor
S	strain rate tensor
Sc	Schmidt number
T	temperature (K)
T_0	stagnation temperature (K)
$\mathcal{T}_j$	subgrid scale turbulent diffusion

t	time (s)
u, v, w	x, y and z-component of velocity (m/s)
u_τ	wall friction velocity (m/s)
U	freestream streamwise velocity (m/s)
V	volume of computational cell (m^3), diffusion velocity
$\dot{\omega}$	mean reaction rate
W	weighting function
x, y, z	streamwise, spanwise and wall-normal coordinate (m)

Superscripts

$+$	wall unit
$'$	fluctuation from mean value
$*$	deconvolved variable, semilocal scaling, van Driest transformation
$\hat{}$	spanwise average, test-filtered variable
$\overline{}$	grid filtered value
$\sim$	favre filtered value

Subscripts

aw	adiabatic wall condition
δ	boundary layer edge conditions
in	inflow plane conditions
∞	freestream conditions
r	recycling station conditions, recovery condition
t	turbulent
w	wall

CHAPTER 1

INTRODUCTION

One of the goals of scramjet powered hypersonic vehicles is to provide a cheap and reliable means for travel to low Earth orbit. To achieve this, such vehicles must travel through flight regimes where densities are high and turbulent boundary layers will be important. Drag due to viscous effects represents a significant proportion of the total drag on a supersonic or hypersonic body for turbulent boundary layers. When considering any propulsive systems, the total drag, including inviscid pressure and viscous skin friction forces, is very similar in magnitude to the thrust force generated. In this situation, any reduction in the viscous drag, even if small in comparison to the total drag, will result in proportionally large performance gains for the vehicle.

One proposed method of achieving a reduction in viscous drag or skin friction is through combustion in the boundary layer. Previous experimental shock tunnel work by Goyne et al. (2000) indicated that drag reductions of 50% were possible. These results were then compared to numerical simulations by Goyne et al. (2000) for the same geometries. The experimental and numerical results agreed that significant reductions were possible, however, the numerical results indicated less of a drag reduction. As well, those numerical simulations, using Reynolds averaged turbulent models, did not reveal the detailed mechanisms "at play".

Reynolds averaged Navier-Stokes (RANS) simulations only resolve the mean flow, while the effects of turbulence are added through a turbulent model. It is in the selection of a turbulence model where the difficulties lie. The flows encountered in realistic flight conditions are turbulent in nature and, as such, the numerical results are at the mercy of the turbulence model. Viscous drag is a difficult quantity to predict accurately. It requires an accurate representation of the turbulent flow

field. Large eddy simulation (LES) uses a spatial filter on the equations of motion. The effect of this filter is that turbulent eddies that are larger than the filter scale are resolved, while eddies that are smaller than filter scale are modelled. LES has the advantage that models are applied only to the smaller, more universal scales and are not required to model the entire turbulence spectrum. The purpose of this work is to use the more advanced LES turbulence modelling technique to not only get a better estimate for the possible drag reductions, but also give a much greater insight into the mechanisms occurring within the boundary layer that produce these reductions.

1.1 Turbulence in Supersonic and Hypersonic Flow

Turbulence plays a significant role in many aerodynamic applications. The significance demonstrates itself through many effects which include mixing in high speed propulsion systems, heat transfer to aerodynamic surfaces, aerodynamic performance through shock-boundary layer interaction, noise generation and wall shear stress (viscous drag).

With such large influence over many important facets of compressible flow, it is essential to gain proper understanding of what influence turbulence has. This idea is best illustrated through the example of the NASA X15 rocket plane that served as a test bed for early scramjets. A lack of knowledge of how the shocks interacted in the turbulent flow led to a severe flow impingement on the support arm of the scramjet module, suspended beneath the craft. This impingement of hot gas almost caused the support arm to be severed (Figure 1.1-1), while also inflicting significant damage to the underside control surfaces of the X15 flight vehicle. Obtaining an accurate understanding of how drag is induced by compressible boundary layers, along with methods of reducing its magnitude are of critical importance in designing the scramjet engines themselves. Currently, there exists a very small difference in the total drag on a scramjet and the thrust generated through combustion (Figure 1.1-2). Hence, only small nett thrust can be generated and any change in the magnitude of the total drag greatly affects the nett thrust.

On any scramjet model, the pressure (inviscid) drag is mostly fixed by the frontal area and the vehicle's shape. Vehicles that accelerate at hypersonic speeds will necessarily be slender. The viscous drag, representing approximately half of the total drag for slender vehicles, can on the other hand be reduced. Figure 1.1-2 (a) shows the breakdown of the inviscid forces in the axial direction. In other words, the figure shows the forces due to combustion and pressure drag over each section of the scramjet at varying test flow stagnation enthalpies (note that negative drag

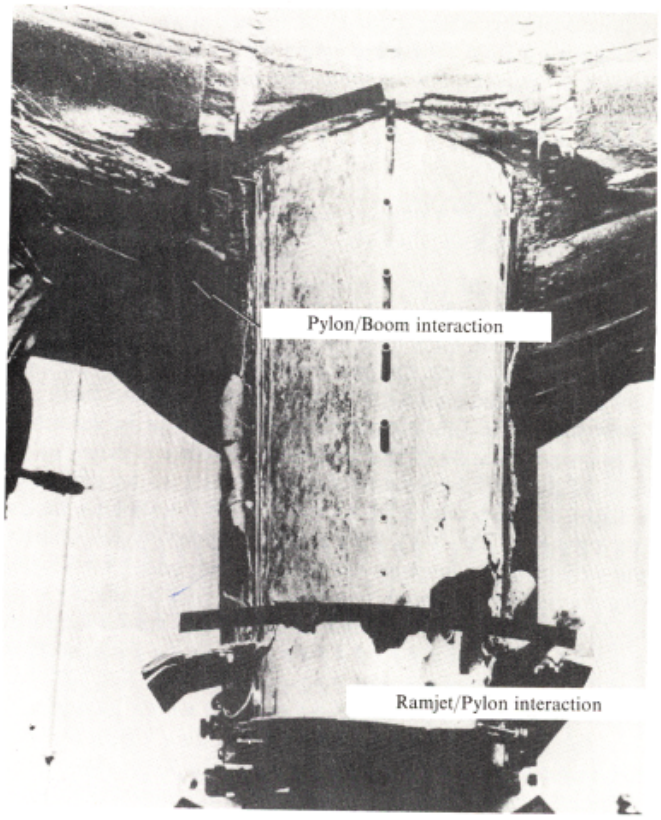

Figure 1.1-1: Damage to the X15 control surfaces and Scramjet boom (Anderson, 1989)

represents thrust). Figure 1.1-2 (b), shows the drag due to viscous effects on each component of a small scramjet engine that was tested in the T4 shock tunnel. As can be seen, it is only for stagnation enthalpies less than approximately 3.5 MJ/kg that the net inviscid thrust is greater than the viscous drag, albeit by a small margin. Hence, reduction in drag would not only yield a proportionally significant increase in thrust, but also permit flight conditions that would otherwise not be feasible.

1.2 Viscous Drag Reduction

Much work over time has been dedicated to the study of reducing drag reduction. Before giving an explanation of how viscous drag can be reduced, it is important to define what viscous drag is.

Viscous drag at the wall (τ_w) is governed by equation (1.1) where μ is the viscosity of the fluid

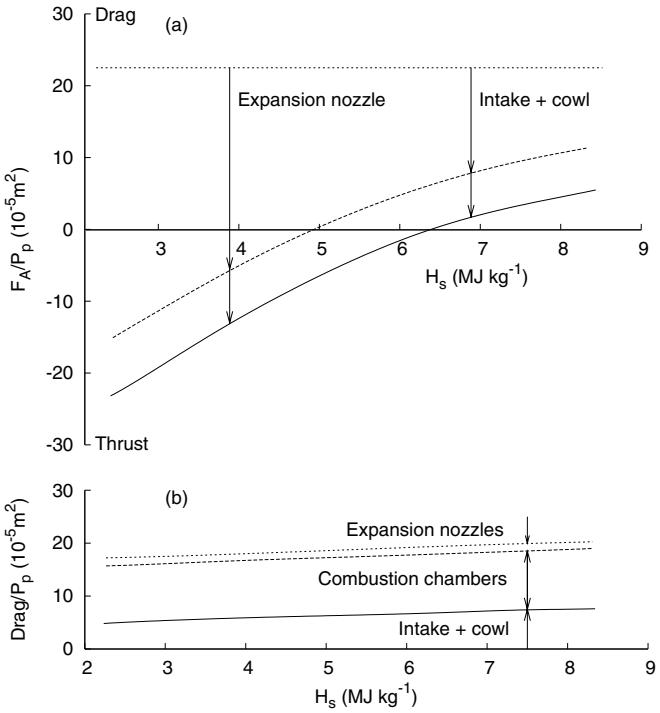

Figure 1.1-2: Thrust and drag on a simple scramjet with combustion. (a) Inviscid axial force, (b) viscous drag. (Paull et al., 1995)

and $\frac{du}{dz}_w$ is the gradient of fluid velocity at the wall. The skin friction coefficient c_f is related to the viscous drag at the wall by equation (1.2) where ρ and U are the density and velocity of the fluid in the free stream respectively.

$$\tau_w = \mu \left(\frac{du}{dz} \right)_w \tag{1.1}$$

$$\tau_w = \frac{1}{2} C_f \rho U^2 \tag{1.2}$$

With the turbulent skin friction representing a large fraction of the total drag on a body at supersonic and hypersonic speeds, it is reasonable to attempt to reduce its magnitude. There has been a variety of methods studied, ranging from passive methods such as surface modifications (riblets, Walsh and Weinstein (1978)), to more active methods of gas injection within the boundary layer (Suraweera, 2006).

While both passive and active techniques have shown significant reductions in turbulent skin fric-

tion, active methods of gas injection appear to be more robust at hypersonic flow conditions (Suraweera, 2006). For instance, longitudinal grooves in a surface, known as riblets, perform well when the riblets are aligned with the local streamline direction. However, under non-ideal conditions their effectiveness is lowered. Furthermore, riblets have not been studied under high supersonic and hypersonic conditions so their effectiveness is unknown. Consequently, this section will focus on turbulent drag reduction through gas injection into the boundary layer. The injection of gas into a turbulent boundary layer generally falls into one of two categories;

- Film cooling
- Boundary layer combustion

1.2.1 Film Cooling

The injection of gas into a boundary layer, either tangentially, or at an angle to the mainstream flow, with the aim of reducing near wall momentum is known as film cooling. While not only reducing skin friction, film cooling also provides a means of thermal protection by reducing wall heating loads. In general, this method entails the injection of some cool, low density gas into the boundary layer of the flow. The cooled gas then reduces the heat transfer to the wall and cools the wall itself. This in turn causes a decrease in Stanton number (C_h) as can be seen via equation (1.3). The Stanton number is a measure of heat flux, $\dot{q}$:

$$\dot{q} = C_h \rho U (H_{aw} - H_w) \tag{1.3}$$

with H_{aw} and H_w being the adiabatic wall and wall enthalpies respectively. The transfer of momentum and heat can then be related via the Reynolds analogy. The Reynolds analogy assumes that the pressure gradient is zero and relates the skin friction to heat transfer as:

$$\frac{C_f}{2} = C_h Pr \tag{1.4}$$

Hence, it follows that a decrease in Stanton number can yield a decrease in skin friction coefficient.

This process has a limited downstream effect since the gas in contact with the wall heats up and mixes with the surrounding fluid, eventually returning the heat transfer rate to its normal value. A more long term effect, however, is noticed through the boundary layer growing thicker, hence reducing the velocity gradient and the wall and, therefore, skin friction.

Rubesin (1954) performed an analysis based on mixing-length theory to show that, for a turbulent boundary layer on a flat plate, injection of a cool low density gas results in large reduction in both heat transfer and skin friction. Following this hypothesis, investigations were undertaken to ascertain its effectiveness and validate this theory. In doing so, a number of different injectant gases were used, along with different injection techniques.

Cary and Hefner (1972) investigated the effectiveness of film-cooling at Mach 6. The cooled gas was injected through a slot at sonic speed, orientated tangentially with the flow along a flat plate. The cooled gas had approximately 60% of the total temperature of the free stream gas. They found that higher free stream Mach numbers resulted in greater skin friction reductions through comparison to baseline results at Mach 3. These improvements were attributed to longer mixing lengths for the higher Mach number flows. However, once mixing began, the greater velocity difference between mainstream and injectant flows led to rapid mixing and decay in skin friction reduction effectiveness. Reductions in skin friction of 40 - 80%, depending on injector size, were found to occur close to the point of injection (with downstream distances of the order of 10 slot heights). However, these reductions quickly deteriorated to between 0 and 20% the further downstream the flow proceeded. These results correlated well with the theory presented above through the Reynolds analogy and the fact that thermal mixing reduced the downstream effectiveness of the technique.

Parthasarathy and Zakkay (1970) also used film cooling to evaluate the performance of coolant gas injected through a tangential slot. The tests were conducted at Mach 6 with a ratio of coolant gas to free stream temperature of 0.635. The test apparatus was instrumented with pressure tapings, heat transfer gauges and a Pitot pressure probe. Using a combination of data from traversing the boundary layer with the Pitot tube, along with static pressure and temperature measurements, the boundary layer profile and, hence, skin friction was reconstructed. As was the case for film cooling through tangential slot injection by Cary and Hefner (1972), the greatest reductions in skin friction were found near the injection slot. A maximum reduction of 60% was recorded in the vicinity of the injection slot. These reductions were correlated with reductions in heat transfer measured, with hydrogen and helium performing the best. An overall reduction of 12% was noted

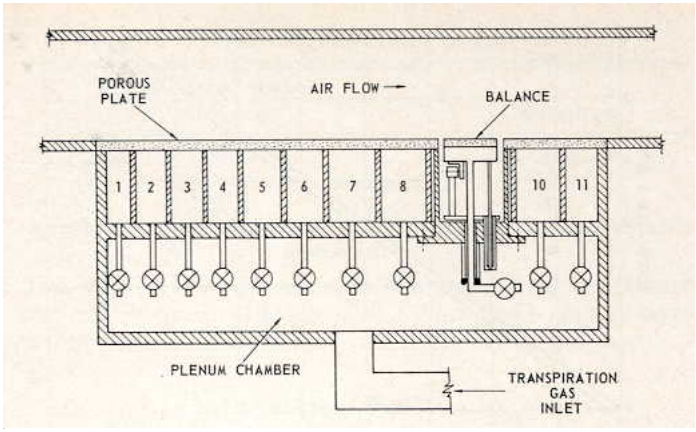

Figure 1.2-1: Porous plate injection test section schematic of Dershin et al. (1967)

when integrating along the surface until the heat transfer returned to the no coolant injection case.

Dershin et al. (1967) also studied the phenomena of film cooling, but used a porous flat plate as the method of mass injection. The injectant gas was nitrogen and it was injected through the plate both before, after and through the skin friction balance (See figure 1.2-1). The experiments were conducted at a nominal Mach number of 3.2 and at a Reynolds number (based on boundary layer momentum thickness) of 3.34×10^4. Reductions of up to 80% were found for increasing amounts of nitrogen injected through the porous plate. More importantly, this work once again showed that the Reynolds analogy presented above, developed by Rubesin (1954), was accurate over the test conditions.

With two methods of coolant injection, Schetz and Van Overeem (1975) undertook a study to compare the relative performance of slot and porous plate injection. The work was performed in the supersonic regime with freestream conditions of Mach 2.9 and total temperature and pressure of 290K and 690kPa respectively. The wall shear stress was measured with floating element balances, much like Dershin et al. (1967). Static pressure and temperature were also measured. All shear stress measurements were taken from the same downstream location with slot injection being performed at the leading edge of the porous plate. The tangential slot was found to provide the greatest reduction in wall shear per unit rate of injection with skin friction levels falling to 30% of the no injection case. Of the two injectants tested, injection of helium performed better than air in reducing skin friction. Schetz and Van Overeem (1975) found that the porous injection method suffered from a roughness-induced rise in shear, identified by only injecting through the slot with the porous plate in place.

Some more recent work on film cooling has been performed by Olsen and Nowak (1995) for a flat plate in Mach 6.4 flow, both with and without incident and swept oblique shock interactions. Both hydrogen and helium were injected into a nitrogen flow field to preclude combustion of the hydrogen coolant gas. Hydrogen achieved 10 - 20% greater reductions in heat flux than helium. The presence of shock waves, expansions and re-compression regions were found to reduce the effectiveness of film cooling. The effectiveness was inversely proportional to the incident shock angle. There were no gains in heat flux reduction in the region downstream of the injection point with increasing coolant mass flow rate. This result indicated that a series of smaller slots spaced in the downstream direction would prove to be a better use of a given coolant mass than injecting all coolant at the leading edge.

Much of the experimental work in skin friction reduction has focused on turbulent flows. However, for completeness, the work performed by Richards and Stollery (1979) on film cooling in laminar hypersonic flow will also be summarised. In this work multiple coolants were injected tangentially to the flow through a slot downstream of the leading edge of the plate at sonic speed. It is due to the lack of turbulent mixing in the laminar flow that greater downstream drag reduction was inferred through reduction in heat flux toward the wall. It is through the lack of mixing that the cool gas remains close to the wall and thus has greater impact. Significant heat flux reductions persisted hundreds of slot heights downstream. A range of injectants were tested, including hydrogen, helium, freon, argon and air. For a given mass flow rate, hydrogen was assessed to be far more effective than any other injectant gas. This trend was reported to follow the inverse of the molecular weight of the gas. Thus, hydrogen was found to be far more effective than helium, which itself is far more effective than air due to the very low molecular weight.

Consequently, hydrogen presents itself as a good candidate for use in drag reduction due to the low molecular weight. This, along with the fact that it is the preferred fuel for scramjets means that, in flight, it would be readily available. The experiments of Richards and Stollery (1979) were done at conditions where hydrogen would not combust. However, realistic flight conditions would sustain hydrogen combustion through viscous heating in the boundary layer. Consequently, further study was required in these flight regimes to ascertain the effect hydrogen combustion would have on the heat transfer and skin friction.

1.2.2 Boundary Layer Combustion

Results of slot injection film cooling experiments had identified hydrogen as a useful skin friction reduction injectant. However, at high speeds, viscous heating within the boundary layer generates temperatures that can sustain hydrogen combustion. Experimental data suggests that turbulent skin friction is reduced by two main processes when combustion occurs within the boundary layer. Firstly, the temperature rise induced by combustion can result in a reduction in flow density which in turn lowers the turbulent Reynolds stresses. It is through the turbulent Reynolds shear stresses and viscous effects that momentum of the fluid is lost to the wall. Hence, it is reasonable to expect that any reduction in turbulent Reynolds shear stress would reduce turbulent skin friction. While this connection can be considered to be rather tenuous, it is the purpose of the present study to identify if other changes such as turbulent velocity transport are significant. Secondly, the combustion results in a thickening of the boundary layer near the wall, decreasing the near-wall velocity gradients and density, giving rise to further reductions in turbulent skin friction levels.

The injection of a gas into a boundary layer for the purposes of combustion was first studied for low, subsonic speeds. Kulgein (1962) injected methane through a porous wall and noticed a reduction in skin-friction from the combustion process. No significant alteration to the Stanton number was identified. The effects of elevated temperature from combustion were offset by the pronounced lowering of the near wall gradients. It was observed that the presence of a reaction zone had no effect on boundary layer turbulent transport other than the associated effects of elevated temperature on molecular transport and thermodynamic properties. In essence, no evidence was found of any reaction generated/inhibited turbulence. Turbulence levels near the wall were, however, observed to increase as a result of mass injection.

Porous wall combustion experiments were also undertaken by Wooldridge and Muzzy (1962) by injecting hydrogen, diluted with nitrogen into subsonic flow. This work introduced the encouraging result for analytical studies that the turbulent Prandtl number could be taken as unity within a turbulent boundary layer. Under a similar configuration, the experimental data of Jones et al. (1971) demonstrated that the combustion significantly altered the velocity and temperature profiles. The near wall velocity gradient and hence skin friction was observed to decrease markedly from cases where there was no combustion. These changes were largely attributed to alterations to the local mean density and viscosity. Multiheaded probes, similar to those of Wooldridge and Muzzy (1962) were used to measure mean flow properties. No turbulence data was measured, however, giving no insight into the influence combustion has, if any, on turbulent transport.

From subsonic flow, the investigation of boundary layer combustion in supersonic flow was a logical progression. Burrows and Kurkov (1973) took detailed composition, Pitot-pressure and total-temperature profiles downstream of a hydrogen injection slot for a Mach 2.44 vitiated air stream. Combustion was observed and profile measurements were taken both near the inlet and exit planes of the experimental apparatus. Tests were also performed by injecting hydrogen into an inert test gas to remove the complication of combustion from the mixing process and to assess the film cooling behaviour. The slow rate of depletion of hydrogen near the wall suggested to the authors that the injection of hydrogen would also provide a good means of skin friction reduction through film cooling with combustion adding to the reductions.

To realise the goal of making supersonic and hypersonic flow more feasible it was necessary to study conditions at higher Mach numbers. The work of Goyne et al. (2000) (first presented in Goyne (1998)) focused on the injection of hydrogen into the supersonic compressible boundary layer through a tangential slot in a duct (Figure 1.2-2). For a mainstream Mach number of 4.5, skin friction, heat transfer and pressure measurements were taken down the duct at equispaced locations (Figure 1.2-2a). The experimental study was conducted in the reflected shock tunnel facility at the University of Queensland. Consequently, high enthalpy flows were studied with the trade off being short test times, of the order of 3 ms. This precluded any turbulence measurements from being made. The experimentally measured skin friction results were compared with the results of numerical simulations using finite-rate chemistry for the combustion processes developed by Brescianini (1993). The numerical analysis solved the two dimensional parabolized Navier-Stokes equations and included the effects of turbulence with the $k - \epsilon$ RANS model. Wall functions were used to remove the subsonic regimes from the flow solution. The conditions within the simulated boundary layer were sufficient to support combustion of the injected hydrogen. The numerical simulations indicated that combustion caused a reduction of approximately 50% in the skin friction. The experiments, on the other hand, yielded an even greater reduction, with decreases of 70 - 80% when compared to the case with no injection. These discrepancies suggest that there are some turbulent transport mechanisms occurring that can not be captured by the RANS simulation. The data also allowed for the estimation of fuel mixing length by measuring the distance downstream to a significant pressure rise.

The experimental measurements and numerical calculations of Goyne et al. (2000) are reproduced in figure 1.2-3 to demonstrate the differences. In interpreting figure 1.2-3, the three cases presented are for increasing hydrogen mass flow rates (0.015, 0.029 and 0.043 kg/s respectively for cases 1, 2 an 3). C_f is the measured skin friction coefficient and C_{fn} is the local skin friction coefficient

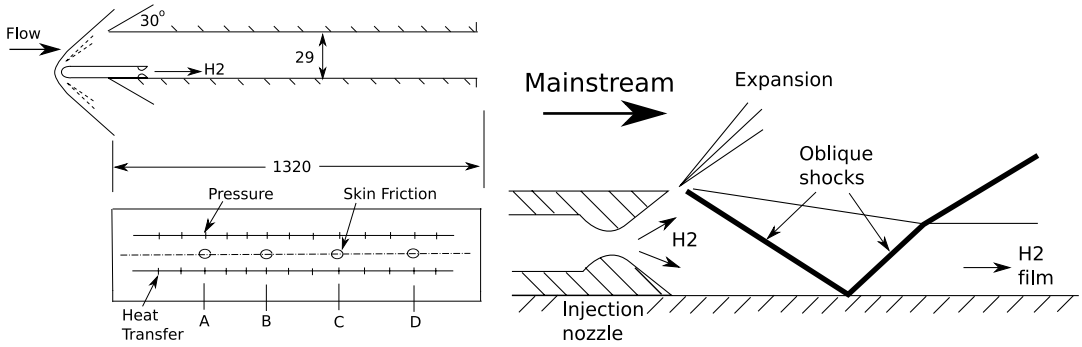

(a) (b)

Figure 1.2-2: Experimental setup of Goyne et al. (2000) (a) test section (b) injection and formation of hydrogen film (dimensions in millimeters)

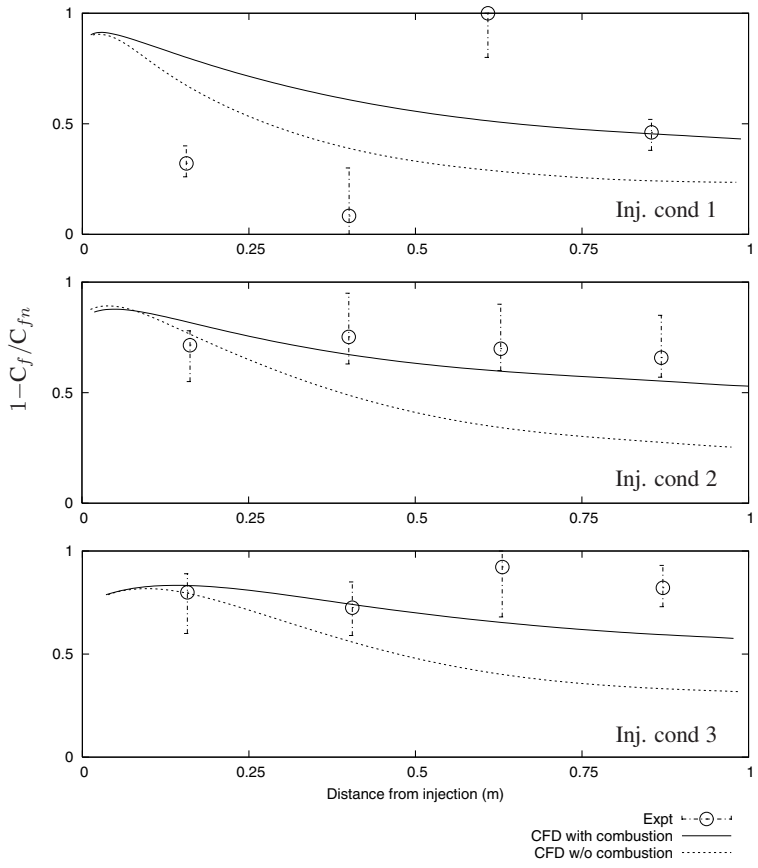

Figure 1.2-3: Skin friction measurements (Goyne et al., 2000)

without hydrogen injection. Hence, a value closer to unity indicates a greater reduction in skin friction.

The combustion of hydrogen had the added benefit of having a skin friction reduction persist for a much greater downstream distance than film cooling alone. The numerical computations showed that the reductions persisted for 5m, approximately 500 injector heights (Figure 1.2-4, Case 2 shown). Unlike in film cooling, the experiments and numerical simulations indicated that the Stanton number was not significantly affected once combustion occurred. Rather, the effect of the combustion was manifested through changes in the mainstream flow. This may indicate that combustion away from the wall (ie. inside a scramjet combustor) could also influence the skin friction. However, Goyne et al. (1999) found that supersonic combustion in the central regions in the experimental scramjet duct did not affect the skin friction levels.

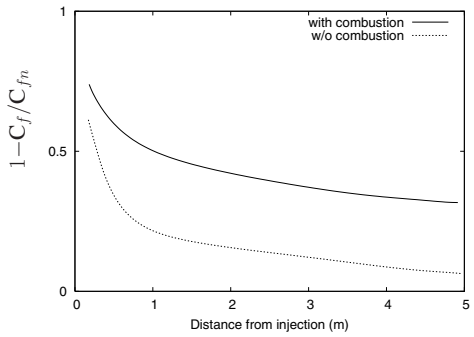

Figure 1.2-4: Downstream effect of boundary layer combustion. (Goyne et al., 2000)

The distance to the initiation of combustion is also of paramount importance to high speed propulsion systems. Rowan (2003) examined the effect of mixing and combustion of hydrogen in the mainstream flow through the use of injection, both normal and tangential to the flow. While skin friction reductions were observed, the tangential injection did not enhance the overall performance of the combustion system.

Suraweera (2006) extended the work of Goyne et al. (2000) to study hydrogen injection into turbulent boundary layers for varying stagnation enthalpies and Reynolds numbers. Nitrogen test gas was used in conjunction with experiments in air to assess the effects of combustion and separate out effects due to film cooling. Similar to Goyne et al. (2000), reduction in skin friction of between 60 and 80 % were observed when comparing to experiments with no hydrogen injection. For the conditions investigated, the Reynolds analogy factor ($2\,C_h\,/\,C_f$) was observed to fall well below the commonly accepted value of ~ 1.0 for turbulent transport. At high skin friction

($> 3.0 \times 10^3$), the Reynolds analogy factor approached 0.3 both with and without hydrogen injection. Molecular dissociation of oxygen was eliminated as a cause, with the results of nitrogen test gas giving similar low Reynolds analogy values.

Larin and Levin (1999) studied numerically, in two dimensions, the effects of heating within a turbulent boundary layer. Results indicated a large reduction in skin friction with a high correlation between increasing heat addition and increasing skin friction reductions. However, there was no indication of how turbulent transport or other properties changed to produce such reductions. This work was extended (Levin and Larin, 2003) to study the effect of electric discharge, modelled through heat addition, within a turbulent supersonic boundary layer at Mach 3. Through quantification of skin friction reduction per amount of added heat, it was possible to arrive at an optimum level of heat addition. Burtschell and Zeitoun (2004) numerically investigated hydrogen combustion within a boundary layer with a strong shock interaction. A two-dimensional axisymmetric finite volume Navier-Stokes code was used to study steady state behaviour. No turbulence modelling was performed and hydrogen combustion was included through one global chemical reaction:

$$H_2 + \frac{1}{2}O_2 \longrightarrow H_2O$$

One of the main goals of the work was to assess and minimize the influence of the hydrogen injection on the flowfield structure. Interestingly, it was again observed that hydrogen combustion reduced heat transfer to the wall.

While experiments and numerical calculations are important, they can be time consuming to complete. An analytical method, on the other hand, would provide a means of estimating skin friction reductions without the time requirements. Stalker (2005) undertook an analytical study into controlling the skin friction within turbulent hypersonic boundary layers by combustion of hydrogen. Shvab-Zeldovich coupling was used in conjunction with the theory of Van Driest to include the effects of hydrogen combustion on the boundary layer. While limiting the analysis to instantaneous combustion of hydrogen, rather than finite-rate reactions, a process was devised to quickly predict the potential skin friction reductions at conditions other than those studied experimentally or numerically. The inclusion of a spontaneous hydrogen combustion reaction, while overpredicting the heat release, provided an upper limit and best approximation for potential drag reductions.

The analysis indicated that the drag reduction for injection and combustion of hydrogen increase three times over the reduction of injection and mixing alone. Interestingly, the analytical results fell between the experimental and numerical results of Goyne et al. (2000). The analytical results

overpredicted the numerical results by 10% or more, while remaining within the limits of measurement accuracy of the experimental measurements. The heat transfer to the wall was observed to decrease with combustion as per the numerical results of Burtschell and Zeitoun (2004) and experiments of Suraweera (2006). It was found that the decrease in near wall temperature gradient outweighed the temperature increases due to combustion.

As is clearly evident, there has been significant research into combustion within turbulent boundary layers. However, to date, there lacks a quantitative understanding of the effects heat addition through hydrogen combustion has on the turbulent structures within supersonic and hypersonic boundary layers. To address this issue, turbulent boundary layer flow will be studied using high resolution numerical procedures in a domain abstracted from the flows commonly found inside scramjets. An example of the regular rectangular domain that is used for this work is given in figure 1.2-5.

1.3 Objectives

The objectives of this research were:

1. To evaluate the performance of currently used subgrid-scale models used in LES - The eddy-viscosity/eddy-diffusivity model and the approximate deconvolution model.
2. To investigate the performance of LES for the calculation of turbulence quantities and near wall transfers for supersonic turbulent boundary layers with and without combustion.
3. To calculate a full set of turbulence quantities within turbulent boundary layers with and without combustion.
4. To provide a quantitative analysis of the effects of hydrogen combustion and heat addition within supersonic turbulent boundary layers.

1.4 Thesis Outline

The following section gives a brief outline of each chapter comprising this thesis.

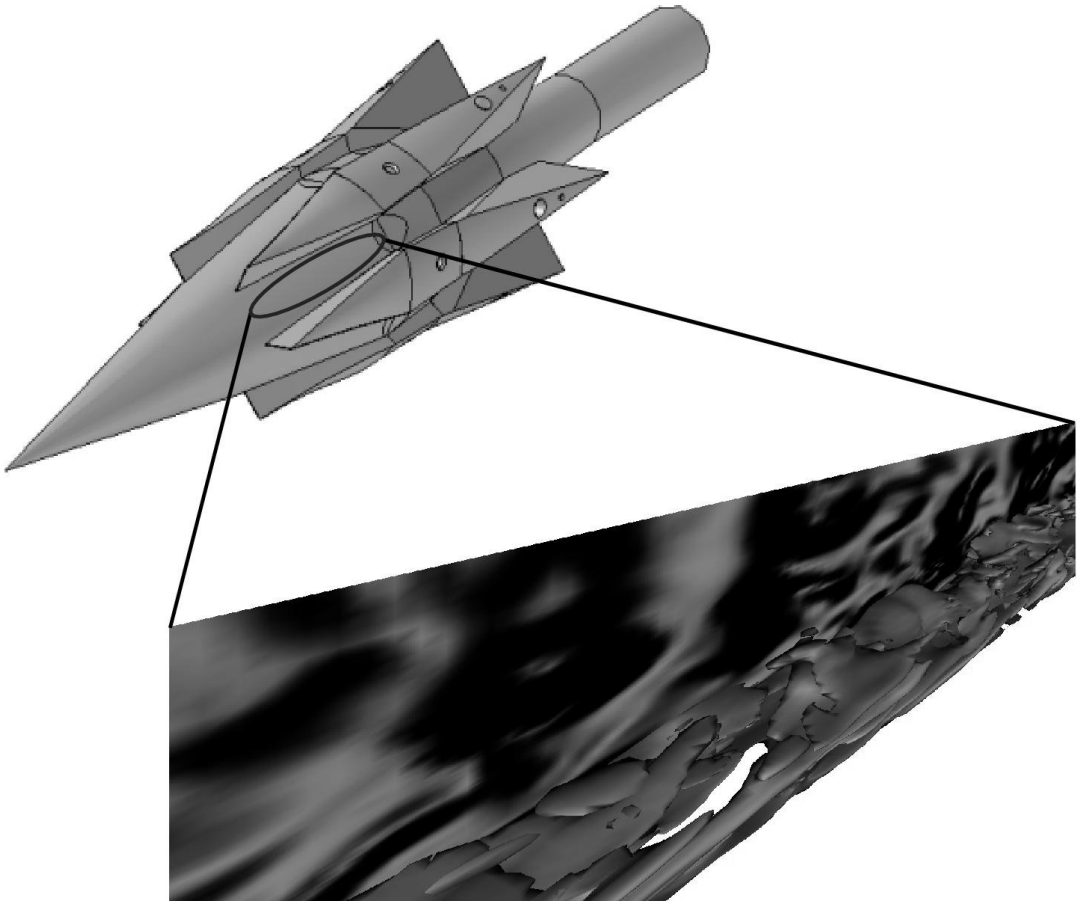

Figure 1.2-5: Example of abstraction of boundary layer flow domain from scramjet flow. Upper left shows a scramjet with the outer cowling removed. Iso-surfaces of vorticity and contour plane of density gradient for the corresponding boundary layer flow shown on the lower right. Scramjet image used with permission (Tanimizu et al., 2006).

Chapter 2 provides a review of the research conducted previously related to the objectives of this research. Experimental work relevant to the validation of the numerical schemes used and the associated measurement techniques is presented. Previous CFD studies of supersonic turbulent boundary layers are also discussed.

Chapter 3 presents the governing equations that describe compressible turbulent flow of a Newtonian fluid. The models and boundary conditions used in closing these governing equations are presented in detail.

Chapter 4 goes through the verification and validation process of the code and numerical techniques by applying it to zero-pressure gradient supersonic turbulent boundary layer flow. The conditions were chosen for the highly desireable ability to make comparisons to both experimental

and Direct Numerical Simulation data sets. Comparisons were also made to experimental results under differing conditions through appropriate normalization. The results allow for identification of dominant transport mechanisms within the compressible turbulent boundary layer.

Chapter 5 presents the results of simulations where heat is added within the supersonic boundary layer via either a source term approach, or through finite rate chemical kinetics. The results are validated against available experimental data. A verification and validation procedure is once again used for the simulations where no heat is added such that a larger experimental data set could be drawn upon. The effect of heat addition on the dominant transport mechanisms is then studied.

Chapter 6 concludes the work with a summary of the influences of heat addition on flow properties and transport mechanisms. Suggestions are made for future research into drag reduction in supersonic turbulent boundary layers through combustion processes.

1.5 Accomplishments

Throughout the course of this work the following accomplishments were made:

1. A highly parallel LES and by default DNS code was developed.
2. The code was validated against DNS and experimental results for supersonic turbulent boundary layers.
3. It was demonstrated that the approximate deconvolution model with relaxation regularization was superior in calculating turbulent quantities and near wall transfers compared to the eddy-viscosity/eddy-diffusivity model for supersonic boundary layer flow.
4. The first LES calculations of supersonic boundary layer flow with hydrogen combustion within the boundary layer were performed.
5. It was demonstated that the addition of heat to the boundary layer results in changes to not only mean quantities such as velocity, density and temperature, but also coherent turbulent structures:

- Reynolds shear stress ($\rho u'w'$) and incompressible Reynolds shear stress ($u'w'$) are noticeably reduced.
- The turbulent ejection process, which makes a significant contribution to turbulent transport of momentum is reduced by approximately 40%.
- Streaks (quasi-streamwise near wall vortices) enlarge with heat addition.
- The pressure-strain redistribution of turbulent velocity fluctuations is diminished.
- Baroclinic torque increases in the boundary layer log-law region and reduces the entrainment of mainstream velocity into the boundary layer by creation of a more diffuse vortex structure.

CHAPTER 2

PREVIOUS COMPRESSIBLE TURBULENCE STUDIES

The previous chapter identifies boundary layer combustion as being a great prospect for the reduction of skin friction in supersonic and hypersonic flight. However, little understanding is possessed by the general community about how these drag reductions occur and what mechanisms are causing them. Thus, to identify these mechanisms, high resolution turbulent numerical simulations are to be used. Before this can be done, the code behaviour must be verified and the results validated against available experimental and numerical data. This chapter examines previous work relevant to supersonic zero pressure gradient turbulent boundary layer flows and is divided into two main sections that consider experimental and numerical work.

2.1 Experimental Work

Because of their significance and simplicity of geometry, supersonic boundary layers have been studied since the early 1950's. The early experiments made measurements of the mean flow properties under mainly adiabatic wall conditions. With the exception of Morkovin and Phinney (1958), it was not until the 1970's that experiments began to measure turbulent fluctuations. Consequently, the major experimental work studying turbulent supersonic boundary layers will be reviewed in three main categories:

- Experimental turbulence measurement techniques

- Mean flow measurements
- Mean flow and turbulence measurements

2.1.1 Experimental Turbulence Measurement Techniques

Before using experimental data for quantitative comparison purposes it is important to briefly remind ourselves of the limitations and restrictions inherent in measuring turbulent quantities even when great care is taken. Further discussion is given for the two main sources of experimental measurements used in this work:

- Hot wire anemometry
- Laser Doppler anemometry

Hot Wire Anemometry

Hot wires have been used extensively in turbulent flow measurements and are still in common use today. In a simple hot wire arrangement, a sensing filament wire spans the space between two supporting prongs. There are two main types of hot wire anemometers; constant temperature and constant current. Constant temperature hot wires use a feedback loop to keep the temperature and resistance at a constant level while using fluctuations in current to deduce fluctuations in heat transfer. Constant current hot wires use a constant current source to heat the filament while making measurements of fluctuating heat transfer from changes in resistance. Two wires can also be used together in a crossed configuration.

To withstand the conditions within supersonic flows, the prongs which hold the wires are tapered to minimise their effect on the flow, while the spacing between the probes and, hence, wire length, must be kept to a minimum to reduce deflections. If mounted normal to the flow, detached shocks can form and measurements must be compensated for this effect. If crossed wires are used, care must be taken to avoid shocks from one wire interfering with the other wire.

Fluctuations of mass flux can also be made by altering the overheat ratio of the wires. At low overheat ratios the wire output is sensitive to thermal fluctuations and largely insensitive to mass

flux variations. Alternatively, for high overheat ratios, the sensitivity now lies with mass flux variations rather than thermal fluctuations. Similarly, by operating at a range of overheat ratios and time averaging the results, turbulent stresses can also be measured.

The difficulty in using hot wires arises in the selection of a filament length (l) and diameter (d). Spatial resolution and, hence, near wall resolution, deteriorates and wire breakage is more common for l/d that is too large. The signal deteriorates because the velocity measured is a spatial average along the length of the sensor, while also being a function of any non-uniformities of temperature distribution. Compounding this problem is the fact that near the wall, the turbulent structures become smaller, further impacting on the spatial resolution of the wire. When the flow becomes transonic, additional sensitivities must be take into account. Alternatively, an l/d that is too small ($l/d < 200$) leads to non-uniform temperature distribution along the wire and significant conduction to the prongs (Smits and Dussauge, 2006). Perry et al. (1979) found that end conduction effects could lead to errors of 10% in *RMS* levels for incompressible flows. It is reasonable to assume similar introduction of error for compressible flows (Smits and Dussauge, 2006).

The selection of wire length is also critical in terms of the quantities measured. Ligrani and Bradshaw (1987) found significant alterations to peak values of normalised streamwise velocity fluctuations (40%) when the wire length was decreased from $l^+ = 60$ to $l^+ = 3$ ($l^+ = l\,u_\tau/\nu$, where u_τ is the friction velocity). It was concluded that to maintain adequate resolution of turbulence to within $\pm\,4\%$, the probe must satisfy $l/d > 200$, leading to very thin and fragile wires.

The frequency response of a hot wire is another important consideration, with the frequency of the turbulent fluctuations generally much higher than the frequency response of the wire (Laderman and Demetriades, 1974). An electronic compensator can be used to resolve the entire frequency content of the flow. Kistler (1959) states that to obtain turbulent intensities to within 5%, the frequency response for the hot wire should exceed $5\,U_\infty/\delta$. For the work of Konrad and Smits (1998), this limitation equates to a frequency response of 100 kHz. This criteria applies for *RMS* measurements for single wires, with measurements for crossed wires being more stringent. Konrad and Smits (1998) report that given the frequency response achieved in their study, the Reynolds shear stress could be underestimated by more than 10%.

Laser-Doppler Velocimetry

Laser-Doppler velocimetry (LDV) is an optical method that measures the velocities of particles seeded within the flow. Some advantages of LDV over hot wire anemometry is that the measurements are of velocity only, hence being unambiguous and the method is non-intrusive, requiring no probes be inserted into the flow. The downside to this method is that the measured velocities belong to the particles that are seeded into the flow, not the flow itself. The particles must on one hand be sufficiently large to be detected, but on the other hand, be sufficiently small that they will follow the flow. The problem becomes even more severe in regions of large velocity gradients (Smits and Dussauge, 2006). The problem of how to introduce the seeding particles is also important, taking away somewhat from the claim of being a non-intrusive method.

In terms of spatial resolution, the LDV technique commonly has a resolution of $200\mu m$ whereas, hot wires are typically no smaller than $500\mu m$ (Smits and Dussauge, 2006). Time histories and space-time correlations are not able to be extracted from LDV data due to the burst-counter approach used to compute the particle velocities.

The various advantages and disadvantages of LDV when compared to hot wires results in overall uncertainties that are not dissimilar. Smits and Dussauge (2006) inspected some typical high quality LDV data and observed accuracies of $\pm 15\%$ in peak values of $\overline{u'^2}$, and $\pm 20\%$ in $\overline{u'v'}$. When measurements using hot-wires and LDV for the same supersonic boundary layer flow are compared, there can exist good agreement between the two techniques (Johnson and Rose, 1975) but there can equally exist some disagreement (Elena and Lacharme, 1988).

2.1.2 Mean Flow Experiments

Compressible turbulent boundary layers differ from those found in incompressible flow. Where the Reynolds number was the most important parameter for incompressible flow, the Mach number becomes an additional parameter for characterising compressible flows. As the velocity decreases towards the wall, a significant Mach number gradient is created. Strong temperature gradients are also generated by the large amounts of viscous dissipation near the wall, introducing Reynolds number variations across the boundary layer that would not exist for incompressible flow. These variations create high viscosity, low density regions where viscous effects become more dominant than they would in a subsonic flow of similar Reynolds numbers.

These significant differences in boundary layer behaviour introduce the requirement for compressible experimental boundary layer data to validate numerical codes. The compilations of Fernholz and Finley (1977) and Fernholz and Finley (1980) provide a concise review of a large portion of the early work on turbulent compressible boundary layer data. It is these early works that provide some of the most reliable data sets, as the fundamental behaviour of turbulent boundary layers was foremost in their minds. Contained within these reports are experimental studies where the experimental arrangements, test conditions and boundary conditions are well documented and a series of mean quantity profiles across the boundary layer are provided.

There is a large volume of experimental work in the compilations for supersonic turbulent boundary layers for varying conditions (zero pressure gradient, favourable pressure gradient, adverse pressure gradient, etc). The validation and verification of this work is primarily concerned with zero pressure gradient flat plate boundary layers. As such, a subset of the documented experiments has been drawn drawn from the compilations.

The work of Coles (1953), Shutts et al. (1955) and Mabey et al. (1974), compiled in Fernholz and Finley (1977, 1980), all studied flat plate boundary layer growth under zero pressure gradient conditions with adiabatic walls. The results reported provide a detailed database of the fluid dynamics within compressible turbulent boundary layers for Mach numbers in the range of 1.7 to 4.5 and Reynolds numbers (Re_θ) from 2 $\times 10^3$ to 26 $\times 10^3$. Unless otherwise stated, the Reynolds number is based upon the momentum thickness, θ, of the boundary layer. It is the upper end of the Mach number range that is of interest for its proximity to the conditions studied with boundary layer combustion within a scramjet.

The work of Coles (1953), cited by Fernholz and Finley (1977, 1980), was performed in a continuous wind tunnel at Mach numbers of 2.0, 2.6, 3.7 and 4.5 with Re_θ of 2000 - 10000. The test boundary layer was formed on the lower surface of a flat plate mounted slightly below the tunnel centre-line. Profile measurements were made using a wire fence trip. Twenty seven static pressure holes were provided along with three copper-constantan thermocouples and three floating element balances for wall shear stress measurements. Mabey et al. (1974), cited by Fernholz and Finley (1977, 1980) studied six Mach numbers from 2.5 - 4.5 for a zero pressure gradient adiabatic flat plate flow. Reynolds numbers ranged from 5000 - 26000. Twenty two instrument plugs were provided arranged in five longitudinal rows along the plate centreline. Both investigations provided mean flow profiles, skin-friction coefficients and boundary layer shape factors. The shape factors of a boundary layer are calculated as various ratios of boundary layer displacement, momentum

and 99% thickness. It is a challenging task for three-dimensional Navier-Stokes codes to predict skin-friction coefficients and shape factors as it requires accuracy throughout the entire boundary layer. Hence, these quantities provide a good check for a numerical code.

Shutts et al. (1955), cited by Fernholz and Finley (1977), undertook a study of turbulent boundary layers, making skin friction measurements on a smooth, thermally insulated flat plate at Mach 1.7 - 2.5 and Reynolds numbers from 6 $\times 10^3$ to 12 $\times 10^3$. Eight instrumentation stations were provided along the plate centre-line at 4 inch intervals for wall shear stress and profiles (velocity and temperature). Static pressure was measured at 2 inch intervals on the centre-line of the plate. Static pressure, velocity and temperature profiles and wall shear stress were measured on separate runs. The wall shear stress was measured using balances that were 1 inch in diameter. Traverse gear was used for profile measurements. The authors interpolated the static pressure readings to the locations of the profile measurements and assumed no variation in static pressure through the boundary layer. Constant total temperature was also assumed to reduce the profiles. Once again, skin friction coefficient and shape factors are given. However, the limited range of Mach numbers precluded the use of these data sets for mean flow validation at Mach numbers considered later in this work.

2.1.3 Mean Flow and Turbulent Fluctuation Experiments

The transport of mass, momentum and energy within boundary layers is strongly influenced by turbulence. Understanding turbulent flow is a key component in studying such transport mechanisms. In this section, experiments where turbulent quantities in supersonic boundary layer are measured will be discussed.

When compared to mean flow data, experimental turbulence data is significantly scarcer. The reason for this scarcity lies in the fact that measuring turbulent quantities is extremely difficult in supersonic boundary layers. This complexity only increases as the Mach number increases. Measurement of the turbulence flow field is principally used as an aid to the computational modelling of turbulent effects. The compilation of Fernholz and Finley (1981) provides a survey of some turbulence data. More recently Konrad and Smits (1998) conducted experiments where turbulence data was measured. Making measurements of turbulence data requires long test times to traverse the regions of interest. This automatically precludes turbulence data from being extracted from impulse facilities. Instead, large test time facilities such as low enthalpy blowdown tunnels are

used.

Turbulent Fluctuations

Of the three components of fluctuating velocity, the streamwise velocity fluctuations (u') are the most commonly measured. The majority of measurements are made using hot-wire anemometry and cover a wide range of Mach numbers ($1.7 \leq M_\infty \leq 7$) and a more limited range of thermal wall conditions ($0.5 \leq T_w/T_{aw} \leq 1.0$). Consequently, the effect of wall heat transfer in supersonic flow on turbulence quantities is not well known (Dussauge et al., 1996).

Kussoy et al. (1978) studied the effect of pressure gradient and Reynolds number on compressible turbulent boundary layers at Mach 2.3. This work was included in the compilation of Fernholz and Finley (1981), with the work being unique for studies of pressure gradient effects in providing both mean and fluctuating data at a good number of locations. Centre bodies were inserted into the test section to impose a shock free compression on the boundary layer.

The data obtained upstream of the pressure gradient interaction is of value for zero pressure gradient flows as it was not yet affected by the downstream pressure rise (Fernholz and Finley, 1981). However, like all experimental distributions, the turbulent fluctuations have an undocumented upstream history that may influence the results. The Reynolds number (Re_θ) studied by Kussoy et al. (1978) of 15,000 can still be considered as high for numerical work. Fluctuating measurements were taken using a single constant temperature hot-wire and was operated at very high overheat ratios. Results were not taken for transonic local Mach numbers as the probe did not operate well in this regime. Similarly, Horstman and Owen (1972) studied a cooled wall zero pressure gradient boundary layer at Mach 6.4 and also made measurements of velocity fluctuation levels with hot-wire anemometry.

To ascertain the effect of measurement techniques, a Mach 2.9, adiabatic, zero pressure gradient turbulent boundary layer was studied by Johnson and Rose (1975). Measurements of streamwise and spanwise velocity fluctuations and their correlations were made using both hot-wire anemometry and laser-Doppler velocimetry. Good agreement was found to exist between the two techniques. Elena and Lacharme (1988) used laser Doppler anemometry and hot-wires to study the behaviour of a Mach 2.3 turbulent boundary layer at a Reynolds number (Re_θ) of 5,650. Comparison of streamwise velocity fluctuations revealed those measured by laser Doppler anemometry to

be systematically higher than those by hot-wire anemometry near the wall. The authors found that results obtained using laser Doppler anemometry was significantly more reliable than hot-wire anemometry for the conditions examined. These different observations highlight the difficulties in making experimental measurements of turbulent fluctuations. Data from both laser Doppler velocimetry and hot-wire anemometry will be used for comparison purposes in later chapters.

In the more recent work performed by Konrad and Smits (1998) turbulence measurements were obtained for a three dimensional turbulent boundary layer in the absence of shock waves. The experiments were performed at Mach 3 with a Reynolds number (Re_θ) of 84,000. Wall conditions were nearly adiabatic with a flow total temperature of 265K and wall temperature of 275K. A 20^o curved fin was used to cause a gradual increase in static pressure and hence generate results, which show the effects of compression and three-dimensionality produced in more complex geometries. Despite this added flow complexity, results are given for regions prior to encountering the curved fin and for which comparisons can be made with computed data. Measurements were made with hot wires, yielding velocity and temperature profiles along with turbulence levels and stresses.

The trends in turbulent fluctuating velocity are highly dependent on the Mach number and Reynolds number of the experiments. Still, to the current day, the sample of measurements to draw upon is small. In trying to collapse the available experimental data to a common trend there is an added complexity in the choice of length scale. When scaling with inner layer coordinates (z^+) there is no indication of profile similarity (Fernholz and Finley, 1981). Moreover such a scaling demonstrates that experimental measurements are limited to the outer regions of the log layer. Plotting fluctuation levels against wall normal distance scaled with boundary layer thickness has the disadvantage that not only is the boundary layer thicknesses ill defined and hard to measure, but the trends near the wall become very compressed and difficult to interpret. The most appropriate length scale parameter used to discern any universal trends, as suggested by Fernholz and Finley (1981), is the velocity defect thickness (Δ^*). Being an integral thickness it is quite insensitive to boundary layer thickness (δ), while being a fixed proportion of the boundary layer thickness

The choice of normalization parameters plays a key role in the ability to establish trends in turbulent experimental data. For instance, when the streamwise velocity fluctuation is conventionally normalized by the friction velocity (u_τ) and the length scale is normalized by boundary layer thickness the Reynolds number dependence is removed, but there remains a clear decrease in fluctuation levels with Mach number (see figure 56 in Dussauge et al. (1996)). However, if the defect thickness is used for the length scale, recognisable trends arise. It is also desirable to establish

trends for the spanwise and wall normal velocity fluctuations if possible. Compared to streamwise fluctuations there is considerably more scatter for the measurements of spanwise and wall normal velocity fluctuations. The level of wall normal velocity fluctuation increases with Mach number, in contrast to the decreasing trend of the spanwise fluctuations (Fernholz and Finley, 1981). However, the scarcity of experimental measurements of this quantity from other experiments precluded any conclusions from being drawn. Even when using the friction velocity and defect thickness as scaling factors, the only limited conclusion that can be drawn about the spanwise and wall normal fluctuation levels is that they exhibit maximum fluctuations near the wall and decrease towards the outer boundary layer edge.

Reynolds Stress

Much of the confusion in collapsing turbulent velocity fluctuation levels is removed by examining the Reynolds stresses. It is these Reynolds stresses that govern the mean momentum transport that are believed to have a relationship with the eddying motion of turbulence and hence turbulent transport (Bernard and Wallace, 2002). The fluctuating velocity profiles are often scaled by the mean density distribution and wall shear stress (ie. $\overline{\rho}\overline{u'^2}/\tau_w$). This scaling suggested by Morkovin (1962) removes Reynolds number and compressibility effects and in turn introduces the Reynolds stresses from turbulent fluctuation levels. Although it seems more logical to the author to compute the Reynolds stresses as $\overline{\rho u'^2}$, little difference is observed between this approach and simply scaling fluctuation levels with mean density. This suggests that the mean density and velocity fluctuations can be considered as decoupled.

The streamwise normal stress has been well studied. The collection of experimental data in Dussauge et al. (1996) shows a regular behaviour in the streamwise normal stress distribution for supersonic flows when scaled with wall shear stress and defect thickness. Moreover, there is fair agreement with the incompressible results of Klebanoff (1955).

A less regular behaviour is found for the spanwise and wall normal components of the normal stress distributions. The study of Elena and Lacharme (1988) found that the behaviour of the spanwise fluctuating velocity, when scaled to account for compressibility, was nearly identical to results obtained in subsonic boundary layers. However, the scarcity of measurements of this quantity from other experiments precluded any conclusions from being drawn. Unlike the work of Elena and Lacharme (1988), the spanwise normal Reynolds stress measured by Johnson and Rose

(1975) using hot wires and laser Doppler-anemometry did not behave like incompressible data nor did the two methods agree. In measuring streamwise fluctuations from the hot-wire, Johnson and Rose (1975) had to neglect the pressure fluctuations. However, the hot-wire results agreed with those taken using laser Doppler-anemometry. Pressure fluctuations were not neglected, however, for the hot wire measurements of spanwise fluctuations. As pointed out by the authors, this would have suggested better agreement for the spanwise, rather than streamwise, fluctuations between the two measurement techniques. However, neither procedure offered a direct measurement of spanwise fluctuations. Consequently, limited conclusions can be drawn with respect to spanwise Reynolds stress behaviour and the similarity to incompressible flow.

In considering the spanwise and wall normal stress distributions, the only general patterns that exist for such quantities is a rise towards a peak near the wall and a corresponding drop-off towards the boundary layer edge. The levels of scatter in spanwise and wall normal distributions makes evaluation of the relative fluctuations of these two quantities difficult. From the knowledge of subsonic boundary layer behaviour, we would expect the wall normal contribution to be greater than the spanwise contribution. If the scaling of Morkovin (1962) were to rigorously apply, this same phenomena should occur in supersonic flow. However, Konrad and Smits (1998) observed normal stress levels for spanwise and wall normal directions to be approximately equal. The relative behaviour of the spanwise and wall normal Reynolds normal stresses has been suggested to be dependent on the Reynolds number (Smits and Dussauge, 2006). A DNS study by Martín (2004) of the conditions examined by Elena and Lacharme (1988) gave good agreement, suggesting that the experimental data and associated observations of relative stress levels and similarity to incompressible flow has merit. The Reynolds number studied by Konrad and Smits (1998), on the other hand, was an order of magnitude higher, giving further impetus to the Reynolds number dependency argument.

A significant component of turbulent boundary layer behaviour is the Reynolds shear stress. The total shear stress across the boundary layer is given by:

$$\tau = \mu(\partial u/\partial z) - \overline{\rho}\overline{u'w'} \tag{2.1}$$

where smaller order of magnitude terms are neglected. In the immediate vicinity of the wall, the total shear stress is dominated by the viscous component and the Reynolds shear stress is zero. This region is termed the inner layer. As one moves away from the wall through the boundary layer the mean velocity derivative reduces rapidly and the dominant component of total shear stress become the turbulent Reynolds shear stress in what is known as the outer layer. Sandborn (1974), through a review of experimental total shear stress measurements normalized by wall shear stress,

established a best fit. Fair agreement is obtained with experimental data such as Konrad and Smits (1998), Elena and Lacharme (1988), Kussoy et al. (1978) and Johnson and Rose (1975). Laderman and Demetriades (1979) found that if the hot-wire signals were corrected to account for the frequency response limitations, agreement with Sandborn's best fit was obtained at distances much closer to the wall than if they were not corrected. These results demonstrate that the suggestion of Morkovin (1962), that compressibility has a passive effect on turbulence is valid for the Reynolds shear stress. Elena and Lacharme (1988) and Johnson and Rose (1975) made measurements of the Reynolds shear stress with both laser-Doppler and hot-wire anemometry. The results of Elena and Lacharme (1988) all lay below the best fit curve of Sandborn, however, the hot-wire data lay significantly lower, leading to the conclusion that the hot-wires could be unreliable for these quantities. Johnson and Rose (1975), on the other hand, noticed only small differences between the two techniques. This discrepancy in Reynolds shear stress results illustrates the observations of Fernholz and Finley (1981) that the available experimental data lies scattered within $\pm 15\%$ of the best fit of Sandborn (1974). Hence, there exists a broad range of Reynolds shear stress behaviour that can be accepted as valid.

Coherent Structures

Turbulent flow can be described in terms of coherent structures. These coherent structures can be thought of as regions of space and time where the turbulence adheres to some sort of pattern. Turbulent flow contains structures with scales ranging from the size of the flowfield domain to many orders of magnitude smaller. The interactions between the coherent structures is extremely complicated and beyond experimental capabilities to fully describe, but the interactions can be captured in LES calculations. The coherent structure approach is also very useful in improving the general understanding of turbulence and the associated transport mechanisms. While being well documented in subsonic, incompressible boundary layer flow (Robinson, 1991), knowledge of the spatial structure within supersonic compressible boundary layers is sparse.

Compressible flow visualizations first identified the existence of structures that were comparable to those found in subsonic boundary layers. Horstman and Owen (1972) undertook the earliest study into coherent structures within a Mach 7.2 compressible boundary layer. Large scale motions were noted to remain coherent several boundary layer thicknesses downstream. More recently, in their study of boundary layer transition at Mach 8 Huntley et al. (2000) noticed ejection of fluid from the wall that is characteristic of a hairpin vortex structure. Such a structure was first proposed by

Theodorsen (1955) (cited in Smits and Dussauge (2006)).

Spina and Smits (1987) undertook a thorough study of coherent structures in an undisturbed supersonic turbulent boundary layer. Fernholz et al. (1989) comprehensively details the experimental investigation. A turbulent Mach 2.9 boundary layer was studied for an approximately adiabatic wall with Re_θ of 80,000 under zero pressure gradient conditions. The purpose of this work was to give insight into the large-scale motions that existed in supersonic boundary layers that were observed in shadowgraphs and schlieren photographs of earlier experiments. Constant temperature hot-wire anemometry with high overheat ratios was used to measure fluctuations in mass flux. Measurements were taken using two wires at a fixed separation distance over time such that the space-time correlations were used to calculate so called "average structure angles". At a given angle, a structure will arrive at the two wires at different times. The peak in the space-time correlation gives the dimensionless delay time (t_{max}) between these events and given the separation distance of the two wires (Δ) and local mean velocity, the angle (β) is calculated via:

$$\beta = arctan\left(\frac{\Delta}{\overline{U}t_{max}}\right) \tag{2.2}$$

A number of separation distances were trialled, but the separation distance remained fixed as the boundary layer was traversed. Throughout the majority of the boundary layer an average structure angle of 45^o was observed while being independent of the wire separation distance used. This value is greater than the structure angle reported by Alving and Smits (1990), when varying separation distance was used. It was reasoned by Fernholz et al. (1989) that differences in structure angles can be attributed to different approaches of defining separation distance and that a small separation allowed for a local angle measurement, rather than one inferred from a larger scale measurement. The results of Alving and Smits (1990) appeared to reach a point where the structure became independent of the separation distance used, yielding structure angles near the middle of the boundary layer of 30^o.

Ganapathisubramani et al. (2006) introduced a new technique of wide-field particle image velocimetry to study a Mach 2 turbulent boundary layer. This technique examined the large-scale coherence of turbulent structures at two wall normal locations. Instantaneous velocity fields were reported and clearly exhibited long coherent structures in the streamwise direction, commonly known as streaks, that are similar to those first observed in incompressible flow. The spanwise velocity fluctuations exhibited far less coherence and was confined to mainly short, compact regions of alternating positive and negative fluctuations. The data presented demonstrated consistent agreement with 'hairpin vortex' models proposed for incompressible boundary layers.

A method of estimating the length scale of coherent structures through autocorrelation of velocity fluctuations was also presented by Ganapathisubramani et al. (2006). The results indicated an increasing streamwise length scale of the streamwise coherent structures as wall normal distance increased through the logarithmic region of the boundary layer. This result was in contrast to the decreasing length scales observed in the experiments of Smits et al. (1989) through corelations of mass flux fluctuations.

2.2 Numerical Work

This section concentrates on previous numerical work for supersonic turbulent boundary layer flow, primarily under zero-pressure gradient conditions. The results obtained and conclusions drawn in these works has been used to guide the current work. Many more simulations have been conducted using Reynolds-averaged equations, however, these works will not be included in this review because time-averaged turbulence models are not used for any key results. Moreover, such RANS simulations do not resolve turbulent structures found within the flows, which are believed to be extremely important. Direct Numerical Simulations (DNS) and Large-Eddy Simulations (LES) on the other hand are capable of providing insight into the flow physics through the unsteady formation of turbulent structures.

A great amount of work has been undertaken in studying turbulence in general compressible flow through the use of both DNS and LES. However, less has been done on the study of supersonic boundary layers. This section will provide a review of the computational work in compressible turbulent boundary layer simulations while the details of the numerical techniques used in performing such turbulent simulations will be left until Section 3.5.

Numerical computations present themselves as a very appealing alternative to experiments. Despite associated limitations, numerical computations can produce the complete state of the gas at any point in three dimensional space at any time. Many quantities such as vorticity and other higher order turbulent statistics which can be extracted from numerical results cannot easily be obtained experimentally.

Limitations of numerical computations arise from the accuracy of numerical methods used. It would be ideal and advantageous to use the most accurate spectral methods to solve all problems. However, such an approach is only easily applied to flows that are homogeneous in all directions.

Such a stipulation automatically disqualifies spectral methods from problems, even simple ones, of engineering importance. As a consequence, lower order numerical schemes must be used in place of spectral methods. The limitations of current day computing power adds further to the limitations. The issue of computational power poses serious limitations on LES work but is even worse for DNS. Even a 'large' direct numerical simulation with a resolution of 1,000 - 2,000 cells in any direction automatically limits the ratio of smallest to largest scales in the flow to 3 orders of magnitude. Real flows would contain a greater range of scales. The problems becomes worse with increasing Reynolds number. LES is less affected by making the assumption that below a certain size, all turbulent scales are isotropic and hence can be included through an assumed model.

Despite these limitations, the somewhat imperfect numerical data sets remain useful. For instance, near wall behaviour is of critical importance to engineering design. In typical experimental facilities where the Reynolds number is high, it becomes difficult to take measurements of key turbulence quantities in the near wall region (Section 2.1.1). Numerical results can also be used to determine the relative importance of physical mechanisms within a flow, even if the results are not completely accurate. It is in these situations that numerical computations play a very important role. At the current point in time, both DNS and LES appear to be accurate enough to reliably compute global flow properties in homogeneous and simple wall flows (Smits and Dussauge, 2006).

The following sections will give details of relevant numerical simulations and is divided into two sections:
• Direct Numerical Simulations (DNS)
• Large-Eddy Simulations (LES)

2.2.1 Direct Numerical Simulations

The most accurate method of numerical simulation is Direct Numerical Simulation (DNS). Given the correct grid resolution, DNS is highly reliable in that it employs no models to include turbulence as it attempts to resolve everything. It is limited, however, by the computational cost. This impacts on what problems can be studied using this technique. Despite this, DNS provides an extremely valuable validation point for numerical techniques that trade off large computational cost for lower formal accuracy but can be used to study problems of more practical interest. Furthermore, it plays a significant role in describing basic flow physics in simplified configurations

and serves as a milestone before researchers can understand higher-level problems.

DNS, much like LES had it's beginnings in the 1970 for the incompressible flow regime. From the humble beginnings of decaying isotropic turbulence, flows with significant shear layers and more complicated geometries, such as backwards facing steps, have been computed. It was not until the 1980's that compressible isotropic turbulence DNS was being computed. In later times studies were made of compressible channel flow by Coleman et al. (1995) and Huang et al. (1995), turbulent boundary layers by Guarini et al. (2000), Maeder et al. (2001) and Martín (2004) and shock boundary layer interaction by Adams (2000).

Coleman et al. (1995) made a DNS study of supersonic channel flow at Mach 1.5 and 3 with cooled iso-thermal walls. While being one of the first cool-wall DNS of compressible channel flow, it was noted that the sharp gradients in mean density and temperature played a large role in the flow behaviour and scaling.

In studying the problem of compressible turbulent channel flow between very cold walls further, Huang et al. (1995) analysed the turbulent kinetic energy budget. It was found that compressibility effects due to density and pressure fluctuations were not significant. The insignificance of compressibility and pressure dilatation was taken as a possible explanation of the success of density-weighted transformations in compressible flows. The validity of the strong Reynolds analogy (SRA) proposed by Morkovin (1962) under adiabatic conditions was also examined. Central to the analogy is the assumption of negligible total temperature fluctuations. The results, however, did not support the SRA for adiabatic flows with significant total temperature fluctuations observed. In turn, a more general representation, including effects of heat transfer was derived. For turbulent boundary layers with adiabatic thermal wall conditions Guarini et al. (2000) found good agreement with the SRA despite again having non-zero total temperature fluctuations. The success of the SRA was attributed to the relationship between total and static temperature fluctuations rather than the assumption of negligible total temperature fluctuations. The modifications proposed by Huang et al. (1995) to incorporate heat transfer effects were also applied to the adiabatic wall simulations because the conventional SRA did not accurately return the expected unity value. The modified approach was noted to bring the data closer to unity.

Following these first computations, DNS has become more computationally attainable. Adams (2000) performed a DNS of turbulent boundary layer and shock wave interaction over a compression ramp; Martín and Candler (2000) studied reacting turbulent boundary layers at Mach 4; Xu and Martin (2004) studied the effect of inflow boundary conditions for Re_θ up to $12,800$; and

Martín (2004) created a database of turbulent boundary layers with a Mach number range of 3 to 8 and wall to freestream temperature ratio of 2 to 5.5. This DNS database was later used to estimate, through *a priori* testing, time scales associated with LES subgrid-scale terms (Martín, 2005).

In a contradiction to the usual "no model" nature of DNS there is a form of DNS, known as Temporal DNS (TDNS), that has been used successfully in compressible turbulent boundary layer simulations. Maeder (2000) applied a variant of this technique, extended TDNS (ETDNS) to a spatially developing boundary layer. ETDNS differs from TDNS in that the solution is computed at a series of downstream stations, allowing for mean streamwise development of the profiles (figure 2.2-1). However, as is the convention in TDNS, periodic boundary conditions are used in the streamwise direction. To negate the effect of enforcing periodic boundary conditions in a direction that is not truly homogeneous, forcing functions are used. Without their inclusion, the velocity profiles develop temporally in a non-self-similar way, adversely influencing the turbulent statistics. The forcing terms reintroduce streamwise development of the profiles. Maeder et al. (2001) notes that an equivalent spatial DNS would require one order of magnitude greater resources than an ETDNS approach.

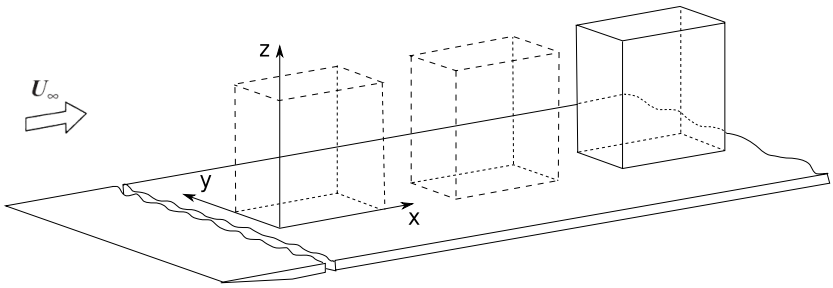

Figure 2.2-1: Principle of ETDNS. Maeder et al. (2001)

Maeder et al. (2001) studied Mach 3, 4.5 and 6 turbulent boundary layers with $\mathrm{Re}_\theta \approx 3000$. The thermal wall conditions were close to adiabatic and comparisons with experimental data and theoretical predictions were successfully made. An interesting conclusion was that even though compressibility effects were small for Mach numbers below 5 (Morkovin, 1962), the Strong Reynolds Analogy drawn from this assumption did not appear to be valid.

2.2.2 Large-Eddy Simulations

The method of LES was originally devised for incompressible flows. It has been widely and successfully applied to a great variety of low speed flows. The conventional method of extending incompressible turbulence models to compressible flows has been to account for variable density. LES has been no exception, however, there has been fewer subgrid-scale models proposed, due in part to the added complexity of the unclosed terms introduced in the energy equation.

Eddy-viscosity/eddy-diffusivity models commonly applied to incompressible flow were indeed extended to compressible, variable density flows (Martín et al., 2000). The question of which of the subgrid-scale terms must be modelled and which can be neglected is investigated by Martín et al. (2000) for decaying isotropic turbulence. Urbin et al. (1999) applied the Smagorinsky eddy-viscosity subgrid-scale model, for the subgrid-scale stress, to the interaction of a Mach 3 turbulent adiabatic boundary layer with a shock generated by a compression corner. Despite the relatively simple subgrid-scale model used and the fact that model coefficients must be predetermined, skin friction was computed to within 3% of theoretical values and profiles of Reynolds stresses demonstrated good agreement with experimental data. The Smagorinsky model was applied in the large eddy simulation of a high Reynolds number turbulent compressible jet by DeBonis and Scott (2002). Again, even this relatively simple subgrid-scale model was able to reproduce the physics of the turbulent jet flow. The comparisons made with experimental data were good and were seen as an advance on previous RANS numerical results in the literature.

The dynamic eddy-viscosity model and eddy-diffusivity model for subgrid-scale heat flux was introduced to compressible flow by Moin et al. (1991), removing the need for assumptions of model coefficients. This work assumed that all energy equation subgrid-scale terms, of which there are many (Section 3.1), other than the SGS heat flux, could be neglected. High order numerical methods were used by Rizzetta and Visbal (2004) to evaluate the performance of the Smagorinsky and Dynamic eddy-viscosity models on a spatially developing supersonic boundary layer. It must be noted that a significant drawback of such high order methods is maintaining the order of accuracy near a wall boundary. This issue has been addressed by Nagarajan et al. (2003). The scheme employed by Rizzetta and Visbal (2004) was temporally second-order and spatially sixth-order. Results identified the overprediction of streamwise velocity fluctuations and underprediction of wall normal velocity fluctuations that are typical of the numerical resolution commonly used in LES flowfields. The results were concluded to be somewhat insensitive to subgrid-scale model, but the Smagorinsky model was observed to be more diffusive. This result is not unexpected as

the Smagorinsky model has no ability to adapt to the local flow conditions.

Erlebacher et al. (1992) introduced a compressible extension of the mixed model that consisted of a combination of a Smagorinsky eddy-viscosity term and scale-similar term for the subgrid-scale stress tensor. The scale-similar model was used further by Martín (2000) to investigate the shock-capturing abilities of LES. Shock-capturing numerical techniques, including total variation diminishing (TVD) and essentially nonoscillatory (ENO) schemes, are used when high momentum freestream flow meets low momentum fluid from the boundary layer creating shocks. By introducing a compressibility ratio to identify shock locations and only applying shock capturing upwinding in those regions, a significant decrease in numerical dissipation was found to occur and give more accurate predictions when compared to analytical results. However, shocks are not expected to form within boundary layers for flows with freestream Mach numbers below 5 (Smits and Dussauge, 2006) due to the low turbulent Mach numbers generated. This point is demonstrated by the study of a Mach 2.5 turbulent boundary layer by Stolz and Adams (2003) finding no shocks within the boundary layer. The results did indicate the presence of large-scale bursting events, leading to large density gradients that were three-dimensional in character. Such bursting events have also been observed experimentally by Huntley et al. (2000).

Lenormand et al. (2000) applied a modification to the standard eddy-viscosity/eddy-diffusivity approach. The mixed-scale model, while still requiring the *a priori* specification of model coefficients, alleviated some of the associated drawbacks by applying a one-parameter model for eddy-viscosity introduced by Sagaut and Grohens (1999). In doing so, the eddy-viscosity became a nonlinear combination of the strain rate tensor and the kinetic energy of the highest resolved frequencies. The kinetic energy of the highest resolved frequencies was shown to be nearly identical to the kinetic energy of the subgrid scales and hence became a function of the subgrid scale flow conditions. This model was extended to include a selection function based on the local angular fluctuation of vorticity. Turbulent regions are identified by a threshold angle and the subgrid-scale model is applied appropriately. Significantly, the use of a selection function did not result in consistently better results. Tromeur et al. (2003), on the other hand, successfully applied the mixed-scale model with the selection function modification to study aero-optical effects in a Mach 2.3 boundary layer under different wall conditions.

El-Hady and Zang (1995) modelled the subgrid scales of a Mach 4.5 transitional boundary layer flow along a cylinder under zero-pressure gradient conditions in yet another manner. The dynamic eddy-viscosity model, where the model coefficients are determined by the flow conditions, was

applied while an alternative subgrid-scale model was also applied in the form of the Structure Function dynamic model. Proper asymptotic behaviour in the subgrid scale model was observed near the wall for both approaches. The structure function model differs from the dynamic eddy-viscosity models in that is uses a second-order velocity structure function to parametrize the small scale unresolved field. It is based upon the concept of spectral eddy viscosity where the eddy viscosities are proportional to the kinetic energy at the cutoff wavenumber. Structure function models evaluate the kinetic energy locally in physical space via the application of a structure function. The approach of Normand and Lesieur (1992), where structure functions were applied to a transitioning Mach 5 boundary layer over a flat plate, was followed by El-Hady and Zang (1995). Only the contributions to the structure function normal to the strong shear in boundary layers were considered. While Normand and Lesieur (1992) had no DNS data to compare with, the application of this structure function model by El-Hady and Zang (1995) resulted in favourable comparisons with recent DNS results.

A further short-coming in the Smagorinsky eddy-viscosity subgrid-scale models is their inability to accurately represent transition to turbulence. Ducros et al. (1996) related this behaviour to the subgrid-scale model's dissipative nature keeping the flow laminar by supressing turbulent fluctuations. To overcome this, a variation of the structure function subgrid-scale model was presented. The filtered structure function model differs from the conventional structure function procedure in that the large scale fluctuations are removed by filtering prior to the computation of the structure function. By application to a $M_\infty = 0.5$ spatially developing boundary layer, the model was able to confirm the presence of near wall streaks, hairpin vorticies and bursting events.

At the opposite end of the subgrid-scale model spectrum lies an approach proposed by Oran and Boris (2001). The Monotonically Integrated LES (MILES) technique utilizes the artificial numerical dissipation of the underlying numerical schemes and discretization to represent the true subgrid-scale dissipation. However, the flux-limiting schemes often used in compressible flow simulations introduce extra and often unwanted dissipation to the numerics. Grinstein and Fureby (2002) address the interaction of flux-limiting schemes and the corresponding implicit subgrid-scale models created by the MILES approach. It is argued by Grinstein and Fureby (2002) that an advantage of MILES over conventional subgrid-scale models is that commutation errors are avoided through no use of explicit filtering. However, it is pointed out that relying on arbitrary numerical methods may not provide the correct distribution of energy for the resolved scales. Rather, the challenge is to identify features that need to be included in the flux limiters to obtain true physical properties.

Yan et al. (2002) studied a supersonic flat plate boundary layer at a Reynolds number (Re_δ) of 2×10^4 using MILES. A globally second order method was used in both time and space. The absence of strong flow discontinuities removed the need for flux-limiting, simplifying the problem. The simulations were performed with both isothermal and adiabatic wall conditions at Mach numbers of 2.88 and 4. The mean streamwise and spanwise velocity and temperature profiles and Reynolds stress components were presented and compare well with experimental work of Zheltovodov and Yakovlev (1986) and Konrad and Smits (1998). Skin friction and wall heat transfer are also calculated for the purposes of comparison with the Reynolds analogy ratio.

Garnier et al. (1999) observed that the numerical dissipation inherent in MILES was not able to represent the subgrid-scale dissipation accurately. This was a logical conclusion since it is obvious that the numerical dissipation cannot adjust itself to different problems, much less different flow conditions within a domain. Nonetheless, MILES, which is otherwise known as coarse grid DNS, still is commonly used as a first approximation to the solution which is then further advanced on a finer grid either with some form of subgrid-scale model or sufficient resolution for full DNS.

Recently, methods based on explicit filtering techniques have been proposed by Domaradzki et al. (1998) and Adams and Leonard (1999). Unlike the eddy-viscosity/eddy-diffusivity models, information contained in the resolved scales is used to reconstruct an approximation of the true unfiltered solution. This process is akin to deconvolution first used in geology where filtering effects in measurements are removed (Bayless and Brigham, 1970). In doing so, it is no longer necessary to invoke the eddy-viscosity/eddy-diffusivity approximations to obtain closure for the governing equations nor is it necessary to specify any model constants *a priori*.

Stolz (2000) and Stolz et al. (2001b) detail the approximate deconvolution model (ADM) that uses specially weighted explicit filtering to approximate the unfiltered solution. By computing the approximation to the unfiltered solution, the flux terms could be computed without need for additional closures. A method of relaxation regularization was employed to include the effects of the scale not represented on the grid. Stolz (2000) performed an *a priori* analysis using various subgrid-scale models, including ADM and an instantaneous DNS flow field of Adams (2000). Correlations were made for subgrid-scale terms between the DNS field and LES. The results of ADM were the only subgrid-scale model with correlations in excess of 95%.

ADM was then applied to the interaction of a turbulent boundary layer with a shock with a free stream Mach number of 3 and Reynolds number (Re_θ) of 1685. The domain consisted of an 18^o compression ramp to induce a shock which would then interact with the turbulent boundary layer.

A high degree of agreement with filtered Direct Numerical Simulation data was demonstrated.

In a similar vein, Stolz and Adams (2003) simulated a spatially developing supersonic turbulent boundary layer at Mach 2.5 and two Reynolds numbers (Re_θ) of 4530 and 10,049 with ADM. Successful comparisons were made to experimental data and theoretical predictions. Results computed and compared to experiments included wall shear stress and boundary layer shape factor. Turbulent statistics, such as RMS velocity fluctuations, Reynolds stresses and turbulent Prandtl number were also calculated and compared to results from direct numerical simulations. Following this work, ADM has been applied to supersonic channel flow by Mathew et al. (2003) where the effects of grid resolution were assessed through comparison to the DNS data of Coleman et al. (1995). All LES results demonstrated uniform convergence towards their respective DNS solutions, suggesting good behaviour of ADM.

2.3 Conclusion

There exists a good base of experimental data for the validation of numerical methods and turbulence models in supersonic turbulent boundary layer flow. Trends in turbulent stresses and fluctuations have been identified as clearly as possible given the sometimes limited data sets. More recent experimental data has enabled large scale turbulent structures that play significant roles in turbulent transport to be identified and measured.

It is clear from the review of experimental and numerical work in compressible turbulence that neither one represents itself as the ideal technique for exploring new physical processes causing the reduction in skin friction. Both methods have associated error sources, however, it is fortunate that these error sources are somewhat complementary. For example, experimental data can provide good descriptions of the flow field away from the near wall region at more realistic Reynolds numbers while numerical simulations, although limited by discretization, can give a fair assessment of the near wall behaviour.

From a numerical standpoint, DNS still presents itself as the ideal, though most expensive, numerical technique and serves as a poignant source of data for LES validation. Simulations to date, though restricted to the lower end of the Reynolds number spectrum and relatively simple geometries, have yielded a great amount of information and understanding of flow behaviour that would

otherwise still be unresolved. It is these observations that must be made before more complicated flow phenomena can be completely understood.

Finally, as is evident in the preceding sections there have been many closures proposed to model the subgrid-scale terms in the governing equations in LES. There has been a clear progression and development of these models in the literature, however, there is no correspondingly clear best performing model. Of the many forms of subgrid-scale model the following chapters will define and assess the relative performance of three. The Smagorinsky model is first tested due not only to its simplicity but also its relatively successful application to LES since its inception. The mixed-scale model is then studied as it represents a development of the Smagorinsky model where the local flow state influences the dissipation levels. Finally, ADM is assessed as it shows considerable promise and does not employ *a priori* coefficient specification or eddy-viscosity/eddy-diffusivity assumptions. This is a desirable feature and gives us reasonable confidence to apply the method to new flow processes.

CHAPTER 3

GOVERNING EQUATIONS, NUMERICAL METHODS AND COMPUTATION

"I am an old man now, and when I die and go to heaven there are two matters on which I hope for enlightenment. One is quantum electrodynamics, and the other is the turbulent motion of fluids. And about the former I am rather optimistic."

Sir Horace Lamb, Applied Mathematician
Meeting of the British Association for the Advancement of Science

This chapter details the methodology followed for the simulation of compressible turbulent boundary layers with LES. The chapter begins with a definition of the governing equations. A detailed account of the numerical methods employed follows and includes a general description of techniques of turbulence modelling. The key issues of solution initialization and boundary conditions are covered. The chapter concludes with an in-depth description of the subgrid-scale closure methods used in the work presented in later chapters.

Some assumptions have been made in applying the equations governing fluid flow. It is assumed that the gas is a continuum and that the smallest turbulent scales are larger than the mean free path of a given gas molecule. The gases considered are assumed to be thermally perfect gases with a constant Prandtl number describing the ratio between viscosity and thermal conductivity.

3.1 Governing Equations

Due to the nature of the flows studied, turbulence plays a key role in the behaviour. To include the effects of turbulence, three approaches exist to solve the fully turbulent Navier-Stokes equations.

- The Reynolds Averaged Navier-Stokes (RANS) approach to turbulence modelling is a fully statistical approach. Only the statistical average of the solution (often reduced to a time-averaged solution) is computed while the effects of all turbulence is re-introduced to the flow through purely modelled quantities. All higher order statistical characteristics, such as turbulent fluctuations are modelled, rather than directly computed. With these limitations, the RANS equations were not deemed suitable to study the effects of heat addition within turbulent boundary layer.

- Direct Numerical Simulation (DNS) lies at the opposite end of the spectrum from RANS. DNS is a fully deterministic approach in that all spatial and temporal scales are directly computed. In doing so, all information about the flow is computed and hence DNS provides a wealth of important information of the turbulence. However, DNS requires very small mesh sizes to resolve scales down to the Kolmogorov length scale and time steps that are small enough to represent the smallest dynamical scales. Because of this, the study of turbulent boundary layers at Reynolds numbers of interest becomes prohibitive due to large computational costs.

- Large Eddy Simulation (LES) can be thought of as a hybrid deterministic/statistical approach. LES uses a scale separation idea (Table 3.1): the large scales of the flow, which are anisotropic and are highly sensitive to the flow configuration are computed directly, just like DNS, while the small flow scales, which are assumed to be much more isotropic and hence universal are parametrized with a subgrid-scale model.

  This separation of scales is performed through the introduction of a filter in the form of the computational mesh itself. The grid can be visualised as capturing the larger eddies while allowing the smaller eddies to pass through the filter (Figure 3.1-1). Hence, LES provides the ability to analyse turbulent parameters, albeit, restricted to the large scales, without the excessive computational cost.

The varying levels of modelling employed in each turbulence model approach and degree of computational cost is summarized in figure 3.1-2. Clearly, LES provides the middle ground between

Table 3.1-1: LES scale separation

I: Grid Scale	-	large energy carry
	-	directly resolved
II: Subgrid Scale	-	low energy
	-	energy dissipating effect
	-	modelled via universal relationships

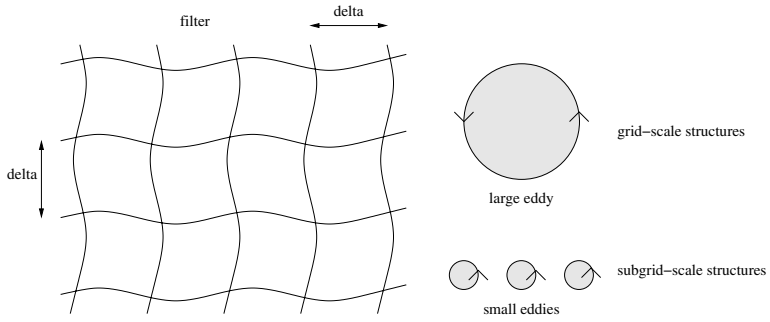

Figure 3.1-1: LES filtering approach

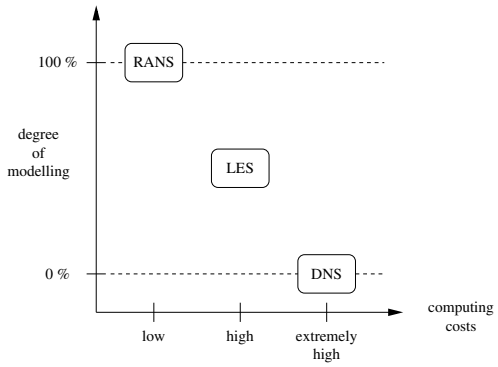

Figure 3.1-2: Degree of computational cost vs. modelling for turbulence modelling techniques

DNS and RANS simulations in terms of additional computational effort. LES futher benefits from the fact that the bulk of the turbulent fluctuations are resolved by the computational grid rather than modelled by an assumed behaviour, as in RANS, without going to the extremes of DNS .

Much of the previous LES work in the compressible flow regime has centered around the use of Favre-filtering. Doing so avoids the introduction of extra subgrid scale terms into the conservation equations. These advantages manifest in extra terms not appearing in the equation of conservation of mass (Piomelli, 2001) and the absence of triple correlations between density and velocity components (Wilcox, 2002) ($\overline{\rho' u_i' u_j'}$) arising due to the fact that density is an additional unknown.

In doing so, we are treating the momentum per unit volume (ρu) as the dependent variable. It is worth remembering that Favre-filtering is simply a convenient notation and no formal simplifications result (Smits and Dussauge, 1996). In selecting the Favre-filtered forms of the governing equations over the Reynolds averaged forms, it is pertinent to wonder what form of averaging is intrinsic in experimental measuring instruments. For example, hot-wires operated at high overheat ratios tend to be primarily sensitive to mass flux variations and hence measurements can be considered as Favre-filtered, however, the assumptions employed to obtain instantaneous velocity measurements can introduce additional uncertainty. If experimental data were to be considered as Reynolds averaged it is useful to know how significant any differences could be. The analysis of Smits and Dussauge (1996) suggests that for adiabatic boundary layer flow the difference between Favre-filtered and Reynolds averaged velocity is generally less than 1.5%, whereas for strongly cooled boundary layers this difference can increase to 5%. It is useful to keep such uncertainties in mind when considering comparisons between numerical and experimental results.

3.1.1 Transport of Mass, Momentum and Energy

The Favre-filtered variable is defined as:

$$\widetilde{f} = \frac{\overline{\rho f}}{\bar{\rho}} \tag{3.1}$$

where:

$$\bar{f} = \frac{1}{V}\int_V G f dV \tag{3.2}$$

and G is the chosen filtering function. Commonly used filter functions include a sharp Fourier cutoff filter and a top-hat filter. The Fourier cutoff filter is defined in spectral space whereas the top-hat filter is defined in physical space. With the code used being a finite volume formulation it is pertinent to use the top-hat filter where the filtering function is defined as:

$$G(x) = \begin{cases} 1/\overline{\Delta} & \text{if } |x| \leq \overline{\Delta}/2 \\ 0 & \text{otherwise} \end{cases} \tag{3.3}$$

and $\overline{\Delta}$ is the grid spacing.

The Favre filtered conservation of mass and momentum equations are as follows:

$$\frac{\partial \overline{\rho}}{\partial t} + \frac{\partial \overline{\rho} \widetilde{u}_i}{\partial x_i} = 0 \tag{3.4}$$

$$\frac{\partial \overline{\rho} \widetilde{u}_i}{\partial t} + \frac{\partial \overline{\rho} \widetilde{u}_i \widetilde{u}_j}{\partial x_i} = -\frac{\partial \overline{p}}{\partial x_i} + \frac{\partial \widetilde{\sigma}_{ij}}{\partial x_j} - \frac{\partial \tau_{ij}}{\partial x_j} \tag{3.5}$$

where p is the pressure and $\widetilde{\sigma}_{ij}$ is the viscous stress tensor defined as:

$$\widetilde{\sigma}_{ij} = \overline{\mu} \left(\frac{\partial \widetilde{u}_i}{\partial x_j} + \frac{\partial \widetilde{u}_j}{\partial x_i} - \frac{2}{3} \delta_{ij} \frac{\partial \widetilde{u}_k}{\partial x_k} \right) \tag{3.6}$$

If nothing is done to modify the resolved quantities to account for effects of turbulent scales not resolved by the computational mesh, unclosed subgrid scale terms result. Here, the unclosed term $\tau_{ij} = \overline{\rho}(\widetilde{u_i u_j} - \widetilde{u}_i \widetilde{u}_j)$ is the subgrid-scale (SGS) stress.

The unclosed terms that arise through Favre-filtering of the energy equation depend on the chosen form. Options available include the conservation of internal energy, enthalpy, or total energy per unit mass. There does not appear to be any advantage or simplification in taking either equation over the others (Piomelli, 2001). For instance, the pressure dilatation term must be modelled in the internal energy and enthalpy formulations, but not in the total energy formulation. Whereas, the total energy formulation can require modelling of turbulent diffusion (Martín et al., 2000).

The equation for conservation of internal energy introduces three unclosed terms given the assumption of Vreman et al. (1995) (ie. $\bar{q}_j - \widetilde{q}_j = 0$). The unclosed terms include the divergence of the subgrid-scale heat flux, the subgrid-scale contribution to viscous dissipation and SGS pressure dilatation.

Similar unclosed terms arise if the conservation of enthalpy equation is used. The SGS contribution to viscous dissipation, divergence of subgrid-scale heat flux and a velocity-pressure gradient term, which when decomposed yields pressure dilatation, all require modelling. The pressure-dilatation term has been neglected by such researchers as Erlebacher et al. (1992), Moin et al. (1991), El-Hady (1994) and Speziale et al. (1988). On the other hand, Vreman et al. (1995) found

that the SGS pressure-dilatation term was of the same order as the divergence of SGS heat flux in the DNS of mixing layer at Mach number from 0.2 - 0.6 and, as such, proposed a scale similar model for this term. Piomelli (2001) states that it is safe to neglect pressure dilatation at low to moderate temperatures. The pressure dilatation and viscous terms were found to be negligible in the simulation of isotropic decay of homogeneous turbulence with a turbulent Mach number of 0.52 by Martín et al. (2000). The associated uncertainties over which terms require inclusion resulted in the conservation of enthalpy no longer being considered.

The remaining option is to consider the conservation of total energy per unit mass. Using the total energy per unit mass as a basis for the conservation equation requires modelling of turbulent diffusion, SGS heat flux and viscous diffusion at the SGS level while avoiding the issue of pressure dilatation modelling. The assumption of Vreman et al. (1995) that $\bar{q}_j - \widetilde{q}_j = 0$ is used once again.

The three formulations of Favre-filtered energy equations are presented below for conservation of internal energy, enthalpy and total energy per unit mass respectively:

$$\frac{\partial(\bar{\rho}\widetilde{\epsilon})}{\partial t} + \frac{\partial}{\partial x_j}(\bar{\rho}\widetilde{u}_j\widetilde{\epsilon}) + \frac{\partial \widetilde{q}_j}{\partial x_j} + \bar{p}\widetilde{S}_{kk} - \widetilde{\sigma}_{ji}\widetilde{S}_{ij} = -C_v\frac{\partial Q_j}{\partial x_j} - \Pi_{dil} + \epsilon_v \tag{3.7}$$

$$\frac{\partial(\bar{\rho}\widetilde{H})}{\partial t} + \frac{\partial}{\partial x_j}(\bar{\rho}\widetilde{u}_j\widetilde{h}) + \frac{\partial \widetilde{q}_j}{\partial x_j} - \frac{\partial \bar{p}}{\partial t} - \tilde{u}_j\frac{\partial \bar{p}}{\partial x_j}\widetilde{\sigma}_{ji}\widetilde{S}_{ij} = -C_v\frac{\partial Q_j}{\partial x_j} - \Pi_{dil} + \epsilon_v \tag{3.8}$$

$$\frac{\partial}{\partial t}(\bar{\rho}\widetilde{E}) + \frac{\partial}{\partial x_j}\left[(\bar{\rho}\widetilde{E} + \bar{p})\widetilde{u}_j + \widetilde{q}_j - \widetilde{\sigma}_{ij}\widetilde{u}_i\right] = -\frac{\partial}{\partial x_j}\left(\gamma C_v Q_j + \frac{1}{2}\mathcal{T}_j - \mathcal{D}_j\right) \tag{3.9}$$

where $\epsilon = C_v T$ is the internal energy per unit mass, $H = \epsilon + p/\rho$ is the enthalpy per unit mass and $E = \epsilon + u_i u_i/2$ is the total energy per unit mass. The viscous heat flux is given by:

$$\tilde{q}_j = -\widetilde{k}\frac{\partial \widetilde{T}}{\partial x_j} \tag{3.10}$$

The influence of the SGS can be observed by the unclosed terms on the RHS of Eq's 3.7, 3.8 and 3.9. The SGS heat flux, pressure dilatation, viscous dissipation, turbulent diffusion and viscous diffusion respectively are defined below:

$$Q_j = \bar{\rho}\left(\widetilde{u_j T} - \widetilde{u}_j \widetilde{T}\right) \tag{3.11}$$

$$\Pi_{dil} = \overline{pS_{kk}} - \bar{p}\widetilde{S}_{kk} \tag{3.12}$$

$$\epsilon_v = \overline{\sigma_{ji} S_{ji}} - \widetilde{\sigma}_{ji}\widetilde{S}_{ji} \tag{3.13}$$

$$\mathcal{T}_j = \bar{\rho}\left(\widetilde{u_j u_k u_k} - \widetilde{u}_j \widetilde{u_k u_k}\right) \tag{3.14}$$

$$\mathcal{D}_j = \overline{\sigma_{ij} u_i} - \widetilde{\sigma}_{ij}\widetilde{u}_i \tag{3.15}$$

and we define the velocity strain rate:

$$S_{ij} = \frac{\partial u_i}{\partial x_j} + \frac{\partial u_j}{\partial x_i} - \frac{2}{3}\delta_{ij}\frac{\partial u_k}{\partial x_k} \tag{3.16}$$

The total energy per unit mass formulation has the desirable feature that it is a conserved quantity, ie. all the SGS terms can be cast in conservative form and, as such, shall be used in this situation. The other forms were included for completeness.

3.1.2 Gas State

Along with conservation of mass, momentum and total energy, an equation is required that relates the pressure to the internal energy and density of the flow. For non-reacting flow simulations at relatively low temperatures the perfect gas equation is sufficient and hence, will be of the form:

$$p = \rho R T \tag{3.17}$$

where R is the gas constant for the particular gas.

For reacting flow simulations the finite-rate chemistry module of Gollan (2003) is employed. The gas is treated as a mixture of thermally perfect gases where the thermodynamic state is determined by the state variables internal energy, density and the mass fraction of each species. The finite-rate chemical kinetics scheme is considered to be the most complete description of chemical reactions. It allows for the variation of reaction rates that occur as a result of changes in temperature and species concentration.

For the calculation of flows involving chemical processes an additional conservation equation must be solved. The conservation equation for mass fraction f of species i is written:

$$\frac{\partial \overline{\rho}\widetilde{f}_i}{\partial t} + \frac{\partial \overline{\rho}\widetilde{u}_k\widetilde{f}_i}{\partial x_k} + \frac{\partial \mathcal{F}_{ik}}{\partial x_k} = \frac{\partial \overline{\rho}\widetilde{f}_i\widetilde{V}_{ik}}{\partial x_k} + \overline{\dot{\omega}} \tag{3.18}$$

where $\overline{\rho}\widetilde{f}_i\widetilde{V}_{ik}$ is the molecular diffusion flux of species i in direction k. The contribution of the molecular diffusion in high speed flows is usually neglected and is for the presented work. Two terms remain from Eq (3.18), namely the mean reaction rate $\overline{\dot{\omega}}$ and the subgrid scale turbulent transport $\mathcal{F}_{ik}$. The mean reaction rate is computed using finite-rate chemical kinetics, while the subgrid scale turbulent transport term is used to represent the transport of species on scales unresolved by the computational mesh. By neglecting the subgrid scale term, the assumption is made that there is perfect mixing of species at the subgrid scale level. The inclusion of combustion through chemical kinetics and the associated assumptions are discussed in more detail in Section 5.3.2.

3.2 Numerical Method

Three common methods of discretization exist for the solution of the governing equations; Spectral, finite-difference and finite volume methods. The discretization technique employed can influence the results obtained if no care is taken when addressing associated drawbacks. For instance, discretization methods can introduce aliasing errors due to inadequate resolution (figure 3.2-1) and truncation errors through the removal of high order terms in the Taylor series expansion.

Spectral methods, as discussed previously, use a Fourier representation of the flow equations and are considered to be very accurate. This accuracy is mainly due to a very high order truncation error, suggesting lesser aliasing of the power spectrum. Spectral methods can, on the other hand, still suffer from aliasing errors due to interactions of nonlinear terms (Bilson, 2004). However, the primary disadvantage of spectral methods is the lack of flexibility in implementation of boundary conditions. This limitation practically restricts spectral methods to domains that are homogeneous in all directions.

Finite difference discretization has been used extensively in solving the Navier-Stokes equations.

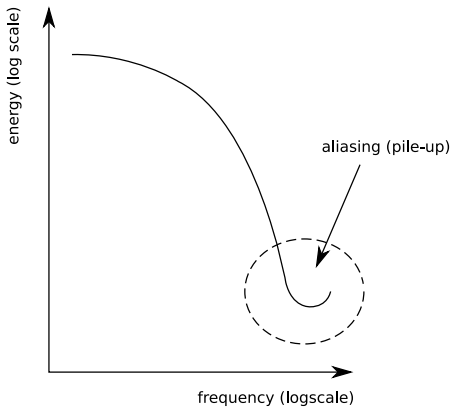

Figure 3.2-1: Aliasing of power spectrum for a poorly resolved computational mesh (adapted from Bilson (2004))

Unlike spectral methods, truncation errors can be significant, however, higher order methods have been formulated to alleviate such errors (Nagarajan et al., 2003; Rizzetta and Visbal, 2004). The use of high order methods has led to questionable conservation properties and to investigations into improving the conservative nature of higher order techniques (Vasilyev, 1999). Despite improvements in the conservative properties, higher order methods still have difficulty in coping with the one-sided nature of the no-slip condition at a wall (Bilson, 2004).

Finite volume methods have inherently good conservation properties, due mainly to the surface integral taken around a control volume that represents a computational cell. Finite volume approaches, like finite difference, are relatively simple to implement with second order accuracy. This more readily permits the study of complicated flow geometries. The work of this thesis has been to extend an existing two-dimensional finite volume flow solver to three dimensions with the addition of LES routines (Jacobs et al., 2007a,b). It is the suitability of finite volume methods to model complex geometries that has lead to their use in this work. Although second order finite volume methods are less accurate than spectral or high order finite difference methods, there is evidence to suggest the suitability of second order finite volume methods to LES of compressible flows (von Kaenel et al., 2002). For the finite volume scheme employed, the computational grid is fitted to the geometry containing the fluid and remains stationary throughout the simulation time. The grid was uniform in the streamwise and spanwise directions and was stretched in the wall normal direction to provide high resolution in the near wall region, while avoiding excessive resolution away from the wall.

3.2.1 Finite-Volume Methods

In finite volume form the governing equations Eq [3.4,3.5,3.9] are expressed as:

$$\frac{\delta}{\delta t}\int_V U\,dV + \int_S (F - G)\,dA = \int_V Q\,dV \tag{3.19}$$

To simplify the equations below, the notation for denoting a mass weighted quantity ($\tilde{}$) is removed. The array of conserved quantities (per unit volume) is:

$$U = \begin{Bmatrix} \rho \\ \rho u \\ \rho v \\ \rho w \\ \rho E \\ \rho f_{is} \end{Bmatrix} \tag{3.20}$$

The flux vectors are split into inviscid and viscous components F, G respectively, with the viscous component split further into resolved and subgrid scale components.

$$F = \begin{Bmatrix} \rho u \\ \rho u^2 + P \\ \rho uv \\ \rho uw \\ \rho Eu + Pu \\ \rho f_{is} u \end{Bmatrix} \hat{i} \quad + \quad \begin{Bmatrix} \rho v \\ \rho uv \\ \rho v^2 + P \\ \rho vw \\ \rho Ev + Pv \\ \rho f_{is} v \end{Bmatrix} \hat{j} \quad + \quad \begin{Bmatrix} \rho w \\ \rho uw \\ \rho uv \\ \rho w^2 + P \\ \rho Ew + Pw \\ \rho f_{is} w \end{Bmatrix} \hat{k} \tag{3.21}$$

$$G_{\text{viscous}} = \begin{Bmatrix} 0 \\ \sigma_{xx} \\ \sigma_{xy} \\ \sigma_{xz} \\ \sigma_{xx}u + \sigma_{xy}v + \sigma_{xz}w + q_x \\ \rho f_{is} V_{x,is} \end{Bmatrix} \hat{i} \quad + \quad \begin{Bmatrix} 0 \\ \sigma_{xy} \\ \sigma_{yy} \\ \sigma_{yz} \\ \sigma_{xy}u + \sigma_{yy}v + \sigma_{yz}w + q_y \\ \rho f_{is} V_{y,is} \end{Bmatrix} \hat{j}$$

$$+ \left\{ \begin{array}{c} 0 \\ \sigma_{xz} \\ \sigma_{yz} \\ \sigma_{zz} \\ \sigma_{xz}u + \sigma_{yz}v + \sigma_{zz}w + q_z \\ \rho f_{is} V_{z,is} \end{array} \right\} \hat{k} \tag{3.22}$$

$$G_{\text{sgs}} = \left\{ \begin{array}{c} 0 \\ -\tau_{xx} \\ -\tau_{xy} \\ -\tau_{xz} \\ -\gamma C_v Q_x - \frac{1}{2}\mathcal{T}_x + \mathcal{D}_x \\ 0 \end{array} \right\} \hat{i} \quad + \quad \left\{ \begin{array}{c} 0 \\ -\tau_{xy} \\ -\tau_{yy} \\ -\tau_{yz} \\ -\gamma C_v Q_y - \frac{1}{2}\mathcal{T}_y + \mathcal{D}_y \\ 0 \end{array} \right\} \hat{j}$$

$$+ \left\{ \begin{array}{c} 0 \\ -\tau_{xz} \\ -\tau_{yz} \\ -\tau_{zz} \\ -\gamma C_v Q_z - \frac{1}{2}\mathcal{T}_z + \mathcal{D}_z \\ 0 \end{array} \right\} \hat{k} \tag{3.23}$$

and Q is an algebraic vector of source terms.

$$Q = \left\{ \begin{array}{c} 0 \\ 0 \\ 0 \\ 0 \\ Q_{\rho E} \\ \dot{\omega} \end{array} \right\} \tag{3.24}$$

Structured grids are used, with cell averaged values being stored at the cell centres. The inviscid fluxes are computed using the AUSMDV flux calculation method of Liou and Steffen (1991) and Wada and Liou (1994). Cell-interface values used in the flux calculation process are obtained by a second-order reconstruction that uses piecewise quadratic interpolation.

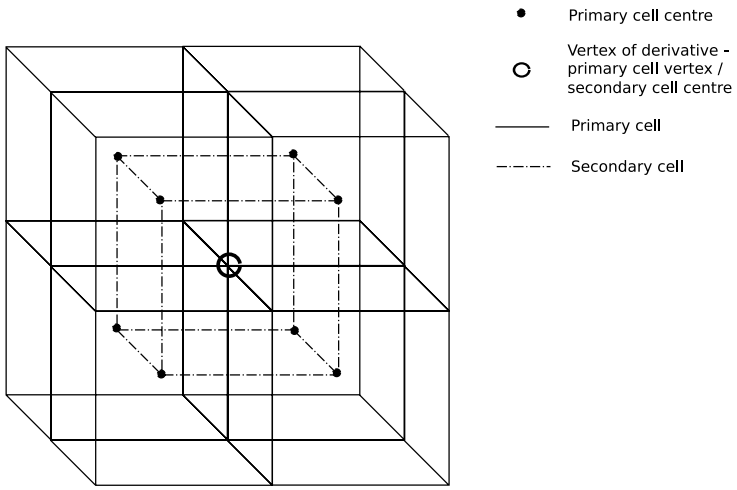

Figure 3.2-2: Secondary cell geometry

The spatial derivatives required for use in the viscous stress and subgrid scale terms are obtained by application of Gauss' divergence theorem over secondary cells resulting in second order accuracy. The vertices of a secondary cells are located at the primary cell centres (figure 3.2-2). The derivatives for each primary cell interface are then averaged for the four vertices, or secondary cell centres, that comprise the interface. Gauss' divergence theorem is defined by the symbolic equation:

$$\iiint_V (\nabla \cdot \mathrm{F})\, dV = \iint_{\partial V} \mathrm{F} \cdot dS \tag{3.25}$$

where F is a continuously differentiable vector field defined in the neighborhood of volume V and ∂V is the boundary of V oriented by outward-pointing surface normals.

The discretized components of the Navier-Stokes equations are integrated in time using a stable low-storage third order Runge-Kutta scheme (Spalart et al., 1991). The use of higher-order time advancement reduces the errors introduced by the directional splitting nature of the numerical method.

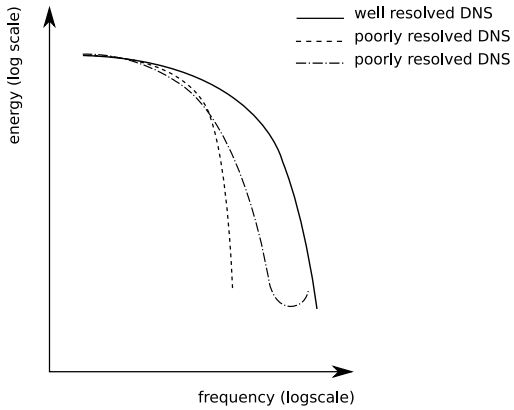

Figure 3.2-3: Manifestation of poor resolution on turbulent energy power spectrum (adapted from Bilson (2004))

3.2.2 Grid Resolution Verification

LES has the requirement that the large scale eddies must be resolved by the computational mesh. The best way to verify if the numerical grid is sufficient in capturing the correct level of turbulent detail is through examining the power spectrum. The power spectrum is computed from the Fourier transform of the fluctuating velocity signal over a spatial coordinate. The effects of poor resolution can be identified by aliasing at high wavenumber/frequencies (figure 3.2-1). The power spectrum should also demonstrate a sufficient decay in energy content (Maeder et al., 2001) to indicate that the appropriate range of scales are captured. Furthermore, the truncation errors associated with second order schemes used in LES and computational grids that are coarser than those of DNS can also lead a faster drop off in energy (figure 3.2-3).

The adequacy of the grid resolution used in this work for LES was assessed by examination of the power spectrum of velocity fluctuations. Whenever possible, the results were checked against available DNS data for the power spectrum and other turbulent quantities. It was observed throughout the course of this work that the grid resolution was limited by the associated computational expense. This was particularly noticeable when the wall to freestream temperature ratio was low. This issue is discussed further in later chapters, however, grid convergence is still identified with respect to well established experimental data.

3.3 Initial Condition Generation

To initialise a turbulent flow solution, we must prescribe not only the mean variables, but also their turbulent fluctuations for the desired Mach number and Reynolds number. One conventional method of flow initialisation is to impose the desired turbulent mean profile over the entirety of the domain and to superimpose random fluctuations with a flat frequency spectrum. The imposed flow solution is then allowed to evolve into a realistic flow field with appropriate energy spectra and turbulent structures. This procedure, however, can result in significant computational expense before any meaningful data is extracted. Often, the prescription of non-physical turbulent fluctuations can result in final conditions that are not desired or lead to a buildup of turbulent energy whereby the simulation becomes unstable and cannot continue.

Martín (2004) developed a procedure for flow initialisation where the initial flow solution has the desired Mach number, Reynolds number and boundary conditions. Furthermore, the turbulent fluctuations imposed have a more realistic energy spectrum and turbulent structure. Consequently, the time to allow the initial conditions to develop into true turbulence is reduced, while the more physical nature of the initial turbulent fluctuations avoids numerical instabilities.

The procedure first involves a Reynolds Averaged Navier Stokes simulation with Baldwin-Lomax (Baldwin and Lomax, 1978) turbulence model. The calculation is performed over a flat plate with the desired freestream conditions. The domain is then traversed until the location of desired Reynolds number (Re_θ) is identified. This process allows for the generation of the appropriate mean flow profiles with the desired freestream Mach number, boundary layer momentum thickness and boundary conditions. Any errors in quantities such as skin friction can be corrected by the later LES simulations, although it must be kept in mind that the larger the error, the larger the time before the true conditions are realised.

Given an appropriate mean profile, the desired turbulent velocity fluctuations are then transformed from the turbulent field of a subsonic, incompressible DNS simulation (Spalart, 1988). To make the transformation, two assumptions are made: 1) Morkovin scaling holds for velocity fluctuations and 2) when viewed in wall units, the near wall turbulence structure is similar. While these assumptions may or may not strictly hold, it is a good guess of the turbulent structure that is needed here and one which is better than random perturbations. The velocity fluctuations are then

calculated via the relation given by Martín (2004):

$$\left(\sqrt{\frac{\overline{\rho}}{\overline{\rho}_w}}\frac{u_i'}{u_\tau}\right)_{M>1} = \left(\sqrt{\frac{\overline{\rho}}{\overline{\rho}_w}}\frac{u_i'}{u_\tau}\right)_{M<1} \tag{3.26}$$

where the relationship is evaluated at corresponding non-dimensional wall normal locations, z^+. Martín (2004) found no benefit in using inner and outer layer scalings for velocity fluctuations.

A difficulty not documented by Martín (2004) is that the incompressible DNS of Spalart (1988) only reported *RMS* velocity fluctuations. Consequently, a distribution had to be assumed for the true fluctuating values. It was found that assuming the velocity fluctuations were bounded by:

$$-3 \times \sqrt{\overline{u_i'^2}} < u_i' < 3 \times \sqrt{\overline{u_i'^2}} \tag{3.27}$$

with random distribution between those bounds, the buildup of turbulent kinetic energy and the relaminarisation of the flow was avoided.

The strong Reynolds analogy is then used to calculate the corresponding thermodynamic fluctuations. Namely:

$$T' = -b(\gamma - 1)M^2\frac{u'}{\overline{u}}\overline{T} \tag{3.28}$$

$$\frac{\rho'}{\overline{\rho}} = -\frac{T'}{\overline{T}} \tag{3.29}$$

where $b = \min(0.8, b_{T>0})$ is a constant to ensure that temperature remains positive over the whole flow field.

The resulting turbulent fluctuation field is now based upon a true wall normal distribution but still with unphysical random magnitude. It was found to be necessary to apply a standard top hat filter (Eq (3.71)) in all three physical directions to give the turbulent flow some structure. This approach is akin to that of Martín (2004), however, the application of a filter in that work was for assuring zero initial fluctuations outside of the boundary layer. The net effect of this procedure is the generation of turbulent structures and energy spectra that resemble a realistic turbulent boundary layer.

3.4 Boundary Conditions

One of the most difficult tasks in performing Large eddy simulation for any flow is the complete specification of boundary conditions. The true boundary condition depends on the flow states outside of the domain, which are not known and, hence, must be modelled in some way based on the known interior solution. Specifically, two of which, the inlet and outlet, pose the greatest problems in implementation.

In simulating a spatially developing boundary layer we typically require a very large number of grid points in order to simulate from initial laminar state through to transition to a fully developed turbulent state. However, an alternative method exists which significantly reduces the computational time through reducing the domain size. This method, proposed by Lund et al. (1998) for incompressible flow, and later extended to compressible flow by Stolz and Adams (2003), is dubbed the Recycling and Rescaling Method.

The outflow boundary condition poses difficulties over and above those normally associated with supersonic outflow boundary conditions. If the outflow is subsonic, zero order extrapolation to the 'ghost cells' of the domain can no longer be used. Since the flow contains a mixture of subsonic and supersonic flow throughout the boundary layer, special treatment is required to prevent the reflection of waves back into the domain from the subsonic portion. In this work the non-reflective boundary conditions of Thompson (1990) were implemented.

The boundaries normal to the spanwise direction ($y = 0$ and $y = L_y$) are assumed to be periodic. In doing so, care must be taken to ensure that the domain remains large enough in the spanwise direction such that turbulent structures can be captured. At the wall boundary ($z = 0$), along the bottom of the domain, a no-slip condition ($u_w = v_w = w_w = 0$) is enforced with constant wall temperature ($T_w =$ constant). The boundary at the top of the domain ($z = L_z$), given sufficient distance from the boundary layer, imposes the desired freestream conditions.

3.4.1 Rescaling and Recycling Method

The simulation of spatially developing supersonic turbulent boundary layers can prove to be extremely computationally expensive. Hence, an inflow condition that reduces spatial domain re-

quirements is advantageous. Choosing an appropriate turbulent inflow condition is of critical importance to the feasibility and quality of any LES work.

The Rescaling and Recycling method, first proposed by Lund et al. (1998) and extended to compressible flow by Stolz and Adams (2003), satisfies the important LES requirement that a temporally (time) varying inflow is specified. The advantage of using the RRM is that it allows control over the desired inlet boundary layer properties, such as boundary layer thickness, momentum thickness and friction velocity. Furthermore, the transient region downstream of inflow required to achieve developed turbulent boundary layers is reduced when compared to both a laminar profile or uniform freestream inflow.

Central to this method are the assumptions that in the recycling region the wall is isothermal, the streamwise mean pressure gradient is zero and the ratio of boundary layer thickness (δ) to momentum thickness (θ) does not change in the streamwise direction.

The inflow streamwise, spanwise and wall-normal velocity components ($\mathcal{U}, \mathcal{V}, \mathcal{W}$ respectively), density ($\mathcal{R}$) and temperature ($\mathcal{T}$) are computed from corresponding samples taken at the recycling station x_r: u, v, w, ρ, T (Figure 3.4-1). The mean value of spanwise velocity at inflow is set to zero. Excluding spanwise velocity, each quantity is averaged in the spanwise direction and thus the sampled data remains a function of wall normal coordinate (z) and time (t). For instance, the streamwise velocity is sampled as:

$$\hat{u}(x_r, z, t) = \frac{1}{L_y} \int_0^{L_y} \tilde{u}(x_r, y, z, t) dy \tag{3.30}$$

To remove temporal variation of the profiles at the inflow, a sliding time average is also applied using a second-order Butterworth filter:

$$\mathcal{U}(x_{in}, z, t) = (1 - \alpha)\mathcal{U}(x_{in}, z, t - \Delta t) + \alpha \hat{u}(x_r, z, t) \tag{3.31}$$

where Δt is the time step size and $\alpha = \Delta t / T_s$ with $T_s \simeq 8\delta_0 / u_\infty$ as a suitable sampling period.

Under the further assumption of the validity of the law of the wall and law of the wake for the van Driest transformed velocity profile, it is possible to use inner and outer scaling for $\mathcal{U}$ and other quantities. Under this scaling, the velocity profile is not dependant on streamwise location, instead, the inflow profiles can be scaled via a ratio of the friction velocity at the inflow to that at the recycling sampling station:

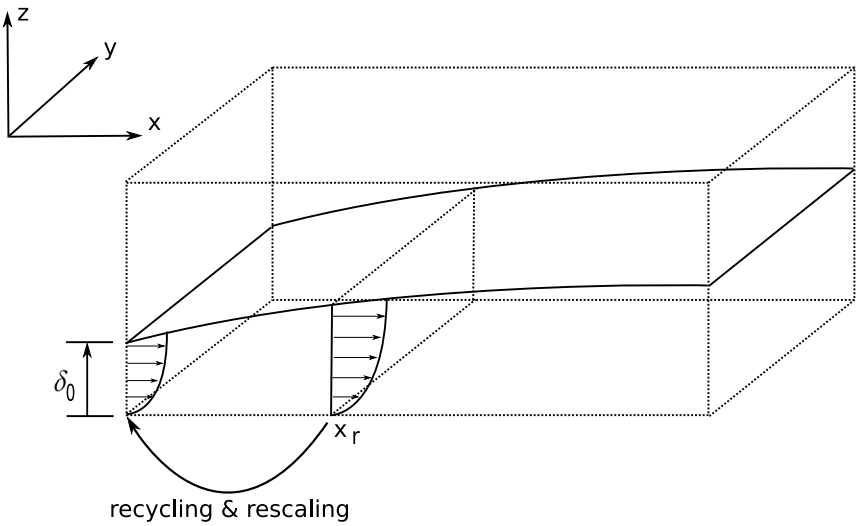

Figure 3.4-1: Schematic of the rescaling and recycling technique (Stolz and Adams, 2003)

$$\gamma = u_{\tau,\,in}/u_{\tau,\,r}.$$

It can be assumed from experiments (Fernholz and Finley, 1977) that a relation exists between wall friction velocity (u_τ) and momentum thickness (θ). Such assumptions allow for the scaling ratio to be computed from the desired momentum thickness at inflow (θ_{in}) and momentum thickness at the recycling station θ_r via:

$$\frac{\theta_r}{\theta_{in}} = \gamma^8$$

and through the further assumption that the ratio of boundary layer to momentum thickness does not change:

$$\frac{\delta_r}{\delta_{in}} = \gamma^8 \tag{3.32}$$

Consequently, the mean streamwise velocity at inflow for the inner region is computed from:

$$\mathcal{U}(x_{in}, z, t) = \gamma\, \hat{u}(x_r, \gamma z, t) \tag{3.33}$$

and for the outer boundary layer region:

$$\mathcal{U}(x_{in}, z, t) = (1-\gamma) U_\infty \gamma\, \hat{u}(x_r, \gamma^8 z, t) \tag{3.34}$$

The mean wall normal velocity component ($\mathcal{W}$), density ($\mathcal{R}$) and temperature ($\mathcal{T}$) are scaled in the same way and is shown for streamwise velocity ($\mathcal{U}$)

For turbulent inflow, fluctuations in flow parameters are important and must also be scaled. Essentially, the flowfield at the recycling station is decomposed into a time mean and fluctuating component. The fluctuations are found by taking samples in y, z and time at the recycling station and subtracting the spanwise average:

$$\tilde{u}(x_r, y, z, t) = \hat{u}(x_r, z, t) + u'(x_r, y, z, t) \tag{3.35}$$

Again, inner and outer scaling is applied to the fluctuations to compute $\mathcal{U}'(x_{in}, y, z, t)$ from $u'(x_r, y, z, t)$. The same scaling technique used for the mean velocity components is used here for the fluctuating components.

Since the inner and outer layers of the boundary layer are treated separately, a weighting function proposed by Lund et al. (1998) is used to blend the two regions and is given by:

$$W(\eta) = \frac{1}{2} + \frac{1}{2}\,\frac{\tanh\left(\frac{4(\eta-0.2)}{0.6\eta+0.2}\right)}{\tanh(4)} \tag{3.36}$$

where $\eta = \frac{\gamma^8 z}{\delta}$.

Following the scaling detailed above, the inflow profiles are computed according to:

$$\begin{aligned}
\mathcal{U}(x_{in}, y, z, t) &= \beta[\,\gamma\,\hat{u}(x_r, \gamma^8 z, t) + (1-\gamma)\,U_\infty + \gamma\,u'(x_r, y, \gamma^8, z, t)\,] \\
&\quad +(1-\beta)[\,\gamma\,\hat{u}(x_r, \gamma z, t) + \gamma\,u'(x_r, y, \gamma z, t)\,] && (3.37)\\
\mathcal{V}(x_{in}, y, z, t) &= \beta\gamma\,v'(x_r, y, \gamma^8, z, t) \\
&\quad +(1-\beta)\gamma\,v'(x_r, y, \gamma z, t) && (3.38)\\
\mathcal{W}(x_{in}, y, z, t) &= \beta[\,\gamma\,\hat{w}(x_r, \gamma^8 z, t) + \gamma\,w'(x_r, y, \gamma^8, z, t)\,] \\
&\quad +(1-\beta)[\,\gamma\,\hat{w}(x_r, \gamma z, t) + \gamma\,w'(x_r, y, \gamma z, t)\,] && (3.39)\\
\mathcal{T}(x_{in}, y, z, t) &= \beta[\,\gamma\,\hat{T}(x_r, \gamma^8 z, t) + \gamma\,T'(x_r, y, \gamma^8, z, t)\,] \\
&\quad +(1-\beta)[\,\gamma\,\hat{T}(x_r, \gamma z, t) + \gamma\,T'(x_r, y, \gamma z, t)\,] && (3.40)\\
\mathcal{R}(x_{in}, y, z, t) &= \beta[\,\gamma\,\hat{\rho}(x_r, \gamma^8 z, t) + \gamma\,\rho'(x_r, y, \gamma^8, z, t)\,] \\
&\quad +(1-\beta)[\,\gamma\,\hat{\rho}(x_r, \gamma z, t) + \gamma\,\rho'(x_r, y, \gamma z, t)\,] && (3.41)
\end{aligned}$$

with $\beta = W(\,\gamma^8 z/\delta_{0,r})$.

Following the same procedure as Stolz and Adams (2003), linear interpolation is used to map coordinates $z \rightarrow \gamma z$ and $z \rightarrow \gamma^8 z$.

3.4.2 Non-Reflecting Boundary Conditions

The non-reflecting boundary conditions of Thompson (1990) are implemented at the outflow plane. The characteristic form of the hyperbolic terms of the governing equations are solved, applying an inviscid non-reflecting condition. A sponge layer in conjunction with the non-reflecting condition was applied, as recommended by Adams (1998) and Stolz and Adams (2003), but no significant influence was noted. Due to the high speed nature of the freestream flow the non-reflecting portion of the boundary condition when subsonic flow exited the domain, was not exercised to any great extent. When the outflow was supersonic, zero order extrapolation was used.

Thompson (1990) began by considering the governing equations if terms of primitive quantities defined:

$$U = \begin{pmatrix} \rho \\ P \\ u \\ v \\ w \end{pmatrix} \tag{3.42}$$

To establish the boundary condition for the streamwise direction (x) the inviscid governing equations were written at:

$$\frac{\partial U}{\partial t} + A\frac{\partial U}{\partial x} + C = 0 \tag{3.43}$$

The eigenvalues of A represent the characteristic wave components at the boundary and are defined as:

$$\lambda_1 = u - a, \qquad \lambda_2 = \lambda_3 = \lambda_4 = u, \qquad \lambda_5 = u + a \tag{3.44}$$

The eigenvalues λ_1 and λ_5 are the velocities of the sound waves in the negative and positive directions; λ_2 is the entropy advection velocity; and λ_3 and λ_4 are the speed at which velocities v and w are convected in the streamwise direction.

Through a combination of the eigenvectors of A and the eigenvalues it is possible to return to a formulation based on conserved variables while retaining any of the characteristic wave com-

ponents. The condition for subsonic outflow requires that no upstream waves enter the domain. As such, the non-reflecting boundary condition sets the amplitude of the incoming wave to be constant, hence stipulating no wave motion. A non-reflecting condition at the outflow plane is enforced by setting $\lambda_1 = 0$. Such a suppression of incoming waves is suited for problems where nothing is known about the external solution.

3.5 Subgrid-Scale Modelling

Each of the SGS terms introduced in Section 3.1 require some form of closure. This is the stage in the solution process where relationships are applied to model the transfer of energy and momentum between the resolved scales and those subgrid and also how the energy and momentum is lost once within the subgrid scale. Two commonly used subgrid-scale models, the eddy-viscosity, eddy-diffusivity model and mixed scale model are summarised below. Both approaches require model parameters to be specified prior to use. The approximate deconvolution model of Stolz et al. (2001b), which removes this requirement is also presented.

3.5.1 Eddy-Viscosity and Eddy-Diffusivity Method - Smagorinsky

Eddy-viscosity and eddy-diffusivity models allow closure of the governing equations Eq [3.4,3.5,3.9] through the calculation of relevant subgrid scale terms. For the conservation of momentum (Eq 3.5) the subgrid scale stress,τ_{ij}, is modelled via the resolved strain rate (S_{ij}) and eddy-viscosity, ν_t.

$$\tau_{ij} - \frac{\delta_{ij}}{3}\tau_{kk} = \nu_t S_{ij} \tag{3.45}$$

The isotropic component of the subgrid-scale stress tensor is neglected (Erlebacher et al., 1992; Lenormand et al., 2000; Tromeur et al., 2003).

The classical approach for eddy-viscosity, eddy-diffusivity type models was first proposed by Smagorinsky (1963). The eddy-viscosity is modelled as a product of a length scale (commonly taken to be

the filter width, or grid spacing $\overline{\Delta}$) and the velocity at that scale ($\overline{\Delta}\tilde{S_{ij}}$). A constant, C_s, is included to close to model.

$$\nu_t = -2C_s^2\overline{\Delta}^2\bar{\rho}|\tilde{S}| \tag{3.46}$$

where:

$$|\tilde{S}| = \sqrt{S_{ij}\,S_{ij}/2} \tag{3.47}$$

The main problem with such an approach is the requirement for an appropriate constant, C_s, to be set. Incompressible flow commonly sets the constant to 0.18. However, for compressible wall bounded flows, such a value can yield an over-dissipative behaviour. Lenormand et al. (2000) propose a reduction in the parameter to 0.1. Furthermore, in regions near a wall the model of Smagorinsky (1963) does not vanish. In these near wall regions there is reduced growth of small scale turbulence and thus less turbulent transfer to subgrid scales. Hence, to include this behaviour the length scale, $l_m = \Delta$, is reduced via a van-Driest-type damping function proposed by Piomelli (1993):

$$l_m = \Delta\left[1 - exp(-z^+/a)^3\right]^{\frac{1}{2}} \tag{3.48}$$

where z^+ is the wall-normal distance expressed in wall units ($z^+ = \frac{z\,u_\tau}{\nu_w}$, $u_\tau = \sqrt{\frac{\tau_w}{\rho_w}}$) and a is a constant equal to 25.

The eddy-viscosity approach is known to not accurately model the effects of the unresolved small scale turbulence on the resolved scales on its own without further modification. *A priori* tests on a compressible plane mixing layer performed by Vreman et al. (1995), comparing the subgrid-scale stress tensor calculated using DNS and the tensor calculated by the eddy-viscosity subgrid-scale model, yielded low correlations between 0 and 0.4. The reason proposed was the purely dissipative nature of an eddy-viscosity subgrid scale model with non eddy-viscosity models correlating considerably better. Lenormand et al. (2000) observed similar behaviour, with the eddy-viscosity model consistently underperforming other non eddy-viscosity models.

A similar model is also used to close the conservation of energy equation (3.7). The subgrid scale heat flux (Q_j) is modelled using an eddy-diffusivity model of the form (Martín et al., 2000):

$$Q_j = -\frac{\rho \nu_t}{Pr_t} \frac{\partial \tilde{T}}{\partial x_j} \tag{3.49}$$

where ν_t is the eddy-viscosity that is computed as above and the turbulent Prandtl number Pr_t must be specified. For isotropic decaying turbulence it was shown by Martín et al. (2000) that the turbulent diffusion term ($\mathcal{T}_j$) was comparable to the subgrid scale heat flux. A model was proposed by Knight et al. (1998) to parametrize the turbulent diffusion:

$$\mathcal{T}_j \simeq \tilde{u}_k \tau_{jk} \tag{3.50}$$

The subgrid scale viscous diffusion term ($\mathcal{D}_j$) was not included in the analysis with eddy-viscosity/eddy-diffusivity subgrid scale models. Martín et al. (2000) concluded that the errors introduced by not using a model were tolerable given the small contribution to turbulent energy content in isotopic turbulence.

3.5.2 Eddy-Viscosity and Eddy-Diffusivity Method - Mixed-Scale Model

The mixed-scale model of Lenormand et al. (2000) and Sagaut and Grohens (1999) is an extension of the Smagorinsky model and depends on both the large resolved scales and the smaller unresolved scales. A one parameter (α) family of models was proposed to improve the prediction of eddy-viscosity in such a way that it adapts to the local flow state and vanishes in fully resolved and near wall regions. The eddy-viscosity is a nonlinear combination of the shear stress magnitude ($|\tilde{S}|$), the length scale (Δ) and the kinetic energy of the highest resolved frequencies (q_c^2). The high frequency modes, known as the test field are calculated from the entire resolved field by the application of a low-pass (test) filter. The high freqency kinetic energy q_c^2 is evaluated by:

$$q_c^2 = \frac{1}{2} \left(\tilde{u}_k - \hat{\tilde{u}}_k \right)^2 \tag{3.51}$$

where $\hat{\tilde{u}}_k$ represents the test filtered velocity.

The eddy-viscosity is then computed as:

$$\nu_t = C_m |\tilde{S}|^\alpha \left(q_c^2 \right)^{\frac{(1-\alpha)}{2}} \Delta^{(1+\alpha)} \tag{3.52}$$

For $\alpha = 0$ the model collapses to the mixing length model, while for $\alpha = 1$ we regain the eddy-viscosity model of Smagorinsky (1963). The value recommended by Lenormand et al. (2000) of $\alpha = 0.5$ is used in this work. The parameter C_m which is a function of α was found by Lenormand et al. (2000) to be 0.06 on the basis of an equilibrium assumption between energy dissipation and transfer rates.

The subgrid-scale heat flux (Q_j) formulation (Eq (3.49)) and subgrid scale turbulent diffusion ($\mathcal{T}_j$) formulation (Eq (3.50)) remains unchanged while using the eddy-viscosity calculated in Eq (3.52).

In the LES of a supersonic turbulent boundary layer, Lenormand et al. (2000) found that the mixed-scale model performed better than a wall damped, purely eddy-viscosity model, such as that discussed in the previous section, when examining velocity and temperature fluctuations and Reynolds stress correlations. Tromeur et al. (2003) successfully used the mixed-scale model in the evaluation of aero-optical effects in turbulent boundary layers and found good agreement with experimental mean and fluctuating profiles.

3.5.3 Approximate Deconvolution Model

The development of the approximate deconvolution model (ADM) overcame one of the most significant problems of the earliest subgrid-scale models - the specification of model coefficients. ADM uses information contained in the scales resolved by the computational grid and uses it to reconstruct an approximation to the unfiltered solution. This in turn allows for the incorporation of subgrid-scale terms without needing to use eddy-viscosity/eddy-diffusivity approaches. Procedures such as the dynamic eddy-viscosity model also remove the need for specification of model coefficients, however, the computational cost of ADM is lower than the costs associated with the dynamic eddy-viscosity model (Stolz et al., 2001a).

The ADM procedure has its origins in deconvolution models. Deconvolution models were first used for compressible flows by Domaradzki and Saiki (1997), Domaradzki et al. (1998) and Kuerten et al. (1999). The first application of the approximate deconvolution model was for simulation of decaying isotropic turbulence (Stolz and Adams, 1999). ADM was then applied to incompressible channel flow (Stolz et al., 2001a), shock boundary layer interaction (Stolz et al., 2001b) and supersonic channel flow (Mathew et al., 2003) demonstrating considerable robustness. Since then, ADM has also been applied successfully to aeroacoustic noise prediction of aircraft

engines by Bodony and Lele (2003). All of these applications of ADM demonstrate that it provides a sound means of incorporating the unresolved effects of turbulence without the need for assumed behaviour of turbulence (ie. eddy-viscosity) or *a priori* input of model coefficients.

Classically, a deconvolution process can be thought of as a technique to eliminate undesired filtering effects on a received signal (Bayless and Brigham, 1970). Such techniques are used in research areas as far afield as geophysical research to enhance measurements from slowly responding measuring devices. If we consider the output, $y(t)$, being related to the input, $s(t)$ by the convolution integral:

$$y(t) = \int_{-\infty}^{\infty} s(t)\, G(t-\tau)\, d\tau \tag{3.53}$$

with the system response, $G(t)$, known *a priori*, it is through the deconvolution, or inverse filtering, process of $y(t)$ that it is possible to solve for $s(t)$.

In the context of turbulence modelling, it is the implicit filtering of the computational grid that is introducing the undesired filtering effects. With the ADM procedure, the unfiltered solution is approximated from the grid filtered solution via a series expansion of repeated filtering operations (Stolz et al., 2001b). Given the approximation to the unfiltered solution, explicitly computing subgrid-scale closures is not required with the flux terms of the governing equations instead being computed directly. However, even if the approximation were to be exact over all of the represented wavenumbers, this approximate deconvolution procedure does not include dissipative effects. To include those effects, regularization is necessary to provide the energy transfer to the dissipation scales.

The deconvolution and regularization model is best understood by applying it to a simplified conservation of momentum equation:

$$\frac{\partial \rho u_i}{\partial t} + \frac{\partial f(\rho u_i)}{\partial x_j} = 0 \tag{3.54}$$

Computation of a solution at discrete locations implies a filtering of Eq (3.54) by the filter implicit in the numerical grid:

$$\frac{\partial \overline{\rho u_i}}{\partial t} + \overline{\frac{\partial f(\rho u_i)}{\partial x_j}} = 0 \tag{3.55}$$

Here the primary filter of ρu_i over the computational domain, $\overline{\rho u_i}$, is given by:

$$\overline{\rho u_i} = G \times (\rho u_i) \tag{3.56}$$

Rearranging the filtered transport equation, while collecting non-closed terms results in the following equation:

$$\frac{\partial \overline{\rho u_i}}{\partial t} + \frac{\partial f(\overline{\rho u_i})}{\partial x_j} = \frac{\partial f(\overline{\rho u_i})}{\partial x_j} - \overline{\frac{\partial f(\rho u_i)}{\partial x_j}} = \mathcal{R} \tag{3.57}$$

For conventional LES approaches subgrid scale models are used for the unclosed terms, $\mathcal{R}$, with the remainder of Eq (3.57) calculated from the computed field $\overline{\rho u_i}$.

Most LES procedures that utilize explicit filtering (separate to the implicit filtering of the numerical grid) choose the cutoff frequency of the filter, ω_c, to be equal to the Nyquist frequency, (ω_n) with wavelength $2h$ (where h is the grid spacing). However, wavenumbers close to ω_n are not well represented by numerical discretization (Stolz et al., 2001b). ADM differs in that the cutoff frequency of the explicit filter is deliberately chosen to be smaller than the Nyquist frequency. By doing so it enables the range of frequencies, $\omega_c < |\omega| \leq \omega_n$, to be used to model the effects of the nonresolved scales, $|\omega| > \omega_n$, on the scale resolved by the computational grid, $|\omega| \leq \omega_c$. These resolved scales, that are in reality influenced by the nonresolved scales, are recovered through an approximate inversion of the primary filter resulting in a field where the nonresolved scales have some influence. Hence, the approximate deconvolution $(\rho u_i)^*$, computed from $\overline{\rho u_i}$, can now be used to calculate the filtered flux term.

$$\mathcal{R} = \frac{\partial f(\overline{\rho u_i})}{\partial x_j} - \overline{\frac{\partial f(\rho u_i)}{\partial x_j}} \approx \frac{\partial f(\overline{\rho u_i})}{\partial x_j} - \overline{\frac{\partial f((\rho u_i)^*)}{\partial x_j}} \tag{3.58}$$

The approximate deconvolution is calculated through the use of the approximate deconvolution operator Q_N:

$$(\rho u_i)^* = Q_N \times \overline{\rho u_i} \tag{3.59}$$

Ideally, the approximate deconvolution operator should be the inverse of the primary grid filter (G). The inverse operator of the primary filter is computed as an infinite series of filter operators (Stolz

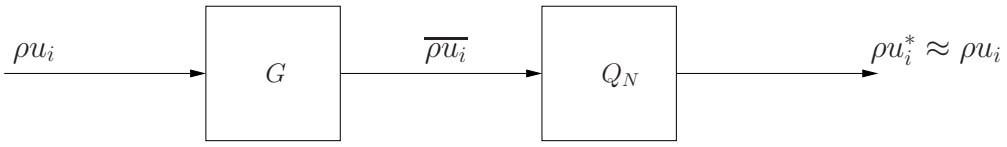

Figure 3.5-1: Block diagram of approximate deconvolution technique

et al., 2001b). Adhering to practicality, the approximate deconvolution operator is calculated as a truncated series expansion:

$$Q_N = \sum_{v=0}^{n} (I - G)^v \approx G^{-1} \tag{3.60}$$

where I is the identity operator and truncating the expansion to $n = 5$ provides sufficiently accurate solutions (Stolz et al., 2001b). This process of using Q_N as the inverse of the primary grid filter (G) (which can be thought of as the system response) is summarised in figure 3.5-1.

Applying deconvolution to the three-dimensional conservation equations in terms of filtered variables and dropping the notation for the filtering implicit in the numerical grid we obtain:

$$\frac{\partial \rho}{\partial t} + \frac{\partial (\rho u_j)^*}{\partial x_j} = 0 \tag{3.61}$$

$$\frac{\partial \rho u_i}{\partial t} + \frac{\partial}{\partial x_j}\left((\rho u_i)^* \frac{(\rho u_j)^*}{\rho^*} + \check{p}^* \delta_{ij} - \check{\sigma}_{ij} \right) = 0 \tag{3.62}$$

$$\frac{\partial \rho E}{\partial t} + \frac{\partial}{\partial x_j}\left((\rho E)^* \frac{(\rho u_j)^*}{\rho^*} + \check{p}^* \frac{(\rho u_j)^*}{\rho^*} - \check{\sigma_{ij}} \frac{(\rho u_j)^*}{\rho^*} + \check{q}_j^* \right) = 0 \tag{3.63}$$

The $\check{\Psi}^*$ symbol indicates that the quantities Ψ is computed as per their normal definitions, but with deconvolved values.

To gain the full influence of the energy transfer to the nonresolved scales $|\omega| > \omega_n$ a relaxation term is added. The energy transfer from the range of scales $\omega_c < |\omega| \leq \omega_n$ is achieved by subtracting the relaxation term from the governing equations in terms of deconvolved variables. A relaxation parameter, χ, and the difference between grid filtered and deconvolved quantities is used to represent this transfer. Considering, once again, the simplified momentum equation,

(Eq (3.54)), now in terms of deconvolved variables (Eq (3.59)), the addition of a relaxation term results in:

$$\frac{\partial \overline{\rho u_i}}{\partial t} + \overline{\frac{\partial f((\rho u_i)^*)}{\partial x_j}} = -\chi_{\rho u}(\overline{\rho u_i} - \overline{(\rho u_i)}^*) \tag{3.64}$$

Relaxation is an integral part of the deconvolution process and has been used since the work of Adams and Leonard (1999). Not accounting for the transport of energy to the scales not resolved by the computational grid can cause solution divergence. The relaxation parameter, $\chi_{\rho u}$, is determined dynamically to remove any dependence on an *a priori* parameter choice. Hence, the parameter can vary continuously over the domain. The dynamic approach was first proposed by Stolz et al. (2001b) and has since been used successfully by Mathew et al. (2003) and Stolz and Adams (2003). According to Stolz et al. (2001b) the relaxation practically affects only the range of scales $\omega_c < |\omega| \leq \omega_n$ and, hence, the dynamic estimation of the relaxation parameter prevents the growth of energy at small scales.

The dynamic procedure involves taking an Euler step forward in time with a size Δt, once with $\chi_{\rho u} = 0$ and again with $\chi_{\rho u} = \chi_{\rho u_0}$. Where $\chi_{\rho u_0}$ is a positive estimate of the parameter, such as a positive constant, for time $t = 0$ or the value from the previous timestep for $t > 0$. To determine an appropriate value for the relaxation parameter, $\chi_{\rho u}$, the energy contained in the frequency range $\omega_c < |\omega| \leq \omega_n$ is estimated by application of a structure function to the difference between filtered and deconvolved quantities ($\phi = \overline{\Psi} - \overline{\Psi}^* = (I - Q_N \times G)\overline{\Psi}$). A local second-order structure function at grid point $\xi = (\xi_x, \xi_y, \xi_z)$ given by:

$$F_2(\xi, t) = ||\Phi_{\rho u}(\xi + \mathbf{r}, t) - \Phi_{\rho u}(\xi, t)||^2_{||\mathbf{r}||=h} \tag{3.65}$$

where $\Phi_{\rho u} = \{\phi_1, \phi_2, \phi_3\}$, $\phi_i = (I - Q_N \times G) \times \overline{\rho u_i}$ and h is the computational grid spacing.

From the structure functions it is now possible to estimate how much energy is to be transferred to the nonresolved scales. The difference in structure functions $F_2(\xi, t + \Delta t)|_{\chi_{\rho u}=0} - F_2(\xi, t)$ estimates the energy generated for the time increment by the wave numbers which are not well resolved but are represented on the computational grid ($\omega_c < |\omega| \leq \omega_n$). The difference $F_2(\xi, t + \Delta t)|_{\chi_{\rho u}=0} - F_2(\xi, t + \Delta t)|_{\chi_{\rho u}=\chi_{\rho u_0}}$ is an estimation of how much energy is dissipated for $\chi_{\rho u} = \chi_{\rho u_0}$.

As a consequence we can determine $\chi_{\rho u}$ via:

$$\chi_{\rho u} = \chi_{\rho u_0} \frac{F_2(\xi, t+\Delta t)|_{\chi_{\rho u}=0} - F_2(\xi, t)}{F_2(\xi, t+\Delta t)|_{\chi_{\rho u}=0} - F_2(\xi, t+\Delta t)|_{\chi_{\rho u}=\chi_{\rho u_0}}} \tag{3.66}$$

To complete the model $\Phi_\rho = \phi_1 = (I - Q_N \times G) \times \overline{\rho}$ and $\Phi_{\rho E} = \phi_1 = (I - Q_N \times G) \times \overline{\rho E}$ are used as relaxation parameters for the conservation of mass (3.61) and conservation of energy equation (3.63) respectively. Including all relaxation parameters results in the full set of equations to be solved in the approximate deconvolution model:

$$\frac{\partial \rho}{\partial t} + \frac{\partial (\rho u_j)^*}{\partial x_j} = -\chi_\rho (\rho - \rho^*) \tag{3.67}$$

$$\frac{\partial \rho u_i}{\partial t} + \frac{\partial}{\partial x_j}\left((\rho u_i)^* \frac{(\rho u_j)^*}{\rho^*} + \check{p}^* \delta_{ij} - \check{\tau}_{ij} \right) = -\chi_{\rho u} (\rho u_i - (\rho u_i)^*) \tag{3.68}$$

$$\frac{\partial \rho E}{\partial t} + \frac{\partial}{\partial x_j}\left((\rho E)^* \frac{(\rho u_j)^*}{\rho^*} + \check{p}^* \frac{(\rho u_j)^*}{\rho^*} - \check{\tau}_{ij} \frac{(\rho u_j)^*}{\rho^*} + \check{q}_j^* \right) = -\chi_{\rho E} (\rho E - (\rho E)^*) \tag{3.69}$$

It must be noted that only one relaxation parameter ($\chi_{\rho u}$) exists for the three conservation of momentum equations. In practice, when beginning from an arbitrary guess for relaxation parameter, the dynamic procedure should be iterated 4 - 8 times, after which, it is sufficient to update these parameters every 5 - 10 flow iterations.

3.5.4 Filtering Methods

In the present study, the large-scale governing equations are implicitly filtered by the numerical grid. Explicit filtering is used by both the mixed scale eddy-viscosity/eddy-diffusivity model and the approximate deconvolution method.

For the test-filtering of the Mixed-Scale model, a second-order top-hat filter was used and calculated from:

$$\hat{f}_i = f_i + \frac{h_f^2}{24} \frac{\delta^2 f}{\delta x^2} = f_i \frac{h_f^2}{24} \left(\frac{f_{i-1} - 2f_i + f_{i+1}}{h^2} \right) \tag{3.70}$$

where h_f is the filter width and h is the grid width. A filter width (h_f/h) is then selected to formulate the discrete filter function. Choosing a filter ratio of 2 and $\sqrt{6}$ yields Simpson's rule

and the trapezoidal rule respectively. Following the implementation of Lenormand et al. (2000) and Tromeur et al. (2003), the trapezoidal rule is used for this work. A filter ratio of $\sqrt{6}$ generates a test filter stencil of:

$$\hat{f}_i = \frac{1}{4}(f_{i-1} + 2f_i + f_{i+1}) \tag{3.71}$$

The approximate deconvolution method utilises a five-point discrete filter of the form:

$$(G \times f)|_i = \overline{f}_i = \sum_{j=-\nu_l}^{\nu_r} \alpha_j f_{i+j}. \tag{3.72}$$

with the property $\nu_l + \nu_r = 4$. The spatial location of a point within the filter stencil is defined as $r_j = ||\mathbf{x}(i_x + j, i_y, i_z) - \mathbf{x}(i_x, i_y, i_z)||$ for $j = -\nu_l, ..., \nu_r$. The coefficients (α_j) for cells away from the wall, as specified by Stolz et al. (2001a), are given as a function of α_{-2}, which is determined by an additional condition:

$$\alpha_0 = \frac{1}{2} - \alpha_{-2} - \frac{1}{2} \times \frac{r_{+1}\, r_{-1} + 2\, r_{+1}\, r_{-2}\, \alpha_{-2} + 2\, r_{-2}^2\, \alpha_{-2} - 2\, r_{-1}\, r_{-2}\, \alpha_{-2}}{r_{+2}\,(r_{+1} - r_{+2} - r_{-1})} \tag{3.73}$$

$$\alpha_{-1} = \frac{1}{2} \times \frac{r_{+1}^2 - r_{+2}\, r_{+1} + 2\, r_{-2}^2\, \alpha_{-2} + 2\, r_{-2}\, \alpha_{-2}\, r_{+2}}{(r_{+1} - r_{+2} - r_{-1})\,(r_{+1} - r_{-1})} \tag{3.74}$$

$$\alpha_{+1} = -\frac{1}{2} \times \frac{2\, r_{-2}^2\, \alpha_{-2} + r_{-1}\, r_{+2} + r_{-1}^2 + 2\, r_{-2}\, \alpha_{-2}\, r_{+2}}{(r_{+1} - r_{+2} - r_{-1})\,(r_{+1} - r_{-1})} \tag{3.75}$$

$$\alpha_{+2} = \frac{1}{2} \times \frac{r_{+1}\, r_{-1} + 2\, r_{+1}\, r_{-2}\, \alpha_{-2} + 2\, r_{-2}^2\, \alpha_{-2} - 2\, r_{-1}\, r_{-2}\, \alpha_{-2}}{r_{+2}\,(r_{+1} - r_{+2} - r_{-1})} \tag{3.76}$$

The final condition to determine α_{-2} comes from enforcing a vanishing moment of third order on the filter kernel, G:

$$\Delta^3\, M^3(x) = r_{+2}^3\, \alpha_{+2} + r_{+1}^3\, \alpha_{+1} - r_{-1}^3\, \alpha_{-1} - r_{-2}^3\, \alpha_{-2} = 0 \tag{3.77}$$

In the immediate vicinity of a wall, a symmetric five-point stencil cannot be used. For a cell one point off the wall, an asymmetric set of filter coefficients, α_j, exist for $-1 \leq j \leq 3$.

$$
\begin{aligned}
\alpha_0 &= \frac{1}{2} \times \frac{-r_{+2}\, r_{+1} + r_{+2}^2 + r_{+2}\, r_{-1} + r_{+1}\, r_{-1} + 2\alpha_{+3}(r_{+1}\, r_{+3} + r_{+1}\, r_{-1} - r_{+3}^2 - r_{-1}\, r_{+3})}{r_{+2}(-r_{+1} + r_{+2} + r_{-1})} \\
\alpha_{-1} &= -\frac{1}{2} \times \frac{r_{+1}^2 - r_{+2}\, r_{+1} - 2\, r_{+2}\, \alpha_{+3}\, r_{+3} + 2\, \alpha_{+3}\, r_{+3}^2 - 2\, \alpha_{+3}\, r_{+1}^2 + 2\, \alpha_{+3}\, r_{+2}\, r_{+1}}{-r_{+1}^2 + r_{-1}^2 + r_{+2}\, r_{+1} + r_{+2}\, r_{-1}} \\
\alpha_{+1} &= \frac{1}{2} \times \frac{r_{-1}^2 - 2\, r_{-1}^2\, \alpha_{+3} - 2\, r_{+2}\, \alpha_{+3}\, r_{+3} + r_{+2}\, r_{-1} - 2\, r_{+2}\, r_{-1}\, \alpha_{+3} + 2\, \alpha_{+3}\, r_{+3}^2}{-r_{+1}^2 + r_{-1}^2 + r_{+2}\, r_{+1} + r_{+2}\, r_{-1}} \\
\alpha_{+2} &= \frac{1}{2} \times \frac{-2\, r_{+1}\, \alpha_{+3}\, r_{+3} + r_{+1}\, r_{-1} - 2\, r_{+1}\, r_{-1}\, \alpha_{+3} + 2\, \alpha_{+3}\, r_{+3}^2 + 2\, r_{-1}\, \alpha_{+3}\, r_{+3}}{r_{+2}(-r_{+1} + r_{+2} + r_{-1})}
\end{aligned}
$$

Again, we impose the vanishing third order moment for the filter kernel and arrive at a solution for α_{+3} by solving:

$$\Delta^3\, M^3(x) = r_{+3}^3\, \alpha_{+3} + r_{+2}^3\, \alpha_{+2} + r_{+1}^3\, \alpha_{+1} - r_{-1}^3\, \alpha_{-1} = 0$$

For cells immediately adjacent to a wall where no meaningful ghost cell data exists, the values remain unfiltered. The filtering coefficient calculation subroutines used in this work were provided by Steffen Stolz and were re-written and modified to fit within the existing code structure.

3.5.5 Approximate Deconvolution Method Solution Process

The numerical solution process used for the large-eddy simulation with the ADM subgrid-scale model differs slightly from a conventional solution process. The solution process is outlined below to enable complete understanding of the process for a single explicit Euler time-step. In this work, time integration is performed with an explicit Runge-Kutta time advancement method. In turn, these steps can be applied to each Runge-Kutta sub-step.

(1) Deconvolve $\overline{\Psi}(t_n)$ to obtain $\overline{\Psi}^*(t_n)$

(2) Compute deconvolved flux term $F(\overline{\Psi}^*)$

(3) Estimate χ_ψ as described in Eq (3.66) if necessary

(4) Compute relaxation regularization $\chi_\psi(\overline{\Psi}(t_n) - \overline{\Psi}^*(t_n))$

(5) Combine flux term and relaxation regularization to obtain time derivative $\delta\overline{\Psi}(t_n)/\delta t$

CHAPTER 4

LARGE-EDDY SIMULATION OF WALL BOUNDED FLOWS

Before investigating the effect of heat addition into the scramjet boundary layer, large-eddy simulations (LES) of turbulent supersonic compressible boundary layer flow have been performed. The turbulent boundary layer domain lies far downstream of the equivalent leading edge and is shown schematically in figure 4.1-1. The simulations are used to validate the subgrid scale models and determine the relative performance of each model presented for different grid resolutions. The Smagorinsky and mixed-scale eddy-viscosity/eddy-diffusivity models and approximate deconvolution models were used to include the effects of the subgrid scale turbulence. The former models use *a priori* specification of model coefficients whereas the latter adjusts itself to the local conditions and does not make use of an eddy-viscosity/eddy-diffusivity assumption. The simulations were performed at Mach 4.5 with Reynolds number, $Re_\theta = 3570$ at near adiabatic wall conditions. These conditions allowed for direct comparison to the experimental data of Coles (1953) (Fernholz and Finley, 1977) and Direct Numerical Simulation (DNS) of Maeder et al. (2001). By having both experimental and DNS data for the same conditions, we can have great confidence in the subgrid scale models and numerical schemes. Figures for this chapter appear together starting on page 108.

4.1 Results

Large-eddy simulations have been performed to evaluate the ability of the three subgrid scale models to capture the turbulent behaviour and features of compressible turbulent boundary layers. The subgrid scale models are used on a number of numerical grids to demonstrate grid convergence. However, it must be remembered that in LES the solutions still remain grid dependant to some extent with the resulting contributions of the subgrid scale models tied to the numerical grid used. The main aim of this section is to ensure that LES can compute the skin friction found in turbulent boundary layers, while also capturing the turbulent fluctuations, stresses and transport mechanisms. For clarity, the Smagorinsky eddy-viscosity/eddy-diffusivity, mixed-scale eddy-viscosity/eddy-diffusivity and approximate deconvolution models will be referred to as S, MS and ADM respectively.

4.1.1 Computational Details

For the purposes of validation and determining grid convergence, four numerical grids were used and are summarized in table 4.1-1. The freestream conditions were chosen to match the experimental work of Coles (1953), cited in Fernholz and Finley (1977) while also being in close agreement with the experiments of Mabey et al (1974), cited in Fernholz and Finley (1977). The conditions also conveniently closely match the DNS simulations of Maeder et al. (2001). However, the wall to freestream temperature ratios differed by approximately 6% (see Table 4.1-2). All grids used were wall resolving in that all of the large turbulent structures that control the near wall behaviour are resolved. The numerical resolutions required to resolve these turbulent structures are not precisely defined. Instead, previous LES work is used to guide the choices made. Spectral simulations that are wall resolving and use no wall models have been found to provide accurate results with non-dimensionalised grid spacings of $\Delta x^+ \approx 100$ and $\Delta y^+ \approx 30$ (Piomelli, 1993) in the streamwise and spanwise direction respectively. The non-dimensionalised grid spacings are defined as $\Delta x^+ = \frac{\Delta x\, u_\tau}{\nu_w}$ and $\Delta y^+ = \frac{\Delta y\, u_\tau}{\nu_w}$ respectively. With the finite-volume formulations suffering from truncation errors, these resolutions should be reduced somewhat. For instance, Lenormand et al. (2000) defined a fine LES mesh as having non-dimensional grid spacings of $\Delta x^+ = 35$ and $\Delta y^+ = 14$. Such grid spacings are typical of compressible turbulent boundary layer grids used for LES. In contrast, Rizzetta and Visbal (2004) successfully used a coarser LES mesh for supersonic boundary layer flow with $\Delta x^+ = 84$ and $\Delta y^+ = 22$. This highlights the need to inspect results obtained for the chosen flow problem to ensure that whatever the resolutions, the

results are insensitive to further increases. The requirements for the wall normal direction are more well defined. In the wall normal direction the minimum grid resolutions should conform to $\Delta z^+ < 1$. The above demonstrates that there is some leeway in determining the required resolutions, so long as the results are validated against experimental and/or DNS data. The current grids have been selected in accordance with the recommendations given above. The influence of both increasing grid resolution and wall normal domain size were investigated to determine their significance.

For the case studied in this and later sections, the coarse grid simulations were initialised according to the procedure presented in Section 3.3. Subsequently, the initial solutions of the finer grids were interpolated from coarser grid simulation results.

Table 4.1-1: Computational parameters for large-eddy simulation of boundary layer flow

Grid	Domain size	Grid size	Δx^+	Δy^+	Δz^+
A	29 δ x 3.6 δ x 2.5 δ	120 x 40 x 60	59	22	0.2
B	29 δ x 3.6 δ x 2.5 δ	200 x 56 x 100	35	15	0.1
C	29 δ x 3.6 δ x 3.5 δ	120 x 40 x 80	59	22	0.16
D	29 δ x 3.6 δ x 3.5 δ	200 x 56 x 130	35	15	0.1

Table 4.1-2: Physical simulation parameters

Case	M_∞	T_w/T_∞	$C_f \times 10^{-3}$	u_τ
Coles (1953)	4.50	4.65	1.48	41.2
Mabey et al (1974)	4.52	4.77	1.08	36.1
DNS, Maeder et al. (2001)	4.50	4.38	1.51	39.5
LES, current work	4.50	4.65	1.4 - 1.45	40.2

4.1.2 Mean Flow

Throughout the duration of a simulation the turbulent kinetic energy was monitored. The purposes of this monitoring was to identify at which point the flow turbulent has stabilised. The turbulent kinetic energy ($\frac{1}{2}\left(u'^2 + v'^2 + w'^2\right)$) at a point is computed and recorded for each time step. The statistics of the boundary layer flow are sufficiently well known with many authors having pro-

Table 4.1-3: Effect of grid resolution and subgrid-scale model on skin friction coefficient and boundary layer shape factors for Mach 4.5 conditions with $\delta = 1.5 \times 10^{-2}$m

Grid	Subgrid-scale model	$C_f \times 10^3$	H_{12}	H_{32}	Re_θ	Re_{δ_2}
A	S	1.4	9.72	1.79	4600	1050
	MS	1.50	10.1	1.79	4600	1060
	ADM	1.38	9.42	1.83	4900	1120
B	S	1.4	9.98	1.80	4400	1010
	MS	1.55	10.04	1.81	4615	1050
	ADM	1.39	10.08	1.81	4627	1048
C	S					
	MS	1.4	9.87	1.78	4816	1080
	ADM	1.38	9.3	1.80	4730	1070
D	S					
	MS	1.41	9.3	1.8	4760	1036
	ADM	1.40	9.74	1.81	4300	980
Coles (1953)†		1.48	10.01	1.81	3910	885
Mabey et al (1974)‡		1.08	9.39	1.83	9520	2310
DNS, Maeder et al. (2001)		1.51	8.91		3305	795

†. Reynolds numbers calculated from provided freestream conditions

‡. Data used for mean flow profile comparison only

duced reliable simulation results using LES. For such simulations it has been sufficient to monitor turbulent kinetic energy at a number of arbitrary locations to identify a stationary state where the variance of the signal no longer diminishes (Bilson, 2004). Once the initial solution transients have disappeared and a stationary turbulent state has been reached, the solution was then allowed to advance further in time with samples of the flow taken at regular intervals. A typical turbulent kinetic energy evolution trace for a point midway through the boundary layer at the recycling station is given in figure 4.1-2, with sampling time as indicated. Once the turbulence had stabilised the process of gathering flow statistics begins. To extract mean flow profiles from an inherently unsteady flow problem, time averaging was employed. Each flow solution is averaged over a time-frame greater than 10 flow-through times (L_x/U_∞). By taking samples at time intervals greater than the average eddy turnover time (δ_0/U_∞), we could ensure that neighbouring time samples are statistically independent. Approximately 20 to 30 samples were taken for each simulation

presented.

Effect of Grid Refinement

The effect of grid resolution is a key phenomena that must be studied in LES. Not only must we ensure that the underlying numerical scheme behaves appropriately, but we must also check that the solution is as independent of the chosen grid as possible. Ensuring that the numerical schemes behave appropriately is known as code verification. Verification differs from validation in that verification ensures that the equations are being solved correctly. Roache (1998) describes verification as "solving the equations right" and validation as "solving the right equations". Verification makes the check that, as some measure of numerical discretization approaches zero, the code converges towards a true solution to the continuum equations. The relevance of this solution to the physical problem is the issue of validation.

To begin with, using the skin friction coefficients reported by ADM, it is possible to extract an observed order of convergence from systematic grid refinement (table 4.1-3). There exists two main options in extracting such order of convergence. Graphical methods use a best-fit curve to extract an order of convergence but require the finest grid solution to be taken as the reference point. Instead, by first computing an order of convergence, then using this order to estimate the exact value, an improvement is made on the graphical methods. This process also provides a reliable method for assessing grid convergence errors. To begin with, the difference between successive grid refinement quantities is defined:

$$\varepsilon_{12} = f_2 - f_1 \tag{4.1}$$

where:

f_2 = coarse grid numerical solution obtained with grid spacing h_2
f_1 = fine grid numerical solution obtained with grid spacing h_1

and

r = refinement factor between the coarse and fine grid ($r = h_2 / h_1 > 1$)

Simple relations exist for calculating the order of convergence, however, these methods often rely on grid doubling (r = 2) and/or constant grid refinement factors. For the solution in three-

dimensions of the unsteady Navier-Stokes equations, grid doubling would increase the cost by a factor of at least 16, representing a computationally daunting task. For grid refinement studies such as the one performed here, neither grid doubling nor constant refinement factors are not used. This, however, poses no problems. For this situation we can calculate the order of convergence by solving:

$$\frac{\varepsilon_{23}}{(r_{23}^{p})} = r_{12}^{p}\left(\frac{\varepsilon_{12}}{(r_{12}^{p}-1)}\right) \tag{4.2}$$

where subscripts 1,2 and 3 refer to the fine, medium and coarse grids respectively. These refinement levels were chosen to correspond to grids D, B and A respectively for case 1. The inclusion of grid C at the expense of grid A made verification calculations highly sensitive due to the normalized resolution of grid C being very similar to that of grid B. Using the near wall spacing divided by the wall normal domain height (z^{+}/L_z), we can study the convergence of skin friction coefficient as $z^{+}/L_z \rightarrow 0$. This incorporates the effect of increasing computational mesh resolution and increasing domain height.

Figure 4.1-3 graphically shows the variation of skin friction coefficient given in table 4.1-3 as grid discretization approaches zero. Solving Eq (4.2) proves to be highly sensitive to differences in c_f of less than 0.1%. However, the analysis indicates an observed order of convergence of between 0.9 and 1.0, depending on what tolerance is taken in solving the equation. Figure 4.1-3 plots both a linear curve fit and one based on an observed order of convergence of 0.9, showing little sensitivity to the chosen order.

Identifying the overall order of convergence allows for an estimate of the skin friction coefficient given infinite numerical resolution. Following the graphical methodology and extending both curve fits to zero size discretization returns a skin friction coefficient of approximately 1.41×10^{3}, demonstrating little divergence from computed values.

Alternatively, the Grid Convergence Index (GCI) offers a simple method of calculating an estimate of the Richardson error in a reported value and hence an estimate of the exact numerical solution. Two common methods of error estimation exist. The most simple and straightforward technique presented by Roy (2003) extrapolates an estimate of f_{exact} and uses the difference between it and the computed value as the error. The estimate of f_{exact} is computed, given the order of convergence, via:

$$f_{exact} = f_1 + \frac{\varepsilon_{21}}{r_{12}^{p}-1} \tag{4.3}$$

However, there exists uncertainty in such an estimation as it is not known how close the estimate lies to the true solution. Furthermore, it is also known that even though the original numerical

scheme locally conserves mass, momentum and energy, the extrapolated exact solution is not guaranteed to do so. To overcome the uncertainty of proximity of the estimate to the true solution and also to ensure a conservative error estimate, a safety factor is incorporated. Given the estimate to the exact solution, here computed to be 1.42×10^{-3}, the GCI of Roy (2003) is estimated by:

$$GCI = F_s \left| \frac{f_1 - f_{exact}}{f_{exact}} \right| \times 100 \tag{4.4}$$

Using the recommendation of $F_s = 3$ we arrive at an error estimate of 4.2% in skin friction coefficient.

Alternatively, Roache (1998) details a method using the difference between the medium grid and fine grid solutions. The method of Roache (1998) is considered to be more conservative than mixed-order Richardson extrapolation and given that this process is not commonly used in LES applications, the Roache (1998) method was chosen for use. The error estimator is calculated by:

$$E_1 = \frac{|\varepsilon|}{(r_{12}^p - 1)} \tag{4.5}$$

where the error ($|\varepsilon|$) is computed via:

$$|\varepsilon| = \frac{(f_2 - f_1)}{f_1} \times 100 \tag{4.6}$$

The corresponding GCI is estimated by incorporating a safety factor (again $\mathrm{F}_s = 3$, conservative recommendation of Roache (1998)) via

$$GCI = \mathrm{F}_s \, |E_1| \tag{4.7}$$

The main problem with this approach is that the estimated error in skin friction coefficient is independent of the numerical order of accuracy. It is quite evident that a difference of 2% between medium and fine grid solutions (f_2 and f_1 respectively) would give different true errors if a third-order, rather than first order numerical scheme were used. It is for these reasons that the safety factor (F_s) is incorporated. The Grid Convergence Index for grid D (fine) from equation (4.7) with $\mathrm{F}_s = 3$ is 4.3%.

It is clear that the two methods produce similar error estimates for the grid convergence index. This result was pointed out by Roy (2003), where for error estimates of less than 10-20%, little differences are expected to be observed. Figure 4.1-3 plots the corresponding error bars for the grid D data point. So far, the verification process has demonstrated that the numerical scheme is

behaving in a regular fashion. The process has also allowed for the numerical resolutions to be identified as lying within the asymptotic convergence region.

Returning to the issue of validation, it is now possible to assess the effect of increasing numerical resolution, while comparing to the available experimental and DNS data to ensure that we are solving the right problem. All four grids underpredict the experimentally determined skin friction coefficient by between 4 and 5%. After examination of the experimental values, Fernholz and Finley (1977) suggested that the experimentally determined skin friction coefficient values are slightly high, suggesting better agreement with the LES results. There is no clear improvement between the two different wall normal resolutions used, indicating that the results are largely insensitive to wall normal spacing at these close distances. The DNS of Maeder et al. (2001) slightly overpredicts the skin friction coefficient of Coles, however, the thermal wall conditions did differ somewhat.

Further assessment of validity can be made by computing the boundary layer shape factors. Shape factors H_{12} and H_{32} are defined as δ_1/δ_2 and δ_3/δ_2 respectively. The different thicknesses used in this work are defined as follows:

$$\text{boundary layer thickness} \quad : \quad \tilde{u}(z=\delta) = 0.995\tilde{u}_\infty \tag{4.8}$$

$$\text{displacement thickness} \quad : \quad \delta_1 = \int_0^{\delta_0} \left(1 - \frac{\rho\tilde{u}}{\rho_\delta \tilde{u}_\delta}\right) dz \tag{4.9}$$

$$\text{momentum defect thickness} \quad : \quad \delta_2 = \int_0^{\delta_0} \frac{\rho\tilde{u}}{\rho_\delta \tilde{u}_\delta}\left(1 - \frac{\tilde{u}}{\tilde{u}_\delta}\right) dz \tag{4.10}$$

$$\text{kinetic energy defect thickness} \quad : \quad \delta_3 = \int_0^{\delta_0} \frac{\rho\tilde{u}}{\rho_\delta \tilde{u}_\delta}\left(1 - \left(\frac{\tilde{u}}{\tilde{u}_\delta}\right)^2\right) dz \tag{4.11}$$

Unlike the skin friction coefficient, the boundary layer shape factors do show some improvement with increasing grid resolution (table 4.1-3). Shape factors are notoriously difficult to calculate accurately with the requirement being not only good near wall resolution, but also good resolution toward the boundary layer edge. The shape factors calculated lie within 1 - 2% of the experimental results. Shape factor H_{12} shows the most sensitivity to the numerical resolution, but indicates that for all subgrid scale models presented, good performance is obtained for grid B. There is little change in H_{32} with grid resolution. In contrast, the DNS of results underpredict both the experimental and current LES results. Maeder et al. (2001) still interpreted the comparison between experimental and numerical values as good agreement.

Given the wall and boundary layer edge conditions and boundary layer momentum defect thick-

nesses (δ_2) it is possible to compute Reynolds numbers based on these quantities. We define:

$$\mathrm{Re}_\theta = \frac{\rho_\delta \tilde{u}_\delta \delta_2}{\mu_\delta} \tag{4.12}$$

$$\mathrm{Re}_{\delta_2} = \frac{\rho_\delta \tilde{u}_\delta \delta_2}{\mu_w} \tag{4.13}$$

When compared to experimentally computed values, the Reynolds numbers also show improvement with increasing grid resolution (table 4.1-3). However, it is important to note that the Reynolds number length scale is very sensitive to the definition of boundary layer thickness (δ, Eq (4.8)). This uncertainty in boundary layer thickness flows on to the calculations of δ_1 and δ_2 through the integral bounds. Fernholz and Finley (1977) point out that the selection of a boundary layer edge is somewhat arbitrary. The criteria commonly used to guide the selection of the experimental boundary layer edge point are so various as to permit variations in δ of 60% or more (Fernholz and Finley, 1977). Hence, any difference in interpretation of boundary layer thickness criteria by Coles (1953) can account for any of the differences observed. Despite this, in considering grids A, B and D, there still exists a trend towards the experimental values of Coles (1953).

Figure 4.1-4 shows the van Driest transformed mean streamwise velocity profile, normalised by friction velocity and plotted in wall units for the four grids examined. The transformation of a compressible boundary layer is defined as:

$$u^+ = \int_0^{u^+} \sqrt{\frac{\rho}{\rho_w}} du^+ \tag{4.14}$$

where $u^+ = \overline{u}/u_\tau$ and the friction velocity, u_τ is defined as:

$$u_\tau = \sqrt{\frac{\tau_w}{\rho_w}} \tag{4.15}$$

Such a transform has the intention of collapsing compressible boundary layer data onto the incompressible linear assumption for the viscous sublayer:

$$u^+ = z^+ \tag{4.16}$$

and the incompressible law of the wall:

$$u^+ = 2.5\, z^+ + 5.2 \tag{4.17}$$

The wall normal spacing is transformed using inner scaling of the form

$$z^+ = \frac{z\, u_\tau}{\nu_w} \tag{4.18}$$

There is significant improvement in mean profile for increasing grid resolution when using an eddy-viscosity/eddy-diffusivity model. However, for both higher resolution grids (B & D) with ADM subgrid scale model, agreement with the theoretical predictions and the DNS data is good.

The mean streamwise velocity, static temperature and streamwise momentum computed with ADM , MS and S models are compared to DNS of Maeder et al. (2001) and experiments of Coles (1953) and Mabey et al. (1974) in figures 4.1-5, 4.1-6 and 4.1-7 respectively. The effect of spatial resolution on the mean velocity field is investigated for all three subgrid scale models. For all grids ADM reproduces the near wall velocity gradient faithfully while both MS and S models show improvements in near wall behaviour with increasing grid resolution. For the remainder of the boundary layer regions, the ADM and MS models show improving trends with increasing grid resolution. Clearly, grid refinement shows improvements in the mean streamwise velocity profiles for the ADM and MS models. The small magnitude of the improvements and good comparison with experimental profiles demonstrates that grid convergence is achieved. The S model, only applied to two grids (A and B), gave an underestimation of the velocity profile near the boundary layer edge for the coarse grid (A), while giving a fuller profile on the fine grid (B).

In considering static temperature profiles, it must be noted that the DNS results of Maeder et al. (2001) used a lower wall temperature ratio and hence higher wall temperature than the experiments and LES simulations. The profiles reported from the ADM simulations show trends toward both the DNS and experimental data with grids B and D showing very good agreement. Similarly for the MS model, grids B and D provide a good representation of the static temperature profiles. For both ADM and MS models, there is little difference between the results of grids B and D, suggesting a good level of refinement has been reached. Like the other two subgrid scale models, the S model also shows a clear improvement with grid resolution. However, the S model does not generally perform as well as the other models presented.

The streamwise momentum profiles provide another check on the effect of spatial grid resolution, while illustrating the effect of domain size. The ADM data clearly indicates the effect of increasing the vertical height of the computational domain. Both grids C and D, with increased computational domain height, did not yield any overestimations of momentum near the boundary layer edge. Most notably, for grids A and B in the region $z/\delta_1 < 2$ there is a bulge in the profile not observed

for grids C and D. Outside of this region and near the boundary layer edge, grid C returns a slight overestimation in streamwise momentum, while grid D reports a lower profile than the experimental and DNS data although it quickly returns to expected values. The MS model paints a somewhat more confusing picture with grid C the only case not returning a large overprediction for $z/\delta_1 \approx 2-3$. The S model once again shows improving trends with increased grid resolution.

From the results obtained at varying levels of grid refinement and domain heights we can conclude that the higher resolution grids provide the best agreement with the experimental and DNS results. Examination of the streamwise momentum profiles identifies the further need for good wall normal domain height. With the exception of the following sections addressing turbulent intensities and Reynolds stresses, most remaining analysis is performed with results obtained from grid D, the highest resolution with $200 \times 56 \times 130$ cells.

Effect of Subgrid-Scale Model

The effect of subgrid-scale model on the mean streamwise velocity profile can also be observed in figure 4.1-4. The mean streamwise velocity profiles are transformed according to equation 4.14 and compared to the linear viscous sublayer assumption and standard law of the wall (equations 4.16 and 4.17). For grids A & B, the S model calculated a greater defect in the mean velocity profile than both the MS model and ADM approach. This effect was most pronounced on the coarse grid. For this reason, the S model is not considered any further. Considering all four grids, the MS model was most sensitive to grid resolution, showing significant improvement with grid resolution. ADM on the other hand was largely insensitive to grid resolution, while also performing the best of all three models. This assessment was made by the ADM process not requiring the same level of resolution as the MS model to return a good transformed velocity profile. Like the DNS results, there was no clear region that closely followed the standard law of the wall. However, the slope is best reproduced by the finer grids (B & D).

The effect of subgrid-scale model on skin friction coefficient, shape factors and Reynolds numbers can also be deduced from table 4.1-3. The S model, despite its shortcomings in mean profile calculation performed well in calculating skin friction, shape factors and Reynolds number. The MS model calculated skin friction values greater than those of experiments for grids A & B, while grids C & D returned lower values. Shape factors remained accurate within 5% for all subgrid scale models studied, with results obtained from ADM simulations proving superior.

Reynolds numbers computed from the numerical results were greater than the experimental points, but tended toward them with improving resolution, akin to the skin friction coefficient behaviour that was observed in the verification process. Again, the ADM calculations obtained the better agreement.

From the plots of mean streamwise velocity, static temperature and streamwise momentum in figures 4.1-5, 4.1-6 and 4.1-7, it is clear that for a given grid resolution, the near wall behaviour is best reproduced by ADM. The MS and S models required the finer grid resolutions to capture this behaviour. Throughout the mid regions of the boundary layer, particularly for static temperature, ADM was able to compute profiles comparable to DNS and experiments at lower resolutions than MS and S models. In the outer regions of the boundary layer all models suffered from an overprediction of streamwise momentum, that was alleviated by grid resolution improvements and increased wall normal domain height.

Overall, ADM was found to perform the best of all models for a given grid resolution, but the MS model was still able to yield good mean profiles for the optimum grid resolution. The following analysis extends the comparison to the examination of turbulent fluctuations and has been performed using the MS and ADM subgrid-scale models.

4.1.3 Turbulent Intensities and Compressibility Effects

Authors such as Coleman et al. (1995) suggest that qualitatively the turbulent structure of incompressible and compressible channel flows is similar. Maeder et al. (2001) investigated to see if similar behaviour could be observed for boundary-layer flows. To make these judgements the compressibility effects must be quantified. We begin with the turbulent Mach number, M_t, defined as:

$$M_t = \frac{\sqrt{2K}}{\overline{a}} \tag{4.19}$$

where $K = \frac{1}{2}u_i'u_i'$ is the turbulent kinetic energy. The turbulent Mach number is a crucial quantity and gives an immediate and accurate representation of the importance of compressibility effects (Smits and Dussauge, 1996). The large amount of kinetic energy that exists in supersonic flow

can produce significant thermal changes when it is converted to heat. With turbulence being a dissipative process, adiabatic thermal processes can contribute to the fluctuating velocity divergence ($\nabla \cdot u'$). Smits and Dussauge (1996) argue that compressibility effects become significant when $\nabla \cdot u'$ becomes large. Following this, they observed that the relative importance of the velocity divergence and hence, compressibility effects, varies with the turbulent Mach number, M_t^2. Thus, capturing the true behaviour of M_t is a good indication of accurate resolution of compressibility effects.

More generally, the importance of turbulent Mach number in representing compressibility effects is observed if, for instance, the turbulent Mach number were to approach unity, local shock waves (*shocklets*) would form. A turbulent Mach number of 0.3 is generally accepted to be the level where compressibility effects become important in determining the turbulence behaviour. This level of turbulent Mach number is reached for freestream Mach numbers in excess of 4 to 5 (Smits and Dussauge, 1996). With the simulated conditions being Mach 4.5 it would be expected to observe that compressibility effects were indeed important. The results of figure 4.1-9 and 4.1-10, showing turbulent Mach number across the boundary layer support this claim with turbulent Mach numbers peaking in the vicinity of 0.4. The turbulent Mach numbers plotted in these figures compare well in near wall behaviour, peak magnitude and outer region trends. As was found for the mean flow, the turbulent Mach number is best represented by ADM when used on grid D.

The turbulent Mach number is computed from the resolved velocity fluctuations. The RMS of the resolved velocity fluctuations are calculated from the instantaneous solutions collected and the corresponding time averaged solution. Due to LES using coarser grids than DNS, it is generally expected that the results of LES would lie below those of DNS. However, it is commonly reported that LES and the associated coarser grids overpredicts the streamwise fluctuations (Rizzetta and Visbal, 2004). Figures 4.1-11 and 4.1-12 plot the RMS of streamwise velocity fluctuations normalized by the mean velocity profile from ADM and MS subgrid-scale models. Except for the coarsest grid, comparison with the DNS results of Maeder (2000) is very good across the whole boundary layer and beyond. ADM can be seen to perform best and again be less susceptible to grid resolution variation. Figures 4.1-13 and 4.1-14 plot the RMS of static temperature fluctuations, normalized by the mean static temperature profile for ADM and MS subgrid-scale models. This quantity was more difficult to represent than the streamwise velocity fluctuations. It required the higher resolution grid and the ADM subgrid-scale model to remove excess temperature fluctuations, while also accurately capturing the near wall behaviour. These results confirm the experimental observations that, while u' decreases monotonically away from the wall, the persis-

tence of T' through the middle layers of the boundary layer leads to a peak in local Mach number fluctuations near $z/\delta \approx 0.5$. The turbulent fluctuations of velocity further demonstrate that the best performing subgrid scale model is the ADM procedure. Consequently, the MS model not be further considered.

To extend comparisons from streamwise velocity fluctuations to spanwise and wall normal velocity fluctuations, experimental data obtained from other flow conditions had to be used. Measurements of spanwise and wall normal fluctuating velocities are considerably less common than the streamwise counterpart, while also exhibiting greater scatter. For instance, Konrad and Smits (1998) found that at high Reynolds numbers, spanwise and wall normal velocity fluctuations were approximately equal throughout the boundary layer. The data of Kussoy et al. (1978) also demonstrated such behaviour. Adding further to the confusion, Elena and Lacharme (1988) found that the spanwise velocity fluctuations for low Reynolds number flows behaved more like subsonic flow whereas, Johnson and Rose (1975) measured both the streamwise and spanwise fluctuating velocity at Mach 2.9 and did not note any similarity to subsonic data. As discussed further in section 4.1.4, the relative levels of spanwise and wall normal fluctuations is highly dependent on Reynolds number (Smits and Dussauge, 2006). Given that Elena and Lacharme (1988) used the lowest Reynolds number, the observed similarity with subsonic flow behaviour appears to be tied to the Reynolds number.

To make comparisons to experimental data obtained under differing flow conditions, Reynolds number effects need to be removed. A common method for removing such dependence from fluctuating velocity measurements is to normalize by friction velocity (u_τ, eq 4.15). The length scale also varies with flow conditions, and consequently must also be accounted for. There exists three common ways of normalizing the length scale so that, in conjunction with normalizing velocity fluctuations by friction velocity, Reynolds number effects can be reduced or removed. The first method is to normalize the length scale by the boundary layer thickness, δ. This process can achieve good results given a well defined criteria for thickness determination. However, experimentally this location can be ill-defined despite consistent methods existing and often being adhered to. Figures 4.1-15 and 4.1-16 show the normalized velocity fluctuations for ADM and MS subgrid-scale models respectively. When compared to experimental data, the streamwise velocity fluctuations that agree with DNS data appear high relative to the experimental values, although the grid resolution trends are encouraging. Spanwise velocity fluctuations, while large for coarser grids, show good agreement for the finer grids. The wall normal fluctuations, despite not reaching the levels reported by Konrad and Smits (1998), are more in agreement with Kussoy et al. (1978),

but demonstrate no clear peak in near wall behaviour.

The second length scale used is the conventional inner scaling method. This process has been used extensively in mean flow measurements, with the ratio of kinematic viscosity at the wall to friction velocity (ν_w/u_τ) used to obtain similarity. Fernholz and Finley (1981) observed that similarity could not be found when using this scaling method. That observation is also clear for the current results, as observed in figure 4.1-17. Such a scaling clearly highlights the limit on how close experimental measurements can be taken to the wall. We can see that the data of Spina and Smits (1987) was limited by probe design and did not extend below $z^+ \approx 1000$, precluding comparison in the near wall region. Konrad and Smits (1998) and Kussoy et al. (1978), on the other hand, were able to extend much closer to the wall ($z^+ \approx 200$). However, the absolute maxima of turbulent fluctuations generally lies closer to the wall, $z^+ < 200$, and consequently no conclusions about the maxima in streamwise turbulent fluctuations can be drawn.

The third method of length scale normalization removes any issues of choosing a suitable boundary layer edge criterion by instead using an integral thickness. The defect thickness (Δ^*) is used to exploit the similarity in the inner and outer regions of the van Driest transformed velocity profile of a zero pressure gradient boundary layer. The defect thickness is defined:

$$\Delta^* = \int_0^\delta \frac{u^*_\infty - u^*}{u_\tau} dz \tag{4.20}$$

where superscript * represents the van Driest transformed velocity. Often, even with an ill-defined value of δ, the defect integral thickness is a fixed fraction of the true δ. Such an assumption is justified given that any flows that have a self similar outer region velocity profile, have a fixed ratio of defect to boundary layer thickness (Fernholz and Finley, 1981). This fact is exploited because Elena and Lacharme (1988) and Konrad and Smits (1998) did not report a defect thickness; instead the ratio (Δ^*/δ) is assumed to be 4. This somewhat arbitrary selection is supported by the data of Kussoy et al. (1978) and Spina and Smits (1987) that reported ratios of 4.3 and 3.6 respectively. Under this scaling, as observed in Fernholz and Finley (1981) and plotted in figure 4.1-18, we see a much more recognizable and common trend in streamwise velocity fluctuations. The spanwise and wall normal velocity fluctuations are plotted in figures 4.1-19 and 4.1-20 respectively using defect integral scaling. Unlike the streamwise velocity fluctuations, the agreement, even amongst experiments, is less convincing. The spanwise velocity fluctuations agree well qualitatively with the experimental data of Konrad and Smits (1998) and not so well with the data of Kussoy et al. (1978). Wall normal velocity fluctuations, on the other hand, show better agreement with Kussoy et al. (1978) and Elena and Lacharme (1988). It appears that the Reynolds number dependence

is not entirely removed for spanwise and wall normal velocity fluctuations by the velocity and length scales chosen. The only conclusion that can be made for the current spanwise and wall normal results is the same as the observation of Fernholz and Finley (1981); the spanwise and wall normal velocity fluctuations, without considering the density profile, display a maximum near the wall and decrease towards the outer boundary layer edge. For all three velocity components, few comparisons can be made about the behaviour of the fluctuating velocities in the inner regions of a compressible boundary layer since experimental data for this region is non-existent.

4.1.4 Reynolds Stresses

The streamwise Reynolds normal stress ($\rho\overline{u'u'}$) and Reynolds shear stress ($\rho\overline{u'w'}$) are normalised by the freestream conditions and compared with the corresponding stresses reported by the DNS of Maeder et al. (2001) in figures 4.1-21 and 4.1-22. The improvements with grid resolution are clear to see for the streamwise Reynolds normal stress. The results are largely independent between grids C and D. For all grids, as observed for the mean flow parameters, the near wall behaviour is reproduced well. There is some overshoot in peak value of streamwise Reynolds normal stress resulting from overprediction of streamwise velocity fluctuations. The results then show the same trends as the DNS data and by $z/\delta = 0.5$ return to DNS values. The Reynolds shear stress shows a fair agreement with the stresses calculated by DNS. The near wall and outer boundary layer edge behaviour also shows clear improvement with increasing near wall resolution. When compared to the near wall behaviour of the streamwise Reynolds normal stress, the wall normal fluctuations appear more damped, resulting in low values in the immediate wall vicinity. The slope of the profile, however, does match the DNS results near the wall. The peak level and mid boundary layer behaviour of the Reynolds shear stress is reproduced by grid D within 10%. However, an early decay in stress level is present for $z/\delta = 0.2$. From here, the effect of wall normal domain length is apparent. The grids with the shorter wall normal domain, A and B, yield larger Reynolds shear stresses around the boundary layer edge than the grids with a larger wall normal domain, C and D. All grids other than grid D, however, suffer from decreasing wall normal resolution and report values which are higher than DNS in the outer region. In considering the comparisons with DNS there will always be some difficulty as only the fluctuations resolved by the LES grid can be included. Additional fluctuation information resolved by the finer DNS grids go unnoticed by LES.

While the comparison of computed Reynolds shear stress to the DNS results showed discrepan-

cies, even for the finest LES grid used, it is possible to make further comparisons to ascertain the validity of the results obtained by the ADM procedure on grid D. In a survey of compressible turbulent boundary layer data, Sandborn (1974) established the existence of a best fit for the shear stress distributions. Across the majority of the boundary layer ($z/\delta \gtrsim 0.1$), the total shear stress (τ, eq 2.1) is dominated by the turbulent Reynolds shear stress. The best fit proposed by Sandborn (1974) is compared to the computed Reynolds shear stress and those reported by the DNS of Maeder et al. (2001) in figure 4.1-23. Interestingly, the LES results lie closer to the best fit of Sandborn (1974). We must still bear in mind that results of later experimental investigations are scattered about this best fit within $\pm 15\%$ (Fernholz and Finley, 1981), suggesting a broad region of validity.

To further verify the Reynolds stress values calculated, while also comparing additional Reynolds stress components not reported in the DNS work, experimental data is used. Again, some form of scaling needs to be used when making comparisons to both subsonic data and supersonic data at different Reynolds numbers. Morkovin (1962) suggested that the mechanisms that govern turbulent transport are the same as those found for low speed flows and the variations in density found in supersonic flows are taken into account by scaling with the local stress. If the streamwise Reynolds normal stress ($\rho u'^2$) is normalised by the wall shear stress ($\tau_w = \rho_w u_\tau^2$), good agreement can be achieved across Reynolds numbers and with incompressible subsonic data. This scaling appears to be valid up to at least Mach 5 (Smits and Dussauge, 2006). Such similarity has not been observed for the spanwise and wall normal Reynolds normal stress (Fernholz and Finley, 1981).

Figure 4.1-24 shows the normalized streamwise Reynolds normal stress with the length scale chosen to be the velocity defect thickness due to its successful application for the velocity fluctuations. Also included is the experimental data of Konrad and Smits (1998), Spina and Smits (1987), Kussoy et al. (1978) and Johnson and Rose (1975). It can be seen that the LES calculations follow the DNS results well and are in quite good agreement with Konrad and Smits (1998). The data of Spina and Smits (1987) and Kussoy et al. (1978) are considerably lower than the other data points, with fair agreement with Konrad and Smits (1998) in the outer region. The overall agreement with DNS and experimental data of Konrad and Smits (1998) is encouraging. Figure 4.1-25 plots the Reynolds shear stress, with the same normalization employed. Using Morkovin scaling for the Reynolds shear stress demonstrates much closer near wall agreement for grids B and D, while comparison across the majority of the boundary layer improves further for grid D.

As stated before, the benefit of this normalization is to facilitate some comparisons of spanwise

and wall normal Reynolds normal stress that were not reported by Maeder et al. (2001). Figures 4.1-26 and 4.1-27 make these comparisons for the spanwise and wall normal Reynolds normal stress components respectively. The hot wire and laser-Doppler velocimetry measurements of spanwise Reynolds normal stress by Johnson and Rose (1975), Konrad and Smits (1998) and Horstman and Owen (1972) all exhibit good agreement given the different experimental conditions studied. The LES simulation for grid D, and to a lesser extent grids B and C, calculates Reynolds stresses for $z/\Delta^* < 0.3$ that lie within the experimental uncertainty range of Konrad and Smits (1998) and also lie within approximately $\pm 10\%$ of all other experimental data. There still exists variation in stress levels for each grid studied, suggesting the true convergence is not yet reached for this quantity. For the outer regions of the boundary layer ($z/\Delta^* > 0.3$), the LES results do not show the same sharp drop-off in stress levels that the experiments indicate. However, it can be clearly seen that grid resolution improvements cause the numerical results to approach the experimental data points. The experimental measurements of wall normal Reynolds normal stress appear to exhibit greater scatter. As was noted by Smits and Dussauge (2006), the wall normal Reynolds normal stress measured by Konrad and Smits (1998) was approximately equal to the spanwise Reynolds normal stress. The measurements of Elena and Lacharme (1988) found that the behaviour of this quantity was more like subsonic incompressible data. Hence, agreement amongst experiments is yet to be achieved. The same conditions as those studied by Elena and Lacharme (1988) ($M = 2.23$ and $Re_\theta = 4452$) were studied with DNS by Martín (2004) with very impressive agreement, giving additional confidence in their profile. Behaviour similar to incompressible data was also measured by Kussoy et al. (1978). This anisotropy between spanwise and wall normal quantities was suggested by Smits and Dussauge (2006) to be strongly dependent on Reynolds number, with Konrad and Smits (1998) studying a Reynolds number an order of magnitude greater than Elena and Lacharme (1988). The wall normal Reynolds normal stress calculated by LES certainly corroborates the data of Elena and Lacharme (1988). The data also provides further evidence of the Reynolds number effects on relative levels of spanwise and wall normal Reynolds normal stresses. From this collection of data we can reach the conclusion that both DNS and experimental results demonstrate good quantitative and qualitative agreement to the LES data.

4.1.5 Two-Point Autocorrelations

To assess the accuracy of the numerical simulations, two-point autocorrelations are calculated along the homogeneous streamwise and spanwise directions. These two-point autocorrelations

can be used to indicate the length scales of the turbulent structures found within the turbulent compressible boundary layer. Furthermore, the distribution of the two-point autocorrelations can assess whether the computational domain is large enough in the streamwise or spanwise directions in order to accommodate the full turbulent dynamics. The assessment of sufficient domain size is made by ensuring that the two-point autocorrelation function is sufficiently decorrelated over half the length of the homogeneous direction being considered. The two-point autocorrelation function in the homogeneous y-direction is given by:

$$R_{\alpha\alpha}(r_y) = \sum_{k=1}^{N_y-1} \alpha_k \alpha_{k+k_r}, \qquad k_r = 0, 1, ..., k-1 \tag{4.21}$$

The two-point autocorrelations of velocity and, hence, the turbulent structures are given in figures 4.1-28 and 4.1-29 for the approximate deconvolution model. Unlike the DNS of Maeder et al. (2001), where the domain is short in the streamwise direction and periodic boundary conditions are used rather than a conventional inflow and outflow configuration, the two-point autocorrelations are allowed to fall to zero, becoming decorrelated within the computational domain. Hence, no direct comparison is made for two-point autocorrelations to those DNS results. Despite this, the qualitative trends of the DNS data are reproduced.

The behaviour of the Reynolds stress profiles of the previous section gave an indication of the presence of turbulent structure within the boundary layer. The anisotropy between streamwise, spanwise and wall normal components cannot be completely explained by the presence of a wall (Bernard and Wallace, 2002). Rather, the anisotropy suggests the presence of turbulent structures, whose behaviour manifests in changes to the Reynolds stress distributions from one that is purely isotropic. The two-point autocorrelations of velocity not only signal the presence of structures, but can also provide an indication of over what distances the velocities and, hence, structures are correlated. If a purely random turbulent field should exhibit no correlation, the observed correlations distributions do indeed suggest the presence of coherent turbulent structures.

In considering the streamwise direction, the two-point autocorrelation of streamwise velocity near the wall shows that the streamwise velocity fluctuations remain correlated over longer distances than other components. This clearly signals the presence of coherent streamwise regions, known as streaks. The two-point autocorrelations of spanwise and wall normal velocity drop off much more sharply indicating a short coherence with a streamwise orientation. This long coherence of streamwise velocity and short coherence of the other two velocity components is consistent with

the very large-scale motions, or 'hairpin packet' model of Kim and Adrian (1999), as observed by Ganapathisubramani et al. (2006). The width of the near wall streaks can be calculated from the minimum two-point autocorrelation of the spanwise velocity component taken in the spanwise direction. The commonly accepted non-dimensional mean spacing of the streaks is 100 wall units ($100y^+$, Smits and Dussauge (1996)). The LES results indicate a minimum which is close to the results of Smits and Dussauge (1996), at approximately $180y^+$. This greater mean streak spacing is commonly attributed to the lower spanwise resolutions used in LES (Keating, 2003).

To make futher examination of the coherent turbulent structures via the two-point autocorrelations, we use the definition of Ganapathisubramani et al. (2006) to give a representative length scale (λ) when the two-point autocorrelation level $R_{\alpha\alpha} = 0.5$. These scales give an indication of the length of coherence of structures in both the streamwise and spanwise directions associated with both low and high speed structures, relative to the mean flow. The technique proposed by Ganapathisubramani et al. (2006) for experimental data gave length scales with a maximum uncertainty of approximately 10%, based on the resolution of the two-point autocorrelations beneath the measured length scale.

Based on R_{uu}, the streamwise length scale, λ_x^u has values of 1.3δ, 0.9δ and 0.5δ at $z^+ = 5$, $z/\delta = 0.5$ and 0.8 respectively. Despite being ill-defined experimentally, the boundary layer thickness (δ) was chosen as the scaling parameter for this study to remain consistent with previous studies in the literature. This shows a decreasing coherence with increasing wall normal distance. The results of Ganapathisubramani et al. (2006), on the other hand, indicate an increasing coherence scale with increasing wall normal distance for measurements within the log layer ($z/\delta \lesssim 0.6$). Interestingly, Smits et al. (1989) found, from two-point autocorrelations of mass flux fluctuations, a decreasing trend in length scales with increasing wall normal distance. The reasons behind this disparity in behaviour is unknown. Despite this, agreement still exists in that their magnitudes are many times smaller than incompressible boundary layer length scales, which are often of a similar size or greater than the pipe radii, which themselves are greater than the boundary layer thickness (Kim and Adrian, 1999).

There does exist greater agreement amongst experiments about the trends in length scales for streamwise velocity in the spanwise direction. Various other experiments performed by Ganapathisubramani et al. (2006); Smits and Dussauge (1996); Bernard and Wallace (2002), found an increasing trend in length scale with increasing wall normal distance. The observed length scales in the present work, λ_y^u, are 0.25δ and 0.36δ at $z^+ = 5$ and $z/\delta = 0.5$ respectively. This suggests

Table 4.1-4: Turbulent length scales determined from ADM simulations on grid D

	λ_x^u	λ_x^v	λ_x^w	λ_y^u	λ_y^v	λ_y^w
$z^+ = 5$	1.3	0.7	0.4	0.25	0.12	0.12
$z/\delta = 0.5$	0.9	0.7	0.6	0.36	0.40	0.24
$z/\delta = 0.8$	0.5	0.6	0.55	0.36	0.34	0.26

that the numerically captured turbulent structures represented by these quantities also increase in scale with increasing distance from the wall. All calculated length scales are summarized in table 4.1-4.

4.1.6 Energy Spectra

A further assessment of numerical resolution is made by calculating the one-dimensional energy spectrum of the turbulent velocity fluctuations. The streamwise and spanwise energy spectra for the fluctuating flow quantity, $q(x, y, z)$, is calculated using:

$$E_q(k_x, z) = \frac{1}{N_x} \sum_{j=1}^{N_x} \hat{q}(k_x, y, z)\hat{q}^*(k_x, y, z) \tag{4.22}$$

$$E_q(k_y, z) = \frac{1}{N_y} \sum_{k=1}^{N_y} \hat{q}(x, k_y, z)\hat{q}^*(x, k_y, z) \tag{4.23}$$

where $\hat{q}(k_x, y, z)$ denotes the Fourier transform of $q(x, y, z)$ (here in the x-direction) and an asterisk denotes the complex conjugate. Averaging is performed in the remaining homogeneous direction and also in time, which is not indicated. A commonly accepted assessment of numerical resolution capturing the turbulent energy cascade is for the turbulent energy content to decrease 3-4 orders of magnitude from the smallest to highest wave numbers resolved (Maeder et al., 2001; Gatski and Erlebacher, 2002).

The calculated energy spectra in the streamwise and spanwise directions, normalized by lowest wavenumber energy content ($E_q(k_x, z)/E_q(0, z)$, Gatski and Erlebacher (2002)), for the approximate deconvolution model on grid D, is plotted in figures 4.1-32 and 4.1-33. The agreement with

DNS is quite good in the spanwise direction for all three velocity components. There is some overestimation of energy content for streamwise and wall normal velocities. This overestimation is most likely associated with the corresponding overestimation of the RMS of streamwise and wall normal velocity fluctuations. At higher wavenumbers, the LES results decay more rapidly where the truncation errors of the numerical scheme introduce additional dissipation. This result has been observed previously for low-order LES (Keating, 2003) and it is to be expected with the LES grids being coarser than those of a DNS. Less agreement with DNS results is obtained in the streamwise direction and is seen as a consequence of spanwise grid spacing that is coarser than that used by Maeder et al. (2001) and possibly the forcing functions used to enforce the ETDNS numerical approach. Some aliasing (energy pile-up, Kosovic et al. (2002)) is also evident at high wavenumbers through truncation errors. The wall normal velocity spectra gives a significant over-prediction in energy content when compared to DNS, while not showing the desired drop-off in energy content. The mixed scale model spectra on grid D (figures 4.1-34 and 4.1-35) do not compare as well with the DNS results and is included to demonstrate the difficulty in obtaining realistic energy spectra with simpler subgrid scale models. The spectra exhibit more pronounced aliasing at high wavenumbers and also give a much quicker drop-off in energy content, consistent with a more dissipative subgrid-scale model. There also exists a more pronounced overestimation of streamwise turbulent energy content for the wall normal velocity fluctuations.

The results display no clear region where the energy cascade adheres to the traditional inertial region -5/3 slope. Generally, at the Reynolds numbers being studied here, an inertial range is not expected (Keating, 2003). This lack of clear inertial range may also suggest that compressibility has an influence on the spectral dynamics of the turbulence precluding an inertial region that follows the -5/3 law. However, this postulation is unlikely with the hypersonic boundary layer study of Laderman and Demetriades (1974) finding a slope that was close to -5/3 in the high wave number region. Smits and Dussauge (1996) assert that while this may be true such measurements are very difficult.

4.1.7 Quadrant and Octant Analysis

Quadrant analysis (Wallace et al., 1972) is used to study the influence of the turbulent flow structures on the Reynolds shear stress distribution. Quadrant analysis partitions the Reynolds shear stress ($\rho u'w'$) into four quadrants based on the instantaneous velocity fluctuations with each corresponding to four different mechanisms. The quadrants are defined as: I (outward interaction):

$u' > 0\,,\ w' > 0$; II (ejection): $u' < 0\,,\ w' > 0$; III (wallward interaction): $u' < 0\,,\ w' < 0$; IV (sweep): $u' > 0\,,\ w' < 0$. These quadrants are defined graphically both in the $u' - w'$ plane and physically in figure 4.1-36.

It is convenient to define ejections and sweeps physically. An ejection is the result of large scale disturbances, often wallward interactions, interacting with a low speed region of the flow near the wall and commonly accompanies the lifting up of near wall streaks. This results in the low speed fluid being thrown out or ejected into this large scale disturbance. Behind these ejections, high speed fluid would enter the region and clear out the chaotic interaction in what is known as sweep. This phenomena can be thought of as a fundamental part of the horseshoe vortex (Spina et al., 1991) and streamwise streak. The inner regions are ejecting low speed fluid upwards ($u' < 0\,,\ w' > 0$) into high speed flow regions, with a corresponding downwash of high speed fluid into a lower speed region ($u' > 0\,,\ w' < 0$).

Experimental studies of boundary layers (Wallace et al., 1972; Antonia et al., 1988) revealed that the greatest contributing mechanisms to the Reynolds shear stress were sweeps and ejections. The quadrant analysis of the LES results plotted in figure 4.1-38, here normalised by the local total Reynolds shear stress, yields similar behaviour. The outward interaction contribution is also observed to be significant in the near wall region for the conditions studied. The sweep and ejection mechanisms regain dominance for $z^+ > 20$. The contribution of the wallward interaction is lower in magnitude. The sweep mechanism (quadrant IV) is found to be the most dominant near the wall, whereas the ejection mechanism (quadrant II) reaches similar levels within the logarithmic region of the boundary layer. The point at which the mechanisms cross over occurs at $z^+ \approx 30$ and agrees fairly well with the experiments of Wallace et al. (1972) and incompressible LES of Keating (2003).

From the LES results, it is possible to assess the probability of each mechanism occurring. Each quadrant's probability of occurrence is plotted in figure 4.1-39. It is seen that the mechanism making the greatest contribution to the Reynolds shear stress, sweeps, also has the highest probability of occurring. This indicates that the sweep mechanism is primarily composed of small magnitude events occurring frequently. The high probability of outward interaction also indicates how such a mechanism can dominate near the wall. Interestingly, the probability of ejections (quadrant II) for $z^+ > 20$ is significantly below that of the sweeps (quadrant IV), while its contribution to the Reynolds shear stress is nearly identical. This suggests that, while the likelihood of an ejection occurring is smaller than that of a sweep, the magnitude of the ejection is sufficiently large enough

to make an impact on the Reynolds shear stress. The overall transport of turbulent Reynolds shear stress and, hence, momentum is summarized in figure 4.1-40.

Compressible boundary layer flows are highly sensitive to the structure of the turbulent temperature field. Octant analysis (Volino and Simon, 1994) allows for the examination of the influence of the temperature field on the turbulent transport of momentum and heat. The Reynolds shear stress and wall-normal turbulent heat flux are divided into eight octants according to the velocity fluctuations u' and v' and the temperature fluctuations T': I (cold outward interaction): $u' > 0\,,\ w' > 0\,,\ T' < 0$; II (cold ejection): $u' < 0\,,\ w' > 0\,,\ T' < 0$; III (cold wallward interaction): $u' < 0\,,\ w' < 0\,,\ T' < 0$; IV (cold sweep): $u' > 0\,,\ w' < 0\,,\ T' < 0$; V (hot outward interaction): $u' > 0\,,\ w' > 0\,,\ T' > 0$; VI (hot ejection): $u' < 0\,,\ w' > 0\,,\ T' > 0$; VII (hot wallward interaction): $u' < 0\,,\ w' < 0\,,\ T' > 0$; VIII (hot sweep): $u' > 0\,,\ w' < 0\,,\ T' > 0\,.$ The definition of the octants is given in Figure 4.1-37.

Previous analysis of incompressible channel flow (Keating, 2003) indicated that octants II (cold ejections) and VIII (hot sweeps) are the largest contributors to both the Reynolds shear stress and turbulent heat flux. Their dominance in both transport mechanisms can be attributed to the fact that both heat and momentum are transported by similar mechanisms, as per the Reynolds analogy. The LES results for compressible turbulent boundary layers given in figures 4.1-41 and 4.1-42 agree with the observations that octants that dominate the Reynolds shear stress also dominate turbulent heat flux. Here octants VI (hot ejection) and IV (cold sweeps) are the greatest components of the Reynolds shear stress and turbulent heat flux as distance from the wall increases. It is interesting to note that under these conditions of compressible flow, the most active octants are the thermal opposite of those for incompressible flow. The dominance of octants IV and VI is expected. The physical nature of an octant VI (hot ejection) is easily understood as a movement of low momentum, high temperature fluid elements away from the wall and in doing so, transporting significant quantities of Reynolds shear stress and wall normal heat flux. Octant IV (cold sweeps) events are the logical partner of octant VI, as it represents the replenishment of low temperature, high momentum fluid from the freestream.

The very near wall behaviour is difficult to assess by examination of their absolute contributions. Instead, the octant contributions are normalized by their local Reynolds shear stress and turbulent wall normal heat flux. Figures 4.1-43 and 4.1-44 plot each octant contribution for Reynolds shear stress and wall normal turbulent heat flux normalized by the local contribution respectively. It can now be seen that there is a significant negative contribution to the Reynolds shear stress associated

with the cold outward interaction mechanism (octant I) near the wall. The negative magnitude signifies that it is acting to reduce the normalized Reynolds shear stress and wall normal heat flux. Octant I events are not as simple to understand as other events. Octant I events suggest there is transport of high momentum and low temperature fluid away from the wall and, hence, from a region of higher temperature. This process is most easily understood by the process of cold fluid entering the near wall region through cold sweeps (octant IV) and reflecting off the wall before diffusion of the cold fluid occurs. The Reynolds shear stress also sees the very near wall region dominated by the hot sweep (octant VIII) mechanism. It is the high momentum components of the streamwise velocity that causes the high temperature fluid to be swept along the wall. For increasing wall normal distance we regain the dominance of octants IV and VI as observed previously. The turbulent wall normal heat flux exhibits similar very near wall behaviour. Like the Reynolds shear stress, there is a large negative contribution from the cold outward interactions (octant I) acting to reduce the turbulent transport of heat. As the wall normal distance increases, octants IV and VI dominate once again.

4.1.8 Turbulent Stress Transport

To get a clear understanding of whether or not the subgrid scale model is capturing the turbulent transport mechanisms, the Reynolds stress is broken down into its contributing terms governing its transport. This technique if often referred to as the Reynolds stress budgets. The transport equation for the Reynolds stress can be written as:

$$\frac{\partial \overline{\rho} u_i' u_j'}{\partial t} = \mathcal{C}_{ij} + \overline{\rho}\tilde{P}_{ij} + \overline{\rho}\tilde{\Pi}_{ij}^{d} + \overline{\rho}\tilde{\Pi}_{ij}^{dl} + M_{ij} - \overline{\rho}\tilde{\varepsilon}_{ij} + \frac{\partial \overline{\rho}\tilde{D}_{ijk}^{t}}{\partial x_k} + \frac{\partial D_{ijk}^{v}}{\partial x_k} \tag{4.24}$$

where the right-hand side is the rate of change of Reynolds shear stress resulting from turbulent convection $\mathcal{C}_{ij}$, turbulent production $\overline{\rho}\,\tilde{P}_{ij}$, the pressure strain $\overline{\rho}\,\tilde{\Pi}_{ij}^{d}$, the pressure dilatation $\overline{\rho}\,\tilde{\Pi}_{ij}^{dl}$, the mass flux variation M_{ij}, the turbulent dissipation rate $\overline{\rho}\,\tilde{\varepsilon}_{ij}$, the turbulent diffusion $\overline{\rho}\,\tilde{D}_{ijk}^{t}$ and the viscous diffusion D_{ijk}^{v} (Maeder et al., 2001). Each of these terms is defined by:

$$\mathcal{C}_{ij} = \frac{\partial}{\partial x_k}(\tilde{u}_k \overline{\rho} u_i' u_j') \tag{4.25}$$

$$\overline{\rho}\,\tilde{P}_{ij} = -\overline{\rho} u_i' u_k' \frac{\partial \tilde{u}_j}{\partial x_k} - \overline{\rho} u_j' u_k' \frac{\partial \tilde{u}_i}{\partial x_k} \tag{4.26}$$

$$\overline{\rho}\,\tilde{\Pi}^d_{ij} = \overline{\rho}\tilde{\Pi}^d_{ij} = \overline{p'\left(\frac{\partial u'_i}{\partial x_j} + \frac{\partial u'_j}{\partial x_i}\right)} - \frac{2}{3}\overline{p'\frac{\partial u'_k}{\partial x_k}}\delta_{ij} \tag{4.27}$$

$$\overline{\rho}\,\tilde{\Pi}^{dl}_{ij} = \frac{2}{3}\overline{p'\frac{\partial u'_k}{\partial x_k}}\delta_{ij} \tag{4.28}$$

$$M_{ij} = \overline{u'_i}\left(\frac{\partial \overline{\sigma}_{jk}}{\partial x_k} - \frac{\partial \overline{p}}{\partial x_j}\right) + \overline{u'_j}\left(\frac{\partial \overline{\sigma}_{ik}}{\partial x_k} - \frac{\partial \overline{p}}{\partial x_i}\right) \tag{4.29}$$

$$\overline{\rho}\,\tilde{D}^t_{ijk} = -\left(\overline{\rho}\widetilde{u'_i u'_j u'_k} + \overline{p'[u'_i\delta_{jk} + u'_j\delta_{ik}]}\right) \tag{4.30}$$

$$\overline{\rho}\,\tilde{\varepsilon}_{ij} = \overline{\sigma'_{ik}\frac{\partial u'_j}{\partial x_k}} + \overline{\sigma'_{jk}\frac{\partial u'_i}{\partial x_k}} \tag{4.31}$$

$$D^v_{ijk} \approx \overline{\mu}\left(\frac{\partial(u'_j u'_k)}{\partial x_i} + \frac{\partial(u'_k u'_i)}{\partial x_j} + \frac{\partial(u'_i u'_j)}{\partial x_k}\right) \tag{4.32}$$

The transport equation for turbulent kinetic energy (ρK, where K is the turbulent kinetic energy) is obtained by taking the trace of Eq (4.24) (Gatski, 1997):

$$\frac{\partial \overline{\rho} K}{\partial t} = \mathcal{C} + \overline{\rho}\tilde{P} + \overline{\rho}\tilde{\Pi}^{dl} + M - \overline{\rho}\tilde{\varepsilon} + \frac{\partial \overline{\rho}\tilde{D}^t}{\partial x_k} + \frac{\partial D^v}{\partial x_k} \tag{4.33}$$

where $\tilde{P} = \tilde{P}_{ii}/2$, $\tilde{\Pi}^{dl} = \tilde{\Pi}^{dl}_{ii}/2$, $M = M_{ii}/2$, $\tilde{\varepsilon} = \tilde{\varepsilon}_{kk}/2$, $\tilde{D}^t = \tilde{D}^t_{iij}/2$ and $D^v = D^v_{iij}/2$.

Figure 4.1-45 shows the budget of the resolved turbulent kinetic energy. The terms described above are normalized by freestream conditions for the purposes of comparison with the DNS of Maeder et al. (2001). The definition of the non-dimensional quantities, conventionally denoted with a *, that is not shown in the above equations for clarity, is given below:

$$\begin{aligned} x^*_k &= \frac{x_k}{\delta} \qquad & \overline{\rho}^* &= \frac{\overline{\rho}}{\rho_\infty} \\ \widetilde{u}^*_k &= \frac{\widetilde{u}_k}{u_\infty} \qquad & P^* &= \frac{P}{\rho_\infty u^2_\infty} \\ \widetilde{\sigma}^*_{ij} &= \frac{\overline{\mu}}{Re_\delta}\left(\frac{\partial \widetilde{u}_i}{\partial x_j} + \frac{\partial \widetilde{u}_j}{\partial x_i} - \frac{2}{3}\delta_{ij}\frac{\partial \widetilde{u}_k}{\partial x_k}\right) \end{aligned} \tag{4.34}$$

The production of turbulent kinetic energy is due to the interaction of the mean streamwise velocity gradient and the Reynolds shear stress, $\rho u'w'$. The turbulent production is reproduced well by LES and exhibits good qualitative and quantitative agreement with the DNS results. The distribution of turbulence production is in keeping with the findings of Klebanoff (1955), that around 75% of total turbulence production within the boundary layer occurs for $z/\delta < 0.2$. The viscous diffusion term

was found to be significantly higher than the DNS values near the wall. In the near wall region, the large mean velocity gradients established gives rise to diffusion in the direction of decreasing velocity. By the same process, as the wall normal distance increases the mean velocity gradients decrease and so too does the contribution of viscous diffusion. For $z/\delta < 0.05$ the viscous diffusion makes a positive contribution with the wall normal velocity fluctuations transporting high turbulent kinetic energy fluid toward the wall. This increased positive viscous diffusion near the wall leads to a corresponding increase in the turbulent dissipation in the near wall region. For $0.05 < z/\delta < 0.1$ the viscous diffusion is responsible for the removal of turbulent kinetic energy, corresponding roughly in magnitude to the energy that it contributes for $z/\delta < 0.05$. Turbulent diffusion exhibits qualitatively similar behaviour to the viscous diffusion term, is well reproduced near the wall, but the minima away from the wall is under-resolved leading to less removal of turbulent kinetic energy in this region.

The turbulent convection, pressure dilatation and mass flux variation were found to be an order of magnitude smaller. These three components were gathered together by Huang et al. (1995) and collectively called the compressibility contributions. As noted by Huang et al. (1995), the compressibility contributions here are small and limited to the near wall region ($z/\delta < 0.2$). The turbulent convection was found to be a small constant value across the boundary layer and the mass flux variation was found to be qualitatively the same as the DNS results, but in the opposite direction. The current results indicate the term to be negative and, therefore, transferring turbulent kinetic energy back to the mean flow.

In the turbulent kinetic energy transport equation, the pressure dilatation term is a representation of the transfer of energy between internal energy and turbulent kinetic energy. Huang et al. (1995) found that the pressure dilatation term was negative in the vicinity of the wall, a feature that is reproduced here with LES. A negative pressure dilatation signifies a transfer of turbulent kinetic energy to internal energy. Following this, a small positive region exists before it relaxes to zero. As seen in the turbulent kinetic budget, the pressure dilatation is negligible compared to most terms. However, a good reproduction is still essential. Figure 4.1-46 shows the pressure dilatation calculated here by LES compared to the DNS of Maeder et al. (2001) and theoretical model of El Baz and Launder (1993). First inspection tells us that the model of El Baz and Launder (1993), formulated for shear flows, does not apply to wall bounded flows with an order of magnitude overprediction. We can also see that there is a fair reproduction of the DNS results by the LES process. The peak value is quite accurate given its small magnitude in the total turbulent kinetic energy budget and the truncation errors associated with the coarser LES grids.

The turbulent kinetic energy budget can be divided into components in the streamwise, spanwise and wall normal direction. The streamwise component, referred to as the streamwise Reynolds normal stress, behaves in an almost identical manner to the turbulent kinetic energy with the exception of the pressure-strain term now appearing. A significant difference also exists, however, in the behaviour of the spanwise and wall normal components other than the pressure-strain. The bulk of the production of turbulent fluctuations occurs from the streamwise component, through the interaction of the mean velocity profile and the Reynolds shear stress. By inspecting the governing transport equation for turbulent Reynolds stress transport, it is the pressure-strain term that is largely responsible for transporting streamwise fluctuations to the other components (Hinze, 1975). The pressure-strain contributions in each direction are plotted in figure 4.1-47. Here we see that the streamwise contribution is negative and represents removal of turbulent fluctuations. Correspondingly, there exists positive contributions mainly to the wall normal direction, but also the spanwise direction representing the production of fluctuations in each direction respectively.

The spanwise and wall normal turbulent kinetic energy budget terms are given in figures 4.1-48 and 4.1-49, without the pressure-strain contributions discussed above. There is no production of spanwise or wall normal Reynolds stress due to interaction with the mean velocity gradient. In the spanwise direction, near the wall, the viscous diffusion term is large and balances the dissipation. The viscous diffusion term becomes a significant transport mechanism near the wall because large values of v' can exist. The turbulent diffusion is almost insignificant. The dissipation of wall normal Reynolds normal stress is much closer to zero and exhibits no significant near wall increase. This behaviour is different to other Reynolds normal stress components and can be understood because the solid wall boundary significantly inhibits any wall normal fluctuations that reach the wall, with any wall normal fluctuations being rapidly transferred to the other two directions. The remaining transport mechanisms in the budget of wall normal Reynolds normal stress are almost negligible. This confirms that the majority of the turbulent kinetic energy lies in the streamwise component.

Figure 4.1-50 shows the budget of resolved turbulent shear stress. The DNS of Maeder et al. (2001) did not report turbulent shear stress budgets and hence provides no means of comparison. The Reynolds shear stress ($\rho u'w'$) is the only non-zero Reynolds stress in fully developed turbulent flow (Bilson, 2004). In other words, the time rate of change of Reynolds shear stress is non-zero as a result of the budget terms not balancing.. The shear stress term is one that is largely responsible for production of the dominant streamwise normal stress ($\rho u'u'$) turbulence through interaction with the mean velocity gradient. The small magnitude of the dissipation sug-

gests that the structures associated with the shear stress occur on the larger scales (Bilson, 2004). The pressure-strain provides the balance for the production of shear stress and thus is primarily responsible for its removal (note that a negative contribution represents production for the Reynolds shear stress). As you move away from the wall, the production remains somewhat balanced by the pressure-strain term when all other contributions are negligible, demonstrating the importance of the pressure-strain term for the shear stress behaviour. The behaviour of the remaining terms, the viscous and turbulent diffusion, while small, is that of a source of Reynolds shear stress near the wall, followed by a small sink region and then diminishing to negligible contribution.

The budgets presented here provide a means for explanation of the self-sustaining nature of turbulence. The mean velocity profile and the Reynolds shear stress provide production of streamwise velocity fluctuations through interaction with each other. From here, the small pressure terms redistribute the turbulent fluctuations to the wall-normal and spanwise directions. The influence of pressure in the redistribution process is understood by the fact that as a fluid element slows or speeds up relative to the mean flow, the pressure will increase or decrease respectively. It is this change in pressure when compared to neighbouring fluid elements that generates acceleration into the other two directions. The wall-normal and streamwise fluctuations then combine to generate Reynolds shear stress and the cycle continues.

4.1.9 Strong Reynolds Analogy

A widely used hypothesis and, hence, key check on the behaviour of supersonic turbulent boundary layers and assessment of the subgrid scale model is to examine the validity of the strong Reynolds analogy (SRA) (Maeder, 2000). This concept was introduced by Morkovin (1962) who suggested that the Reynolds analogy observed for incompressible flow might apply to compressible turbulence by assuming similarities between heat and momentum transfer. We can derive the SRA from the linearized equation relating velocity, temperature and stagnation temperature:

$$\frac{T_0'}{\tilde{T}} = \frac{T'}{\tilde{T}} + (\gamma - 1) M_\infty^2 \frac{\tilde{u} u'}{\tilde{T}} \tag{4.35}$$

If the assumption is made that there exists negligible total temperature fluctuations, while also introducing the local Mach number ($\tilde{M}$) we obtain:

$$\frac{T'}{\tilde{T}} = -(\gamma - 1)\tilde{M}^2 \frac{u'}{\tilde{u}} \tag{4.36}$$

Building on this relation for T' and u', several statistical consequences are given by Guarini et al. (2000):

$$\frac{\text{RMS}(T')/\tilde{T}}{(\gamma - 1)\tilde{M}^2\,\text{RMS}(u')/\tilde{u}} = 1 \tag{4.37}$$

$$Pr_t = \frac{\overline{\rho u' w'}}{\overline{\rho w' T'}} \frac{\partial \tilde{T}/\partial z}{\partial \tilde{u}} \approx 1 \tag{4.38}$$

However, for compressible flows such as the ones of interest, the total temperature fluctuations ($\frac{T_0'}{\tilde{T}}$) are non-zero and can often be of the same order as the static temperature fluctuations (figure 4.1-51). The validity of the assumption of negligible total temperature fluctuations can be examined by taking the cross-correlation of velocity and temperature fluctuations.

$$R_{u'T'} = \frac{\overline{u'\,T'}}{\sqrt{\overline{u'^2}}\sqrt{\overline{T'^2}}} \tag{4.39}$$

If the assumption of negligible total temperature fluctuations were true, the cross-correlation factor ($R_{u'T'}$) should hold a uniform value of -1 throughout the boundary layer. Experimental evidence supports Eq (4.36) in the non-intermittent zone from $0.05 \leq z/\delta \leq 0.7$ and the velocity temperature correlation (Eq (4.39)) to a slightly lesser extent. Figure 4.1-52 shows that for the LES calculations, the correlation is satisfied throughout the boundary layer and is also in fair agreement with experimental results. This result is somewhat surprising given the fact that the total temperature fluctuations are non-zero and significant. The behaviour of the correlation from DNS data of Maeder (2000) and Guarini et al. (2000) does not follow that of experimental data or numerical results from other sources, including this work or the general relationship that $R_{u'T'} < -0.75$ (Smits and Dussauge, 2006). Instead, it behaves more like subsonic flow, with the correlation approaching zero as the boundary layer edge is approached. This disagreement was deemed to be of great interest by Guarini et al. (2000). It was suggested by Gaviglio (1987) that acoustic phenomena in the experimental flow were somehow different in the numerical simulations. However, Guarini et al. (2000) discounted this reason, instead suggesting that there is something wrong with either the experiments or simulations (or both).

The presence of a large negative correlation extending to regions near the wall is supported by the experimental data. Antonia et al. (1988) observed that near the wall low speed streaks corresponded with high temperature streaks and high speed streaks with low temperature streaks. This correlation is reinforced by the contours of instantaneous streamwise velocity and temperature fluctuations for a plane just off the wall given in figure 4.1-56. Here it can be seen that low speed streaks (negative velocity fluctuation) occur in largely the same regions as high temperature streaks (positive temperature fluctuation) and vice versa.

The turbulent Prandtl number (Eq (4.38)) is a useful quantity that can be interpreted as the ratio of the turbulent transport of heat to the turbulent transport of momentum. Consequently, a turbulent Prandtl number approximately of unity can be taken as another illustration of the strong Reynolds analogy. Typically, however, a turbulent Prandtl number of 0.9 is used in practice. This modification can be thought of as taking into account the fact that inbuilt is the assumption that all transport taking place is of the gradient form, even when in reality not all transport should be represented by this form. In figure 4.1-53, the calculated turbulent Prandtl number is compared to the DNS computations of Maeder (2000) and Guarini et al. (2000) and LES of Stolz and Adams (2003). For $z/\delta < 0.6$, both the current LES and DNS of Maeder (2000) agree with Eq (4.38) while the LES calculations of Stolz and Adams (2003) report values of 0.7, except near the wall. Outside of this region, the current LES calculations report turbulent Prandtl numbers up to 1.2. This result is due mainly to the sensitivity of turbulent Prandtl number to small variations in velocity and temperature gradients when they take on small values. However, the trend of an increasing turbulent Prandtl number has also been computed in the DNS calculations of Guarini et al. (2000).

Given the fact that it has been observed that the turbulent Prandtl number is approximately unity and that the velocity and temperature fluctuations are anti-correlated, the question still exists as to how Eqs (4.36) and (4.39) can be satisfied for both numerical and experimental results, while there exists non-zero total temperature fluctuations (a key assumption in their formulation). Gaviglio (1987) found that negligible total temperature fluctuations is sufficient, but not necessary for Eq (4.37) to be valid (Maeder (2000)). Plotting the relationship given by Eq (4.37) in figure 4.1-54 reinforces the validity of the observation of Gaviglio (1987) throughout the boundary layer. This result is further backed up by the observation of Dussauge et al. (1996), that the SRA is closely followed in supersonic boundary layers. The results compare well with the DNS of Maeder et al. (2001) in the near wall and non-intermittent zone. The predicted drop off in SRA in the outer regions of the boundary layer is not consistent with the observations of constant SRA by Smits and Dussauge (1996). The experimental data presented in the work of Gaviglio (1987), reported

to be from Debieve (1983), at a Mach number of 2.32, also agrees well with the LES calculations. Guarini et al. (2000) explains that Eq (4.37) is successful under non-zero total temperature fluctuations if:

$$\frac{\overline{T'^2}}{\tilde{T}^2} \gg \frac{\overline{T_0'^2} - 2\overline{T_0' T'}}{\tilde{T}^2} \tag{4.40}$$

With the exception of near the wall, this condition is confirmed by the simulation results over the region where the SRA applies (figure 4.1-55). While it can be seen that both terms are of the same order, the left-hand side of Eq (4.40) is at least a factor of 4 or greater than the terms on the right. From this we can conclude, as Guarini et al. (2000) did, that the success of the SRA is due to the relationship between static and total temperature fluctuations rather than negligible total temperature fluctuations.

Gaviglio (1987) also showed that the fluctuations of total and static temperature can be directly related to the correlation coefficient under the assumption of validity of Eq (4.37). The correlation coefficient then becomes:

$$R_{u'T'} = \frac{\overline{T_0'^2}}{2\overline{T'^2}} - 1 \tag{4.41}$$

In the case of negligible total temperature fluctuations, the above equation would reduce to $R_{u'T'} = -1$. The values computed by Eq (4.41) agree with the cross correlation results of Eq (4.39) (figure 4.1-52), which suggests that the results are physically plausible and again demonstrates that it is the relationship between static and total temperature fluctuations, rather than negligible total temperature fluctuations, that govern the applicability of the SRA.

For flows where the wall conditions are far from adiabatic and significant heat transfer is occurring, the agreement between Eq (4.37) and experimental data no longer holds. Gaviglio (1987) and Huang et al. (1995) modified the Reynolds analogy to the form:

$$\frac{\text{RMS}(T')/\tilde{T}}{(\gamma-1)\tilde{M}^2\,\text{RMS}(u')/\tilde{u}} \times c\left(1 - \frac{\partial \tilde{T}_0}{\partial \tilde{T}}\right) = 1 \tag{4.42}$$

where $c = 1.0$ and $c = Pr_t$ for each author respectively. Guarini et al. (2000) applied the modified strong Reynolds analogy to near adiabatic wall temperature flow using $c = Pr_t$. The modified strong Reynolds analogy is also plotted in figure 4.1-54 with the DNS results of Guarini et al. (2000) showing an upward trend near the boundary layer edge. Correspondingly, even though the wall conditions are nearly adiabatic for the conditions studied here, the modified SRA is also applied to the current LES data. The application of this modified relationship shows the same increasing behaviour at the boundary layer edge, suggesting the usefulness of this modified relationship in later applications to non-adiabatic walls.

4.1.10 Boundary Layer Structure

An integral part of understanding turbulence is the study of the interaction of the eddies and coherent structures found within a supersonic boundary layer. The previous sections have dealt with the turbulent flow structures from an averaged perspective. By examining instantaneous flow fields it is possible to visualise the turbulent flow structures. Horseshoe vortices have been suggested to play a very important role in boundary layer structure, while accounting for a significant proportion of Reynolds stress generation through ejection and interaction with the mean velocity gradients. At the low Reynolds numbers studied here, the hairpin vortices exhibited a rapid overturning motion, identified through flow animations, that is in keeping with the observations of Head and Bandyopdhyay (1981). Figure 4.1-57 shows contours of density gradient for a slice through the centre of the domain for three instantaneous time samples. It can be seen that the hairpin vortex structures align themselves with the 15^o and 30^o reference lines (Eq 2.1.3), that Smits and Dussauge (2006) suggested would encompass the majority of turbulent structures. The computed structure angles compare well with the 30^o angle of Alving and Smits (1990), which were determined to be independent of wire separation.

The production of turbulent structures is suggested to begin with the formation of streamwise vortices known as streaks. The growth of these streaks occurs until there is a sufficient adverse pressure gradient generated, culminating in the roll up of the vortex into a horseshoe arrangement. A further adverse pressure gradient is generated by the head of the horseshoe vortex, which causes an uplift of the vortex further away from the wall. Identifying these physical processes serves as a further check that the applied numerical schemes are correctly capturing the flow properties. Figure 4.1-58 gives an iso-surface of vorticity magnitude (3×10^5). The presence of both spanwise vortices (streaks) and a horshoe vortex is in evidence here.

The behaviour of the near wall streaks has recently received more experimental attention and is readily examined numerically. Figure 4.1-59 shows a contour plot of instantaneous velocity fluctuations near the wall. From the streamwise velocity fluctuations it is clear to see evidence of strips of velocity fluctuations grouped together over large downstream distances. Like the observations of Ganapathisubramani et al. (2006) in a Mach 2 boundary layer, the characteristic widths appear to be approximately $0.2\delta - 0.4\delta$. The spanwise velocity fluctuation contours reveal a field that is far less coherent. These two observations appear to be consistent with the 'hairpin packet' model. Between the legs of the hairpin vortices we would expect to see elongated coherent streamwise velocity fluctuations and more compact spanwise velocity fluctuations representing the flow drawn towards the legs of the vortices.

4.2 Summary

Large-eddy simulations of supersonic turbulent boundary layer flow have been carried out. These simulations were undertaken to validate the numerical schemes used via direct comparison to both DNS and mean flow experimental data for the same conditions and experimental data scaled appropriately from other conditions. This exercise was successful, with the results showing good agreement with DNS and experimental data points. The approximate deconvolution model was found to be superior to both the Smagorinsky and mixed scale eddy-viscosity/eddy-diffusivity subgrid-scale models. When plotted in the classical inner and outer layer coordinates, both eddy-viscosity/ eddy-diffusivity models were not able to fully capture the expected van-Driest transformed mean velocity profile. Additionally, higher than expected turbulent fluctuations and more rapid turbulent energy drop-offs were also calculated using these models. The Approximate deconvolution model, on the other hand, returned mean profiles and turbulent velocity and temperature fluctuations that were in good agreement with both DNS and experimental results and, hence, was used for the remaining significant conclusions.

The energy spectra was captured well when compared to the DNS data but still suffered increased damping from the coarser grids and lower order numerical schemes at high frequencies. Turbulent Mach number and, hence, compressibility effects were also best represented by the approximate deconvolution model. The Reynolds stresses computed were assessed with respect to the same DNS and experimental data and found to agree well. For the purpose of comparison, the Reynolds stresses was normalized by wall shear stress and length scale was normalized by either boundary layer thickness, velocity defect thickness or using inner layer scaling. The comparisons, however,

were limited to the outer layer region of the boundary layer by the inability of the experiments to make measurements within the inner regions of boundary layers. All trends for increasing grid resolution and wall normal domain size were towards the data used for comparison, unless the quantity was already well resolved and showing grid independence. For all comparisons to experimental data for larger Reynolds numbers, the integral velocity defect thickness was the most appropriate length scale for removing Reynolds number effects.

The auto-correlations of velocity, while not only demonstrating sufficient domain size, indicated the presence of elongated structures, known as streaks, near the wall. The streak width was found to be close to, but greater than mean spacing reported by Smits and Dussauge (2006). Furthermore, the autocorrelations enabled assessment of turbulent structure length scales found within the boundary layer, which were consistent with experimentally determined scales.

The turbulent Prandtl number and strong Reynolds analogy reported by the LES simulations were found to have reasonable agreement with theoretical, experimental and numerical values. The strong Reynolds analogy, that assumes negligible total temperature fluctuations was found to hold despite the existence of significant total temperature fluctuations. The existence of a negative correlation approaching the very near wall region, between streamwise velocity and temperature fluctuations, was found both via a time averaged mean correlation and instantaneous flow fields. Computed values of turbulent stress transport for turbulent kinetic energy were found to be in good qualitative and quantitative agreement with DNS results. Quadrant and octant analysis on Reynolds shear stress and turbulent heat flux, while having no DNS data to make quantitative comparisons to, was found to agree qualitatively with observations made for incompressible flow, while also permitting analysis of dominant mechanisms. The similarity in dominant mechanisms for both Reynolds shear stress and turbulent heat flux further demonstrated agreement with the strong Reynolds analogy between heat and mass transfer. The fact that the turbulent transport mechanisms are correctly represented gives further confidence in the applied numerical procedure. This investigation of transport mechanisms now provides the basis for the assessment of boundary layer heat addition effects in chapter 5.

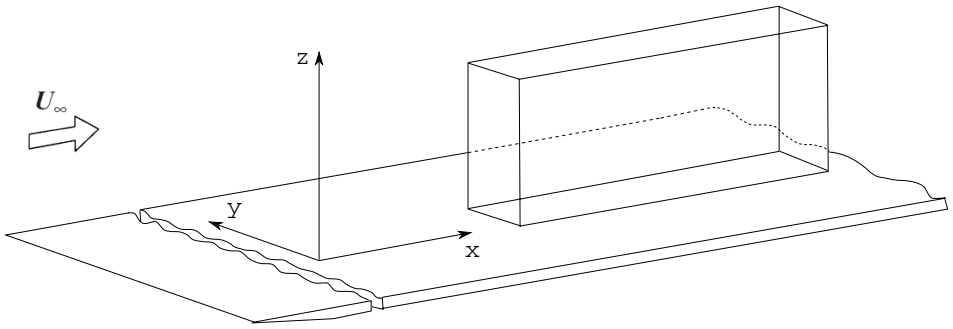

Figure 4.1-1: Computational domain far downstream of leading edge

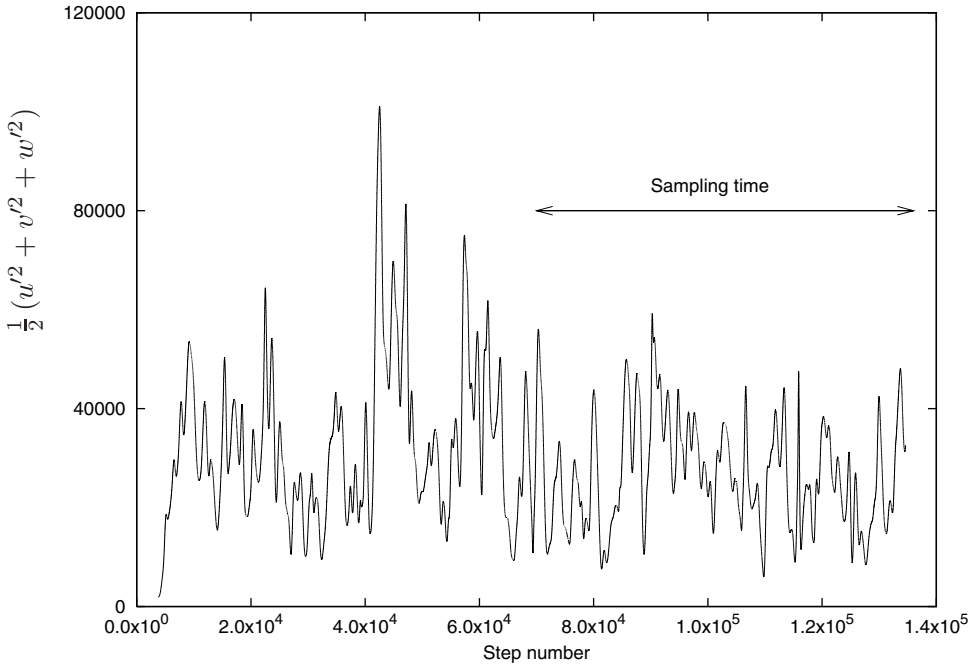

Figure 4.1-2: Development of turbulent kinetic energy with simulation time. Statistical sampling period as shown.

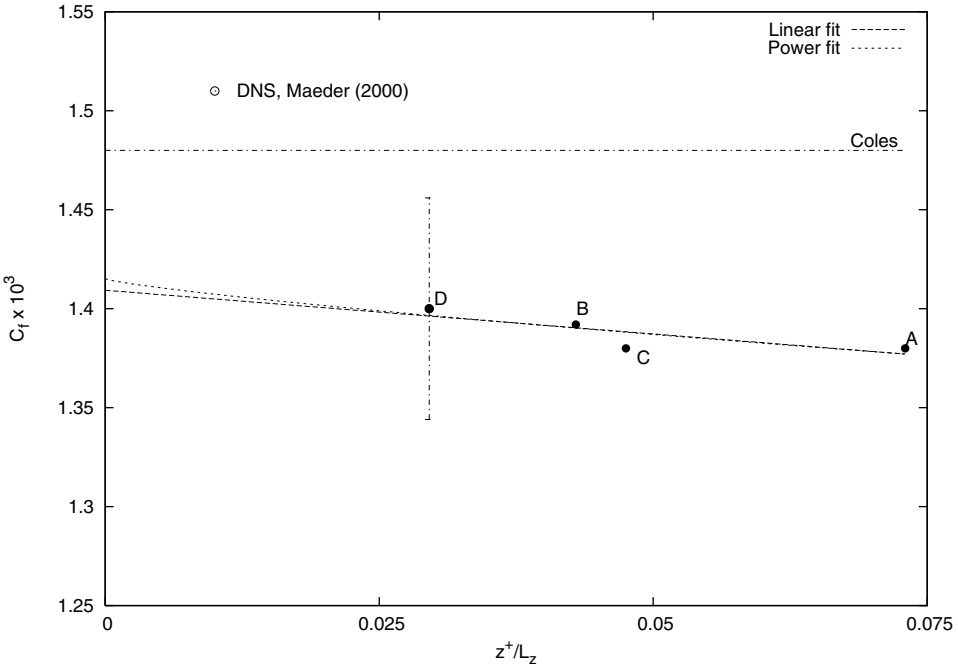

Figure 4.1-3: Convergence of skin friction coefficient with grid refinement as computed with ADM. Error bar indicates grid convergence index error estimator for grid D.

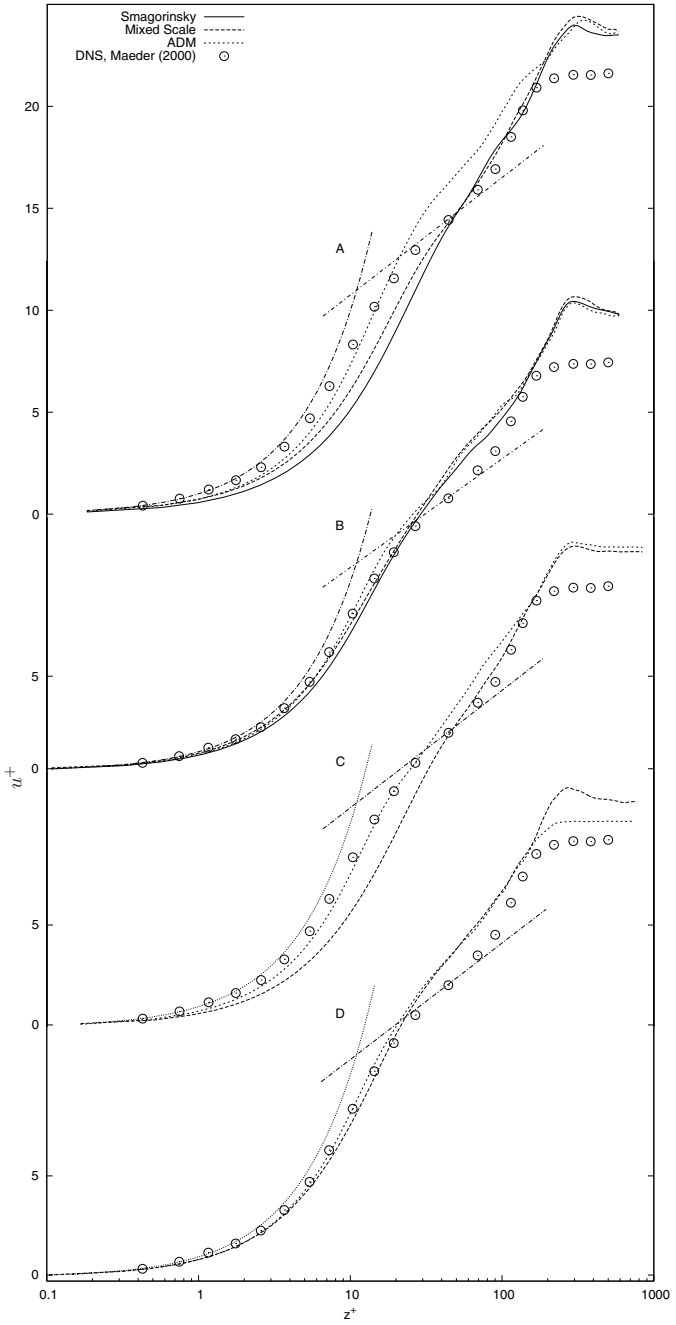

Figure 4.1-4: Effect of grid resolution and domain height on the transformed mean streamwise velocity field. Linear assumption of the viscous sublayer (equation 4.16) and law of the wall (equation 4.17) shown for comparison.

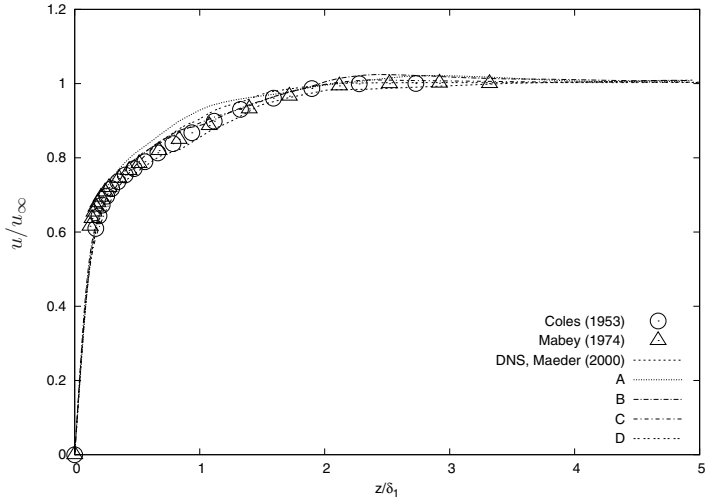

(a) Approximate deconvolution model

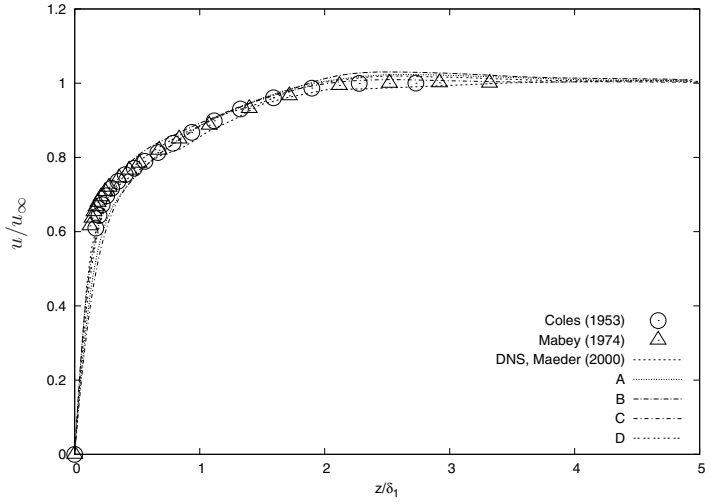

(b) Mixed scale model

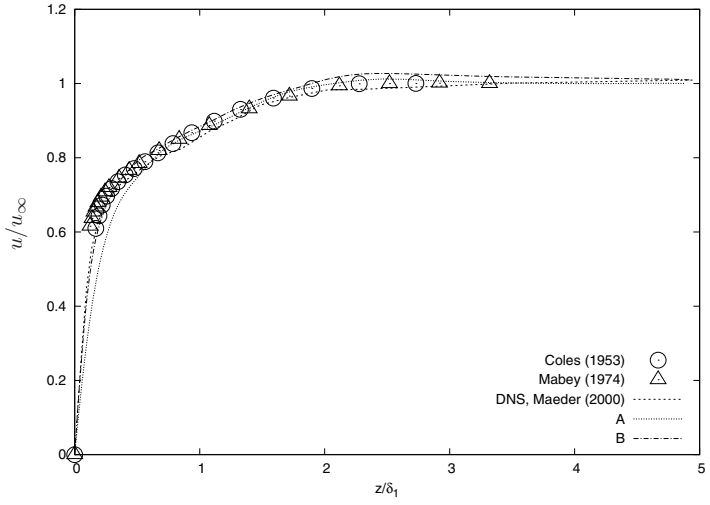

(c) Smagorinsky model

Figure 4.1-5: Mean streamwise velocity flow profiles. Displacement thickness used to emphasize the outer boundary layer region.

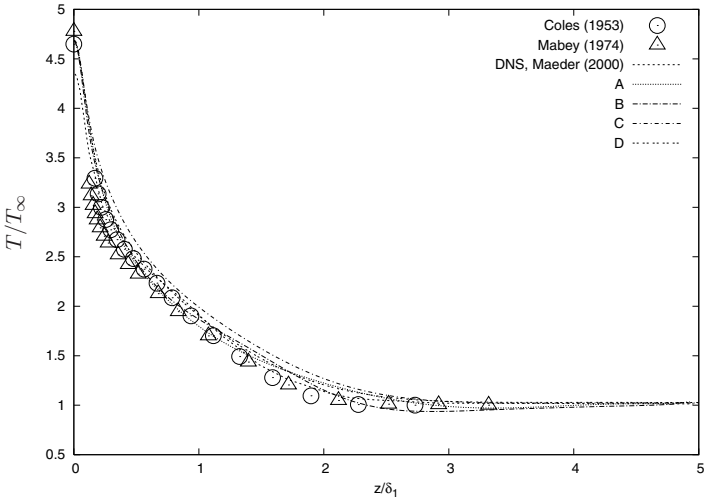

(a) Approximate deconvolution model

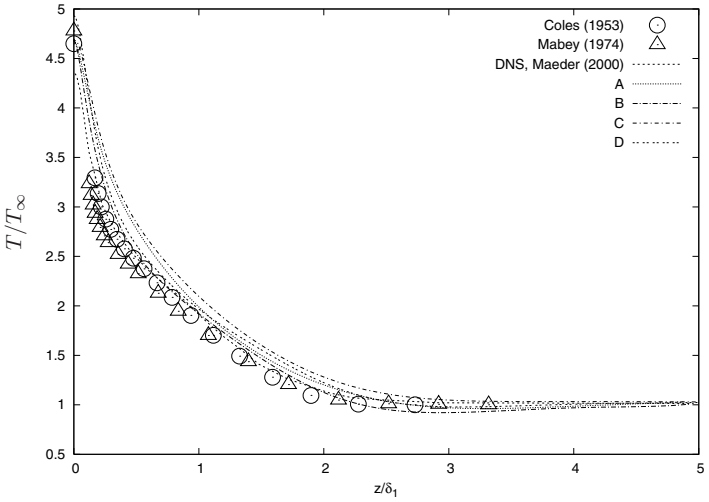

(b) Mixed scale model

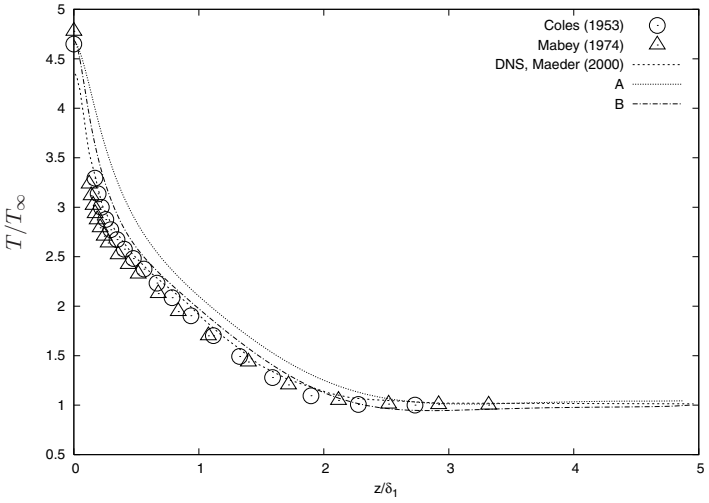

(c) Smagorinsky model

Figure 4.1-6: Mean static temperature flow profiles. Displacement thickness used to emphasize the outer boundary layer region.

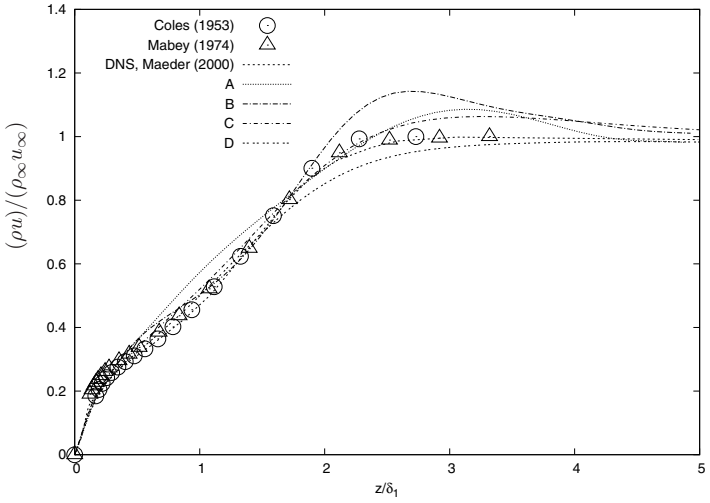

(a) Approximate deconvolution model

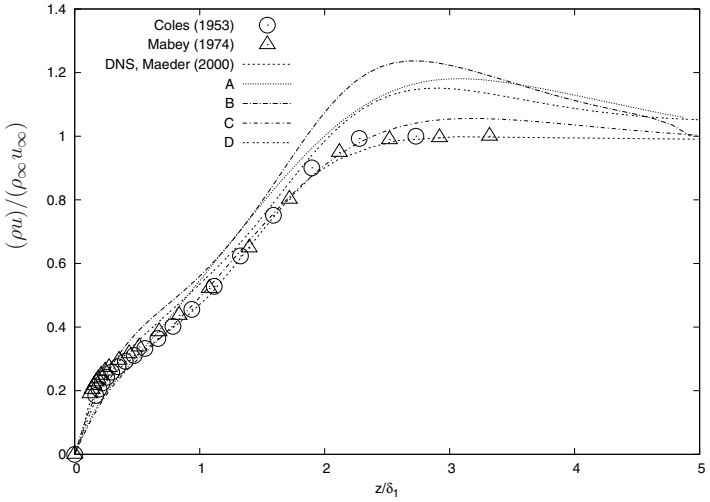

(b) Mixed scale model

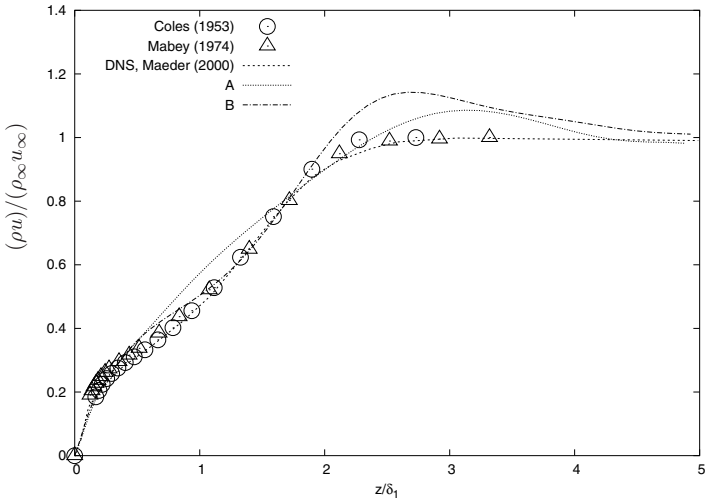

(c) Smagorinsky model

Figure 4.1-7: Mean streamwise momentum profiles. Displacement thickness used to emphasize the outer boundary layer region.

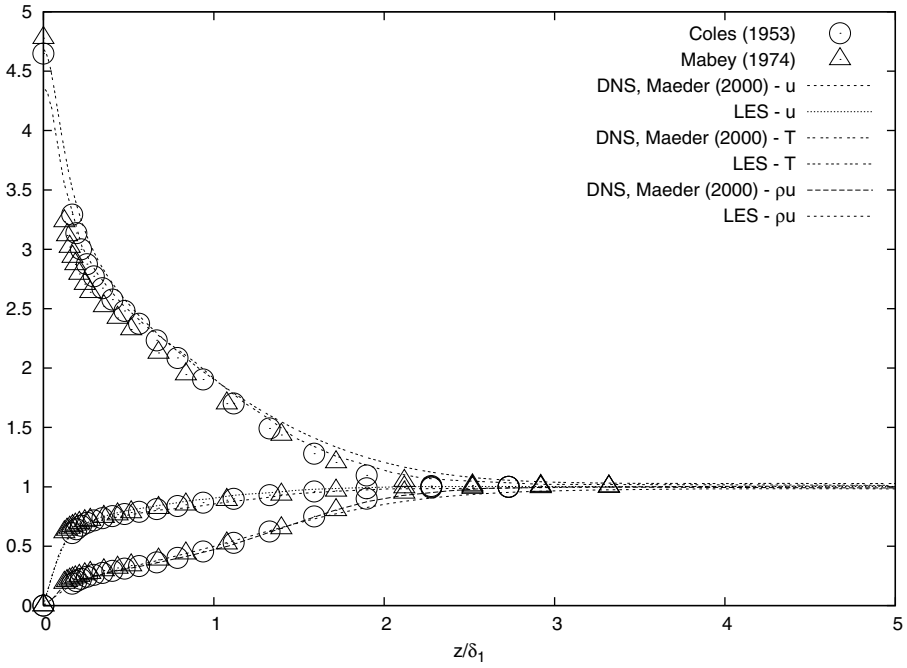

Figure 4.1-8: Approximate deconvolution model mean flow profiles - grid D. Displacement thickness used to emphasize the outer boundary layer region.

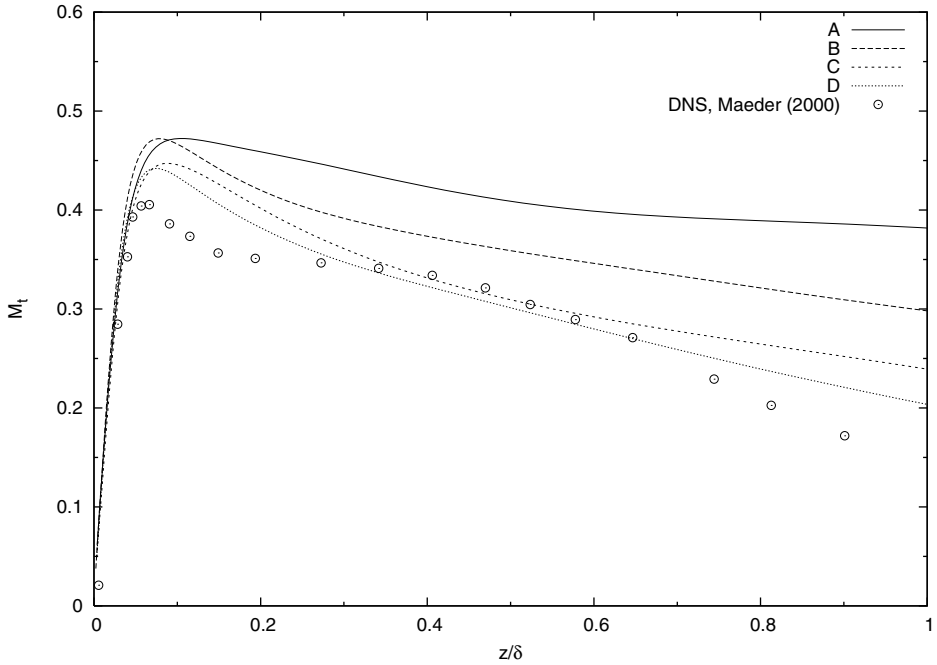

Figure 4.1-9: $Re_\theta = 4000$ - Turbulent Mach number from the Approximate deconvolution Model showing effect of increasing grid resolution and wall normal domain height.

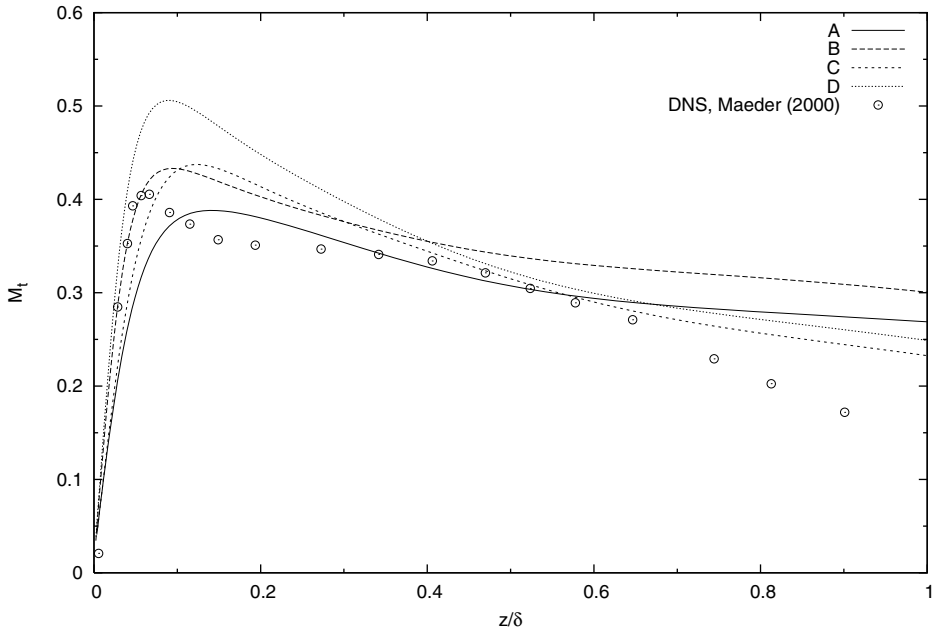

Figure 4.1-10: $Re_\theta = 4000$ - Turbulent Mach number from the Mixed Scale Model showing effect of increasing grid resolution and wall normal domain height.

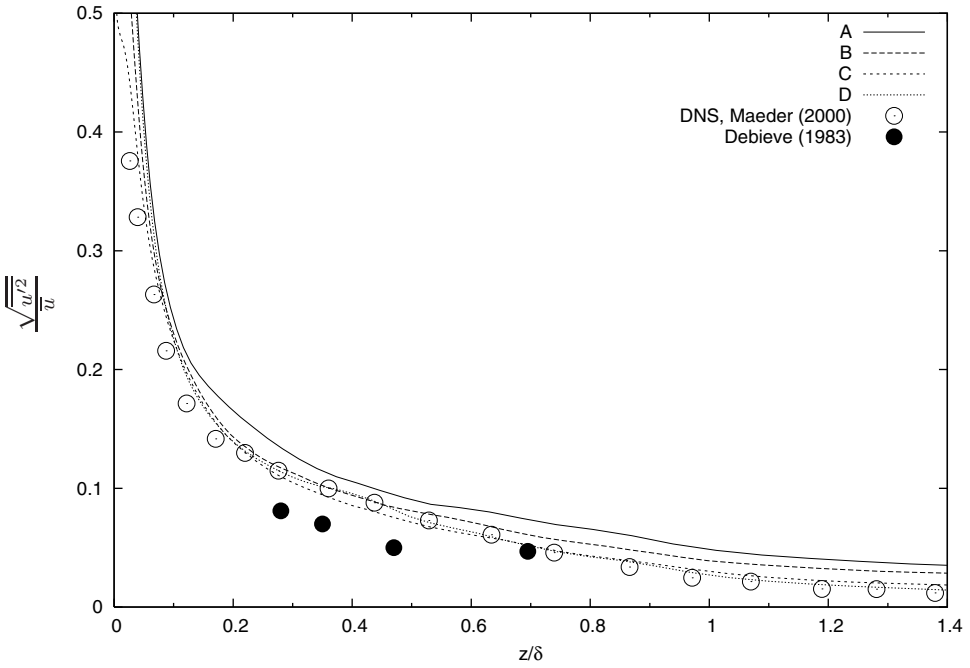

Figure 4.1-11: $Re_\theta = 4000$ - Effect of increasing grid resolution and wall normal domain height on RMS of streamwise velocity fluctuations from the approximate deconvolution model normalized by mean velocity profile.

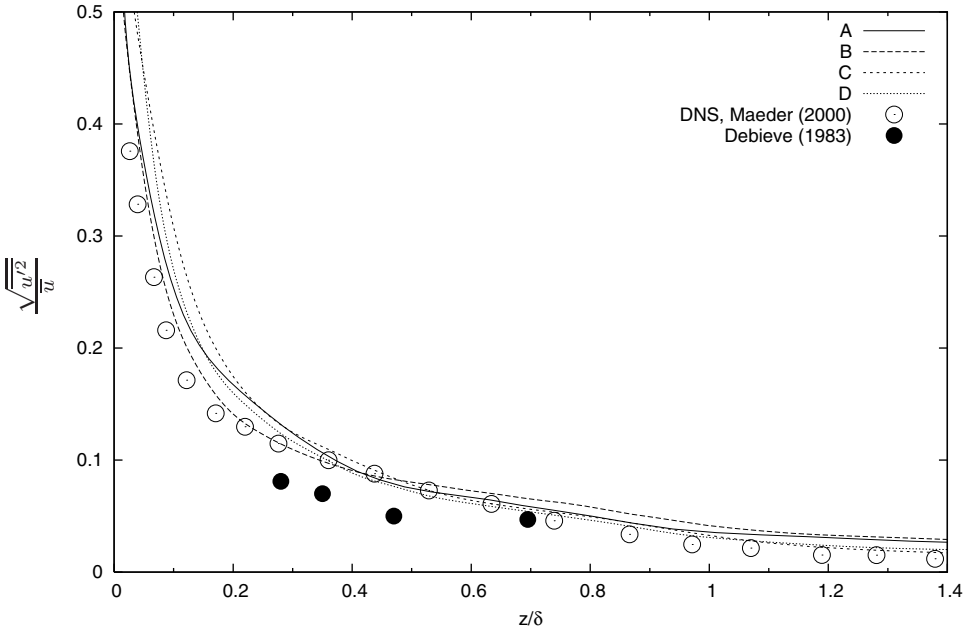

Figure 4.1-12: $Re_\theta = 4000$ - Effect of increasing grid resolution and wall normal domain height on RMS of streamwise velocity fluctuations from the mixed scale model normalized by mean velocity profile.

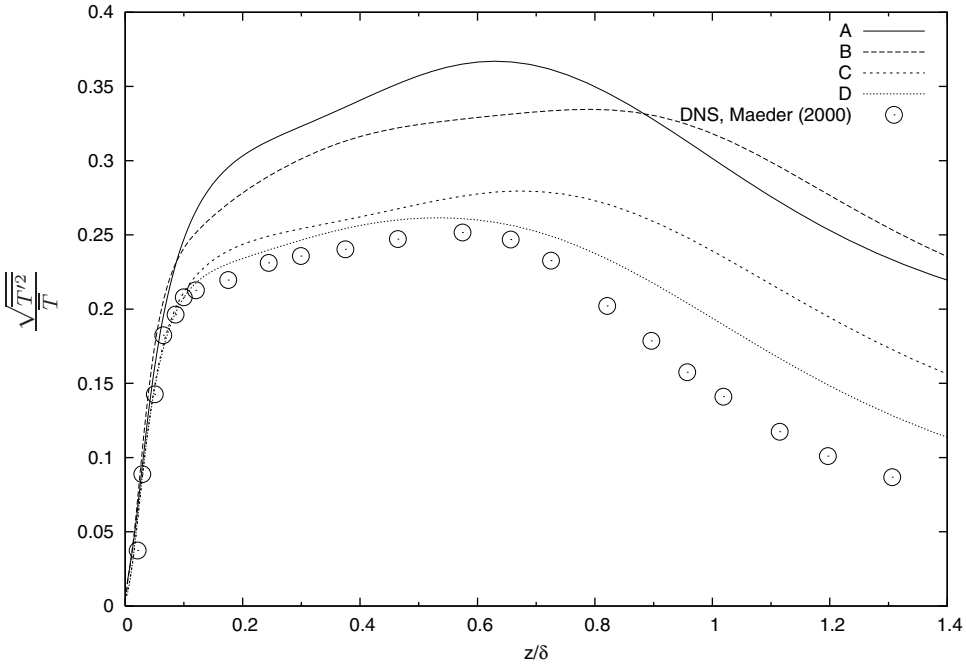

Figure 4.1-13: $Re_\theta = 4000$ - Effect of increasing grid resolution and wall normal domain height on RMS of resolved static temperature fluctuations from the approximate deconvolution model normalized by mean temperature profile.

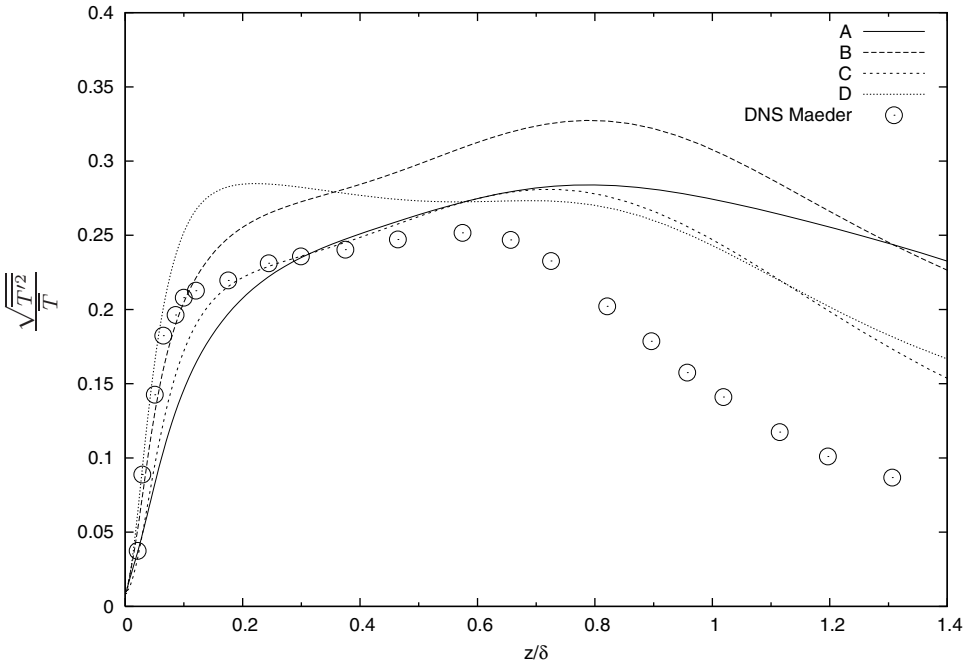

Figure 4.1-14: $Re_\theta = 4000$ - Effect of increasing grid resolution and wall normal domain height on RMS of resolved static temperature fluctuations from the mixed scale model normalized by mean temperature profile.

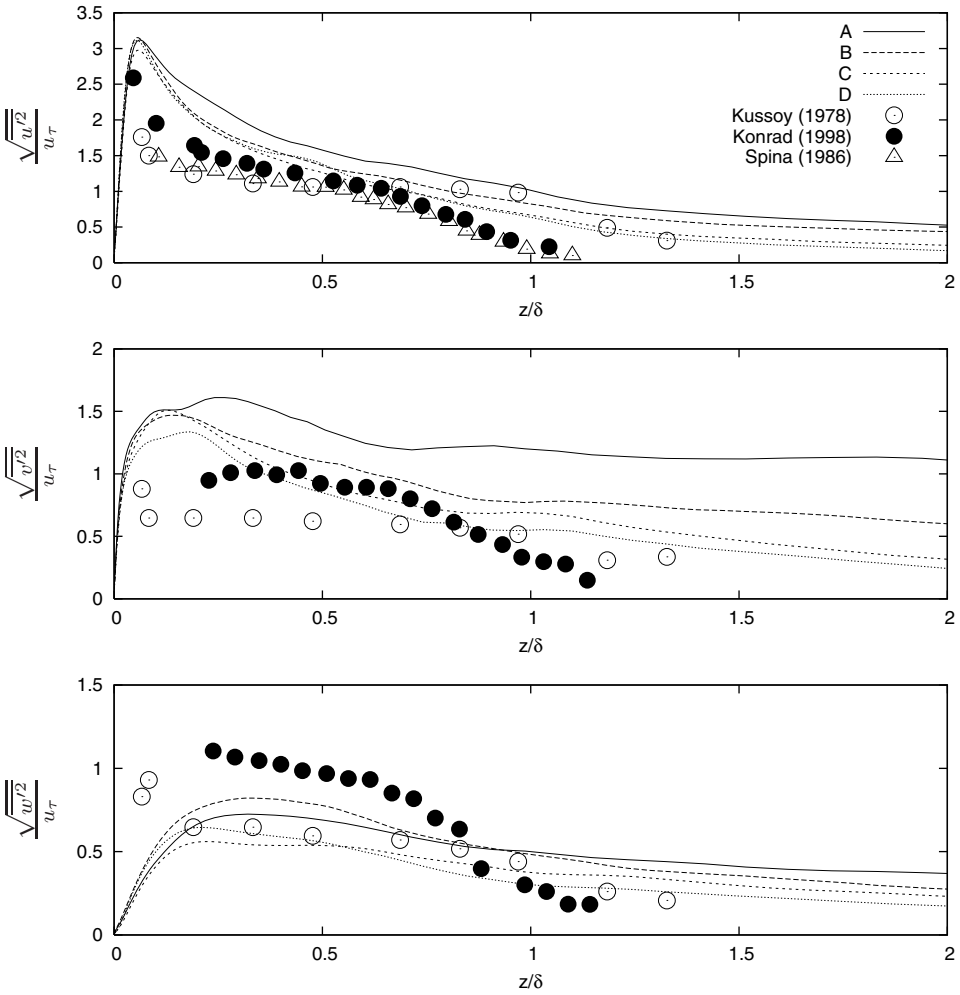

Figure 4.1-15: $Re_\theta = 4000$ - RMS of velocity fluctuations from the approximate deconvolution model normalized by friction velocity. Length scale normalized by boundary layer thickness.

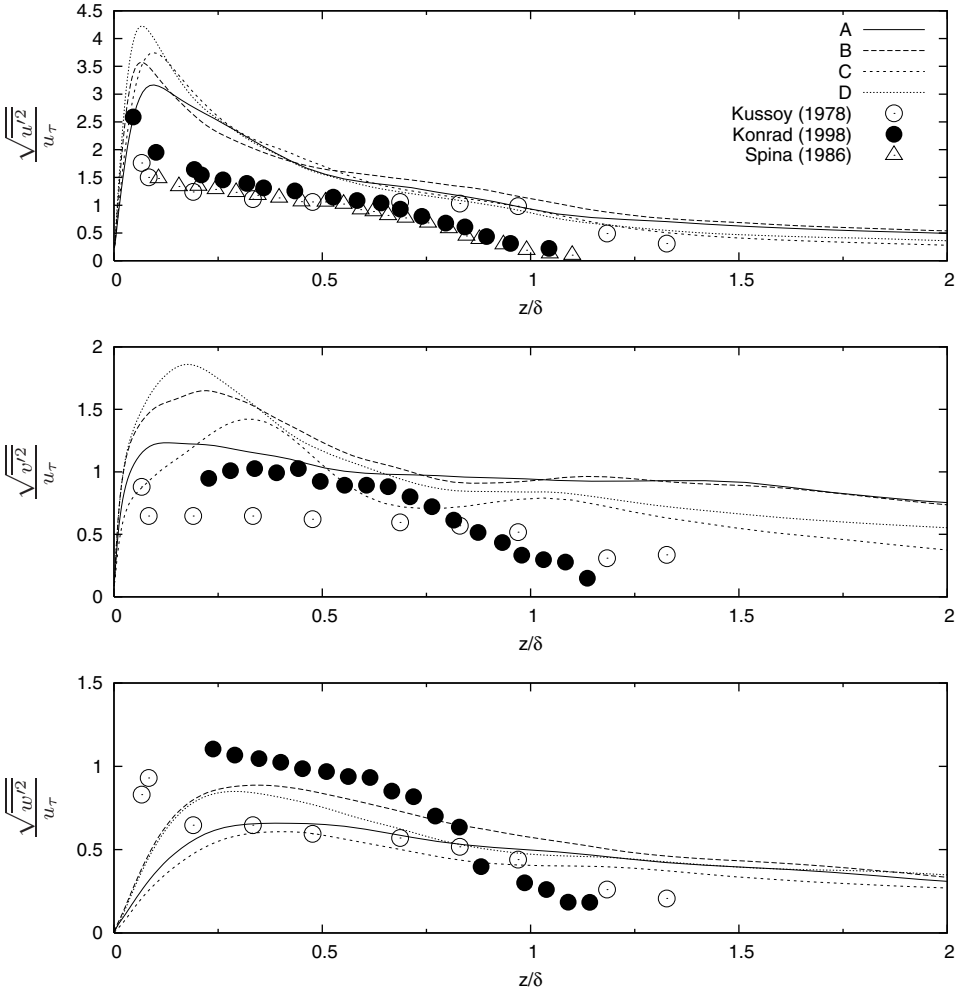

Figure 4.1-16: $Re_\theta = 4000$ - RMS of velocity fluctuations from the mixed scale model normalized by friction velocity. Length scale normalized by boundary layer thickness.

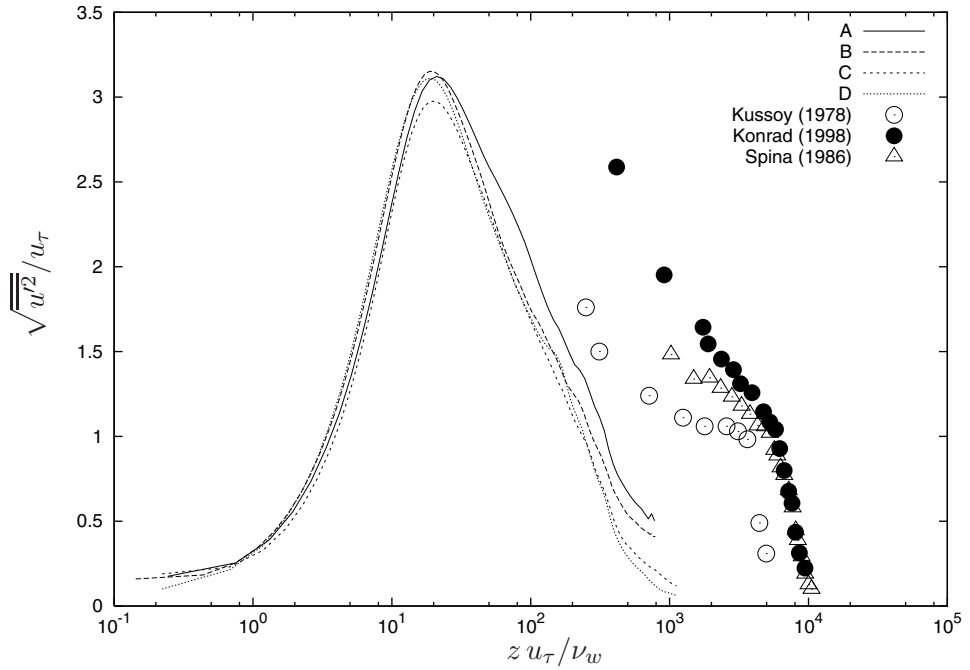

Figure 4.1-17: $Re_\theta = 4000$ - RMS of streamwise velocity fluctuations from the approximate deconvolution model normalized by friction velocity. Inner scaling used for length scale.

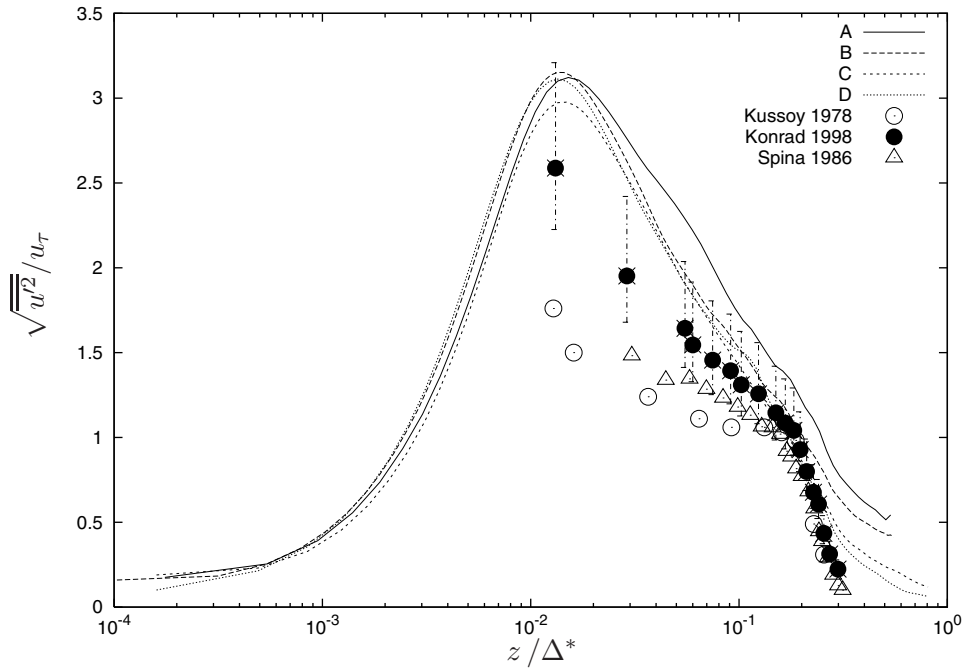

Figure 4.1-18: $Re_\theta = 4000$ - RMS of streamwise velocity fluctuations from the approximate deconvolution model normalized by friction velocity. Velocity defect integral thickness used for length scale.

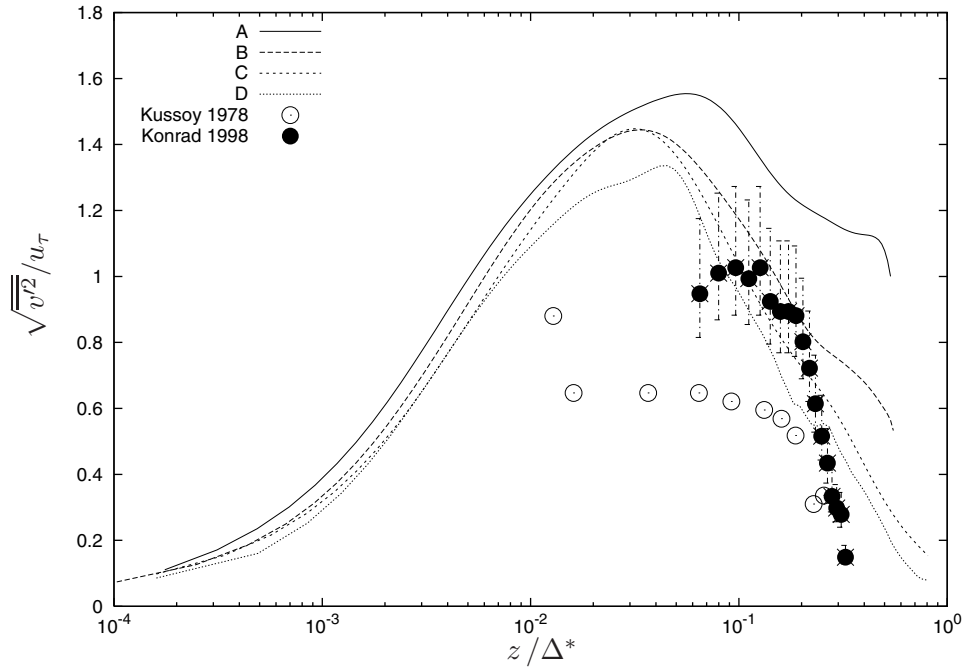

Figure 4.1-19: $Re_\theta = 4000$ - RMS of resolved spanwise velocity fluctuations from the approximate deconvolution model normalized by friction velocity. Velocity defect integral thickness used for length scale.

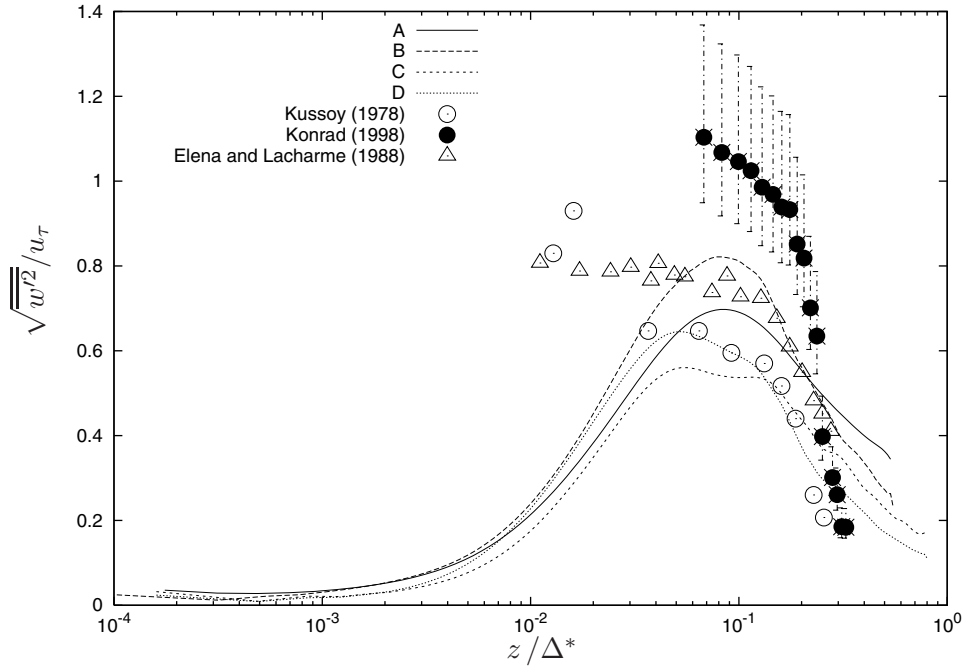

Figure 4.1-20: $Re_\theta = 4000$ - RMS of resolved wall normal velocity fluctuations from the approximate deconvolution model normalized by friction velocity. Velocity defect integral thickness used for length scale.

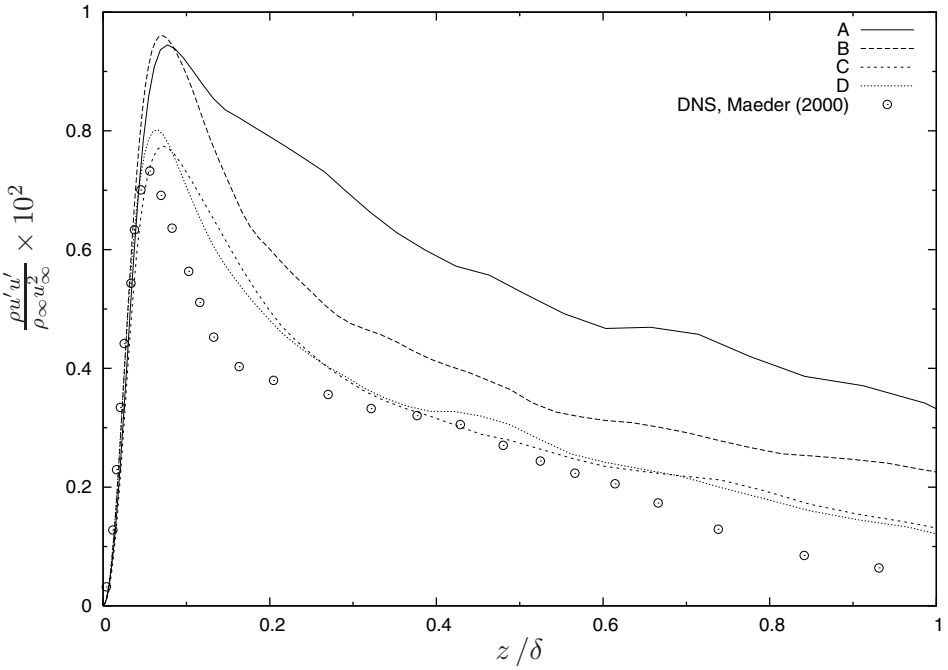

Figure 4.1-21: $Re_\theta = 4000$ - Reynolds normal stress from the approximate deconvolution model normalized by freestream conditions compared to DNS results of Maeder (2000).

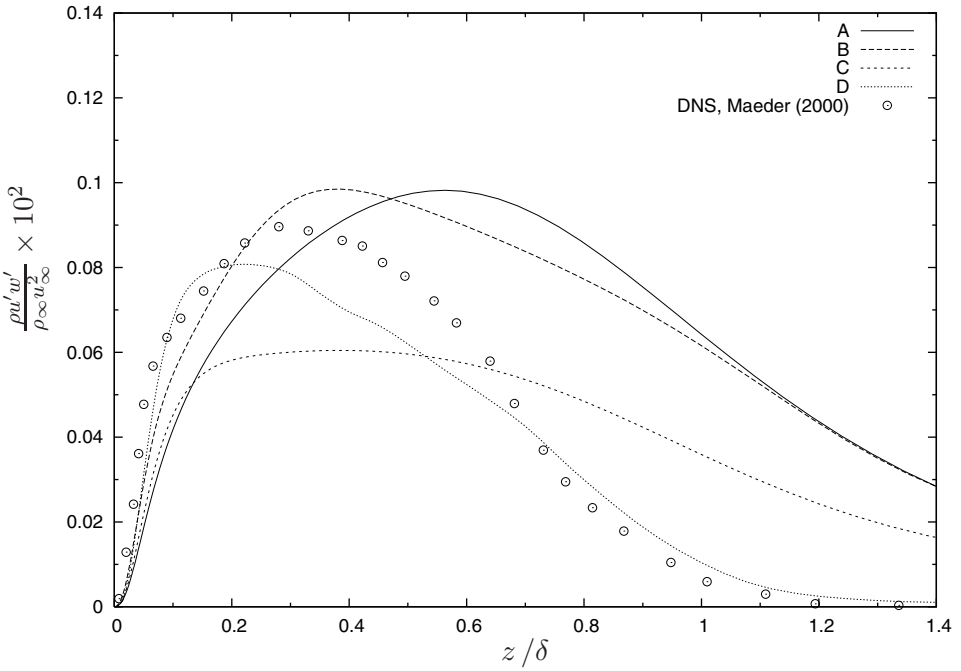

Figure 4.1-22: $Re_\theta = 4000$ - Reynolds shear stress from the approximate deconvolution model normalized by freestream conditions compared to DNS results of Maeder (2000).

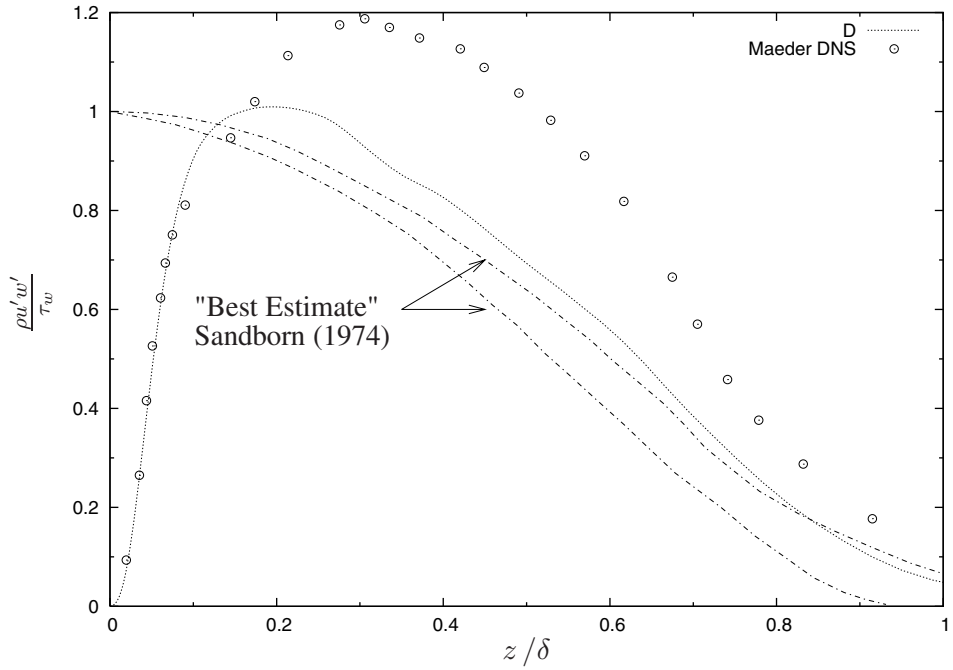

Figure 4.1-23: $Re_\theta = 4000$ - Comparison of Estimated Reynolds shear stress (Sandborn, 1974) with computations from the approximate deconvolution model and the DNS of Maeder (2000) normalized by wall shear stress.

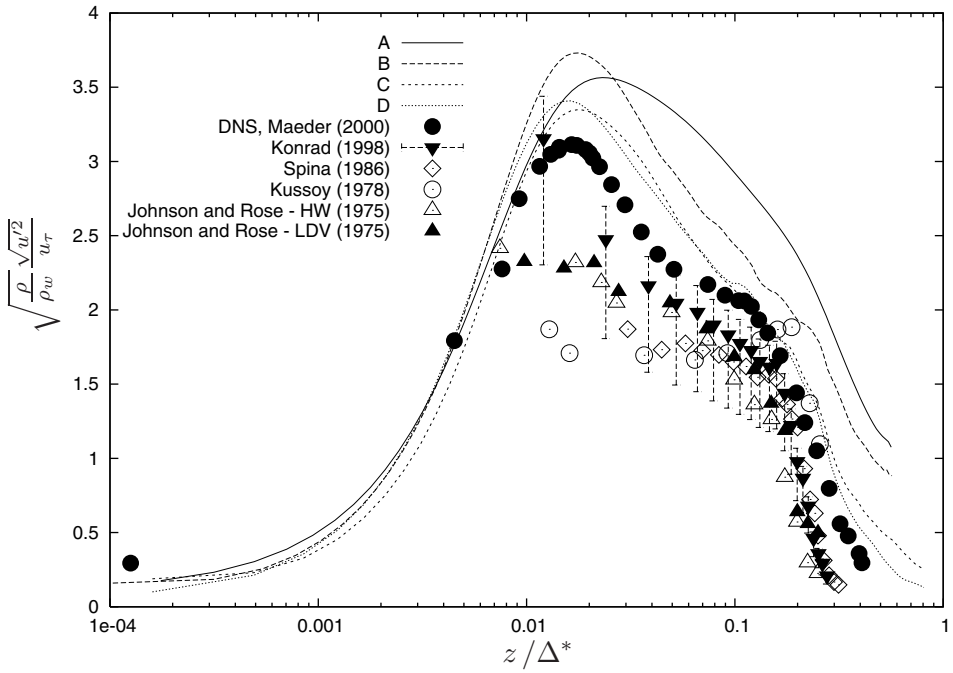

Figure 4.1-24: $Re_\theta = 4000$ - Streamwise Reynolds normal stress from the approximate deconvolution model normalized by wall conditions and velocity defect thickness.

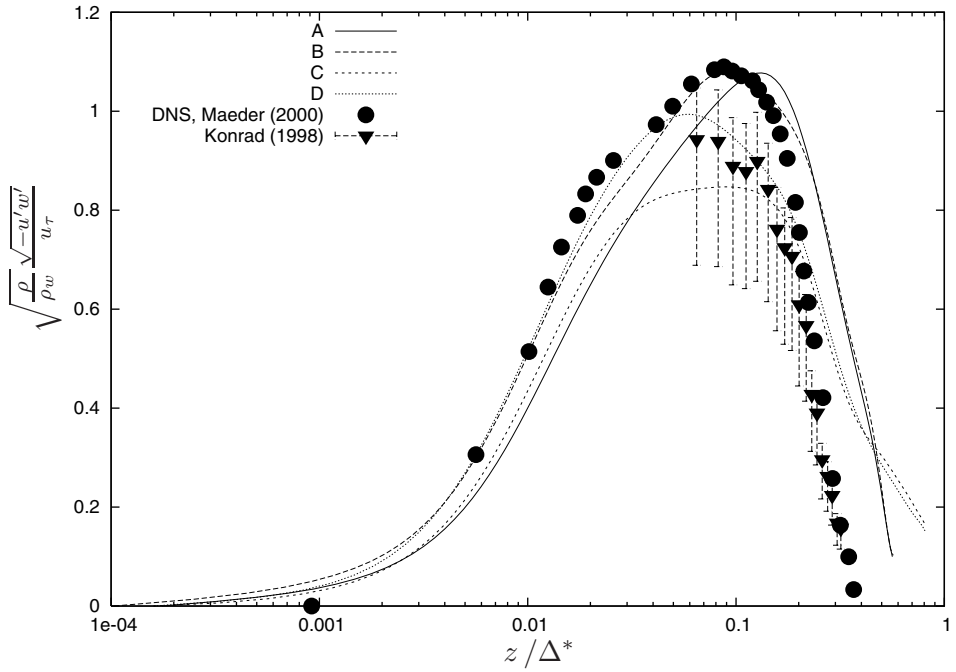

Figure 4.1-25: $Re_\theta = 4000$ - Reynolds shear stress from the approximate deconvolution model normalized by wall conditions and velocity defect thickness.

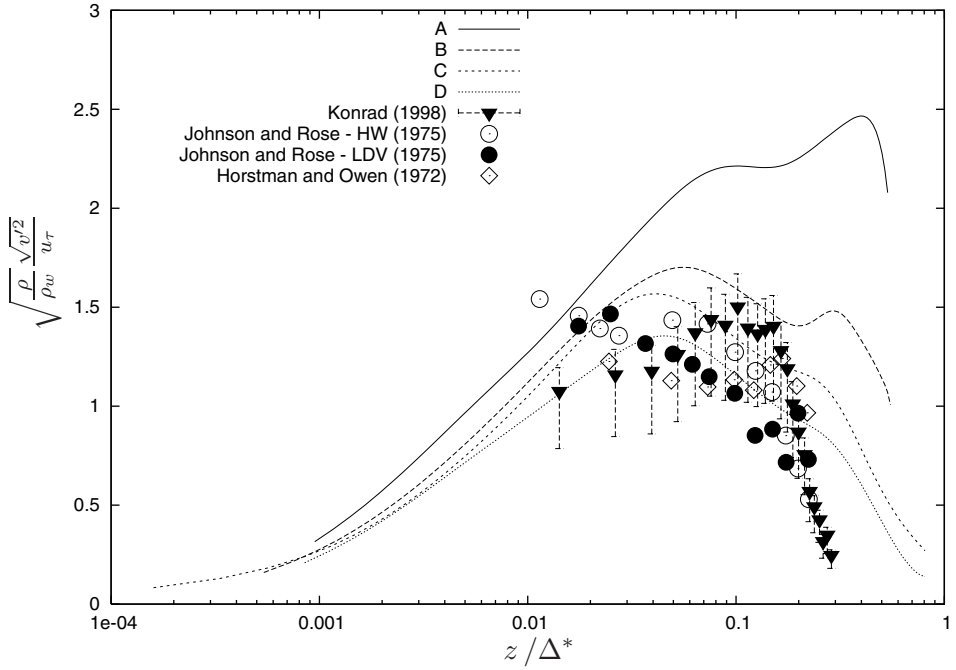

Figure 4.1-26: $Re_\theta = 4000$ - Spanwise Reynolds normal stress from the approximate deconvolution model normalized by wall conditions and velocity defect thickness.

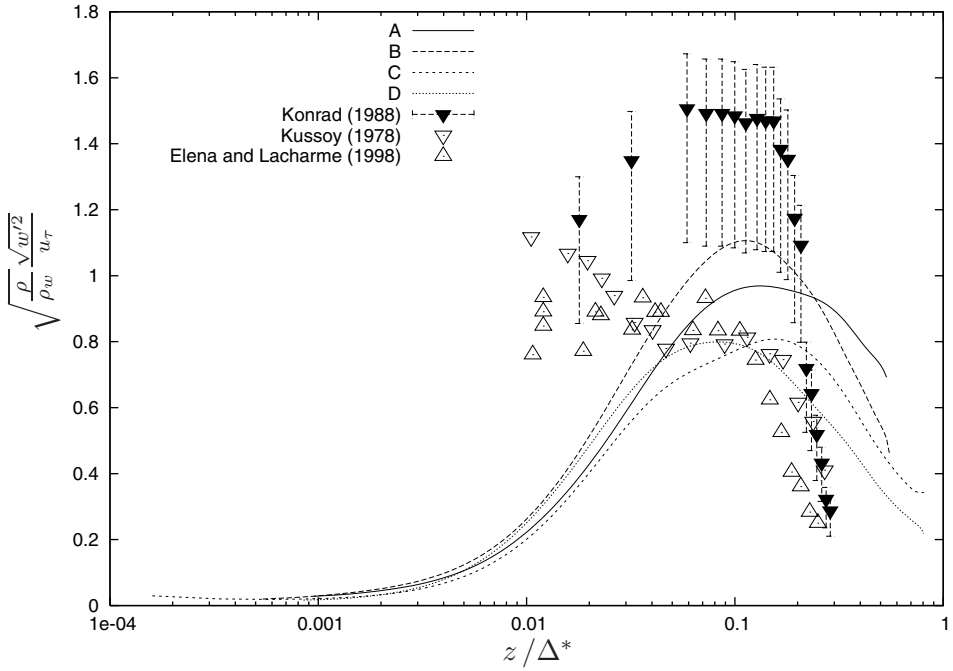

Figure 4.1-27: $Re_\theta = 4000$ - Wall normal Reynolds shear stress from the approximate deconvolution model normalized by wall conditions and velocity defect thickness.

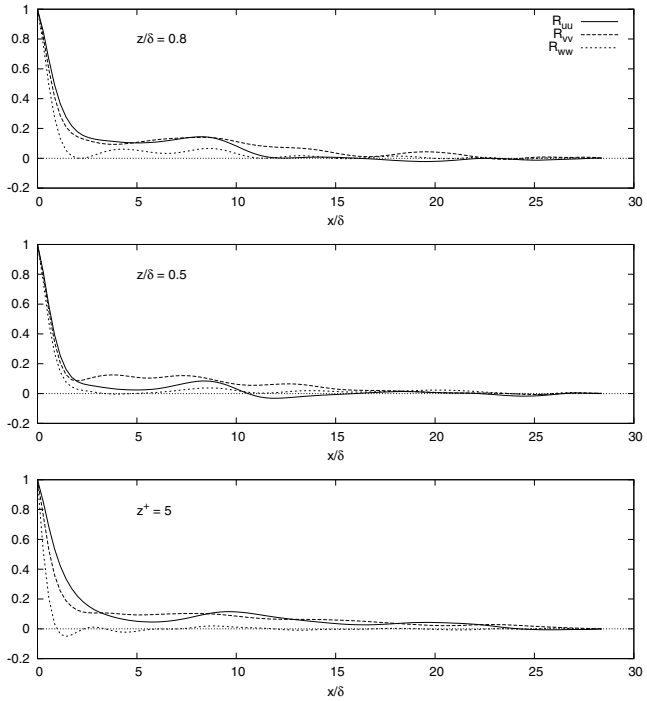

Figure 4.1-28: Streamwise two-point autocorrelation - approximate deconvolution model.

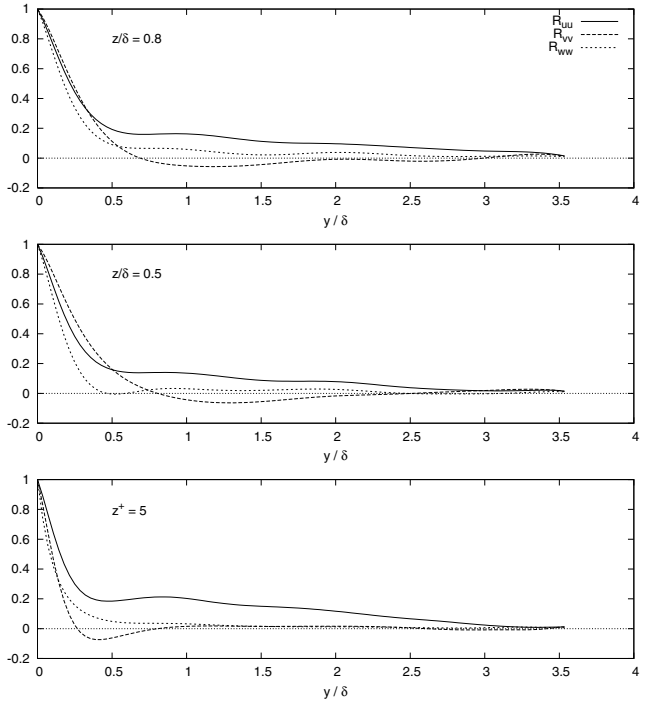

Figure 4.1-29: Spanwise two-point autocorrelation - approximate deconvolution model.

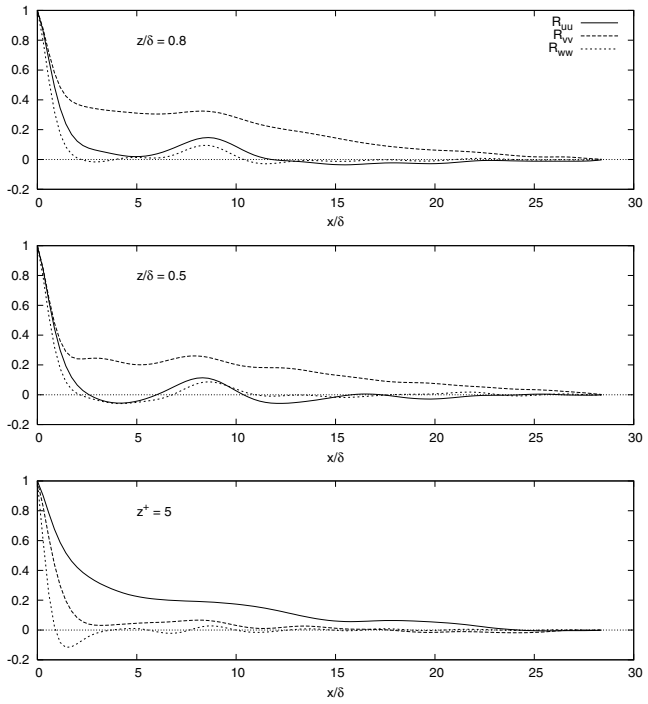

Figure 4.1-30: Streamwise two-point autocorrelation - mixed scale model.

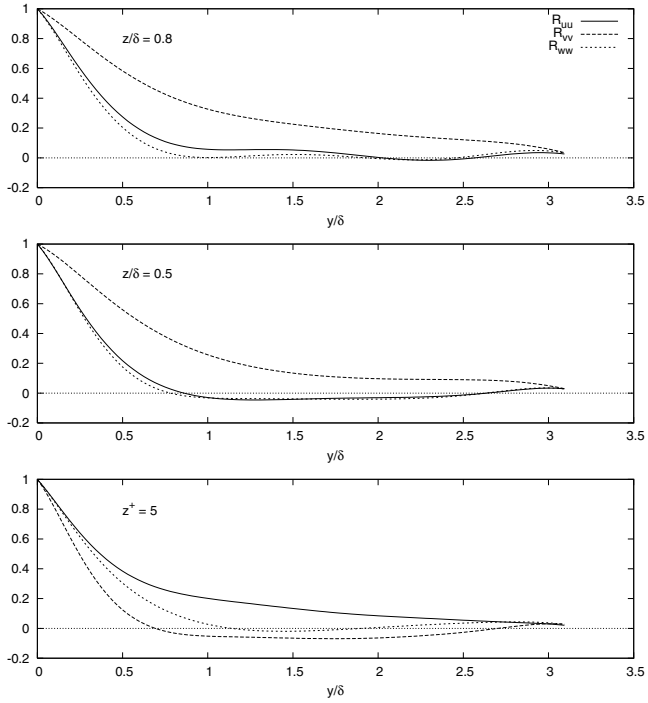

Figure 4.1-31: Spanwise two-point autocorrelation - mixed scale model.

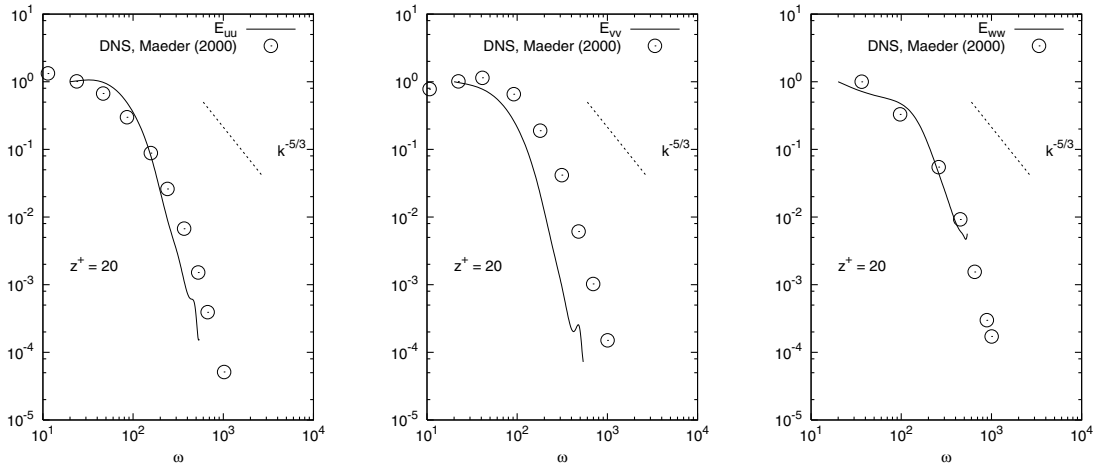

Figure 4.1-32: Approximate deconvolution model - spanwise energy spectra.

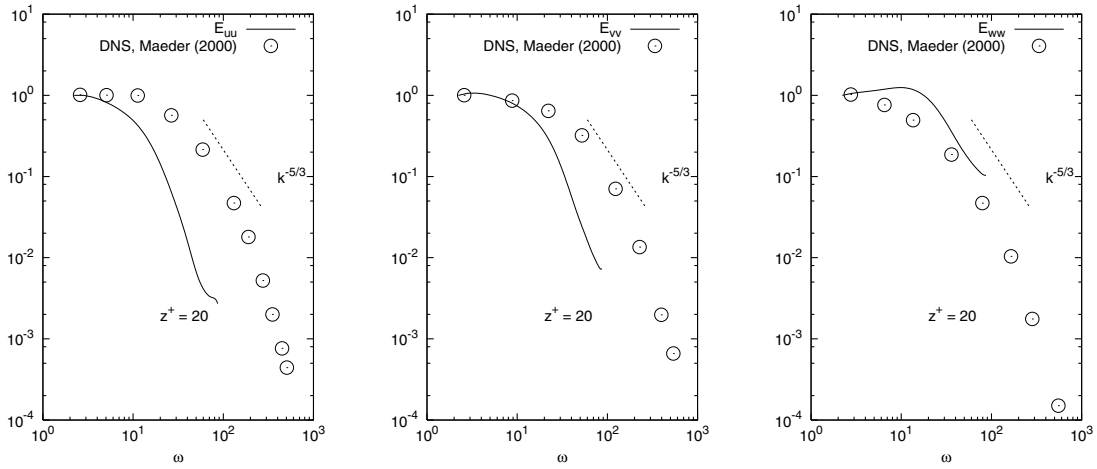

Figure 4.1-33: Approximate deconvolution model - streamwise energy spectra.

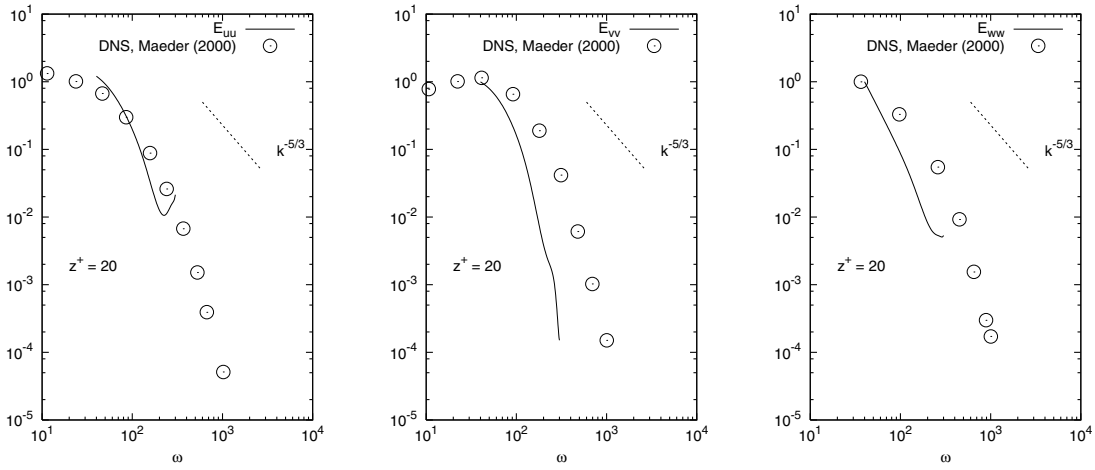

Figure 4.1-34: Mixed scale model - spanwise energy spectra.

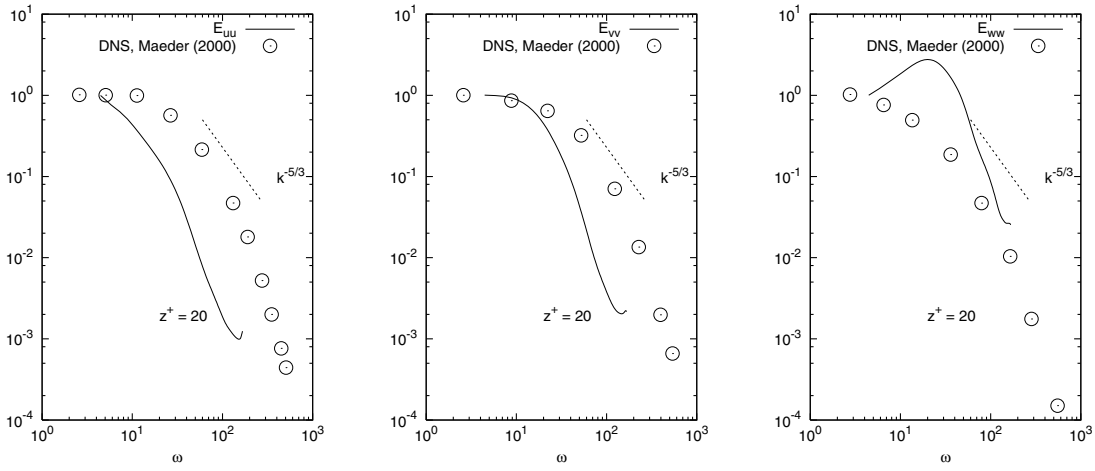

Figure 4.1-35: Mixed scale model - streamwise energy spectra.

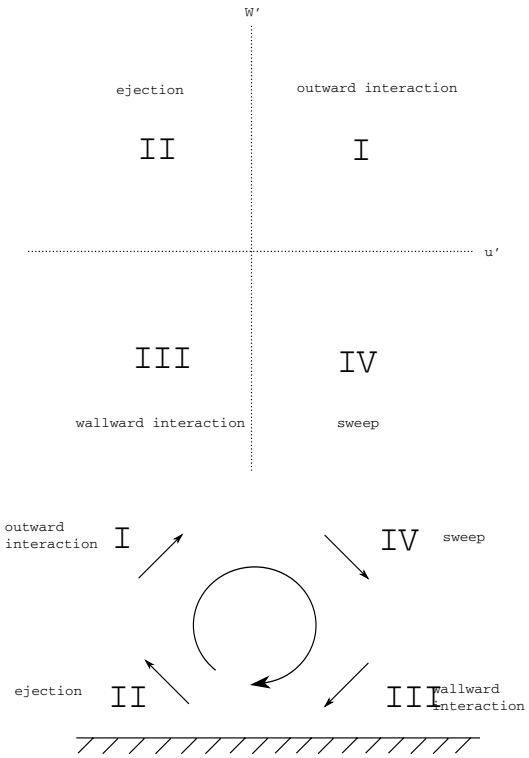

Figure 4.1-36: Definition of quadrants.

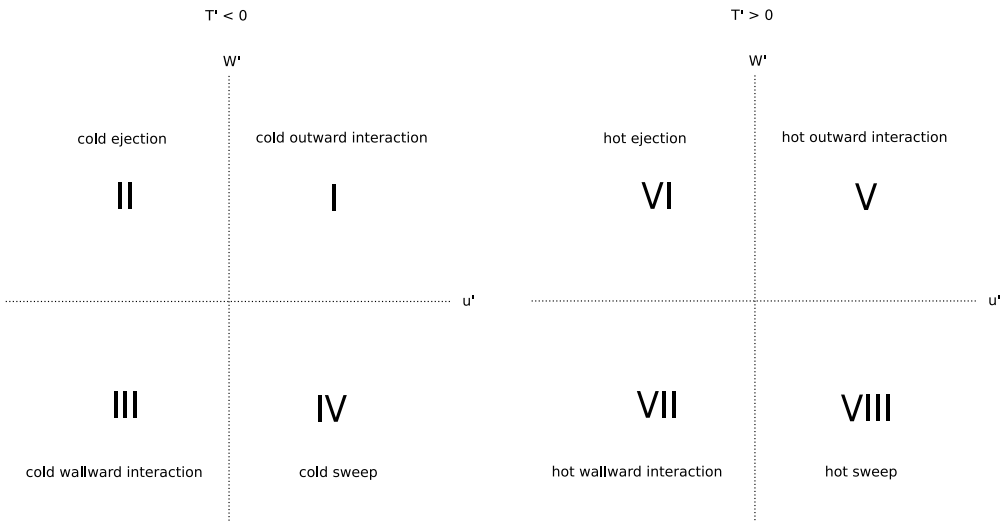

Figure 4.1-37: Definition of octants.

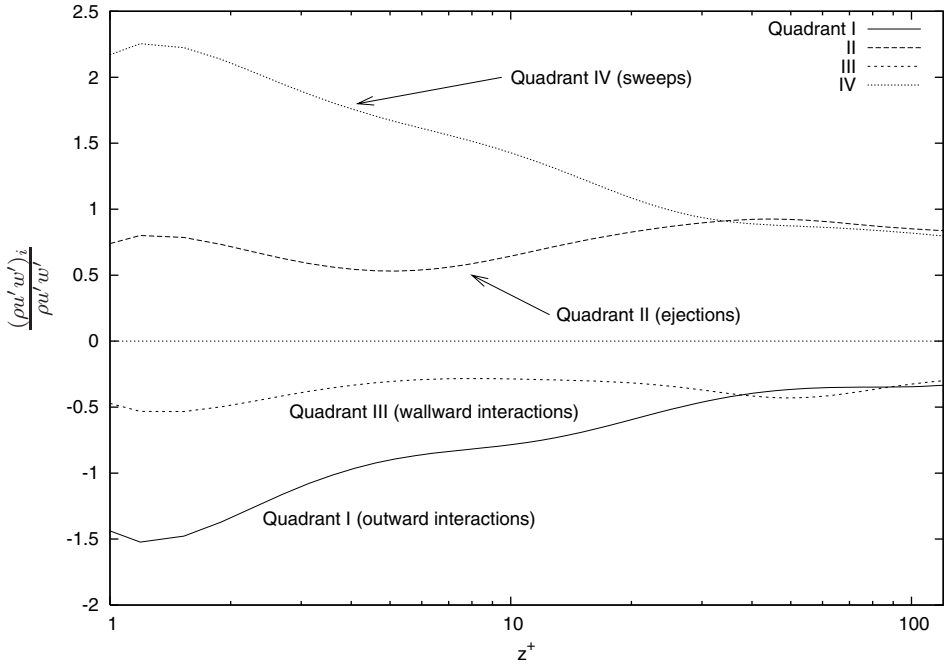

Figure 4.1-38: Classification of Reynolds shear stress into quadrants normalized by local stress based on fluctuating velocity.

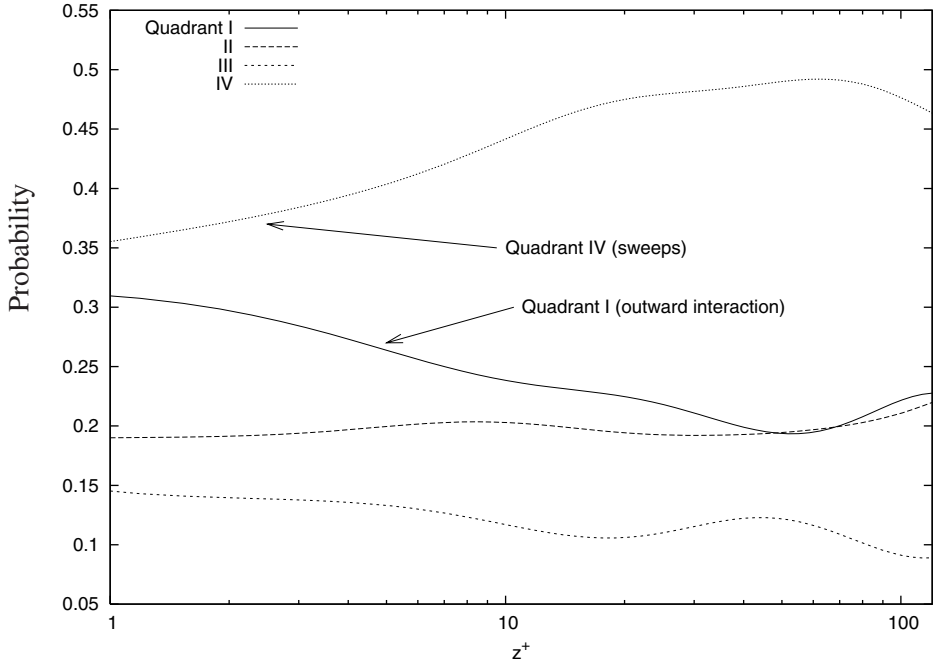

Figure 4.1-39: Probability of each mechanism occurring in a quadrant.

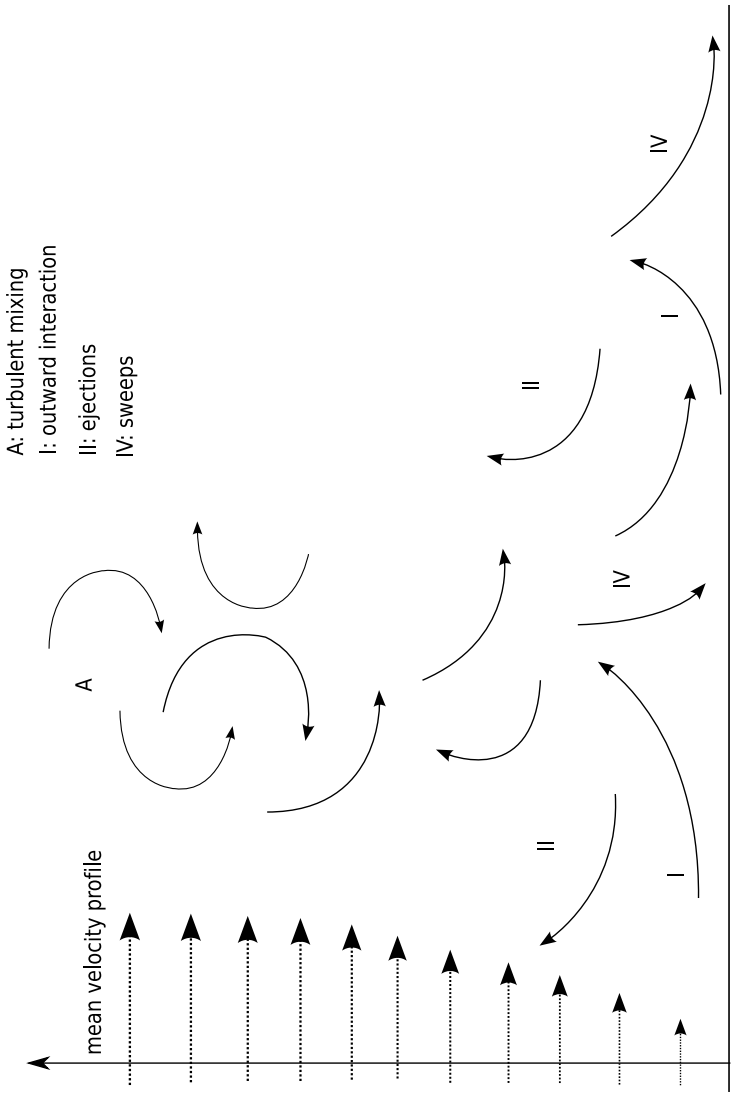

Figure 4.1-40: Schematic of dominant turbulent momentum transport quadrants (adapted from Bilson (2004)).

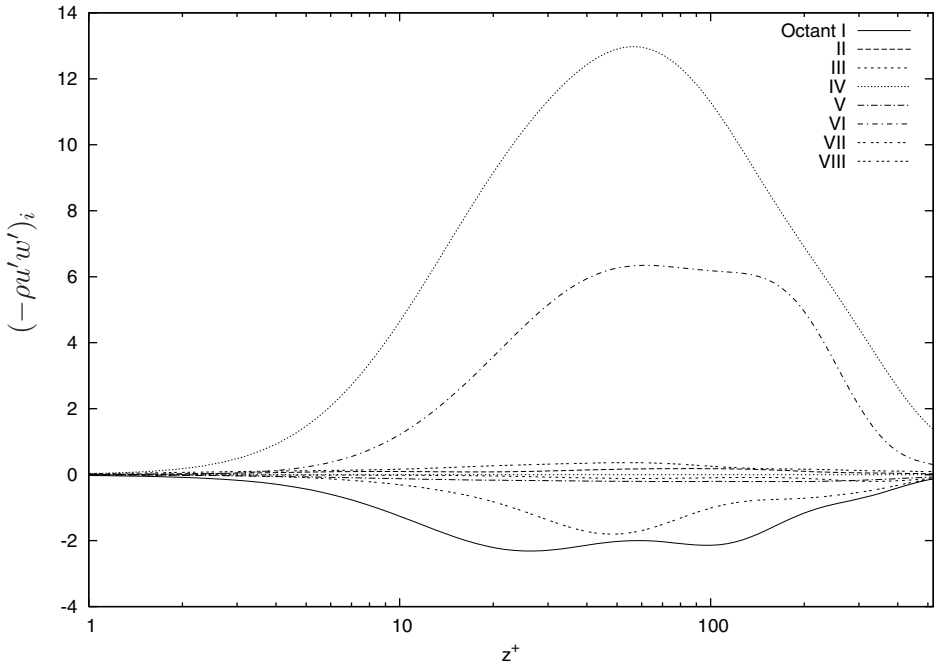

Figure 4.1-41: Classification of Reynolds shear stress into octants based on velocity and temperature fluctuations.

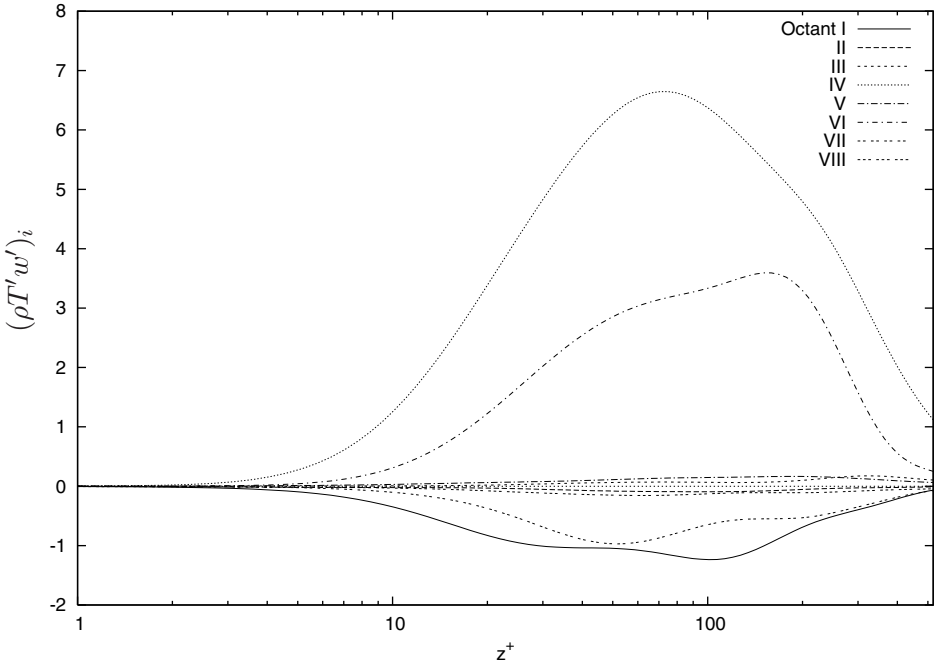

Figure 4.1-42: Classification of wall normal turbulent heat flux into octants based on velocity and temperature fluctuations.

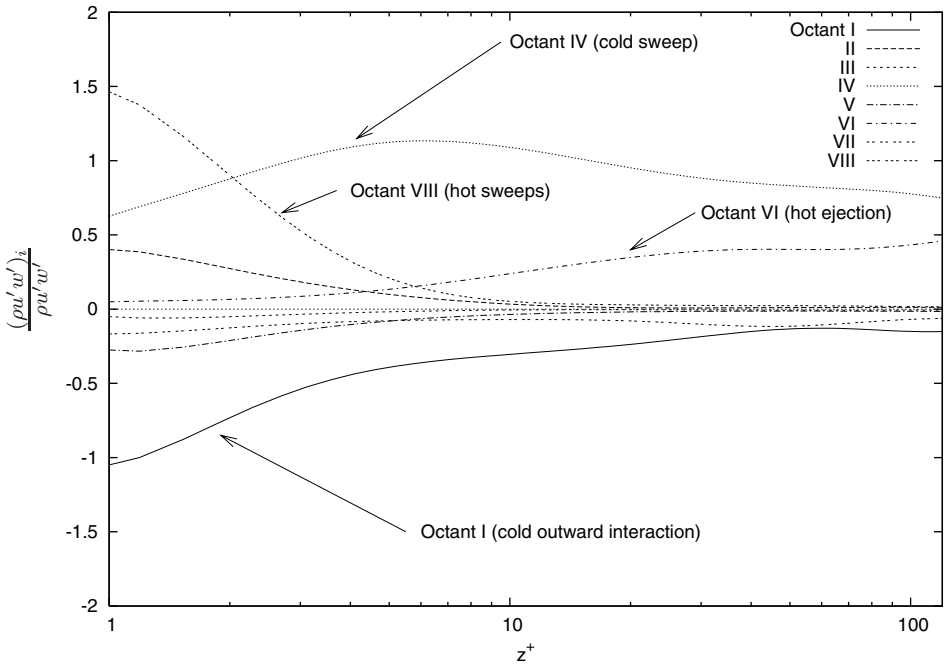

Figure 4.1-43: Classification of Reynolds shear stress into octants based on velocity and temperature fluctuations normalized by local stress.

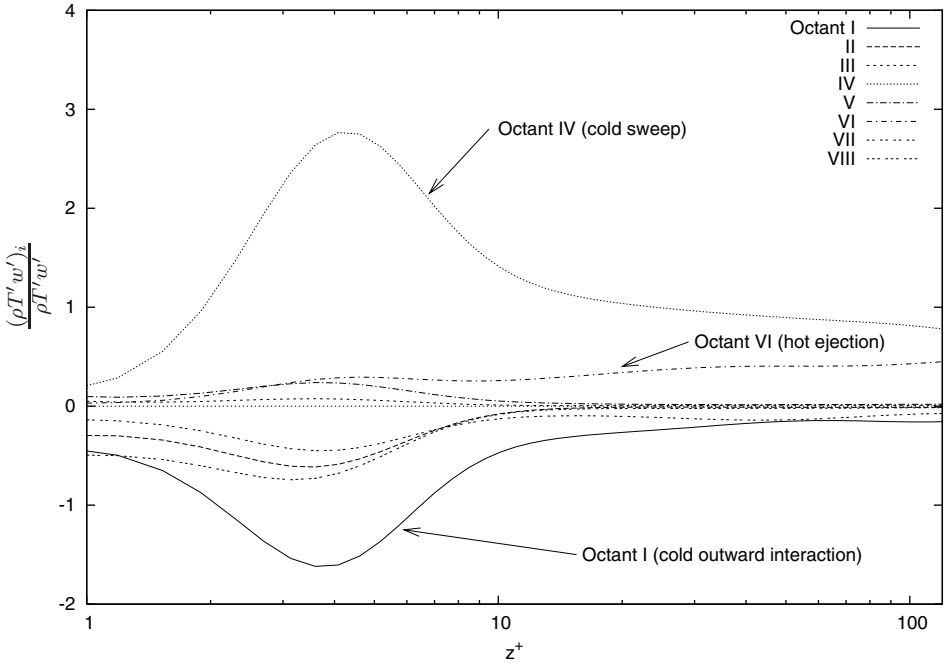

Figure 4.1-44: Classification of wall normal turbulent heat flux into octants based on velocity and temperature fluctuations normalized by local flux.

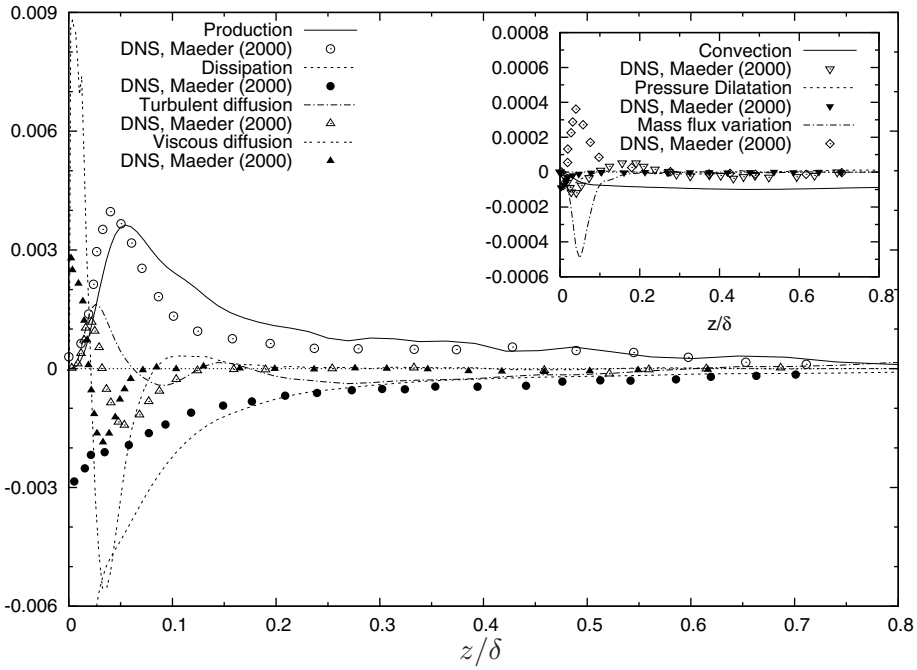

Figure 4.1-45: Turbulent Kinetic Energy budget: Lines - current ADM calculations; points - Maeder (2000).

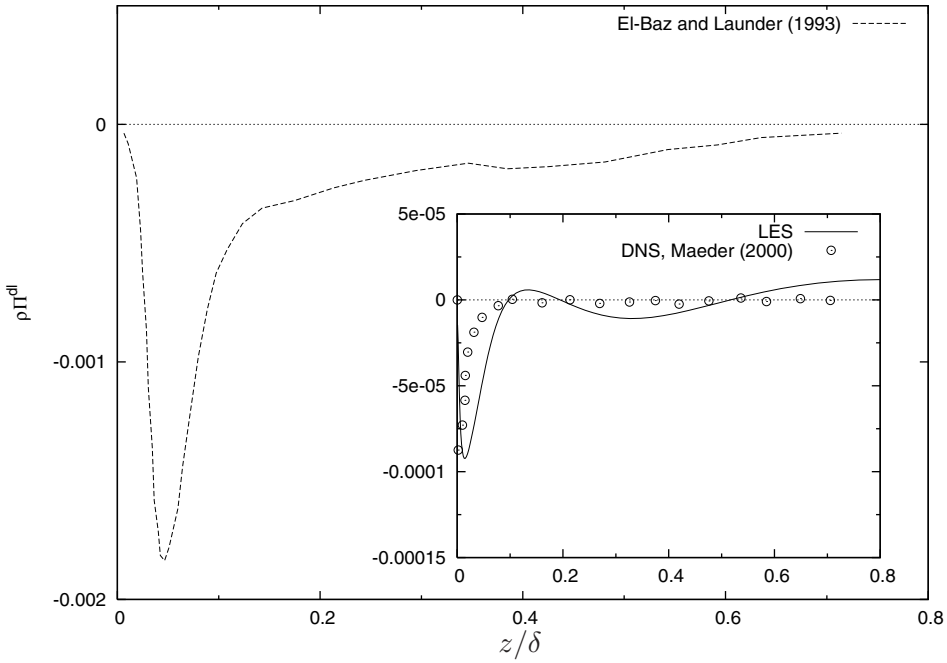

Figure 4.1-46: Pressure dilatation component of turbulent kinetic energy budget.

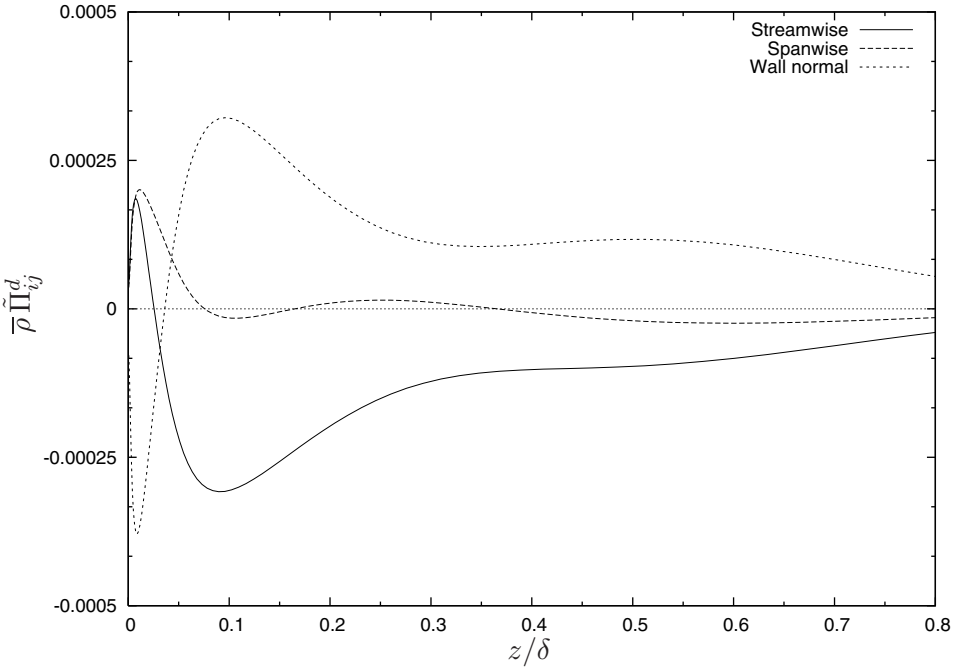

Figure 4.1-47: Pressure-strain component for Reynolds normal stress budget.

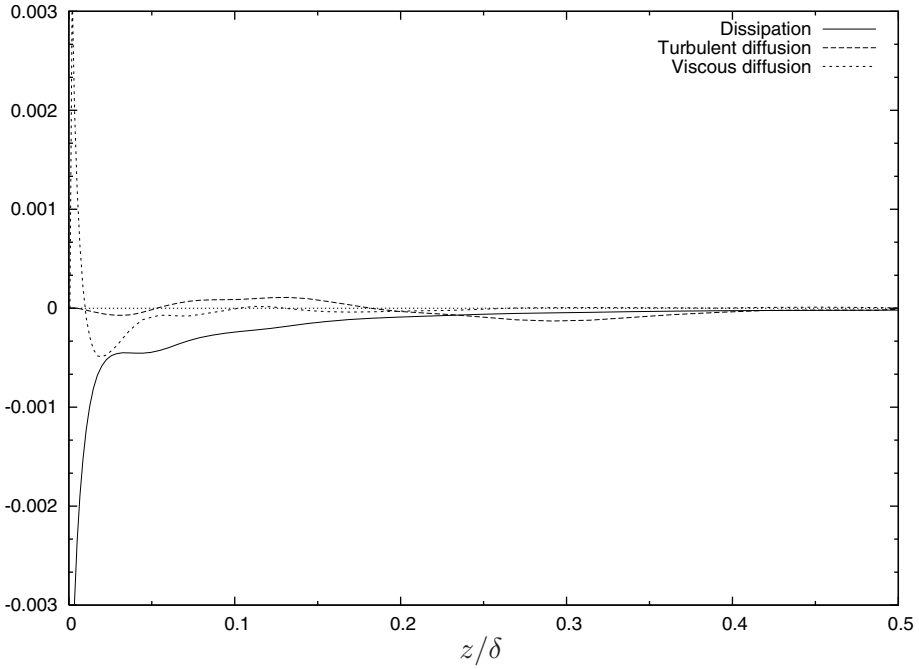

Figure 4.1-48: Spanwise component of resolved turbulent kinetic energy budget.

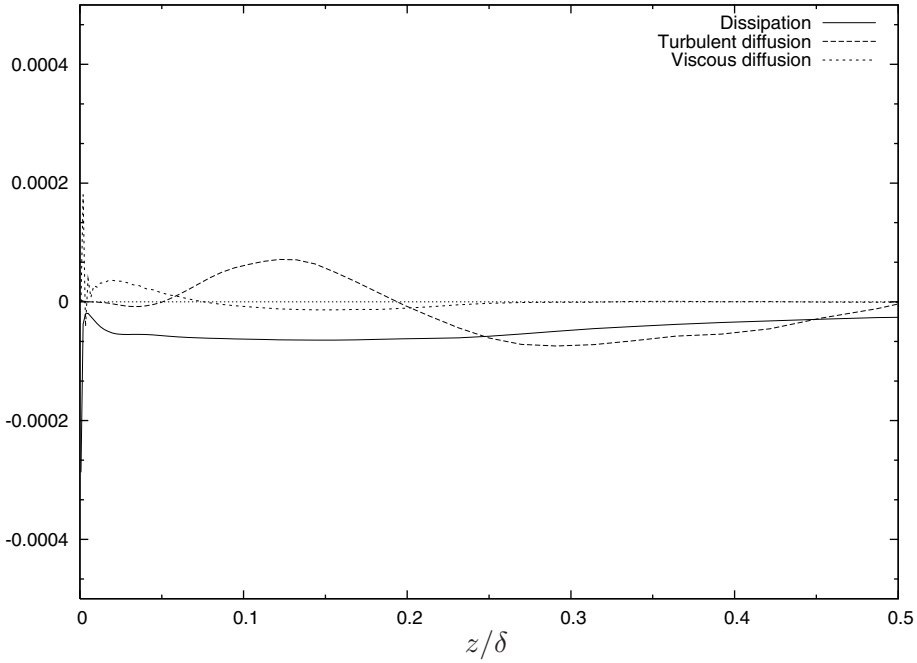

Figure 4.1-49: Wall normal component of resolved turbulent kinetic energy budget.

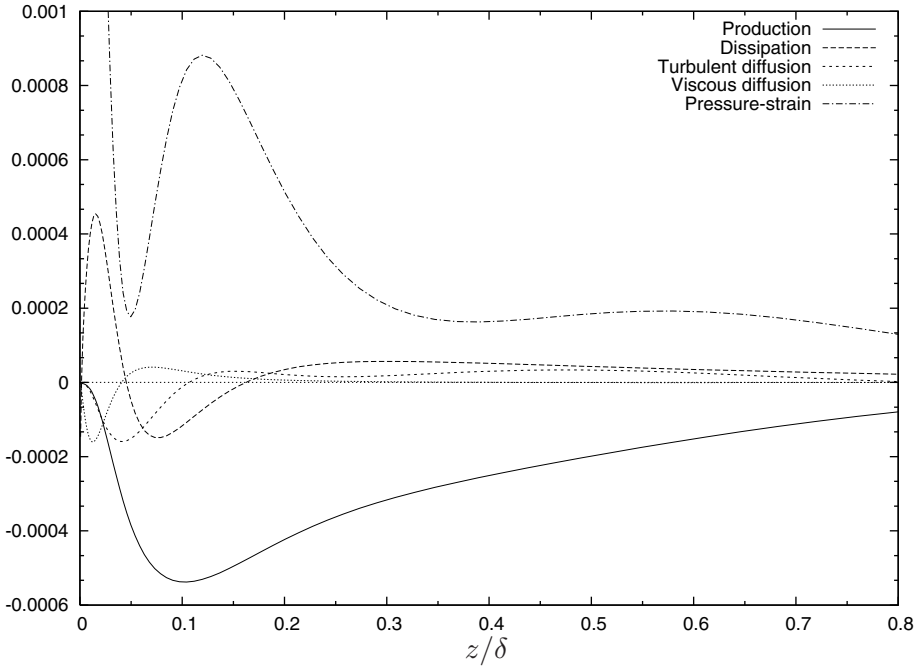

Figure 4.1-50: Reynolds shear stress budget.

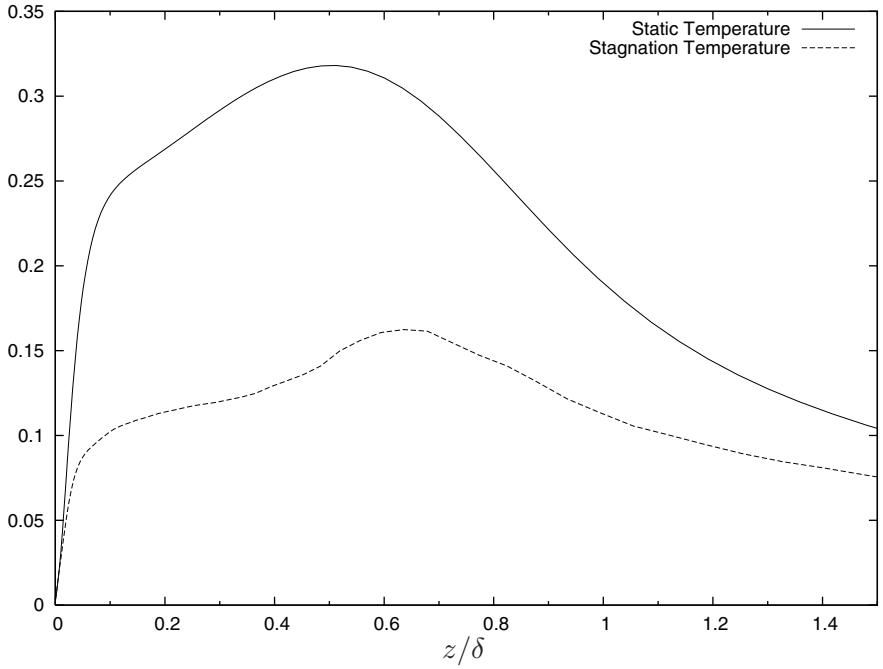

Figure 4.1-51: Relative temperature fluctuations: Static temperature RMS$(\widetilde{T'})/\widetilde{T}$; Stagnation temperature RMS$(\widetilde{T'_0})/\widetilde{T}$.

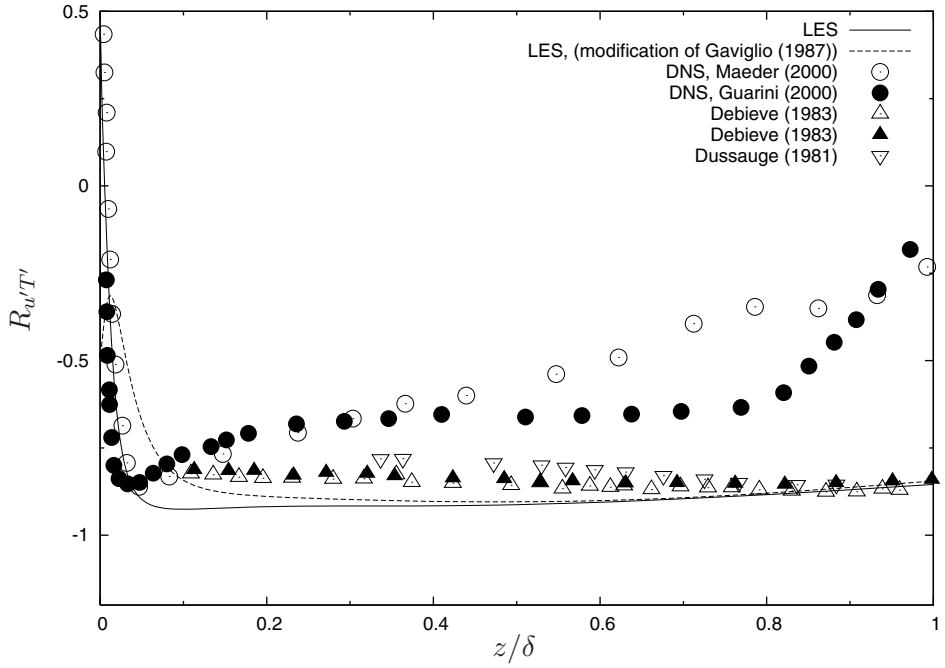

Figure 4.1-52: Comparison of correlation coefficient $R_{u'T'}$ versus z/δ with experiments and DNS.

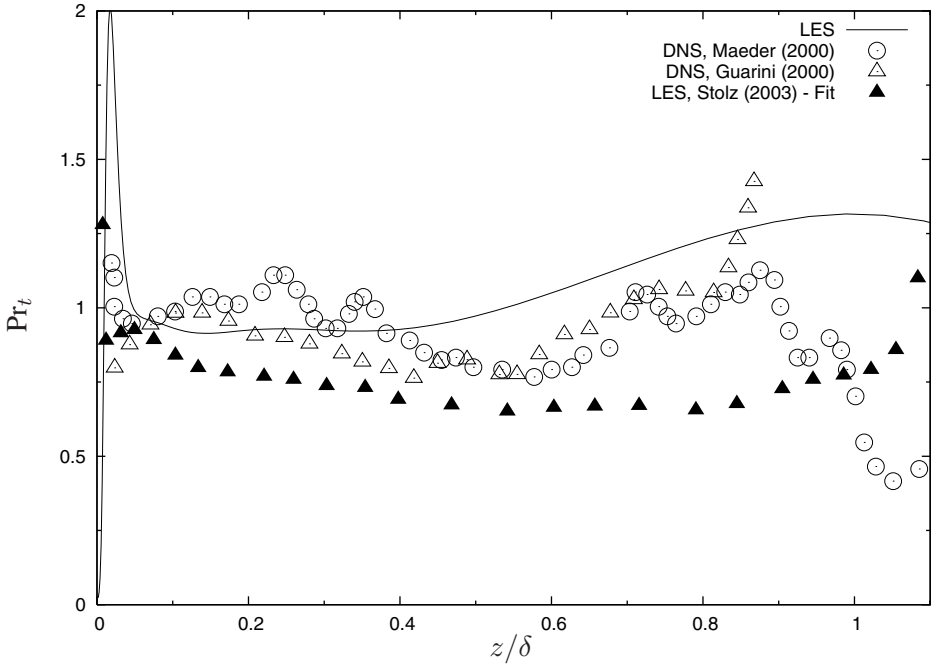

Figure 4.1-53: Comparison of turbulent Prandtl number versus z/δ with experiments, DNS and LES.

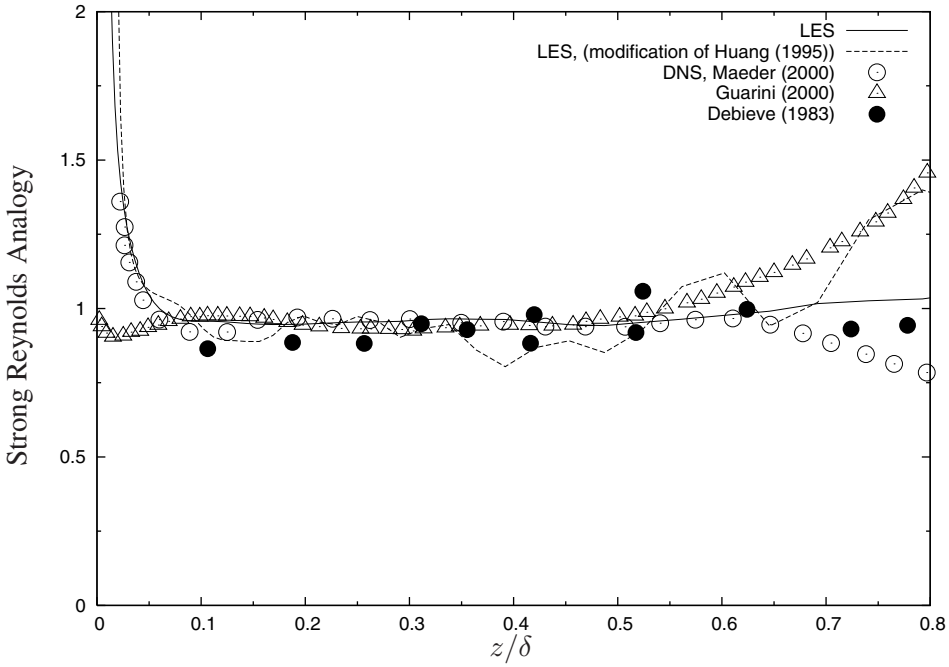

Figure 4.1-54: Comparison of Strong Reynolds Analogy with experimental data from Gaviglio (1987) (original data from Debiève (1983)) and DNS data of Maeder (2000)

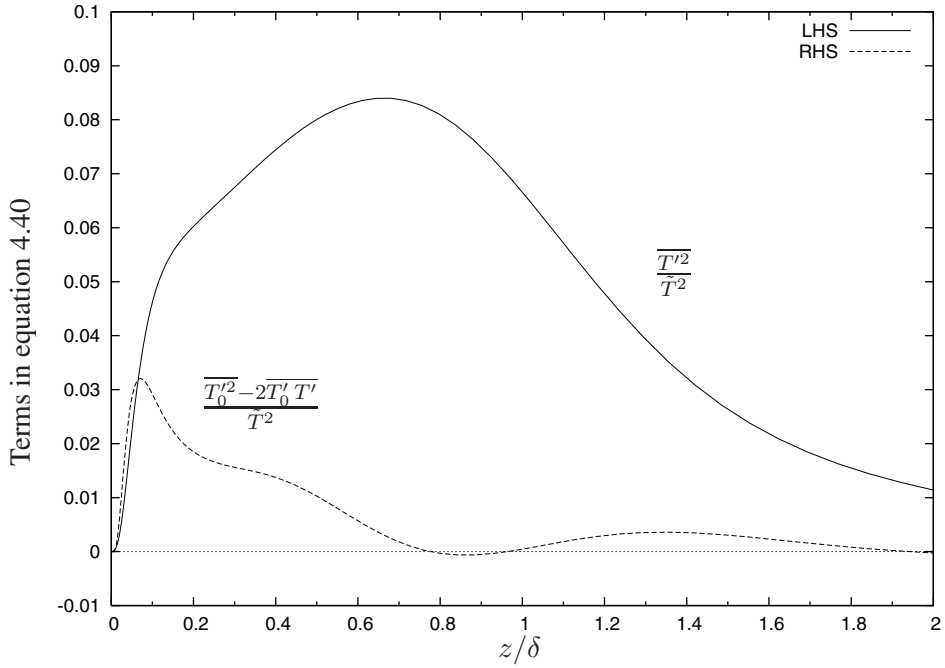

Figure 4.1-55: Comparison of terms in equation 4.40.

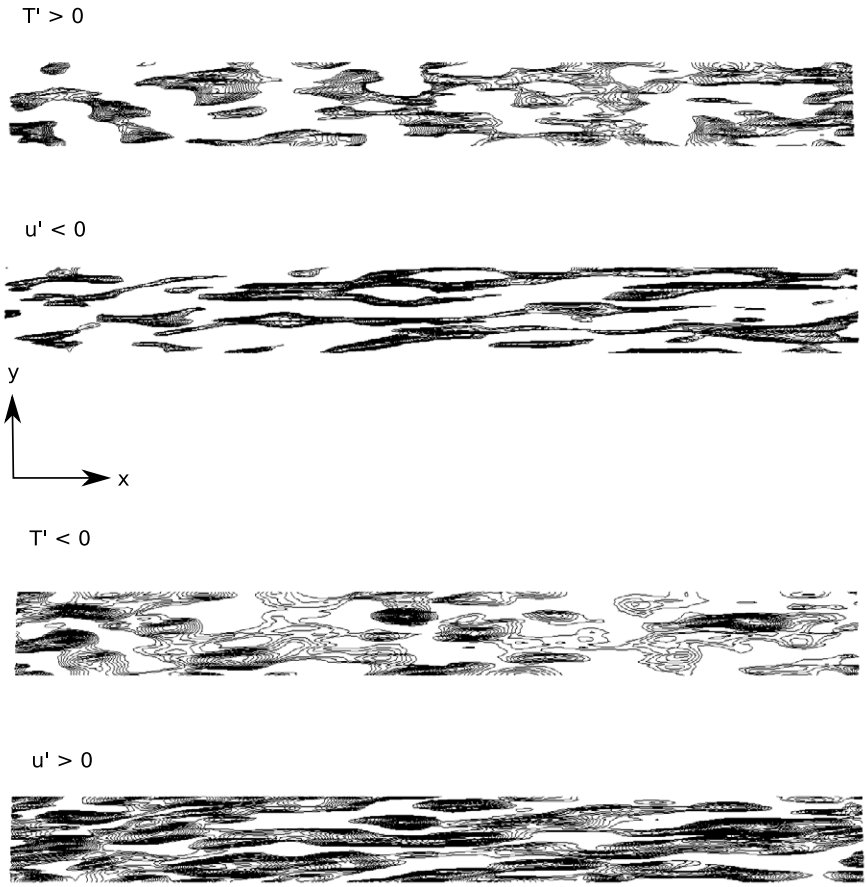

Figure 4.1-56: Instantaneous fluctuations of streamwise velocity and temperature at $z^+ = 5$. Half the domain length and width are shown for clarity.

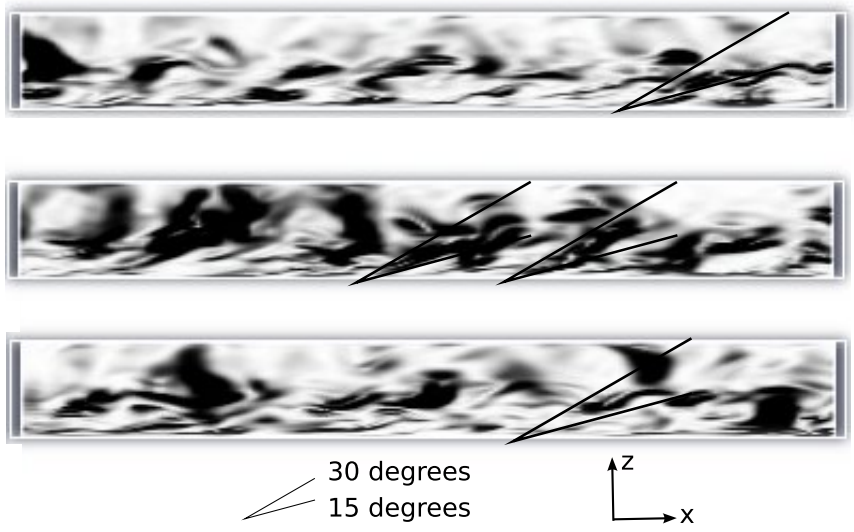

Figure 4.1-57: Contour of density gradient showing hairpin angles for increasing time.

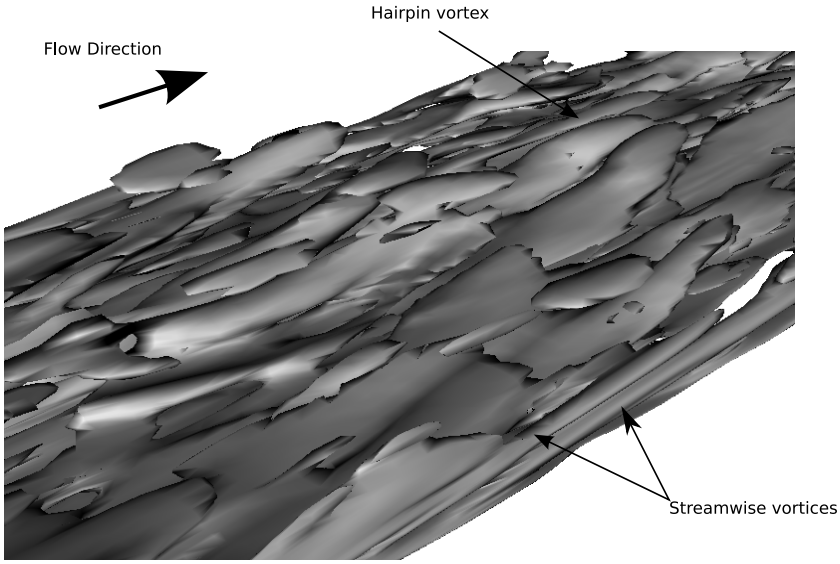

Figure 4.1-58: Iso-surface of vorticity showing boundary layer structure from ADM computations.

Figure 4.1-59: Instantaneous fluctuations of streamwise and spanwise velocity at $z^+ = 5$ ranging from $-4 < u'/u_\tau < 4$ and $-2 < v'/u_\tau < 2$ respectively in increments of $u_\tau/5$. The flow is from left to right. Half the domain length is shown for clarity.

CHAPTER 5

LARGE-EDDY SIMULATION OF HEAT ADDITION IN SUPERSONIC BOUNDARY LAYERS

"But as no two (theoreticians) agree on this (skin friction) or any other subject, some not agreeing today with what they wrote a year ago, I think we might put down all their results, add them together, and then divide by the number of mathematicians, and thus find the average coefficient of error."

Hiram Maxim, early aeronautical designer, 1908

In this chapter, large-eddy simulation has been used to investigate the effect of heat release on the supersonic turbulent boundary layer. The previous chapter showed that when using the Approximate Deconvolution Model (ADM) good results can be obtained for the resolved flow field when compared to both DNS and experimental data. The simulated conditions are those studied experimentally by Suraweera (2006) in a free piston reflected shock tunnel facility at the University of Queensland. The experiments identified the effects of film cooling from hydrogen injection through reductions in the measured skin friction and heat transfer along a flat plate and further decreases due to combustion. The wall to freestream temperature ratio is significantly lower than other cold wall LES undertaken by other authors. Consequently, there is a lack of definite numerical resolution requirements and, combining this fact with the lack of experimental profiles for these conditions, we require the inclusion of a grid resolution study to ensure the solutions are grid independent.

To study the changes that occur in the boundary layer when combustion occurs, chemical energy is introduced. The effects of chemical energy release in the LES simulations are included in two ways. Firstly, a heat source, developed to mimic the combustion of hydrogen, is used to analyse the changes in turbulent flow properties. The second method, used to obtain a more physically correct spatial and temporal distribution of heat addition, makes use of finite rate chemistry. While full LES combustion modelling of flame propagation is not used, the bulk effects of heat addition through finite rate chemistry are captured as desired. Hence, advanced turbulent combustion methods were not necessary for the purposes of this study.

5.1 Computational Details

The numerical methods outlined in section 3.2 are used for the simulations presented here and the numerical grids are detailed in table 5.1-1. The spanwise and wall normal domain sizes were guided by the results of the validation process of the previous chapter. Here the streamwise domain length is extended to maximize the resolution of the effects of heat addition. The low wall to freestream temperature ratio placed a very large computational burden on the resolution requirements when scaling on the wall conditions. The low temperature and correspondingly large density at the wall combine to increase the non-dimensional scaling parameter ($\rho_w u_\tau / \mu_w$). To keep the problem tractable, the streamwise extent of the domain could not be as large as the experimental configuration. However, the shorter numerical domain did not limit the applicability of the results since only a portion of the experimental configuration experienced combustion induced skin friction reduction.

Time averaging is carried out in the same way as the previous chapter's simulations. The approximate deconvolution method was found in the previous chapter to be the best performing subgrid-scale model of the three methods studied through its good agreement with DNS and experimental results. Its ability to obtain good results on grids that were coarser than those required by the eddy-viscosity/eddy-diffusivity based models further emphasized its superiority. All simulations presented in this chapter make use of the ADM subgrid scale model.

The inflow plane for the LES computational domain is taken as the first measurement station of Suraweera (2006), where a significant pressure rise was observed for combustion (figure 5.1-1). This point lies 915mm downstream from the leading edge and 670mm from the hydrogen injector. As was the case in the previous chapter, a Baldwin-Lomax RANS simulation, from the

Table 5.1-1: Computational parameters for large-eddy simulation of boundary layer flow with heat addition. ID is the identifier of the grid

ID	Domain size	Grid size	Δx^+	Δy^+	Δz^+
A	50 δ x 2.0 δ x 2.5 δ	400 x 40 x 90	320	120	2.2
B	50 δ x 1.3 δ x 2.5 δ	900 x 64 x 100	240	85	1.7
C	50 δ x 1.3 δ x 3.5 δ	1200 x 64 x 120	180	85	1.3
D	25 δ x 1.3 δ x 3.5 δ	600 x 64 x 170	180	85	0.6

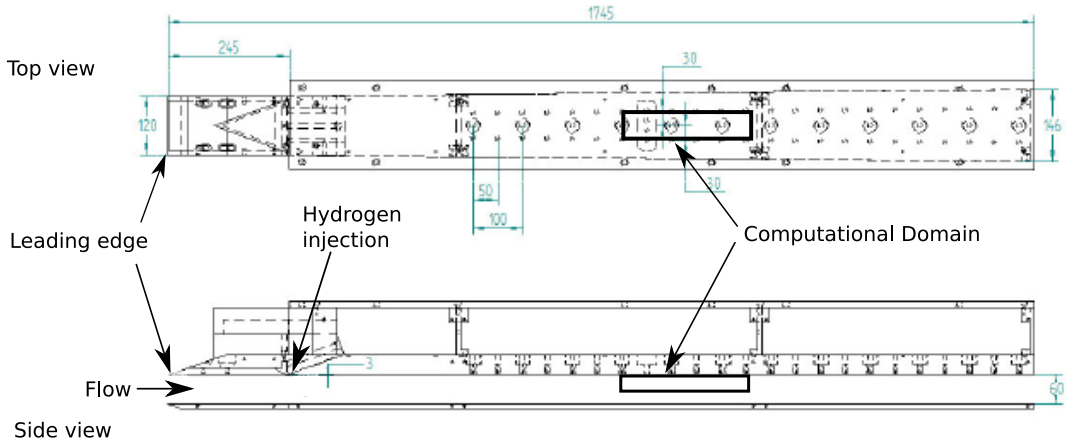

Figure 5.1-1: Experimental configurations with computational domain superimposed. Dimensions in mm, original figure from Suraweera (2006) with permission

leading edge to the first measurement station, was used to calculate the mean inflow profiles with the desired skin friction and boundary condition characteristics for use in the LES simulations (Section 3.3).

The two conditions studied are outlined in table 5.1-2 and correspond to experimental conditions 1 & 3 in the work of Suraweera (2006), where differences in behaviour were noted. The difference in Reynolds number and stagnation enthalpy between the two conditions allows for the assessment of any Reynolds number or stagnation enthalpy sensitivities in combustion affected flow properties. It was also observed experimentally for these conditions, when no hydrogen was injected, that the ratio of Stanton number (C_h) to skin friction coefficient (C_f), known as the Reynolds analogy factor ($2\,C_h/C_f$), decreased for increasing C_f. Under normal circumstances this factor is taken as being in the proximity of 1, while the experimental results indicated this ratio to be 0.5 or lower. This discrepancy was intially reasoned to be due to real gas effects, such as oxy-

Table 5.1-2: Physical simulation parameters

Case	M_∞	u_∞ (m/s)	T_∞ (K)	P_∞ (kPa)	H_s (MJ/kg)
1	4.85	2720.0	808.6	44.75	4.8
2	4.52	3365.0	1449.0	60.8	7.6

Case	Re $\times 10^{-6}$ (m^{-1})	δ_0 (mm)	T_w (K)	T_r (K)
1	17.2	5.1	296.0	3660.0
2	11.08	5.3	296.0	5890.0

gen dissociation. However, experiments with nitrogen test gas demonstrated similar behaviour in Reynolds analogy factor. The trend persisted when Hydrogen was injected and combusted in air. The chosen conditions will allow for assessment of the presence of such a phenomena in the numerical results.

5.2 No Heat Addition

To establish a baseline for comparison, simulations are first presented for the desired conditions without any form of heat addition. These results are used to both verify the behaviour of the code under these flow conditions, validate the results against available experimental data and assess the necessary levels of grid refinement. The nature of the experiments conducted in the impulse facility precluded measurements of any flow profiles, however, the skin friction and heat transfer results of Suraweera (2006) are used for validation purposes. Through comparison of skin friction and heat transfer results we can be confident that the simulations are reproducing the flow conditions studied experimentally. To make comparisons of turbulent stress behaviour, the experimental data used in Chapter 4 is used once again with appropriate normalization to remove Mach number and wall condition dependence. Turbulent statistics, such as two-point spatial correlations, energy spectra and quadrant/octant analysis, are computed and analysed as a further check on the presented results. The ensuing discussion allows for the establishment of a baseline behaviour of the turbulent structures for the conditions studied. Figures for this section appear together, starting on page 161.

Table 5.2-3: Effect of grid resolution on skin friction coefficient and boundary layer shape factors for conditions 1 and 2 with $\delta = 5 \times 10^{-3}$m

Case	Grid	$C_f \times 10^3$	$C_h \times 10^3$	H_{12}	H_{32}	Re_θ	Re_{δ_2}
1	A	1.1	0.45	3.3	1.75	4065	5311
	B	1.4	0.68	3.5	1.78	3958	6690
	C	1.65	0.78	3.2	1.77	3956	6710
	D	1.68	0.90	3.2	1.77	3986	6789
	Suraweera (2006)†	1.7 ± 0.25	0.5 ± 0.07	-	-	-	-
	Spalding and Chi	1.5	0.975‡	-	-	-	-
	Van Driest II	2.07	1.34‡	-	-	-	-
2	A	1.1	0.70	2.88	1.79	2825	7974
	B	1.6	1.02	2.84	1.79	2803	7912
	C	1.95	1.2	2.81	1.82	2764	7803
	D	2.05	1.28	2.77	1.79	2809	7913
	Suraweera (2006)†	2.15 ± 0.39	0.65 ± 0.09	-	-	-	-
	Spalding and Chi	1.95	1.27‡	-	-	-	-
	Van Driest II	2.7	1.75‡	-	-	-	-

†. Data measured at first downstream station

‡. Stanton number calculated assuming $2C_h/C_f = 1.3$

5.2.1 Effect of Grid Refinement

Verification

The numerical code was initially verified in section 4.1.2. However, with new flow conditions being studied here and the associated extra demands placed on the resolution requirements by the wall conditions, it remained important to assess whether or not the current numerical resolutions lay within the asymptotic convergence region. As done previously, the skin friction coefficient is the quantity used to study the convergence characteristics. The length scale chosen here is the wall normal grid size normalized by wall conditions (Δz^+).

For case 1 we begin by considering grids A, B and C (table 5.1-2). Solving equation (4.2) yields an order of convergence, $p \sim 1.2$. This convergence is shown graphically in figure 5.2-1 where the

skin friction results are plotted with both a linear and order 1.2 curve fit. It is then assumed that this order of convergence applies to the results obtained for grid D, where solution of equations 4.5, 4.6 and 4.7 returns a grid convergence error estimate of 6% including the appropriate safety factor. When compared to the experimentally measured skin friction coefficient we see good agreement, demonstrating that not only do the results lie within the asymptotic convergence region, but that the results also make physical sense. Similarly for case 2, by considering grids A, B and C again, the observed order of convergence is $p \sim 1.1$. Extending this order of convergence to grid D yields a grid convergence error estimate of 20.9%. This result demonstrates that as the wall to freestream temperature ratio decreases, the demands on resolution increase, introducing extra uncertainty. Hence with both cases using the same numerical grid resolutions we expect to, and indeed see, an increasing resolution requirement to reach convergent behaviour leading to an increase in error bounds for case 2. This convergence behaviour is shown graphically in figure 5.2-2.

Mean Flow

The effect of spatial resolution on the behaviour of boundary layer shape factors and the computed Reynolds numbers is shown in table 5.2-3. For both cases 1 and 2, there appears to be no significant change in computed mean quantities when moving from grid C to D. Furthermore, when computational costs are high, for instance when using finite rate chemical kinetics, grid B provides sufficient numerical resolution such that the computed mean quantities are unaffected.

The effect of grid resolution is assessed further through examination of the mean streamwise velocity profiles. The mean profiles are taken by averaging the flow properties in the homogeneous spanwise direction and are sampled 10 boundary layer thicknesses downstream of the recycling station to ensure that any inlet transients have decayed.

The van Driest transformation is applied to the mean streamwise velocity profile in figures 5.2-3 and 5.2-4. The figures indicate that either the conditions simulated appear to be outside of the limits of applicability of the van Driest transformation due to the lack of agreement with standard velocity profile behaviour, or that the profiles themselves are flawed. While there is a discernable viscous sublayer and log law region, the log law region in particular does not conform to the standard coefficients. Fernholz and Finley (1980) found that, for some conditions, the low Reynolds number region (ie. close to the wall) began to dominate the inner layer region causing the velocity scaling to fail. Hopkins et al. (1972) also observed poor performance of the van Driest

transformation for nonadiabatic conditions and put this failure down to the low Reynolds number of the flow ($\mathrm{Re}_\theta \approx 5{,}000$). However, the Reynolds number of the mean profiles computed in the previous chapter were of the same order as the current simulation set and failure of the scaling was not observed. The major difference between these results and those of the previous chapter is much colder wall conditions generating highly non-adiabatic conditions. Such wall conditions introduce a large variation in flow properties in the immediate vicinity of the wall.

To account for the mean property variations Coleman et al. (1995) introduced semi-local, rather than wall scaling for the transformation of results from the simulation of compressible, cold-wall, channel flow. This process was later used successfully by Maeder (2000) to collapse Reynolds stress profiles from cold wall DNS. The semi-local scaling replaces ρ_w with $\overline{\rho}(z)$, μ_w with $\overline{\mu}(z)$ and u_τ with $u_\tau^* = \sqrt{\tau_w/\overline{\rho}(z)}$. The improvement in agreement between the van Driest transformed mean streamwise velocity profiles and theory using semi-local scaling for the current results is clear to see in figures 5.2-5 and 5.2-6. The viscous sub-layer is much clearer and, while Coleman et al. (1995) were successful in conforming to the law of the wall with the use of z^+ instead of z^* in the van Driest transformation of the mean velocity profile, the use of the semi-local scaling remains valid. Its validity is due to different simulation conditions being used, ie. a colder wall condition relative to the mainstream flow, hence, the use of z^* is justified as these conditions induce even more significant property variations in the vicinity of the wall. It has been suggested that the additive constant in the law of the wall (equation 4.17) would depend on the heat transfer at the wall. The current results suggest that, while the logarithmic region agrees with the slope of $1/\kappa$, the additive constant should be lowered from 5.2 to 4.2. This difference is best observed for case 1 where the wall to freestream temperature ratio is less severe.

The similarity of the velocity profile in the outer region is verified by plotting the velocity defect versus the normalized wall normal location. The velocity defect thickness is again used for normalization because the boundary layer thickness can be an ill-defined quantity. Unlike the mean van Driest transformed velocity profile, the transformed mean velocity defect profile does not require any form of semi-local scaling (figures 5.2-7 and 5.2-8). This insensitivity of the velocity defect profile correlates with the findings of Laderman and Demetriades (1974) and Maeder (2000), but also stands to reason that away from the wall, the results will be less sensitive to the wall conditions.

The success of the semi-local scaling for the van Driest transformed mean velocity profile appears to be in contradiction with the results of Laderman and Demetriades (1974) for Mach 3 flow over

a cooled wall. It was found that for moderate heat transfer rates to the wall the boundary layer structure was unaffected, as were the turbulent stresses. However, the ratio of wall to freestream temperature studied experimentally is much higher than the conditions examined here, hence, the wall was relatively hotter than the conditions studied here. An indication of whether or not the use of semi-local scaling for the friction velocity is valid is given if the ratio of local to wall shear stress is insensitive to the Mach number (Coleman et al., 1995). Figures 5.2-21 and 5.2-22 [1] show that the shear stress profiles for the current Mach 4.8 simulations and subsonic flow are very similar and, hence, appear insensitive to Mach number.

The sensitivity of the transformed mean streamwise velocity and velocity defect profiles reinforce the conclusions made when considering the boundary layer shape factors and computed Reynolds numbers. The results indicate that the optimal resolution for mean streamwise velocity profile resolution is that of grids B and C. The excessive computational effort required for grid D and comparatively small gain in quality of results rule out its use.

Turbulent Intensities

Experimental data for turbulent supersonic boundary layers with strongly cooled walls was, to the best of this author's knowledge, unavailable. The term 'cooled wall' is often used to describe wall temperatures that are lower than the stagnation temperature of the freestream flow (Laderman and Demetriades, 1974). However, when comparing the ratio of wall temperature to freestream static temperature, the wall temperature can be greater than the freestream static temperature. Despite this unavailability of data, the RMS turbulent velocity fluctuations are normalized in the manner successfully used in the previous chapter and plotted against the same experimental data in figures 5.2-9 to 5.2-14. Clearly, consistent behaviour cannot be observed between the current results and the experimental data.

This poor agreement highlights the fact that for strongly cooled boundary layers, the variation in density across the layer must be taken into account. Such a statement is in agreement with the observations of Coleman et al. (1995), made for channel flow at Mach 1.5 with a wall to freestream temperature ratio of 2.5, and further emphasises the importance of properly accounting for the mean property variations in the scaling used. When the results of Coleman et al. (1995) were scaled without accounting for these variations, the differences between the RMS velocity

[1] Figure numbers appear out of order since these figures appear with other Reynolds stress plots.

fluctuations of low-speed flow and the DNS results were significant and the differences were observed to increase with Mach number. Hence, with the current data representing Mach 4.5 flow, a large over-estimation of velocity fluctuations has merit. Given these discrepancies, statements on the effect of grid resolution are deferred to the next section, where property variations are properly taken into account.

Reynolds Stresses

Given the observations of the previous section, we must account for the variations in mean properties before we can confidently assess the effects of grid resolution. When the streamwise normal stress ($\rho\overline{u'^2}$) is normalized by wall shear stress to remove Mach number dependence (Morkovin, 1962), we are also taking into account the variation in mean properties across the boundary layer. As was observed by Coleman et al. (1995), such scaling leads to a better collapse of the numerical and experimental data. Scaling the turbulent fluctuations with local density and wall shear stress, is akin to scaling with the semi-local friction velocity, as was successfully used for the mean velocity profiles. If we consider the RMS of streamwise velocity fluctuations ($\sqrt{u'u'}$) normalized by semi-local friction velocity (u^*_τ):

$$\frac{\sqrt{u'u'}}{u^*_\tau} = \frac{\sqrt{u'u'}}{\sqrt{\tau_w/\rho}} = \frac{\sqrt{\rho}\sqrt{u'u'}}{\sqrt{\tau_w}} = \sqrt{\frac{\rho}{\rho_w}}\frac{\sqrt{u'u'}}{u_\tau}$$

it becomes clear that semi-local scaling of RMS velocity fluctuations is the same as scaling a Reynolds stress by wall shear stress.

Figures 5.2-15 and 5.2-16 demonstrate the successful use of such scaling for cases 1 and 2 respectively for the streamwise Reynolds normal stress, which is in striking contrast to the comparisons of velocity fluctuations alone. Not only can we see a good agreement with the experimental data, but there is also a clear trend with respect to grid resolutions. Grids B, C and D all yield vastly similar results, with only grid A not able to correctly represent the streamwise Reynolds normal stress. These results further support the conclusion that both grid B or C represent the most efficient computational grids, that was arrived at from examination of mean flow data. The spanwise and wall normal Reynolds normal stresses for case 1 (figures 5.2-17 and 5.2-19 respectively) and case 2 (figures 5.2-18 and 5.2-20 respectively) show similar degrees of grid convergence while also exhibiting good agreement with experimental data. The results from case 2, however, do

show somewhat less grid independence than those of case 1. This again stems from the increased resolution demanded by the lower wall to freestream temperature ratio, however, the results are still acceptable.

The turbulent Reynolds shear stress is an important quantity for boundary layer flow and plays a large role in the transport of momentum towards the wall, thus it is important to ensure we properly capture its behaviour. Sandborn (1974) concluded that the ratio of total shear stress to wall shear stress, when the length scale is normalized by boundary layer thickness, is independent of Mach number and heat transfer. The same observations are made here, where as can be seen in figures 5.2-21 and 5.2-22, even under severe wall heat transfer, the shear stress remains close to the 'best fit' of Sandborn. As discussed in the prior sections, this independence of Mach number is stated to be the key to the success of semi-local scaling (Coleman et al., 1995).

Conclusion

The effect of grid resolution on calculated turbulent quantities has been assessed. For the conditions studied it is clear that the results of grids C and D differ very little. Furthermore, the results obtained for grid B provided mean streamwise velocity, turbulent velocity fluctuations and Reynolds stress profiles, that did not differ markedly from those of C and D. As expected from the lower wall to freestream temperature ratio, case 2 was observed to place greater demands on numerical resolution. The remainder of the results presented in this chapter are taken from grid C, $1200 \times 64 \times 120$. However, if the computational expense is large, for instance, when finite-rate chemical kinetics are included, the results are taken from grid B, $900 \times 64 \times 100$.

5.2.2 Two-Point Autocorrelations

The two-point autocorrelations of the streamwise, spanwise and wall normal velocity fluctuations are computed for both cases 1 and 2. Again the two-point autocorrelations are taken in the homogeneous spanwise and streamwise directions at three wall normal distances. Figures 5.2-23 and 5.2-25 present the results for case 1, while figures 5.2-24 and 5.2-25 present case 2. In their current capacity, these two-point autocorrelations are first used to demonstrate sufficient domain size, but also to assess representative length scales of turbulent structures.

It can be clearly seen that the streamwise domain is more than sufficient for all turbulent structures to be decorrelated for both cases. Encouragingly, the two-point autocorrelations once again demonstrate the presence of coherent streamwise streaks. The streamwise representative length scale of the streamwise velocity coherent structures (λ_x^u, the distance at which $R_{uu} = 0.5$) is again observed to decrease with increasing wall normal distance as observed by Smits et al. (1989), but still in contradiction with the observations of Ganapathisubramani et al. (2006). For case 1, λ_x^u has values of 0.8δ, 0.5δ and 0.45δ at $z^+ = 5$, $z/\delta = 0.5$ and 0.8 respectively and $\lambda_x^u = 0.75\delta$, 0.5δ and 0.4δ for case 2.

The other, and possibly most important, homogeneous direction, where decorrelation of the turbulent structures must be observed is the spanwise direction. For both cases we see that the velocity fluctuations are decorrelated within half of the spanwise domain size ($\frac{1}{2}L_y$), ensuring that turbulent structures are completely captured. The spanwise length scale of the streamwise velocity (λ_y^u), as observed in Section 4.1.5, also demonstrates increasing magnitude with increasing wall normal distance. The length scales observed for case 1 are $\lambda_y^u = 0.06\delta$, 0.18δ and 0.2δ at $z^+ = 5$, $z/\delta = 0.5$ and 0.8 respectively and $\lambda_y^u = 0.05\delta$, 0.19δ and 0.21δ for case 2.

5.2.3 Energy Spectra

The outcome of the grid resolution study identified grid C as being sufficiently accurate. The adequacy of grid resolution of grid C is checked further by calculation of the one dimensional energy spectrum of the velocity fluctuations (equations 4.22 and 4.23). In lieu of results from DNS calculations, with or without spectral methods, we again examine the calculated spectra for a 3-4 order of magnitude decrease in energy content from the lowest to highest resolved wave numbers. The normalized energy spectra ($E_q(k,z)/E_q(0,z)$) are shown in figure 5.2-27 for cases 1 and 2. Again, the spectrum is computed in the homogeneous streamwise and spanwise directions at three wall normal locations.

From the presented figures it can be concluded that the numerical resolution is adequate. For all locations and directions we observe a minimum of approximately 3 orders of magnitude decay in energy content. Near the wall in the spanwise direction for case 1 there is a persistence in energy content for the wall normal velocity fluctuations observed, while the two other velocity components decay. It is suggested that this is a result of the low order numerical scheme used for the LES results. In the spanwise direction for case 2 we see some aliasing/buildup of energy at the

high wave numbers due to truncation errors of the generally second order numerical schemes used. For the other locations and directions examined there is less of a build up in energy at high wave numbers due to the coarse LES grid, but no increase in energy content is observed, suggesting aliasing effects are minimal. This excess energy at the high wave numbers may alternatively be caused by insufficient energy dissipation being provided by the subgrid-scale model.

5.2.4 Strong Reynolds Analogy

The Strong Reynolds Analogy (SRA) was derived from the relationships betwen velocity and temperature fluctuations within boundary layers on adiabatic flat plates. As observed by Smits and Dussauge (2006), experimental investigations of the SRA for heated or cooled boundary layers are rare. To extend the analysis of the similarities between momentum and heat transfer within a boundary layer under strongly cooled conditions we examine the turbulent Prandtl number (Eq 4.38) and the validity of the Strong Reynolds Analogy equation (Eq 4.37).

The transport of momentum is mainly governed by the total shear stress. Near the wall, the molecular viscous transport of momentum dominates the total shear stress, however, for $z \gtrsim 0.1\delta$ the turbulent fluctuations and, hence, the Reynolds shear stress becomes the dominant component (figures 5.2-21 and 5.2-22). Consequently, we can expect for these regions ($z \gtrsim 0.1\delta$) that the turbulent Prandtl number is a good indicator of the relative contributions to turbulent momentum and heat transfer. In the DNS of supersonic turbulent channel flow between very cold isothermal walls, Huang et al. (1995) computed and presented the turbulent Prandtl number. Figures 5.2-28(a) and 5.2-28(b) present the computed turbulent Prandtl numbers for cases 1 and 2 respectively, along with a reproduction of the adiabatic wall LES of Stolz and Adams (2003) and the cold wall DNS of Huang et al. (1995) and Maeder (2000) . Even amongst the referenced numerical data, there is some scattering of results and fairly unsteady profiles. It remains encouraging, however, that the computed turbulent Prandtl numbers of cases 1 and 2 remain in good agreement with the referenced data across the boundary layer. From these results, even under strongly cooled conditions it appears as though the turbulent Prandtl number is not significantly affected by large heat transfer, demonstrating that the results are consistent with Morkovin's hypothesis.

Given the strongly cooled wall conditions, it is no longer expected that the SRA, in the form presented in equation 4.37, will hold. Figures 5.2-28(c) and 5.2-28(d) confirm its inability to hold under non-adiabatic conditions. Instead, the modifications presented by Huang et al. (1995) yield

better agreement with the aforementioned DNS and experimental data of Guarini et al. (2000), when we take into account the significant heat transfer across the boundary layer. This observation is consistent with the additional cold wall DNS results of Maeder (2000).

5.2.5 Reynolds Analogy Factor

The Reynolds analogy factor, discussed previously in section 5.1, is formally defined as:

$$s = \frac{2\,C_h}{C_f} = \frac{1}{Pr_m} \tag{5.1}$$

The Stanton number (C_h), or heat transfer coefficient, is proportional to the temperature difference between the adiabatic wall temperature, or thermal driving force, and the wall temperature as given in equation (1.3).

We can define the turbulent eddy viscosity μ_t and eddy diffusivity k_t as:

$$\mu_t = \frac{-\overline{\rho}\widetilde{u'w'}}{\partial\widetilde{u}/\partial z} \tag{5.2}$$

and

$$k_t = \frac{-C_p\overline{\rho}\widetilde{w'T'}}{\partial\widetilde{T}/\partial z} \tag{5.3}$$

From these quantities the turbulent Prandtl number (defined earlier in equation (4.38)) can be constructed:

$$Pr_t = \frac{\mu_t C_p}{k_t} \tag{5.4}$$

and finally a mixed Prandtl number is defined:

$$Pr_m = \frac{(\mu + \mu_t)C_p}{k + k_t} \tag{5.5}$$

When considering the behaviour at the wall, the turbulent contributions of equations (5.2) and (5.3) to the mixed Prandtl number is zero because of the decay in turbulent fluctuations. Hence, immediately near the wall we can treat the mixed Prandtl number as its molecular value. The molecular Prandtl number is conventionally assumed to be 0.72 and constant across the boundary layer because of its insensitivity to temperature. This suggests that the Reynolds analogy factor for an equilibrium turbulent boundary layer is ~ 1.39.

The Reynolds analogy factor was observed experimentally by Suraweera (2006) to deviate from equilibrium and approach a value of 0.5 and below. These results were, however, confined to skin friction values that were large ($c_f > 3\times10^{-3}$). For the experiment, the large values of skin friction correspond to measurement stations immediately downstream of the backwards facing step created by the hydrogen injection slot. The sudden change in conditions caused by this step requires a finite downstream distance before the boundary layer can again relax to equilibrium. The deviation of a boundary layer from equilibrium, and its associated relaxation back to equilibrium, was studied experimentally by Debieve et al. (1997). A Mach 2.3, fully developed turbulent boundary layer was perturbed by a step increase in wall temperature. The influence of the increase in wall temperature was observed primarily through a departure from equilibrium in the temperature profile, that persisted over 50 boundary layer thicknesses downstream. This corresponded to the final measurement station, so the effects may have persisted longer. Corresponding to the change in wall temperature was a decrease in the skin friction and heat transfer coefficients, demonstrating similarity in behaviour to the flow studied by Suraweera (2006) with the Reynolds analogy factor moving strongly away from equilibrium. The relaxation rate of the Reynolds analogy factor towards equilibrium was slow and decreased with downstream distance. It was postulated that this process could take over 100 initial boundary layer thicknesses before equilibrium is obtained again, if at all. Hence, there is experimental evidence of the Reynolds analogy factor deviating from equilibrium values when step changes in wall conditions are applied to a developed boundary layer.

With the relaxation process to equilibrium being slow, in the case of a backwards facing step geometry of Suraweera (2006), equilibrium may not be obtained until well after any mean reattachment point and once the skin friction coefficient has decayed from its upstream level. The numerical simulations presented here only include a turbulent boundary layer that is close to equilibrium over the entire domain. Consequently, no deviation in Reynolds analogy factor from equilibrium is observed for the simulations presented here (see figure 5.2-29).

5.2.6 Quadrant and Octant Analysis

To establish a baseline behaviour for the dominant transport mechanisms found in strongly cooled supersonic boundary layer flow, the turbulent Reynolds shear stress is divided once again into four quadrants (Section 4.1.7). Plotted as absolute contributions, we again see, as was identified in the results presented in section 4.1.7, that sweeps (quadrant IV) and ejections (quadrant II) remain the

dominant mechanisms contributing to the Reynolds shear stress (figures 5.2-30(a) and 5.2-30(d)). These mechanisms correspond physically to high momentum fluid from the bulk flow entering the lower momentum regions of the boundary layer and the corresponding flow of low momentum fluid ejecting upwards from the near wall region respectively and produce the dominant negative contribution to the Reynolds shear stress. The probability profiles of each mechanism is given in figures 5.2-30(b) and 5.2-30(e). Their high probability suggests that the dominant sweep and ejection mechanisms are in reality a large number of events of relatively small magnitude, as opposed to being infrequent and possessing a larger magnitude.

The viscous transport of momentum can also be decomposed into contributing quadrants. Figures 5.2-30(c) and 5.2-30(f) show that it is the sweep (quadrant IV) events that make the dominant contribution in the near wall. These sweeps bring the high momentum fluid from the mainstream flow towards the wall and, hence, would be expected to make up the bulk of the viscous momentum transfer through the generation of larger velocity gradients. As the wall normal distance increases, the ejection (quadrant II) events begin to make significant contributions to the viscous transport of momentum through an increase in the velocity gradient in the regions away from the wall. This is most notable for case 1 and would be expected as, in this region, ejections (quadrant II) are observed to also dominate the turbulent Reynolds shear stress.

Octant analysis of both the turbulent Reynolds shear stress and turbulent wall normal heat flux is presented in figure 5.2-31. Hot and cold sweeps (octants VIII and IV respectively) and ejections (octants VI and II respectively) are observed to be the largest contributors to both the shear stress and heat flux terms, serving as further indication of the validity of the Strong Reynolds Analogy under these conditions. Considering the octant decomposition of the Reynolds shear stress, the cold sweeps and ejections provide the dominants contributions beneath the region of peak viscous heating ($z^+ \approx 200$). This behaviour suggests that the majority of the turbulent transport of momentum in this region remains tied to the cooler and denser fluid elements. Within and above the region of peak viscous heating, the hot sweeps and ejections clearly dominate. For the turbulent heat flux octants there is slightly different behaviour. Near the wall, the hot sweeps and cold ejections are the dominant contributors and act to increase the turbulent heat flux to the wall. Physically, the hot sweep events transport high energy fluid from the region of peak viscous heating and the freestream regions, where the momentum is high, down towards the wall region. Counteracting this process is the ejection of lower energy and momentum fluid elements from the near wall region up into the higher boundary layer regions. As you move further through the boundary layer, the thermal conditions change and the dominant octants switch from the cold to

hot processes and vice-versa.

There is a counter-intuitive process occurring within the boundary layer for case 2 for the turbulent heat flux. The increasing prevalence of hot outward interaction (octant V) events in the near wall region suggests that there is transport of high momentum and energy fluid elements away from the wall from regions, that one would expect to be dominated by low momentum and energy fluid elements. Its dominance can be attributed to the large transport of high momentum and energy fluid towards the wall through hot sweeps (octant VIII), with some fluid reflecting off the wall before the sweep can diffuse with the nearby fluid.

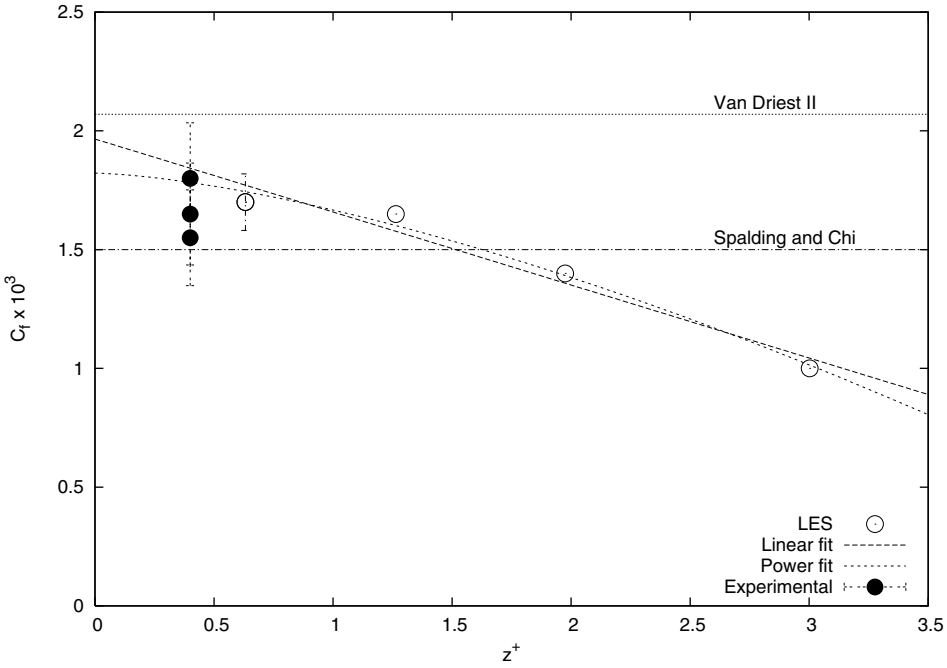

Figure 5.2-1: Convergence of skin friction coefficient with grid refinement - Case 1.

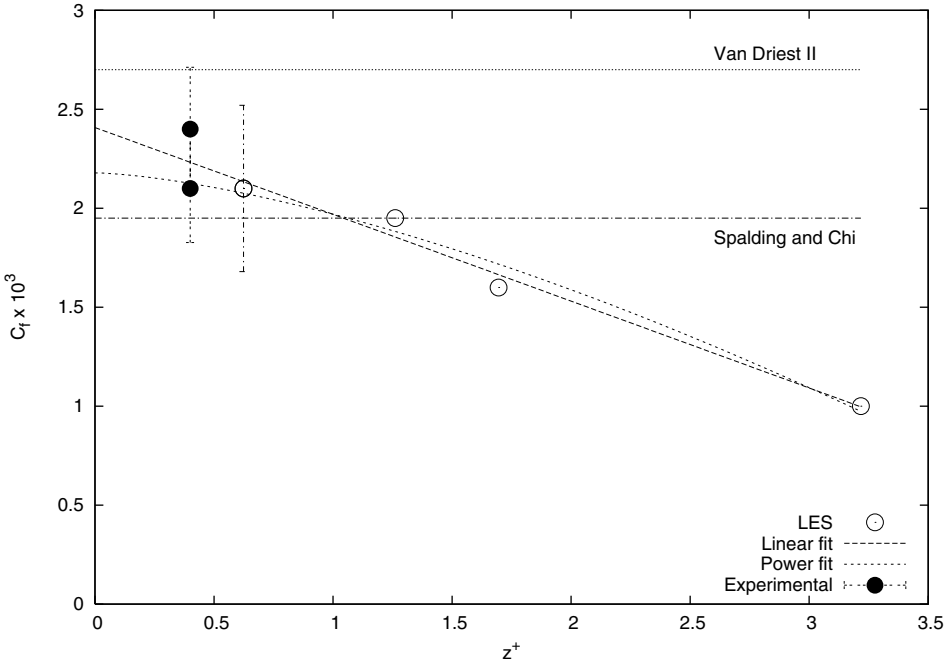

Figure 5.2-2: Convergence of skin friction coefficient with grid refinement - Case 2.

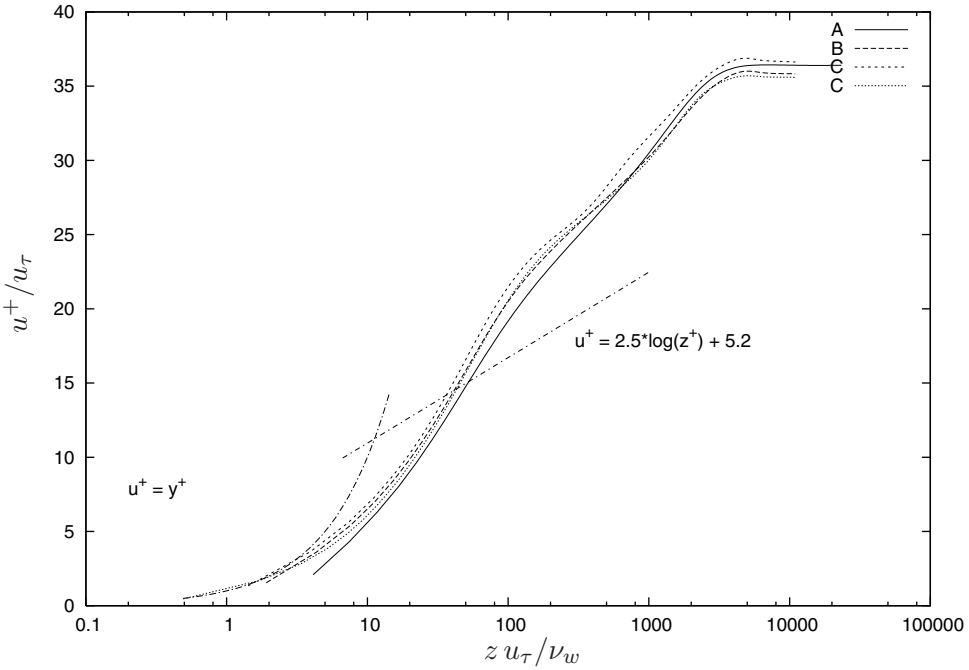

Figure 5.2-3: Effect of grid resolution on transformed mean streamwise velocity profile - Case 1.

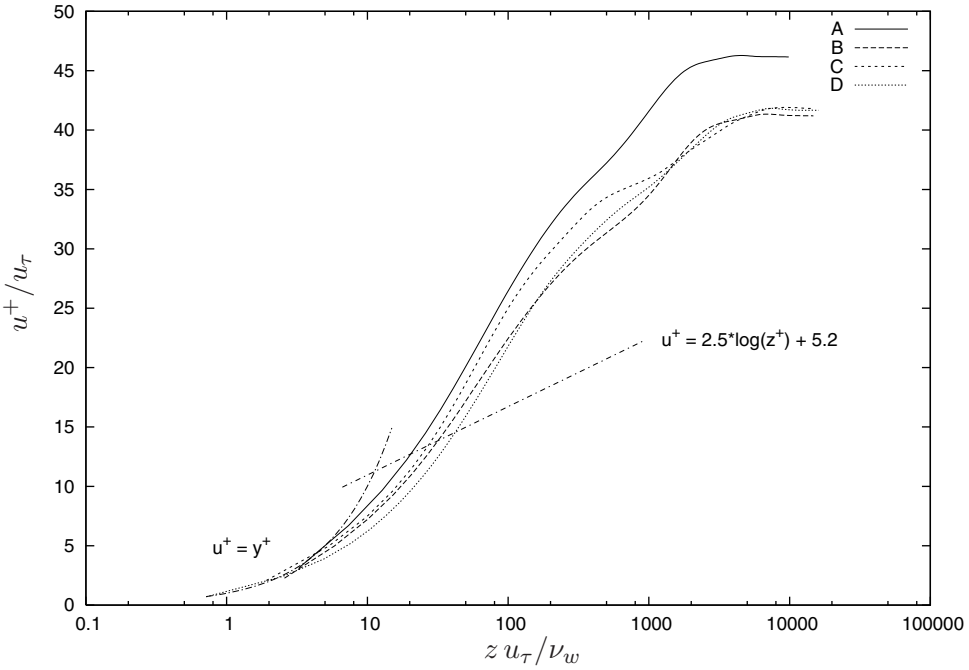

Figure 5.2-4: Effect of grid resolution on transformed mean streamwise velocity profile - Case 2.

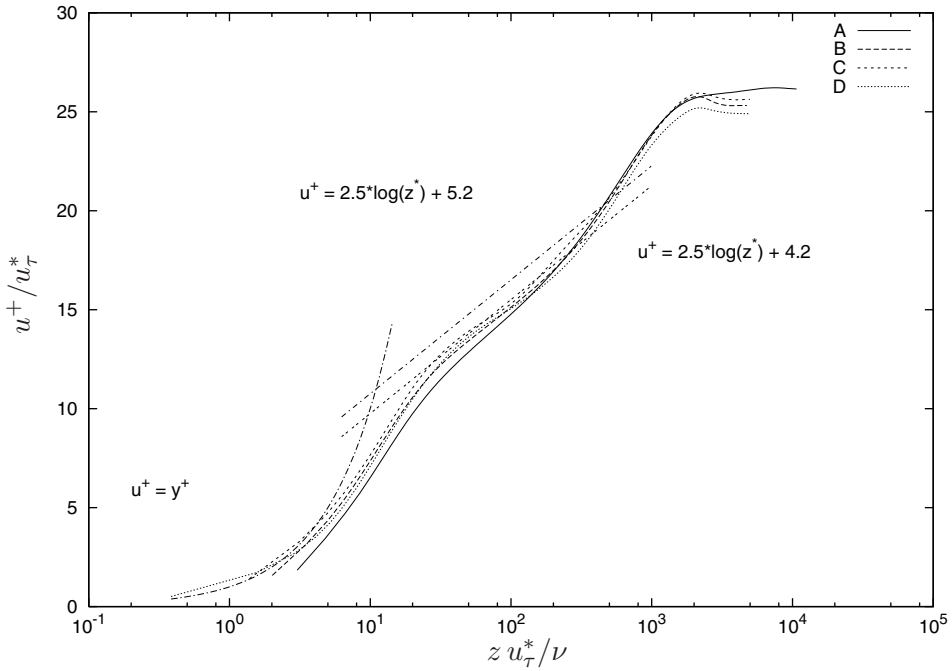

Figure 5.2-5: Effect of grid resolution on semi-local transformed mean streamwise velocity profile - Case 1.

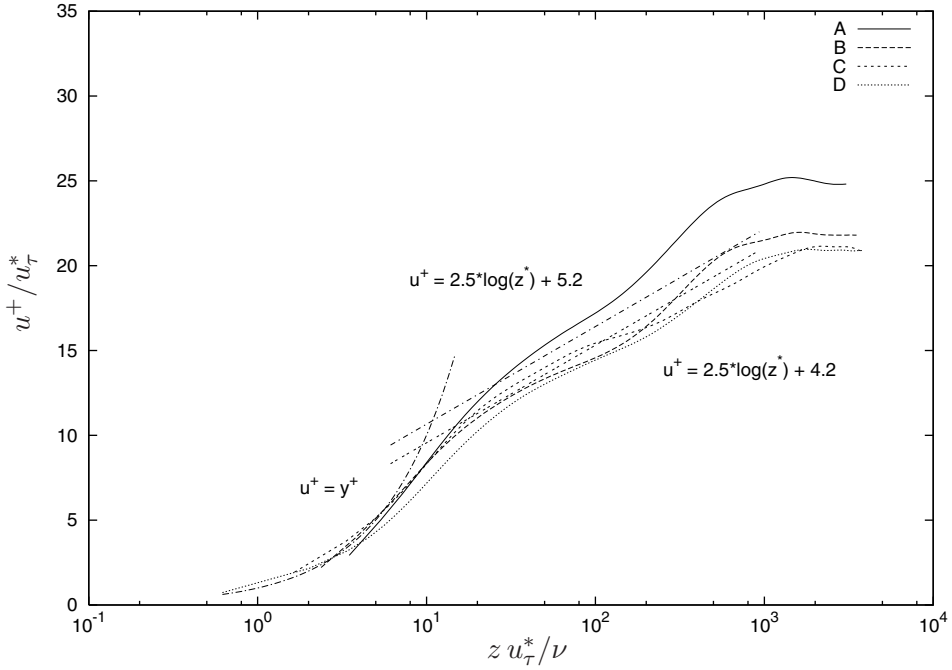

Figure 5.2-6: Effect of grid resolution on semi-local transformed mean streamwise velocity profile - Case 2.

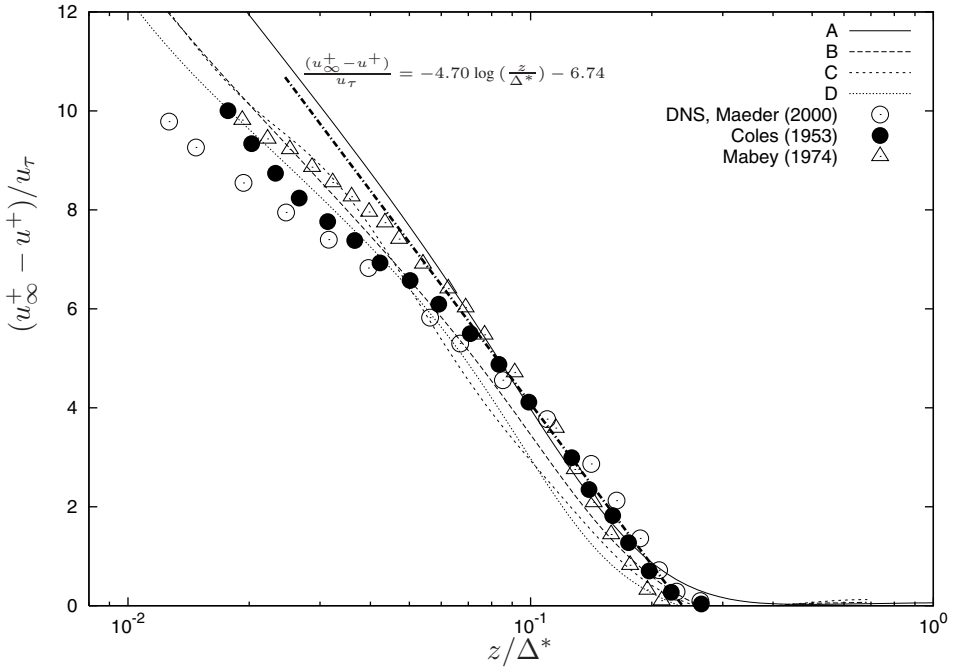

Figure 5.2-7: Effect of grid resolution on transformed mean streamwise velocity defect profile - Case 1.

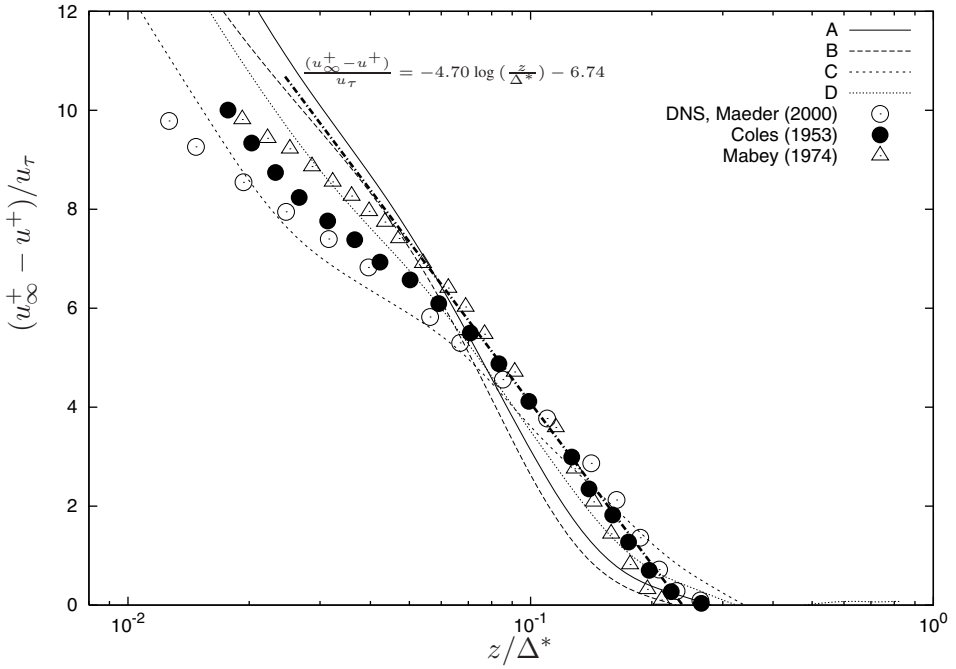

Figure 5.2-8: Effect of grid resolution on transformed mean streamwise velocity defect profile - Case 2.

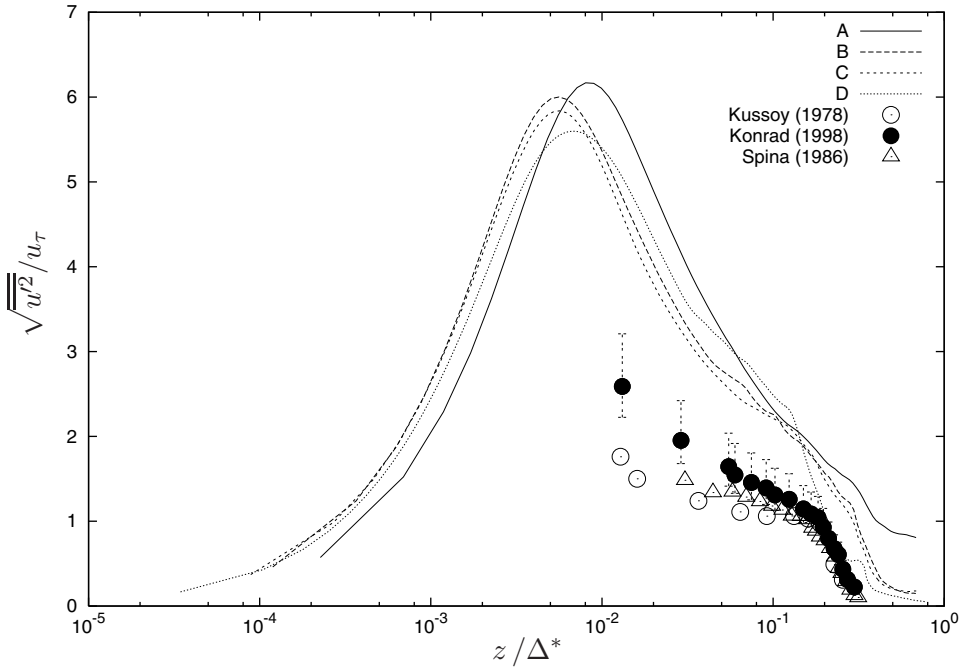

Figure 5.2-9: Effect of grid resolution on RMS of streamwise velocity fluctuations from the approximate deconvolution model normalized by friction velocity and velocity defect thickness with comparison to experimental data - Case 1.

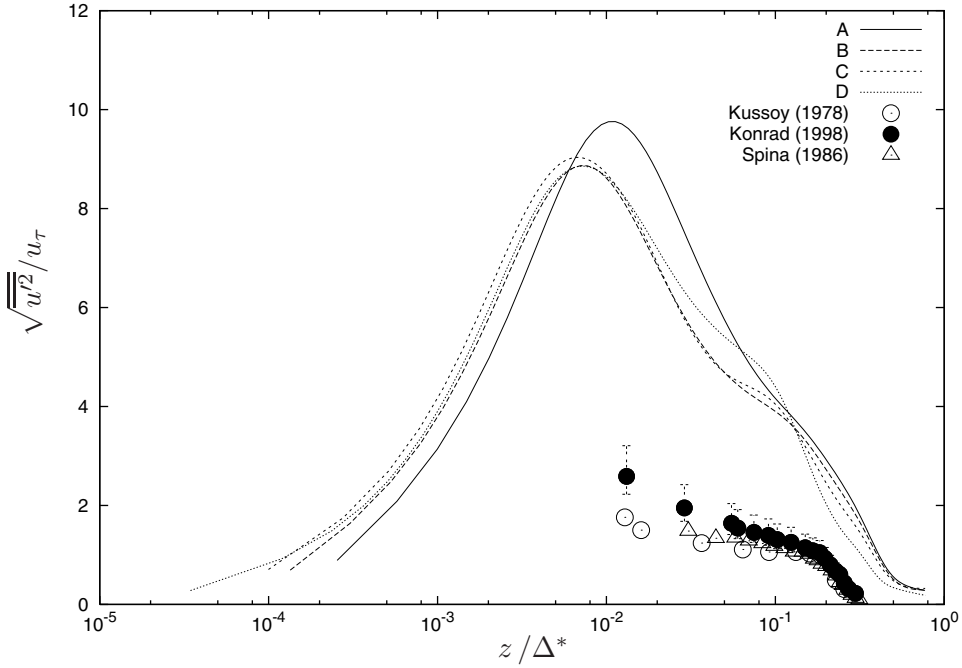

Figure 5.2-10: Effect of grid resolution on RMS of streamwise velocity fluctuations from the approximate deconvolution model normalized by friction velocity and velocity defect thickness with comparison to experimental data - Case 2.

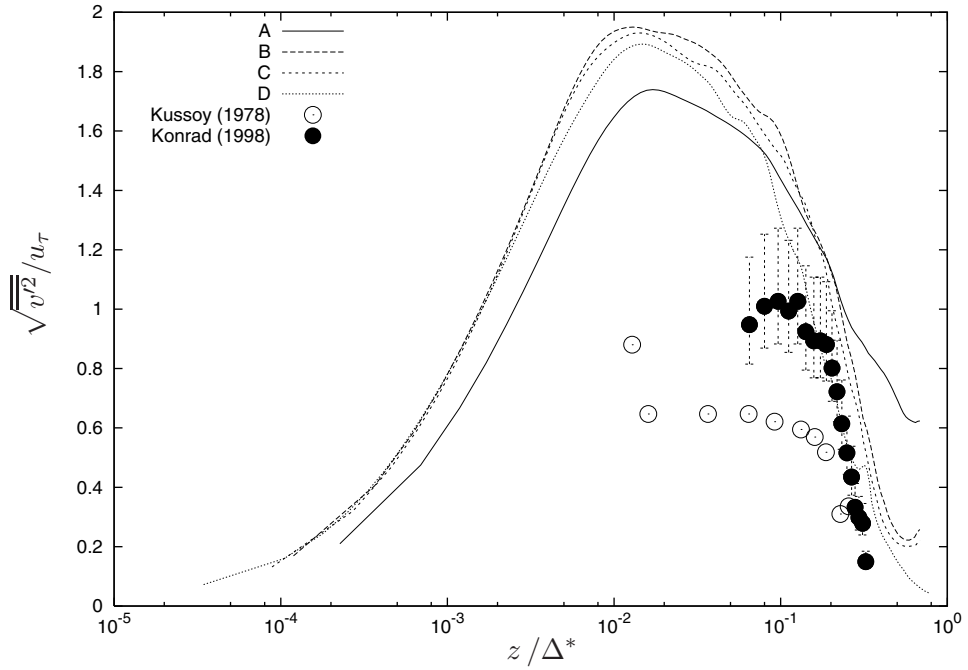

Figure 5.2-11: Effect of grid resolution on RMS of resolved spanwise velocity fluctuations from the approximate deconvolution model normalized by friction velocity and velocity defect thickness with comparison to experimental data - Case 1.

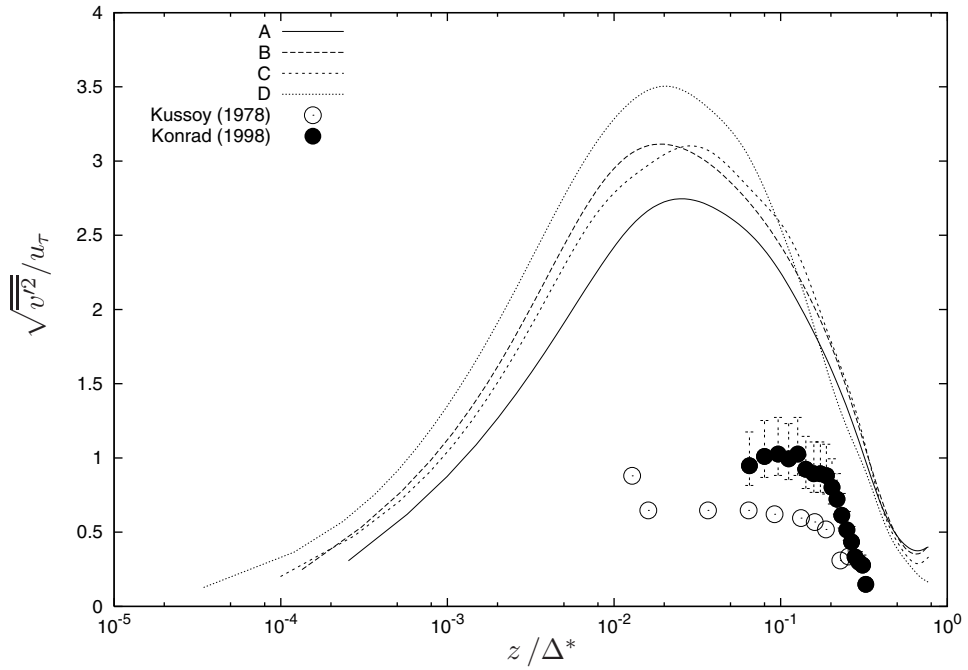

Figure 5.2-12: Effect of grid resolution on RMS of resolved spanwise velocity fluctuations from the approximate deconvolution model normalized by friction velocity and velocity defect thickness with comparison to experimental data - Case 2.

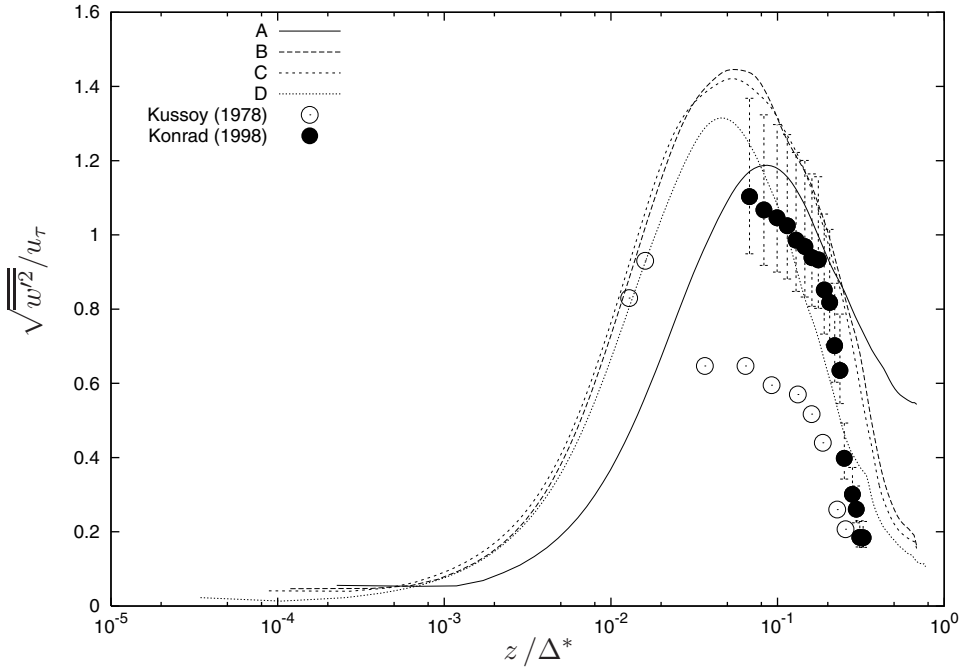

Figure 5.2-13: Effect of grid resolution on RMS of resolved wall normal velocity fluctuations from the approximate deconvolution model normalized by friction velocity and velocity defect thickness with comparison to experimental data - Case 1.

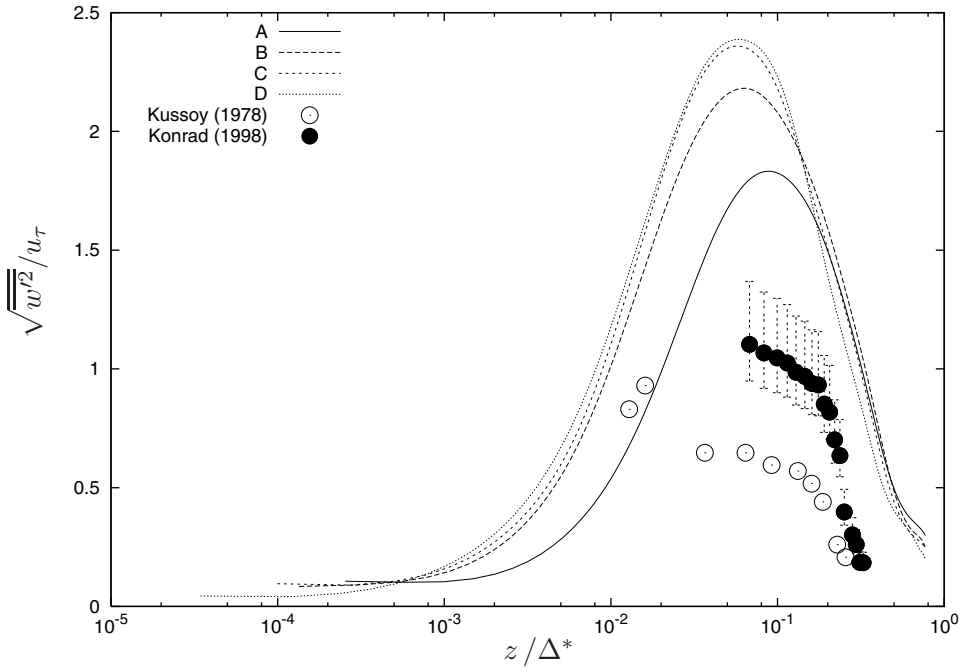

Figure 5.2-14: Effect of grid resolution on RMS of resolved wall normal velocity fluctuations from the approximate deconvolution model normalized by friction velocity and velocity defect thickness with comparison to experimental data - Case 2.

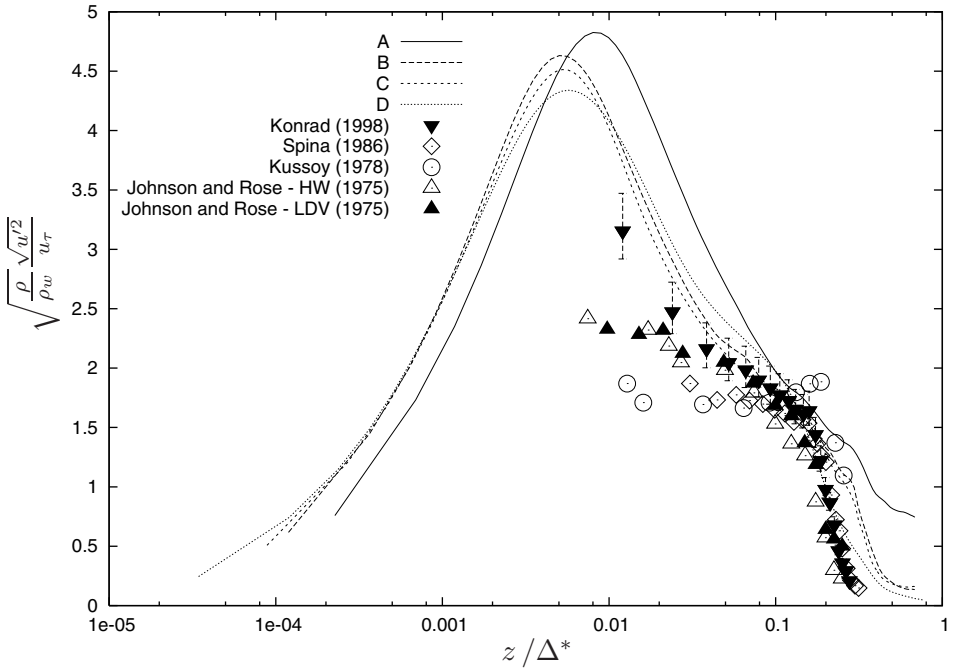

Figure 5.2-15: Effect of grid resolution on streamwise Reynolds normal stress from the approximate deconvolution model normalized by wall conditions and velocity defect thickness with comparison to experimental data - Case 1.

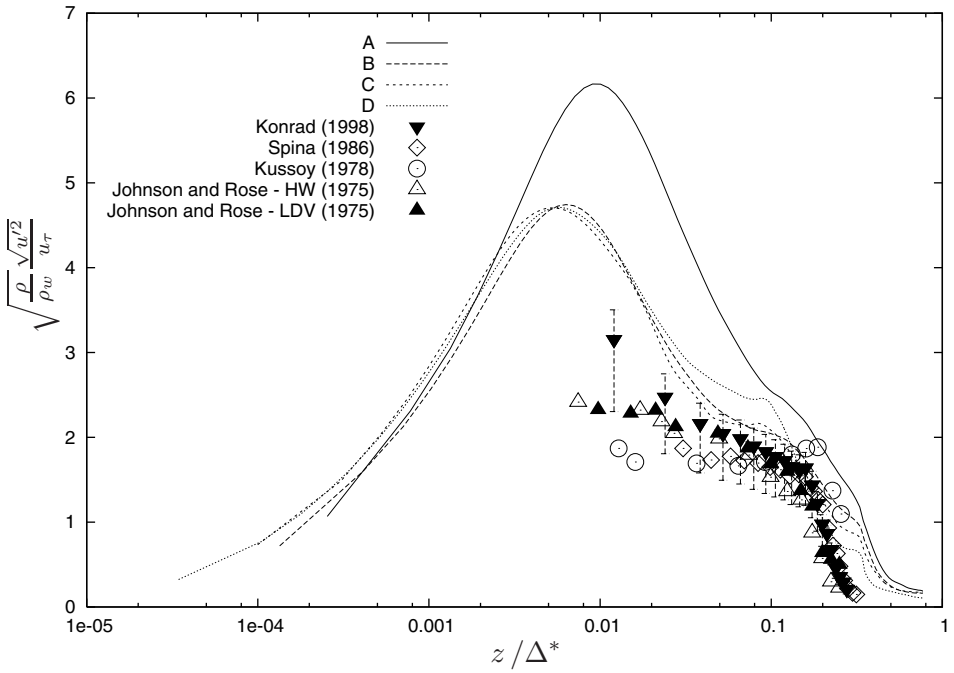

Figure 5.2-16: Effect of grid resolution on streamwise Reynolds normal stress from the approximate deconvolution model normalized by wall conditions and velocity defect thickness with comparison to experimental data - Case 2.

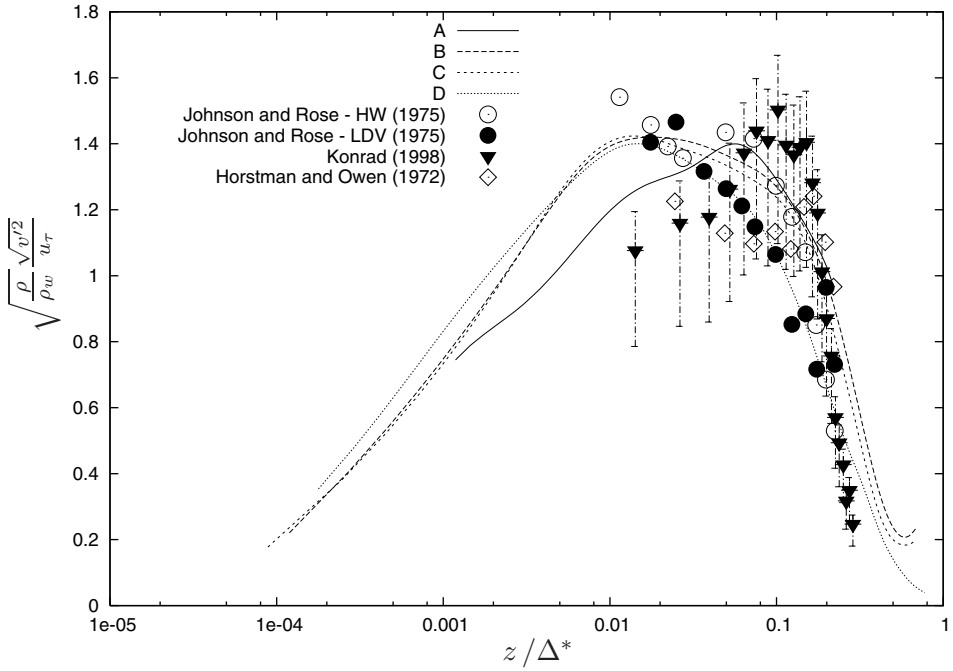

Figure 5.2-17: Effect of grid resolution on spanwise Reynolds normal stress from the approximate deconvolution model normalized by wall conditions and velocity defect thickness with comparison to experimental data - Case 1.

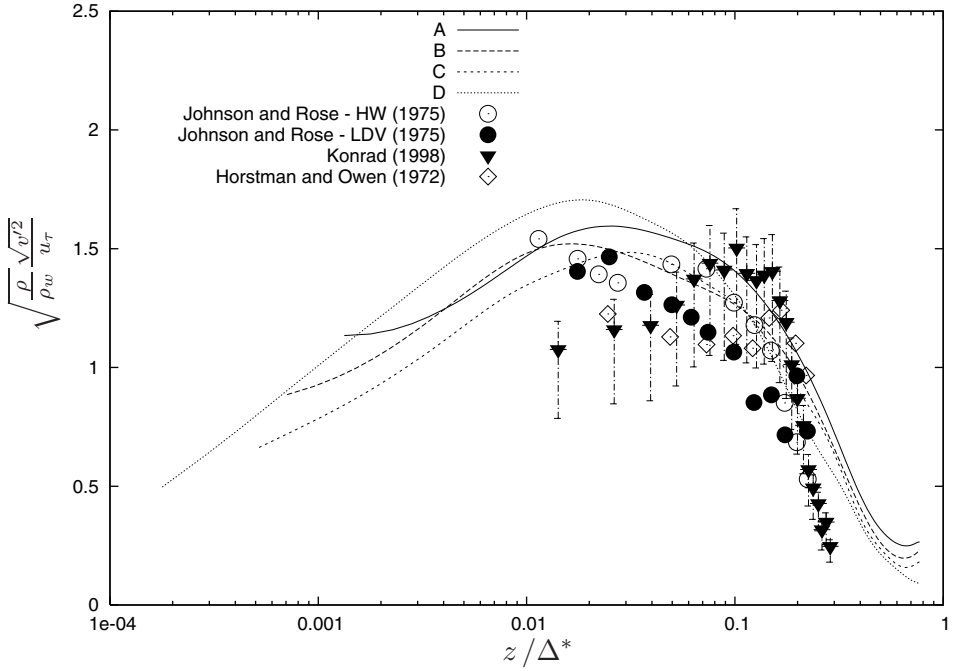

Figure 5.2-18: Effect of grid resolution on spanwise Reynolds normal stress from the approximate deconvolution model normalized by wall conditions and velocity defect thickness with comparison to experimental data - Case 2.

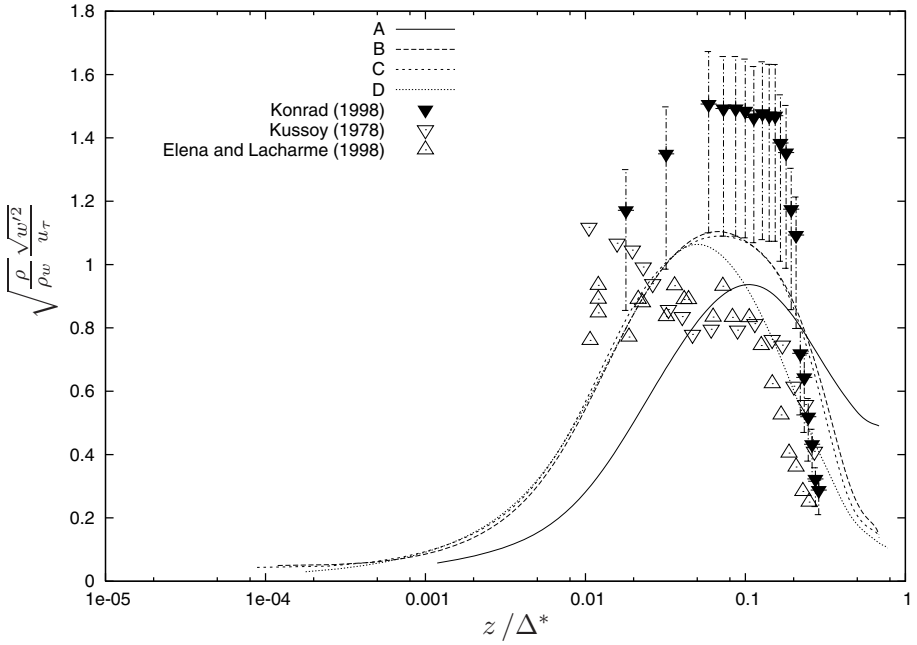

Figure 5.2-19: Effect of grid resolution on wall normal Reynolds shear stress from the approximate deconvolution model normalized by wall conditions and velocity defect thickness with comparison to experimental data - Case 1.

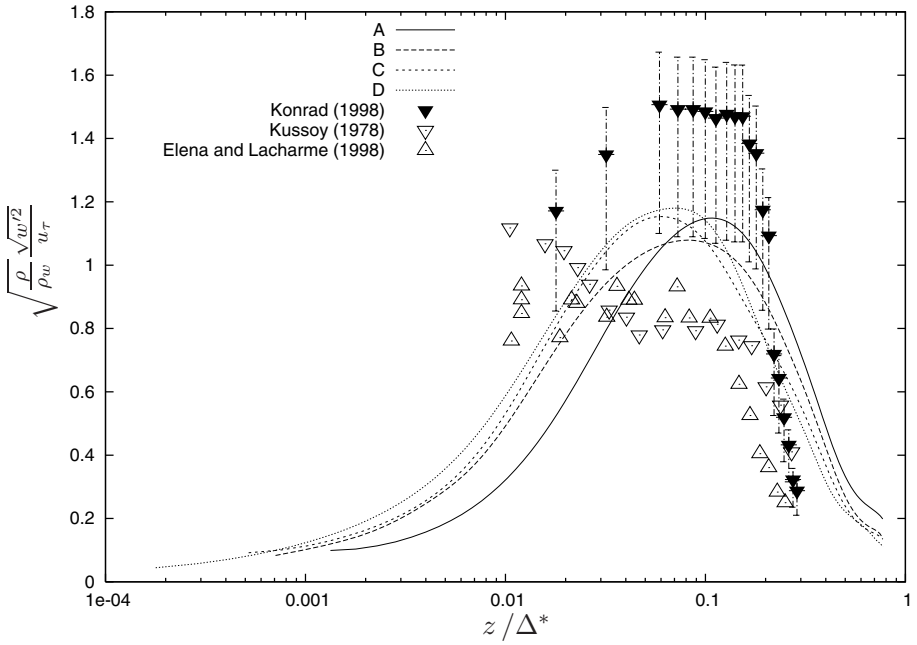

Figure 5.2-20: Effect of grid resolution on wall normal Reynolds shear stress from the approximate deconvolution model normalized by wall conditions and velocity defect thickness with comparison to experimental data - Case 2.

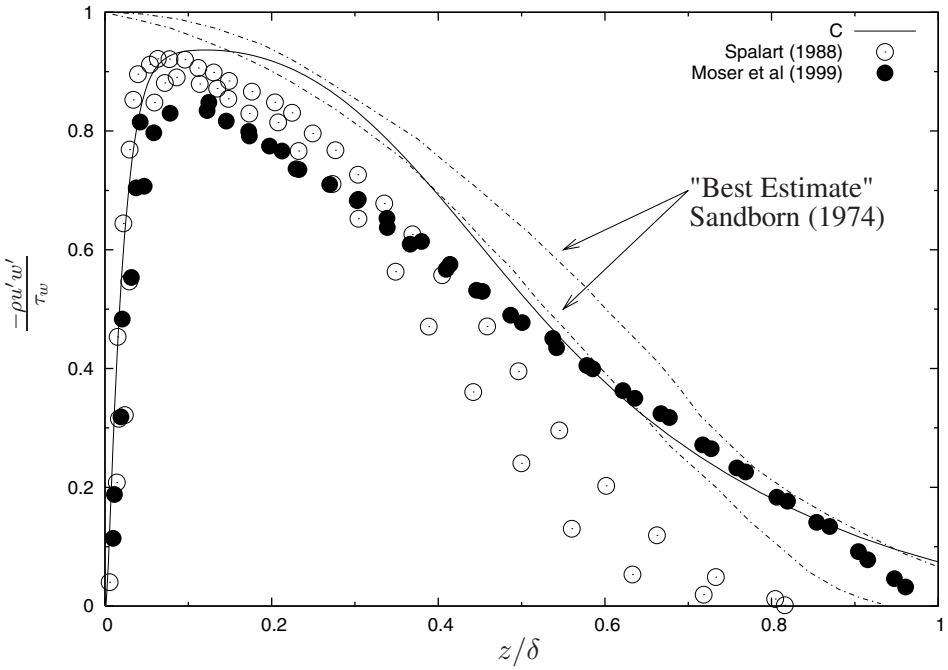

Figure 5.2-21: Reynolds shear stress from the approximate deconvolution model on grid C, normalized by wall shear and compared to best estimate of Sandborn (1974) - Case 1.

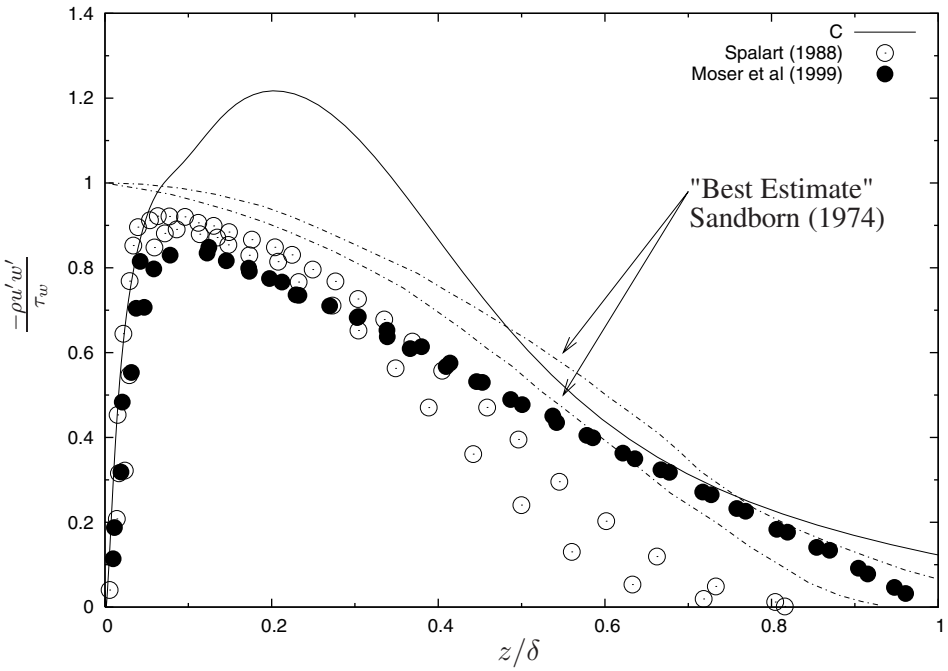

Figure 5.2-22: Reynolds shear stress from the approximate deconvolution model on grid C, normalized by wall shear and compared to best estimate of Sandborn (1974) - Case 2.

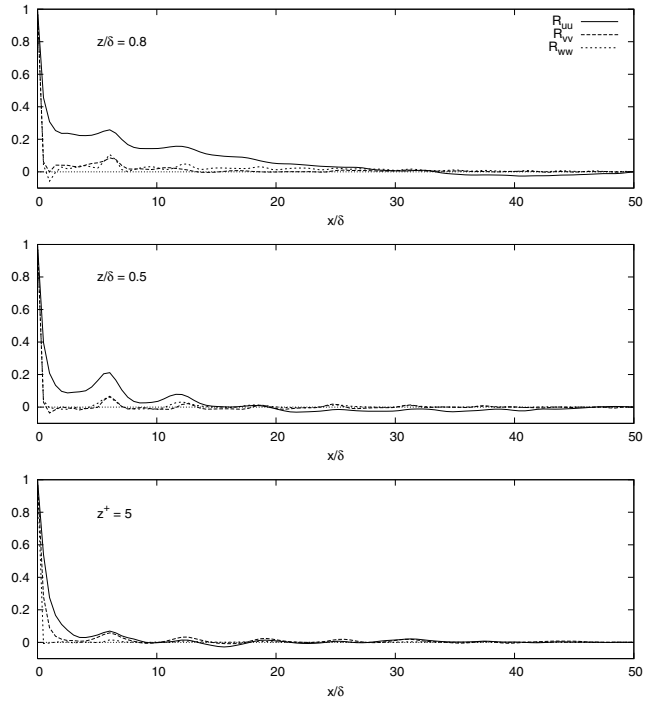

Figure 5.2-23: Streamwise two-point autocorrelation - approximate deconvolution model, grid C - Case 1

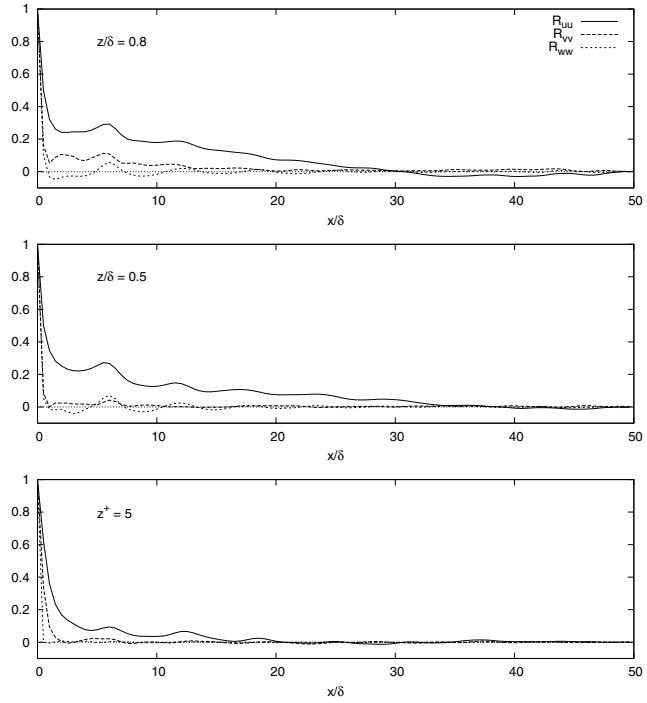

Figure 5.2-24: Streamwise two-point autocorrelation - approximate deconvolution model, grid C - Case 2

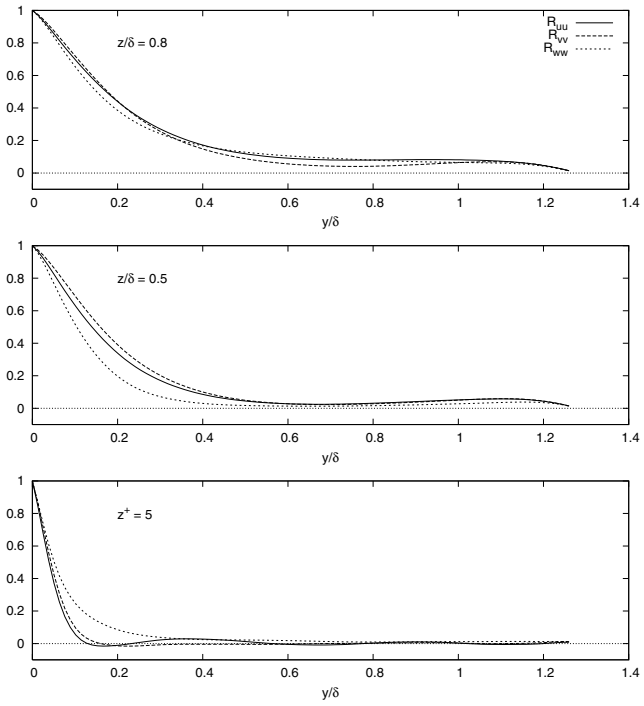

Figure 5.2-25: Spanwise two-point autocorrelation - approximate deconvolution model, grid C - Case 1

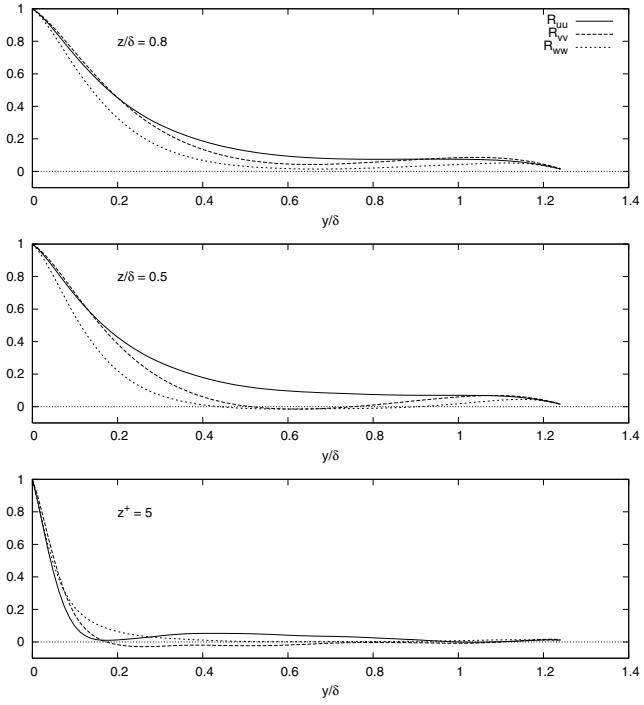

Figure 5.2-26: Spanwise two-point autocorrelation - approximate deconvolution model, grid C - Case 2

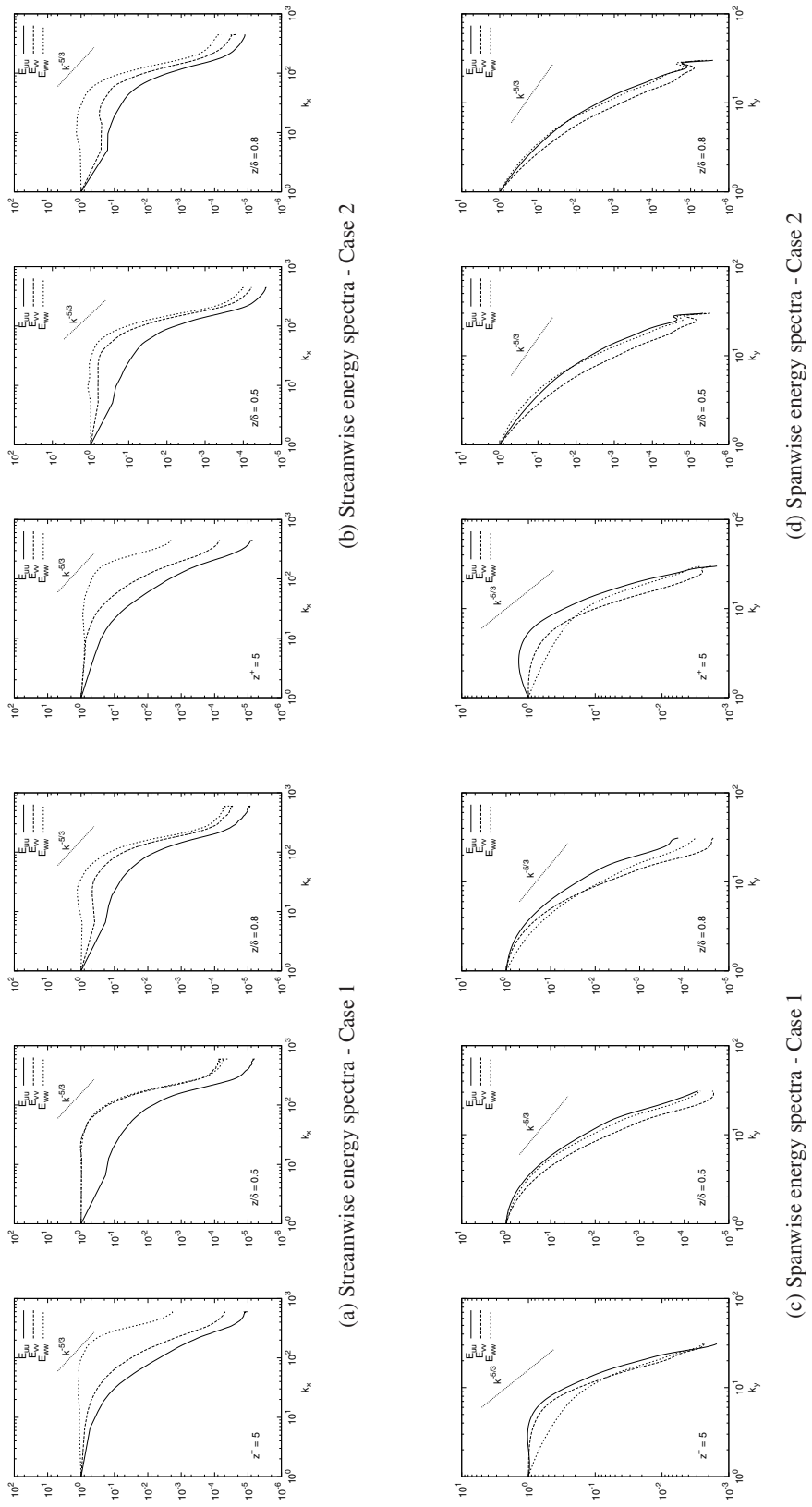

Figure 5.2-27: Approximate deconvolution model turbulent energy spectrum for grid C

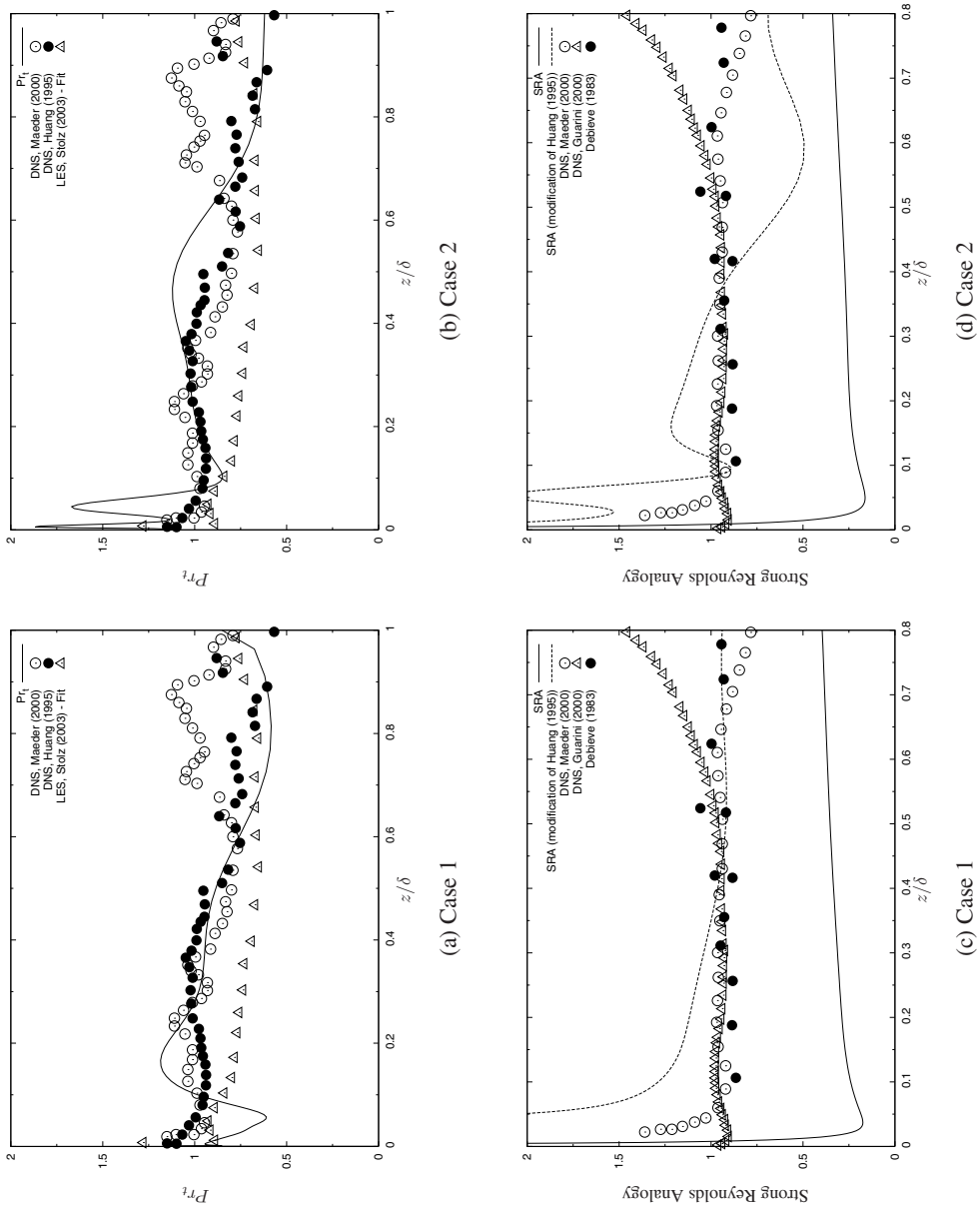

Figure 5.2-28: (a) and (b) Turbulent Prandtl number, (c) and (d) Strong Reynolds Analogy, grid C

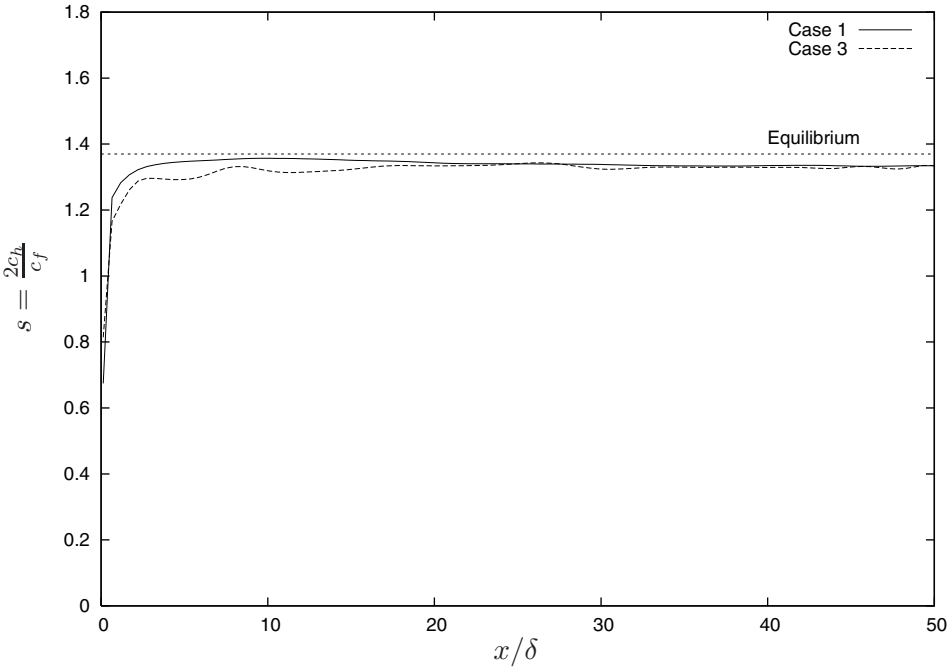

Figure 5.2-29: Reynolds analogy factor, grid C - Cases 1 & 2

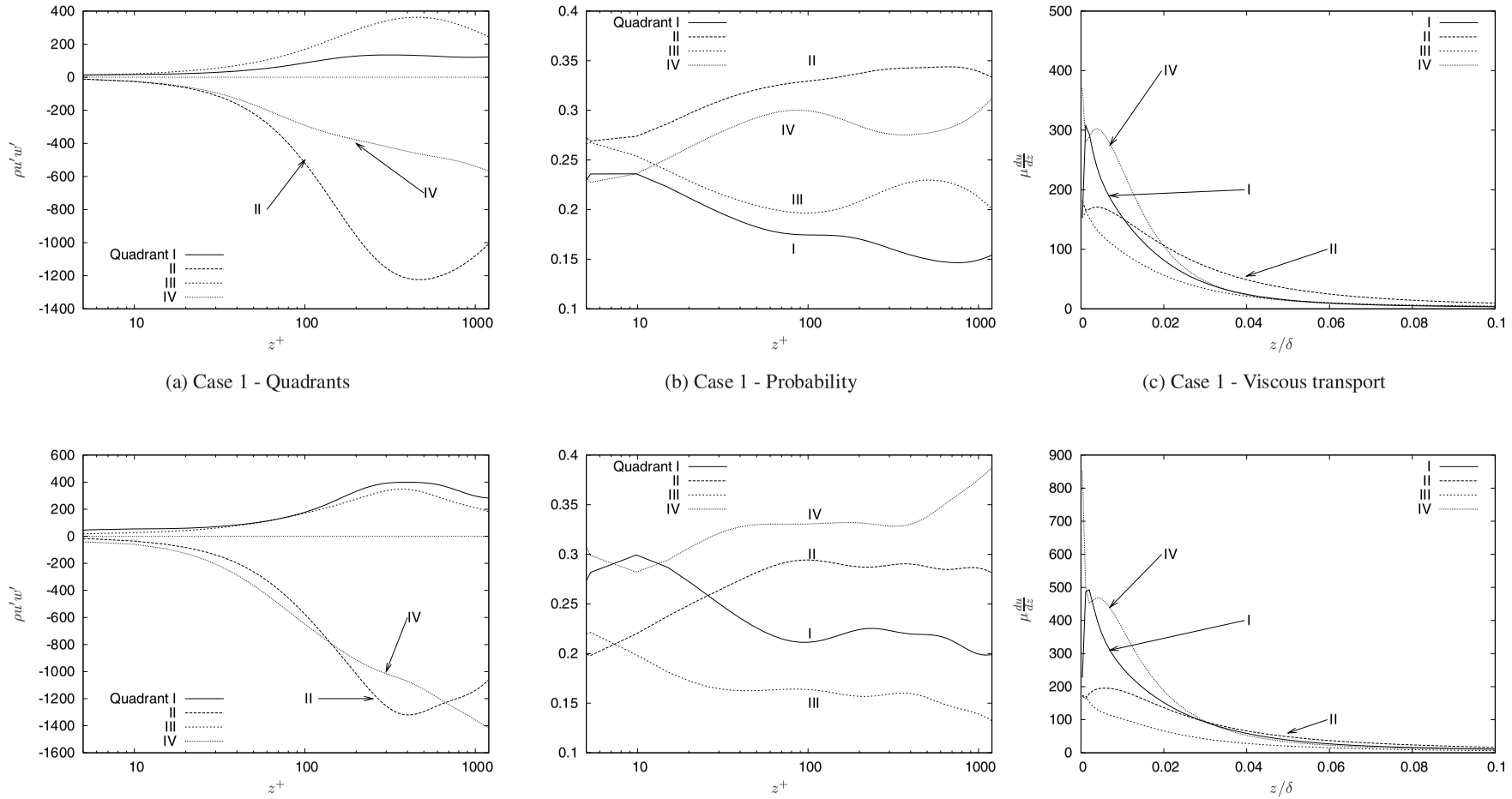

(a) Case 1 - Quadrants

(b) Case 1 - Probability

(c) Case 1 - Viscous transport

(d) Case 2 - Quadrants

(e) Case 2 - Probability

(f) Case 2 - Viscous transport

Figure 5.2-30: Classification of turbulent Reynolds shear stress and viscous transport into quadrants and probability of each mechanism occurring in a quadrant: Quadrant I, outward interaction; quadrant II, ejection; quadrant III, wallward interaction; quadrant IV, sweep.

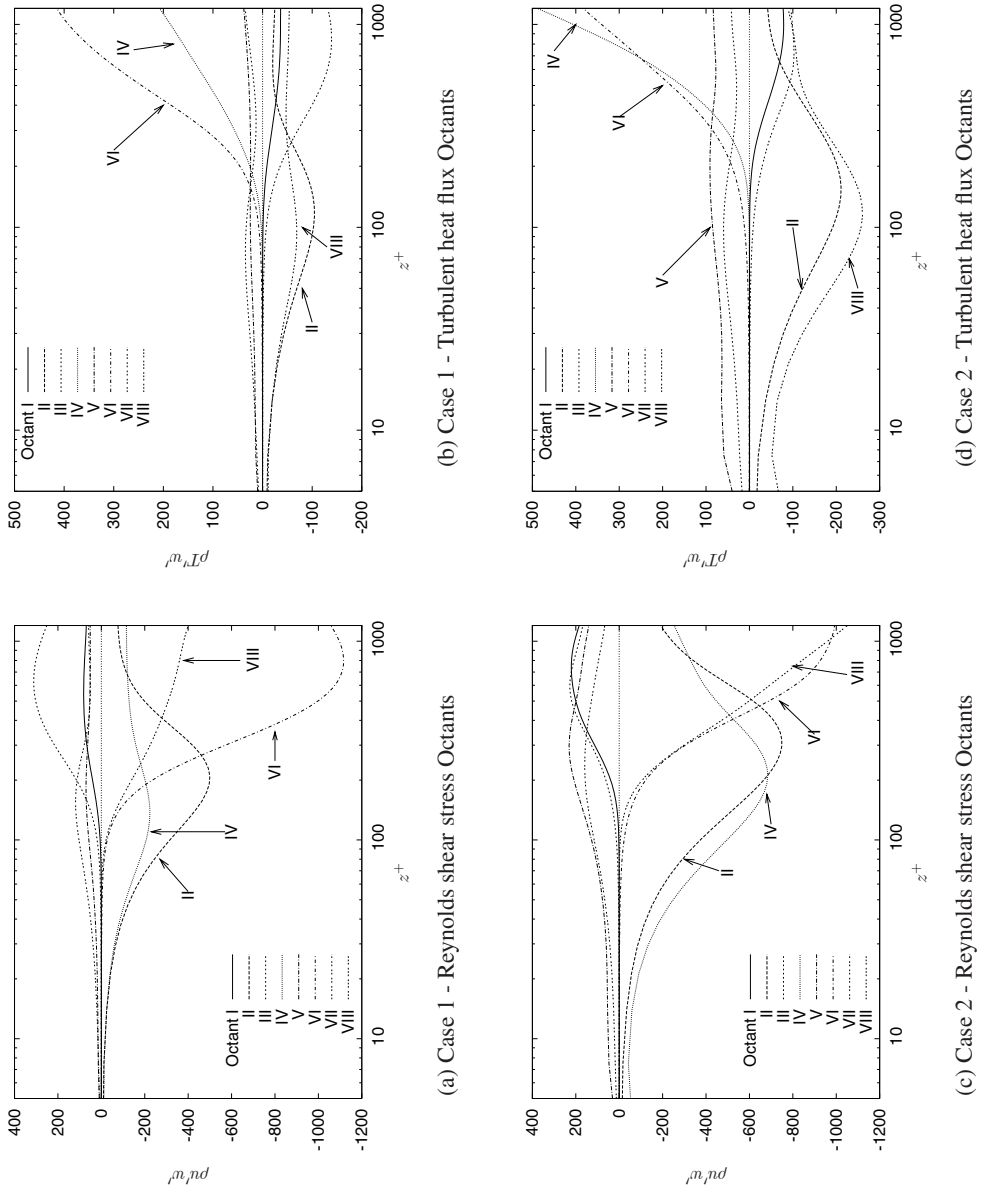

Figure 5.2-31: Classification of Reynolds shear stress and turbulent heat flux into octants: Octant I, cold outward interaction; octant II, cold ejection; octant III, cold wallward interaction; octant IV, cold sweep; octant V, hot outward interaction; octant VI, hot ejection; octant VII, hot wallward interaction; octant VIII, hot sweep.

5.3 Heat Addition

The following sections present the results of heat addition to the supersonic boundary layers. The combustion process is first mimicked through the inclusion of a heat source term and then more accurately modelled with finite rate chemical kinetics of hydrogen combustion. The reduction in wall shear is first identified for both cases 1 and 2, verifying that the numerical scheme is capturing the important physical behaviour. The resulting changes in mean flow properties and mechanisms of turbulent momentum and heat transport are then quantified and analysed in detail to gain a comprehensive description of the turbulent processes that are affected. Figures for this section appear together, starting on page 211.

5.3.1 Modelling Assumptions

Due to the large computational cost of LES at high enthalpy conditions in the presence of cold walls, some assumptions needed to be made to reduce the cost. The main computational saving was made by reducing the streamwise computational domain size. Sufficient length was retained, however, to ensure that the heat addition had sufficient distance to influence the transport processes. By reducing streamwise computational domain size, it was necessary for the cases where finite rate chemical kinetics were used to assume the hydrogen was premixed with the flow at the entrance to the domain. In doing so, the mixing process between fuel and oxidiser has been neglected, however, the goals of this work are to assess the effects of chemical heat release on turbulent transport and, as such, this assumption does not detract from the conclusions that can be made. Consequently, the hydrogen and air were assumed to possess the same flow properties across the thickness of the boundary layer. For the finite rate chemical kinetics calculations the hydrogen and air reactions were modelled using the same reaction scheme as was used by Brescianini (1993). The Evans and Schexnayder 8-reaction scheme, without any corrections for *unmixedness*, was used and concentrations of NO species were not included in the combustion model. In the cases where a constant heat addition region has been used, the heat was added uniformly in time within the boundary layer in a manner representative of premixed hydrogen combustion.

These assumptions limit the ability to make direct comparisons with experimentally measured properties. However, where possible, comparisons are made to experimental data and analytical results to ensure that the results obtained are physically plausible.

5.3.2 Finite Rate Chemistry

The use of finite rate chemistry within turbulent flows is a very complicated process. Pitsch (2006) provides a very comprehensive review of the new field in LES of turbulent combustion. To realize the full predictive capability of combustion in LES many fundamental questions must be addressed. In particular, models governing the interaction of the turbulence and chemistry are still under active research.

The scope of this work is to investigate heat addition to a turbulent boundary layer resulting from the combustion of premixed hydrogen. In premixed combustion the flame fronts are very thin. It is these fronts of heat release that are governed by the interaction of turbulent transport and chemistry. Capturing these flame fronts is one of the main challenges from a numerical resolution standpoint. Often the flame front is entirely on the subgrid scale. To accurately resolve these flame fronts requires an increase in computational cells by an order of magnitude in each direction compared to not resolving the fronts. However, often in published works this issue is neglected and the transport equation of the unburned gas mass fraction is solved without consideration of the flame front discontinuity. There exists combustion models that take into account the flame front discontinuity without resolving them completely, but that level of complexity is not necessary here. Rather, the chemistry exists in this work to provide a more realistic distribution of chemical energy release when compared to constant heat addition regions.

The averaged conservation equation for mass fraction f_i of the species i is defined in equation 3.18. We redefine $\overline{\rho}\widetilde{f}_i\widetilde{V}_{ik}$ as the molecular diffusion flux and $\dot{\omega}_k$ is the volumetric production rate of the chemical reaction of species i. The left-hand side of the equation is made up of the terms for unsteady effect, convection by the mean flow and turbulent transport of species i. The right-hand side comprises the molecular diffusion and reaction rate of species i. Molecular diffusion is often neglected for high Reynolds number flows, however, no formal qualification of high Reynolds number flows or boundaries are generally given (Veynante and Poinsot, 1997). The work of Brescianini (1993) supports this assumption. Numerical simulations of wall injected hydrogen and combustion at supersonic speeds were performed and indicated that the combustion was limited by the large scale mixing. It is this large scale mixing that is resolved by LES.

Equation 3.18 has two terms that can be modelled; the reaction rate and turbulent transport. The reaction rates have received a considerable amount of attention, whereas the turbulent transport has seen less. The turbulent transport can be generally described with a simple classical gradient

eddy-viscosity model:

$$\overline{\rho u_i'' f_k''} = \overline{\rho}\widetilde{u_i'' f_k''} = -\frac{\mu_t}{Sc}\frac{\partial \tilde{f}_k}{\partial x_i} \tag{5.6}$$

where μ_t is the turbulent dynamic viscosity and Sc is the turbulent Schmidt number.

Such classical models do not account for counter gradient transport that is observed to take place in turbulent premixed flames. Recent DNS studies confirm this observation with a mixture of both counter gradient and classical gradient transport behaviour being shown to be possible. Consequently, it was deemed unnecessary to attempt to include the subgrid scale turbulent species transport, as the simple models do not capture the correct behaviour and would only introduce added uncertainty and computational cost.

The model for the reaction rates used herein is an Arrhenius law based on filtered quantities. Such a model neglects subgrid scale contributions by assuming perfect mixing at subgrid scale level. This assumption is akin to neglecting the subgrid scale turbulent transport, as it also implies perfect mixing at the subgrid scale level.

The simplifications discussed above are a requirement to keep the numerical problem tractable. Following the discussion of Chen (2004), we can consider the simulation of turbulent combustion as consisting of three major parts: fluid dynamics, chemical reactions and their interactions. Each component can be thought of as a coordinate direction in three-dimensional space (see figure 5.3-1). For instance, in the fluid dynamics direction moving from RANS to LES and then to DNS increases the computational demands highly non-linearly. Thus, this axis is best envisaged as a logarithmic scale. Similarly, the use of finite-rate chemical kinetics requires computational resources that scale with the square of the number of species (Chen, 2004) and should also be considered logarithmic. The final axis, that governs the interaction between turbulence and chemistry, currently represents the most challenging aspect of turbulent combustion. It is these interactions that are of great importance to ignition, flame structure and propagation, extinction and flame stabilization phenomena. Any improvements for supersonic combustion problems due to the incorporation of turbulence chemistry interactions were found by Möbus et al. (2003) to be insignificant when comparisons were made to results of conventional laminar (no turbulence interaction) chemistry simulations and experimental data (Choi et al., 2006). Norris and Edwards (1997) suggested, after a review of no model LES results studying hydrogen-air jet diffusion flames, that the accuracy of the solution for supersonic flows was more dependent on grid resolution than turbulence-chemistry interactions. Since the present study is limited to the influence of heat evolution from combustion processes on the turbulent boundary layer, the interaction is

deemed to not be important and infinite mixing is assumed.

Of each three components represented in figure 5.3-1, the chemical kinetics represents the largest proportion of computational demands. According to Chen (2004), approaches for speeding up the chemical kinetics must be taken to make LES feasible for engineering problems. For instance, the current simulations took between 6 and 7 times longer when finite rate chemical kinetics were included. McMurtry et al. (1989) made the assumption of simple chemistry for studying heat release on mixing layers of the form:

$$\mathrm{A} + \mathrm{B} \longrightarrow \mathrm{Products} + \mathrm{Heat} \tag{5.7}$$

Further simplifications were made so that the reaction rate was taken as a function of concentration only and did not vary with temperature. Even though the reaction scheme was very idealized, the effects of chemical energy release were still able to be studied. This demonstrates that, while using an Arrhenius reaction rate scheme with no turbulence-chemistry interaction model is very idealized, the effects of chemical energy release can still be studied with confidence.

Model for Chemical Source Terms

The combustion process of hydrogen is modelled by a set of N_r reversible reactions involving N_s species and is implemented in the code module written by Gollan (2003). The governing equation for conservation of species mass fraction (Eq (3.18)) requires calculation of the rate of production of species i for the flow timestep. Using the notation of Anderson (1989) and Brescianini (1993) the reactions are written as:

$$\sum_{i=1}^{N_s} \nu_i' X_i \underset{k_b}{\overset{k_f}{\rightleftharpoons}} \sum_{i=1}^{N_s} \nu_i'' X_i \tag{5.8}$$

where ν_i' and ν_i'' are the stoichiometric coefficients for reactants and products for chemical symbol X_i respectively. The forward and backward reaction rate coefficients, k_f and k_b, respectively are computed from a modified Arrhenius expression:

$$k_f = A_f T^{B_f} exp(-C_f/T) \tag{5.9}$$

Table 5.3-4: Species and reactions of Evans and Schexnayder (1980)

Species		Reactions			
1	O_2	1	$H_2 + M \rightleftharpoons H + H + M$	9	$H_2 + O \rightleftharpoons OH + H$
2	N_2	2	$O_2 + M \rightleftharpoons O + O + M$	10	$H_2 + O_2 \rightleftharpoons OH + OH$
3	H_2	3	$H_2O + M \rightleftharpoons OH + H + M$	11	$H_2 + O_2 \rightleftharpoons H + HO_2$
4	O	4	$OH + M \rightleftharpoons O + H + M$	12	$OH + OH \rightleftharpoons H + HO_2$
5	H	5	$HO_2 + M \rightleftharpoons H + O_2 + M$	13	$H_2O + O \rightleftharpoons H + HO_2$
6	H_2O	6	$H_2O + O \rightleftharpoons OH + OH$	14	$OH + O_2 \rightleftharpoons O + HO_2$
7	OH	7	$H_2O + H \rightleftharpoons OH + H2$	15	$H_2O + O_2 \rightleftharpoons OH + HO_2$
8	HO_2	8	$O_2 + H \rightleftharpoons OH + O$	16	$H_2O + OH \rightleftharpoons H_2 + HO_2$

with a_f and B_f being constants of the reaction and C_f being the activation energy of the reaction. The rate of change of species i in reaction j is computed via:

$$\left(\frac{d[X_i]}{dt}\right)_j = (\nu_i'' - \nu_i') \left\{ k_f \prod_i [X_i]^{\nu_i'} - k_b \prod_i [X_i]^{\nu_i''} \right\}. \tag{5.10}$$

The total rate of change of species i due to all reactions is defined as:

$$\frac{d[X_i]}{dt} = \sum_{j=1}^{N_r} \left(\frac{d[X_i]}{dt}\right)_j \tag{5.11}$$

The reaction scheme used for the current calculations is that described by Evans and Schexnayder (1980). The scheme includes 8 species and 16 reactions, with molecular nitrogen acting as a dilutant and not participating in reactions. The species and reactions are shown in table 5.3-4. Table 5.3-5 gives the reactions rates and constants used.

The mixture of species present is treated as a mixture of perfect gases, hence, C_p and C_v are only functions of temperature. As per the perfect gas model, intermolecular forces are neglected. The enthalpy of the gas is found by integrating the curve fit of C_p giving rise to:

$$\frac{H}{RT} = -a_1 T^{-2} + a_2 T^{-1} \, lnT + a_3 + a_4 \frac{T}{2} + a_5 \frac{T^2}{3} + a_6 \frac{T^3}{4} a_7 \frac{T^4}{5} + \frac{a_8}{T} \tag{5.12}$$

where R is the universal gas constant and coefficients $a_1 ... a_7$ are determined by the species and temperature range. The curve fits assume that all the internal energy modes are fully excited at the given temperature. The component viscosities of the species present are also computed through curve fits. The mixture enthalpy is found as a weighted sum, based on mass fraction, of the

Table 5.3-5: Reactions rates and constants of Evans and Schexnayder (1980); units of k in cm^3 / (mole s)

	Forward rate constant			Reverse rate constant		
	A	B	C	A	B	C
1	5.5×10^{18}	-1.0	51987.0	1.8×10^{18}	-1.0	0.0
2	7.2×10^{18}	-1.0	59340.0	4.0×10^{17}	-1.0	0.0
3	5.2×10^{21}	-1.5	59386.0	4.4×10^{20}	-1.5	0.0
4	8.5×10^{18}	-1.0	50830.0	7.1×10^{18}	-1.0	0.0
5	1.7×10^{16}	0.0	23100.0	1.1×10^{16}	0.0	-440.0
6	5.8×10^{13}	0.0	9059.0	5.3×10^{12}	0.0	503.0
7	8.4×10^{13}	0.0	10116.0	2.0×10^{13}	0.0	2600.0
8	2.2×10^{14}	0.0	8455.0	1.5×10^{13}	0.0	0.0
9	7.5×10^{13}	0.0	5586.0	3.0×10^{13}	0.0	4429.0
10	1.7×10^{13}	0.0	24232.0	5.7×10^{11}	0.0	14922.0
11	1.9×10^{13}	0.0	24100.0	1.3×10^{13}	0.0	0.0
12	1.7×10^{11}	0.5	21137.0	6.0×10^{13}	0.0	0.0
13	5.8×10^{11}	0.5	28686.0	3.0×10^{13}	0.0	0.0
14	3.7×10^{11}	0.64	27840.0	1.0×10^{13}	0.0	0.0
15	2.0×10^{11}	0.5	36296.0	1.2×10^{13}	0.0	0.0
10	1.2×10^{12}	0.21	39815.0	1.7×10^{13}	0.0	12582.0

enthalpies of each species present. An iterative technique is then used to compute the temperature of the gas.

As a final stage, the chemistry is coupled to the fluid dynamics by timestep splitting. By splitting the major processes, the fluid dynamics, including convection of species is first updated (with $\overline{\dot{\omega}} = 0$; see Eq (3.19)) followed by an update of species mass fractions over the same timestep. The update of species mass fraction from chemical processes gives rise to a set of stiff ordinary differential equations (ODEs). The ODEs are advanced a number of times at a chemical timestep until the flow timestep is reached.

The composition of the mainstream flow and pre-mixed hydrogen boundary layer flow is summarized in table 5.3-6. The mass fraction of hydrogen is computed assuming a mass flow rate of 0.03kg/s/m (per unit spanwise width), or equivalence ratio of 0.3 for the flow contained within the boundary layer.

Table 5.3-6: Species concentrations

Species	Mainstream	Boundary layer
$[O_2]$	0.233	0.2237
$[N_2]$	0.76	0.7596
$[H_2]$	0.0	0.0097
[O]	0.007	0.007
[H]	0.0	0.0
$[H_2O]$	0.0	0.0
[OH]	0.0	0.0
$[HO_2]$	0.0	0.0

5.3.3 Heat Source

The other method of including the effects of hydrogen combustion used in this work is achieved by applying an energy source term to a predefined region. This heat addition zone is confined to a region within the boundary layer to replicate as closely as possible the regions where combustion would occur. Heat addition zones have been used previously in the study of the optimal design of Scramjet ducts (Jacobs and Craddock, 1999) and have also been used analytically by Stalker (1989) for Scramjet type flows. It was demonstrated that the expanding fluid undergoing heat addition delivered work, primarily normal to the streamtube, but also along the streamtube. This work was then transfered to adjacent streamtubes through pressure waves with this process continuing until it impinges on a wall. It was through this process and its interaction with the wall that thrust was produced on Scramjet thrust surfaces. Hence, a heat source term approach presents itself as a method of introducing chemical heat release effects, without the computational overhead of computing the complete combustion reactions, while still accounting for the bulk effects.

The source term ($Q_{\rho E}$, Eq (3.19)) was computed *a posteriori* and represented the heating rate per unit volume for the combustion of hydrogen. This term was computed as a function of downstream distance for the desired flow conditions by combining a reduced resolution domain and the solution of the finite rate chemical kinetics. The inflow conditions for the desired boundary layer were premixed with hydrogen at an equivalence ratio of 0.3 and from these coarse simulations the rate of change of internal energy with time was extracted from the solution field. This process was achieved through a finite difference approximation computing the heat source term as a function of downstream distance from the inflow boundary. The rate of change of internal energy was then

parametrized with a best fit polynomial with the heating rate found to closely follow the Gumbel distribution. The Gumbel distribution is an extreme value type I probability density function and has the form:

$$Q_{\rho E} = \frac{\alpha}{\beta} e^{\frac{-(x/L_x-\mu)}{\beta}} \times e^{-e^{\frac{-(x/L_x-\mu)}{\beta}}} \tag{5.13}$$

The coefficients for case 1 and 2 respectively were:

Case	α	β	μ
1	1.1×10^9	0.118	0.3
2	7.0×10^8	0.118	0.3

The specific quantity of energy per unit time is then added to the total energy equation source vector Q, Eq (3.19). The region where heat was added is defined by the following conditions (and shown graphically in figure 5.3-2):

$$\frac{1}{5} \leq \frac{x}{L_x} \leq \frac{9}{10} \qquad \frac{1}{20} \leq \frac{z}{\delta_0} \leq \frac{4}{5}$$

5.3.4 Computational Details

A significant limitation on the grid resolutions used that is worth detailing is the computational requirements. Hence, the code performance determined the maximum grid resolution. The feasibility of each simulation was then gauged on the total simulation time required to capture sufficient statistically independent flow field snapshots. A feasible simulation time was taken to be in the vicinity of or less than 40 days ($\sim 3.46 \times 10^6$ seconds) on, up to 64 CPUs. The run times for each key simulation presented in this chapter is detailed in table 5.3-7. This summary serves as an illustration of the additional computational expense in including the finite rate chemical effects.

5.4 Mechanisms of Momentum Transport Under External Heat Sources

The aim of this section is to investigate the turbulent flow properties of boundary layers that have undergone wall shear stress reduction. The section begins by first identifying a reduction in wall

Table 5.3-7: Code performance and simulation run times. The CPU column represents the number of processors used in parallel.

Grid	Heat models used	CPU	CPU seconds	CPU seconds (wall clock)	Memory
A	-	40	2.42×10^7	6.05×10^5	26 GB
B	-	56	5.93×10^7	1.06×10^6	67 GB
C	-	64	9.68×10^7	1.51×10^6	128 GB
D	-	64	1.55×10^8	2.42×10^6	128 GB
A	Heat source	40	3.63×10^7	9.07×10^5	26 GB
B	Heat source	56	7.67×10^7	1.37×10^6	67 GB
C	Heat source	64	1.16×10^8	1.81×10^6	128 GB
A	Finite rate chemistry	40	1.33×10^8	3.33×10^6	32 GB
B	Finite rate chemistry	56	3.65×10^8	6.52×10^6	84 GB

shear stress and the corresponding changes in mean flow quantities that accompany it. This is then followed by a presentation and discussion of the changes in turbulent transport and structure that result. At all times the changes in computed turbulent quantities are related to the physical processes that are occurring.

In order to see the effects that heat addition has on the large scale structures within a turbulent compressible boundary layer, quantitative measures must be identified. Work done previously by McMurtry et al. (1989) used DNS to investigate the effect of heat release on the structure in turbulent mixing layers. It was found that moderate heat release slowed the development of the large-scale structures and shifted their wavelengths to larger scales. The results were interpreted in terms of turbulent energetics, vorticity dynamics and stability theory. In addition to these interpretations, effects on the mechanisms of momentum transport can also be assessed through examination of mean flow properties, velocity fluctuation statistics, Reynolds stress levels, Reynolds stress transport budgets and turbulent structure visualizations. In doing so, a quantitative assessment of changes to the turbulence within a supersonic turbulent boundary layer when heat was added, either through an external heat source or through combustion of premixed hydrogen, can be provided. It was also possible to identify effects that are due only to heat addition and those that arose as a result of the presence of combustion reactants and products along with the associated heat evolution.

A contour plot of the instantaneous static temperature in the $x-z$ plane is presented in figure 5.3-3 for case 1. The changes that occur to the thermal flow field and their corresponding regions can

be seen for both the heat source and combustion approach.

5.4.1 Mean Flow

The effects of heat addition on the mean flow properties can easily be identified and provide a simple but effective means of observing the influence of heat release on the turbulent boundary layer. A contour plot of the instantaneous static temperature in the $x - z$ plane is presented in figure 5.3-3 for case 1 and the changes that occur to the flow field and their corresponding regions can be seen for both the heat source and combustion approach. All profiles presented in this section are averaged in both the streamwise and spanwise directions for $x/\delta > 25$. To aid in the interpretation of the results, the quantities are presented in dimensional form in the included figures.

Significant changes in bulk velocity profiles were observed by Jones et al. (1971), when combustion occurred in the turbulent boundary layer. If we examine the mean velocity profiles for both cases 1 and 2, plotted in figures 5.3-4 to 5.3-5, the most significant effect is an inflection in the velocity profiles in the heat addition region. The mean streamwise momentum profiles in figures 5.3-6 to 5.3-7 show an even more significant difference from the non-heated profile with the heat addition, resulting in additional decreases in density that couple with the inflection in the velocity profile. It is suggested that these changes in the mean velocity and momentum profiles are not only induced by a direct effect of heat release on the mean flow quantities, but are also induced through changes in turbulent transport within the boundary layer. It is through such changes to the turbulent structures, that the effects of heat addition manifest to create the effect of reducing wall shear stress. The effect of heat addition on the mean static temperature profiles is able to be seen in figures 5.3-8 and 5.3-9 with the increased temperature due to heat release/combustion able to be inferred from these mean profiles. There is reasonable agreement between the heat source and combustion approaches. The differences can be attributed to the different thermal capacities of the ideal gas in the heat source method and the mixture of thermally perfect gases used for the combustion simulation. The peak temperatures are close to the typical average Scramjet combustor temperatures of 2000K (Jacobs and Craddock, 1999).

It is postulated, that heat release increases the boundary layer displacement and, hence, alters the overall velocity gradients. Table 5.4-8 details the changes observed in the mean boundary layer quantities. It is clear to see that the various boundary layer thicknesses that are computed increase

Table 5.4-8: Effect of heat addition and combustion on boundary layer length scales and Reynolds numbers

Case	Heat addition	δ (mm)	δ_1 (mm)	δ_2 (mm)	Δ^* (mm)	H_{12}	H_{32}	Re_θ	Re_{δ_2}
1	Heat source	6.5	2.3	0.35	21.1	6.48	1.82	5160	10380
	Combustion	7.9	2.7	0.42	22.1	6.70	1.82	6391	12840
	No heat	4.8	0.83	0.26	11.8	3.2	1.77	3956	6710
2	Heat source	6.4	1.4	0.39	22.3	3.70	1.82	3800	10716
	Combustion	6.8	1.47	0.38	24.9	3.83	1.82	3740	10540
	No heat	4.8	0.82	0.29	13.9	2.77	1.79	2809	7913

when heat is added. These increases in thickness appear to be a direct result of the new inflections observed in the mean velocity profiles. Interestingly, the displacement thickness increases more than the momentum thickness does, as observed through the increasing shape factor, H_{12}. It appears as though the boundary layer displacement increases, while the decreasing density causes a proportionately smaller increase in momentum thickness. Shape factor H_{32}, on the other hand, shows that the kinetic energy defect thickness behaves in a fashion more like the momentum thickness when heat is added. The effects of an increase in boundary layer thicknesses, however, extends beyond changes to mean quantities. As observed in the previous chapter, and identified in section 5.4.6, it is the mean velocity gradient that interacts with the shear stresses to produce turbulence. Hence, alterations to the mean velocity profile have profound effects on the turbulent generation process and thus, the turbulent transport of momentum.

From table 5.4-9, it is clear to observe that the changes in mean profile manifest in a reduction in skin friction. Such reductions occur due to a combination of phenomena where not only do the mean properties such as velocity and density change, but the turbulent transport of momentum and energy does too. The skin friction coefficients presented are based on the wall shear stress normalized by local boundary layer edge conditions. The changes in boundary layer edge conditions due to heat addition are small, but do result in normalization by a factor that is greater than if the nominal freestream conditions were used. Hence, for clarity and comparison the wall shear stress is also presented.

The reductions in wall shear stress and skin friction computed here do not approach the values measured experimentally by Suraweera (2006). However, as stated previously, neither the heat

addition nor pre-mixed hydrogen combustion methods used in this work take into account the film cooling of a hydrogen stream near the wall. Film cooling is a significant contributor, with the results of Suraweera (2006) indicating that the film cooling skin friction reductions were as large as 30 - 40% for the regions of flow studied here. Furthermore, the experiments of Rowan (2003) found that, for tangentially injected hydrogen that did not combust at an equivalence ratio of two (2), the total skin friction coefficient reduction approached 50%. The significant skin friction reductions combined with the fact that no combustion was observed, reinforces the observation that film cooling plays a large role in drag reduction, while providing an explanation for the lack of direct agreement with the experimental results of Suraweera (2006).

Table 5.4-9: Effect of heat addition and combustion on mean skin friction and wall shear stress. Stress units; Pa

Case	Heat addition	C_f	τ_w	C_f (Suraweera, 2006)	C_f (Stalker, 2005)
1	Heat source	0.92×10^{-3}	710	-	-
	Combustion	1.06×10^{-3}	857	6.8×10^{-4}	8.0×10^{-4}
	No heat	1.65×10^{-3}	1203	-	-
2	Heat source	1.58×10^{-3}	1360	-	-
	Combustion	1.51×10^{-3}	1335	5.4×10^{-4}	1.4×10^{-3}
	No heat	1.90×10^{-3}	1608	-	-

Stalker (2005) provides a theoretical means of calculating the skin friction reduction when hydrogen combustion occurs when gaseous hydrogen is injected tangentially into the boundary layer. Calculations for conditions very close to those of case 2 are presented by Stalker (2005). Given a wall mass fraction of hydrogen of 9.97×10^{-3} for the presented calculations, the analytical solution graphs indicate a combustion skin friction coefficient of approximately 1.4×10^{-3}. As a further check on the computational results, the equations developed by Stalker (2005) to account for combustion within a turbulent boundary layer, were then also applied to the conditions of case 1. Following the analytical procedure the combustion skin friction coefficient was computed to be 8.0×10^{-4}, given the wall mass fraction of hydrogen that is simulated in these calculations. The fact that the analytical results yield greater skin friction reductions than the numerical calculations is in line with the conclusions of Stalker (2005), that the analytical results are thought to yield greater skin friction reductions through overestimation of the effects of combustion. Despite this, the analytical results provide an upper limit of the combustion effects. However, the analytical results do serve as a good estimate of what skin friction reduction we should expect from the LES

computations for the chosen conditions, while also giving further confidence in the numerical results.

The vorticity thickness, defined as the ratio of the maximum velocity difference across the layer to the maximum slope of the mean velocity profile, was another mean flow quantity used by McMurtry et al. (1989) to analyse the growth of a mixing layer under heat release. The vorticity thickness collapses to a measure of wall shear stress for boundary layer flow when the velocity difference across the boundary layer remains nearly constant. It was reasoned by McMurtry et al. (1989) that thermal expansion shifted the flow field in the vicinity of the heat addition region outwards, resulting in a decrease in vorticity thickness. The same phenomena is observed for the wall shear stress values in the current work with the added heat causing an expansion of the boundary layer and lowering of the wall shear stress. It is this expansion that also results in lowering of the magnitude of the turbulent fluctuations (shown in later sections) and hence the vorticity of the flow. We can understand the decreasing velocity fluctuations and flow vorticity by acknowledging the fact that a fluid element undergoing thermal expansion must decrease its vorticity and, hence, local rotation rate, in order to conserve angular momentum.

5.4.2 Reynolds Stresses, Turbulent Intensities and Compressibility Effects

To investigate the changes to the turbulent field when heat is added, the Reynolds stresses, turbulent intensities and compressibility effects are computed. Turbulent Reynolds stresses are a useful indicator of the influence of heat addition. Computing the turbulent Reynolds stress profiles ($\widetilde{\overline{\rho}u_k'u_i'}$) allows for assessment of how much kinetic energy is being transferred from the mean flow to the turbulence for cases with and without heat addition. Similarly, the turbulent intensities allow for assessment of changes in the mass, momentum and energy transport amongst fluid elements, while the turbulent Mach number gives an indication of how compressibility effects change.

Consider again the behaviour of the total shear stress (equation 2.1). With the exception of the near wall region where the velocity gradient is high, the transport of momentum for the total shear stress is dominated by the turbulent Reynolds shear stress component. It is this turbulent component that transports momentum from the mainstream flow to the near wall regions. A dynamical link was established by Bernard and Wallace (2002) between the Reynolds shear stress and the vortical structures present within the boundary layer. Through this link to the vortical structures, it is

a clear extension to link the Reynolds shear stress to the vortex-driven (turbulent) transport of momentum. Any alteration to this turbulent transport process significantly alters the supply of momentum to the regions where viscous effects take over. In essence, the turbulent Reynolds stress, from which the shear stress is formed, gives the mean flux of momentum due to turbulent motion (Bernard and Wallace, 2002). Fukagata et al. (2002) confirmed this observation by noting that the Reynolds shear stress is most important for the determination and, hence, control of the wall shear stress. In fact, because the Reynolds shear stress is a result of a subset of the principal vortical structures (see sections 5.2.6 and 5.4.5), LES provides a good account of its action through direct resolution of their motions (Bernard and Wallace, 2002).

Figures 5.3-10 and 5.3-11 show that the peak turbulent Reynolds shear stress is reduced by up to 35% from the nominal value when heat is added. The locations of the reductions coincide with the velocity inflection region already observed and it is suggested here that the lower turbulent Reynolds shear stresses are the cause. With the turbulent shear stress controlling the transfer of kinetic energy from the mean flow to and from the turbulent fluctuations, it is expected that these reductions in turbulent Reynolds shear stress limit the transport of momentum and, hence, are the main source of changes in velocity profile and wall shear stress reductions. The lowering of the turbulent stresses also implies a weakening of the turbulent vortices in the flow as is identified in section 5.4.4 through examination of the turbulent energy spectra.

The wall normal heat flux ($\widetilde{\overline{\rho} w_k' T_i'}$) is a significant contributor to transport of energy across the boundary layer. When heat is added, the transport of thermal energy to the wall becomes increasingly important. Even in the absence of turbulent transport it would be reasonable to expect that the wall heat transfer would increase. Consequently, any changes in the turbulent transport of energy are of interest, as they can add further to the already increased transport of energy to the wall. Figures 5.3-12 and 5.3-13 present the Reynolds heat flux for cases 1 and 2 respectively for both a heat source and combustion model. The transport of hot and cold fluid elements to and from the wall, however, cannot be fully described by the Reynolds heat flux alone. For instance, cold fluid being transported away from the wall results in a negative Reynolds heat flux, while hot fluid being transported to the wall equally results in a negative contribution. Hence, a complete discussion is referred to the octant decomposition discussion of section 5.4.5. However, in general, we can consider a negative heat flux resulting in additional heat being transported to the wall and a positive component removing heat.

Both cases 1 and 2 yield qualitatively similar behaviour, hence, the discussion of Reynolds heat

flux applies equally to both cases. There is little change in the near wall behaviour of the Reynolds heat flux in the region $z < 5 \times 10^{-5}m$, when heat is added through either method. Outside of this region, there is a clear increase in Reynolds heat flux transporting heat to the wall that is a direct result of the additional heat introduced to the domain. As we progress into the regions of heat addition and combustion, the flux becomes positive and represents the transport of cool flow towards the wall or hot flow away from the wall. This observation appears consistent with the heated regions exchanging energy with the cooler freestream flow. Outside of the boundary layer, when combustion is modelled through chemical kinetics, there is a rapid change in the sign of the Reynolds heat flux signalling that thermal energy is being transported back towards the wall. This phenomena is not observed when heat is added as a source term. The physical mechanisms contributing to this behaviour will be discussed in more detail through octant decomposition in section 5.4.5.

Examination of turbulent kinetic energy can provide a useful way of interpreting the effects heat release has on turbulent motions as it removes the influence of bulk density changes. Reductions in turbulence levels imply lower turbulent transport rates (McMurtry et al., 1989), resulting in a lower exchange of mass, momentum and energy among fluid elements. Turbulent kinetic energy and shear stress are closely related since the turbulent stresses are an indication of the kinetic energy transfer from the mean flow to or from the turbulence. This is then related to the vorticity dynamics by the hypothesis that, for turbulent flows, it is the eddies which manifest as velocity fluctuations that are responsible for a large part of the transport of momentum as well as scalar quantities. Thus, it is expected that when heat release occurs, the eddies weaken and transport less momentum as indicated by the lower than normal turbulent Reynolds shear stress.

To examine the turbulent kinetic energy and make interpretations about the effects of heat release, we decomposed the turbulent kinetic energy into velocity fluctuations in each direction. In doing so, a description of the the dynamics of the turbulent structures present in the flow is able to be obtained. McMurtry et al. (1989) drew conclusions about the influence of heat release by noting changes in the amplitude and distribution of velocity fluctuations found within the flow. For instance, it was found that thermal expansion resulted in a decrease in the average peak magnitude of fluctuations. While the levels of heat addition differ between the current study and that of McMurtry et al. (1989), the same behaviour can be seen here.

The streamwise velocity fluctuations are largely responsible for transport along the wall, whereas it is the spanwise and wall normal fluctuations that introduce the vortex behaviour. While small in

magnitude relative to the streamwise component, the spanwise and wall normal components represent a large portion of the turbulent transport of momentum to and from the wall. In particular, wall normal velocity fluctuations can result in high momentum fluid being swept down towards the wall or low momentum fluid being ejected up toward the mainstream flow. It is through interaction with the streamwise velocity fluctuations that the turbulent Reynolds shear stress is formed, which in turn interacts with the mean velocity gradient inducing the production of turbulence. Hence, changes to the spanwise and wall normal components, despite their relatively small nature can have large effects on the turbulent transport processes.

The RMS fluctuations of the streamwise velocity are given in figures 5.3-14 and 5.3-15. These figures show that near the wall the streamwise velocity fluctuations are largely unaffected by the heat release through either heat source terms or finite rate chemical kinetics. Hence, the streamwise component reveals no change in the mechanisms of turbulent transport along the wall. There is some increase, however, in streamwise velocity fluctuation away from the wall that can be largely attributed to the energy addition of the combustion/heat addition process. Any increase in streamwise velocity fluctuations does not directly lead to greater wall shear stress as these fluctuations must first be redistributed to the spanwise and wall normal directions.

Examination of the spanwise and wall normal velocity fluctuations reveals that not only do changes occur in the mean flow quantities, but also in the turbulent structures themselves. The spanwise velocity fluctuations (figures 5.3-16 and 5.3-17) show a decrease in turbulent activity near the wall, suggesting lower mixing rates. Similar observations are made for the wall normal velocity fluctuations (figures 5.3-18 and 5.3-19). With the wall normal velocity fluctuations being one of the most significant means of transporting momentum to and from the wall, changes in the distribution of the wall normal velocity fluctuations have a considerable influence in the reduction of the wall shear stress. A reduction in the wall normal velocity fluctuations is observed with the peak reduction occurring within the first 1mm of the boundary layer ($\delta \approx 5$mm at inflow) and also corresponding to the location of the inflection in the velocity profiles identified earlier. The reduction extends towards the wall with diminishing effect, eventually returning to the no heat addition case. However, the lower turbulent transport above the near wall region limits the transport of momentum towards the wall. Further demonstration of the key role the wall normal velocity fluctuations play in the transport of momentum and, hence, generation of wall shear stress is evident in the DNS results of Choi et al. (1994). Through local blowing and suction along the wall in the simulations of Choi et al. (1994), the wall normal velocity in the near wall region was opposed and a 25% reduction in wall shear stress was created.

The reduction in spanwise and wall normal velocity fluctuations is caused by a decreasing contribution of the pressure redistribution term, that will be discussed in section 5.4.6. By virtue of a lower pressure contribution there is less redistribution of the streamwise velocity fluctuations to both the spanwise and wall normal directions. Thus, we can observe that the decrease in redistribution inhibits the establishment of a more isotropic turbulence, that would otherwise have been generated had no heat been added.

The reductions in the turbulent Reynolds shear stress identified previously, are due to the combined influence of a reduction in near wall density and the reduction in turbulent velocity fluctuations. The turbulent Reynolds shear stress without the density scaling is plotted in figures 5.3-20 and 5.3-21 to clarify what happens to the turbulent structure when heat is added. Here we can clearly assess that, along with the changes in mean density profile, there remains a change in the turbulent shear generated when heat is added to the boundary layer.

Finally, compressibility effects are observed to decrease through the plots of turbulent Mach number in figures 5.3-22 and 5.3-23. The main source of this reduction is the increasing sound speed, with the associated rise in temperature throughout the boundary layer. The reduction in turbulent Mach number demonstrates that when heat is added to the boundary layer, there is a decrease in the divergence of the fluctuating velocity field. Correspondingly, we would expect that any decrease in divergence of the fluctuating velocity field represents diminished turbulent activity.

5.4.3 Two-Point Autocorrelations

Two-point autocorrelations of velocity fluctuations are computed to assess the changes in turbulent structure length scales. Figures 5.3-24 and 5.3-25 show the two-point autocorrelations for the three velocity fluctuation components at a wall normal location of $z^+ = 5$, for heat addition through a heat source and combustion respectively. The length of the elongated, counter-rotating streamwise vortices known as streaks can be estimated from the near wall two-point autocorrelations. When heat is added, the correlated length is observed to significantly increase (figures 5.3-24(c), 5.3-24(d) and 5.3-25(c)). The two-point autocorrelation of figure 5.3-25(d) does not show an elongation of the streaks. Rather the two-point autocorrelation shows that the streamwise length scale is largely unchanged, but exhibits oscillations which may suggest increased downstream coherence. Physically, it is these streaks that gradually lift up from the wall and terminate in an ejection of fluid away from the wall, thereby contributing to the turbulent transport of momentum. Conse-

quently, if the coherence of these structures increases, we expect to see a corresponding reduction in contribution of the ejection events, that occur when they terminate, to the Reynolds shear stress phenomena. The contribution of ejection events is discussed in more detail in section 5.4.5, but it is interesting to note the close relationship between coherence length and observed turbulent transport phenomena. We can conclude that the addition of heat leads to an increase in streamwise coherence length which corresponds to a reduction in turbulent transport of momentum to the wall.

An increase in streamwise extent of the near wall streaks is not unprecedented. Delo et al. (2004) proposed that any addition to the energetics of the near wall flow perpetuates the turbulent structures. The key to this phenomena appeared to be that the near wall structures are now long enough, such that after an ejection of near wall fluid occurs, the trailing edges of the now longer structures are still in the vicinity of the wall. Thereby, they are able to entrain the ejected near wall fluid before it travels far from the wall preventing interaction with the higher momentum freestream fluid. Furthermore, Martín (2004) observed a decrease in streamwise extent for increasing Mach number boundary layer flow. An increasing Mach number leads to increasingly rapid variations in temperature near the wall. The introduction of heat across the majority of the boundary layer reduces the variation somewhat by introducting a more uniform, but high temperature, region above the peak viscous heating region. Hence, by reducing the thermal variation, the converse phenomena of increasing streamwise extent of the near wall streaks is supported.

The width of the near wall streaks, approximated from the streamwise component of the spanwise two-point autocorrelation, also increases somewhat when heat was added. By increasing their width, there is a decreasing area where the streaks are impinging on the wall and transporting additional momentum. This result is consistent with the findings of Oldaker and Tiederman (1977), where it was concluded that for increasing drag reduction the near wall streaks enlarged both in the spanwise and streamwise directions. Hence, the behaviour of the near wall streaks for high speed compressible flows with heat addition appears to be similar to that of incompressible channel flow. The two-point autocorrelations of the spanwise and wall normal velocity fluctuations are generally similar to and maintain their pre-heat behaviour. Their respective coherence lengths remain small, suggesting compact regions of alternating positive and negative fluctuations.

5.4.4 Energy Spectra

Figures 5.3-26 to 5.3-29 present the calculated energy spectra in the spanwise and streamwise directions respectively for the heat source approach. The results from combustion are very similar to the presented figures and consequently are included in figures A.1-1 to A.1-4. For the sake of comparison, the energy spectrum for no heat addition is shown as points, with every 5th data point plotted, and the energy content is presented in absolute form rather than normalized by the zero wavenumber energy content. A sufficient energy dropoff is still observed for all three fluctuating velocity components, suggesting that the flow is still well resolved and all energy curves maintain a similar energy decay.

The energy content of the fluctuating velocity components does not appear to be greatly affected by the heat release. Near the wall (at $z^+ = 5$), when the spectrum is calculated for the spanwise direction of case 1, there is a reduction in energy content across all wavenumbers, identified by a small decrease in energy level that is most readily identified for lower wavenumbers. However, a small shift on a log scale can represent sufficient changes in flow energy content so as to change the flow behaviour. Physically, the lowering of the energy profile across the wavenumbers suggests a slight weakening of the eddies/vortices. The weakening of the vortices that comprise the dynamics of the flow lessens the entrainment of higher momentum free stream fluid. By realising that it is these largest vortices, at low wavenumbers, that transport most of the momentum to the wall through the entrainment process, the weakening observed here will result in less momentum transport and loss to the wall. Such a reduction is precisely what the lower turbulent shear stresses identified previously indicate. Case 2, on the other hand, for the spanwise direction near the wall shows no significant alteration to the energy spectrum. This disparity in behaviour may be due to the increased stagnation enthalpy making the flow less susceptible to alterations in turbulent dynamics.

We can further interpret the effects of changes in energy spectra through examination of inner-outer interactions. Falco (1977) described the types of organised motion within the turbulent boundary layer as being at least one of two types: Large Scale Motions (LSMs) and typical eddies (figure 5.3-30). The LSMs have size $O(\delta)$, while the typical eddies have a scale that is of the order of the streak spacing (Falco, 1991). Through interaction with the ejection process near a wall, these typical eddies are significant players in the Reynolds stress producing motions. The formation of the typical eddies is a fundamental part of the turbulent energy cascade process. When heat is added, the shifting of the energy profile towards the lower wavenumbers that has

already been identified may represent a weakening of the typical eddies. Their small size prevents this weakening from showing up as significant reductions in the turbulent energy spectrum or in the RMS of velocity fluctuations. Rather, smaller reductions are observed. However, following the above arguments, any reduction in strength of the typical eddies can have a significant influence on the turbulent momentum transport.

Further examination of the energy content reveals that the weakening of the smaller scale structures is limited to the near wall regions. In fact, for the results of case 2, there is some increase in energy for the larger scale structures in the upper regions of the boundary layer. The energy spectrum in the streamwise direction is less affected by the addition of heat, but it can be argued that there is some, albeit small, changes in energy content.

5.4.5 Quadrant and Octant Analysis

Quadrant analysis, as discussed in Section 4.1.7, decomposes the flow into four quadrants corresponding to idealized structures: (I) outward interactions, (II) ejections, (III) inward interactions and (IV) sweeps. The Reynolds shear stress makes the most significant contribution to turbulent momentum transport in a boundary layer and is analysed here. As is seen in figure 4.1-36, the Reynolds stress ($\rho u'w'$) is divided into quadrants based on the direction of velocity fluctuations u' and w'. The analysis in this section concentrates on the observations made and conclusions drawn from case 1. The results of case 2 identify the same dominant mechanisms and behaviours and, hence, are not discussed here for simplicity. The figures relating to case 2 are provided in Appendix A.

When heat is added to the flow through the use of a source term, a reduction in wall shear stress has already been identified. Wall shear stress can be generated by the interaction of the nearest wall structures with those in the bulk flow. The interaction of the vorticity associated with these near wall structures and the bulk flow induces wall shear stress, but these near wall structures must be transported away from the wall to the bulk flow. Consequently, changes in turbulent dynamics that occur in the outer regions of the boundary layer have strong influence on the behaviour of the near wall region (Smits and Dussauge, 2006) and it is through inner-outer interactions that much of the transport of momentum occurs. Brown and Thomas (1977) revealed the relationship between the large scale turbulent motion and the wall shear stress. A characteristic signature in the wall shear stress was revealed as large scale structures passed over the wall. It was suggested

that the wall shear stress was related to the ejection process and concluded that the large scale ejections occurring away from the wall influenced the near wall behaviour.

Figure 5.3-31(a) gives the decomposition of the turbulent Reynolds shear stress into quadrants. It is clear to see that there is reduction in the absolute contribution of the ejection mechanism of between 40 and 50% of the turbulent Reynolds shear stress. Under non-heated conditions, the ejection events are the largest contributors to the Reynolds shear stress, turbulent energy production and transport and are characterised by an intense bursting process of short duration (Wilmarth and Lu, 1972). Wilmarth and Lu (1972) found through conditional sampling of a turbulent boundary layer that approximately 60% of the turbulent Reynolds shear stress could be attributed to ejection events. This demonstrates that the inner-outer interactions occurring through ejection mechanisms, as observed by Brown and Thomas (1977), can lead to reductions in wall shear stress through a reduction in these ejection events. Hence, we can easily identify that a reduction in the contribution of the ejection mechanism has led to the decrease in wall shear stress. The contribution of sweeps (quadrant IV), which transport high momentum fluid towards the wall, remains largely unchanged when heat is added. It is the sweep mechanisms, associated with the streamwise streaks/vortices, that are known to create regions of high wall shear stress on the wall (Kravchenko et al., 1993). Both the outward and wallward interactions (quadrants I and III respectively) show a decreasing contribution, while still remaining in opposition to the generation of Reynolds shear stress, i.e. they maintain a small positive value. The decrease in contribution of outward ejections of high momentum fluid suggests that the sweeps of high momentum fluid impact the wall with less strength, generating less high momentum reflection.

The likelihood of an ejection event (figure 5.3-31(b)) occurring, when heat is added, decreases. This suggests that the strength of the ejections remains the same, but they occur less frequently. This decreased occurrence of the ejections is in keeping with the previously made observations of increased streak length (section 5.4.3). The probability of the sweep mechanisms (quadrant IV) increases with heat addition in the region where it makes the dominant contribution ($100 < z^+ < 1000$). With the sweeps becoming more frequent, while maintaining the same total contribution to Reynolds shear stress, the sweep events must be weaker in nature. This weakening agrees with the decreasing contribution of the outward interactions identified above as fluid reflecting from the wall from a sweep contributes to this phenomena.

When the heat release occurs as a result of chemical heat evolution (ie. combustion), the mechanism of turbulent Reynolds shear stress reduction changes somewhat. The most significant change

in transport mechanisms is an increasing contribution, compared to the unheated flow, of sweeps to the Reynolds shear stress term (figure 5.3-31(d)). This increase alone would conceivably increase the transport of momentum to the wall, leading to an overall increase in wall shear stress. However, this increase is offset by a decrease in contribution of the ejection mechanism that is greater than observed for the heat source approach. With no significant differences in thermal distributions between the heat source and combustion case, this increasing sweep contribution is thought to be due to the presence of different density combustion products altering the boundary layer flow structures. Figure 5.3-31(e) shows the probability of each quadrant event occurring when heat is added through combustion. Compared to the heat source alone, the likelihood of sweeps is increased, suggesting that its increased contribution is due to increased frequency, not severity. A further decrease in ejection probability from the heat source approach also suggests that there is no change in strength of the ejection mechanisms, just a decreasing frequency. Most notably, there is an increase in the probability of the outward interaction mechanism such that it is more likely than the ejection process across the boundary layer. By transporting more high momentum fluid away from the wall, this process serves to further decrease the wall shear stress, while contributing further to offset the increasing sweep contribution.

The viscous transport of momentum is decomposed using the same quadrant decomposition method. The contributions for a heat source term and chemical heat evolution are plotted for case 1 in figures 5.3-31(c) and 5.3-31(f) respectively. For both methods of heat introduction we observe the same trends in the viscous transport of momentum as we did for the turbulent Reynolds shear stress and it is clear to see that quadrant IV events make the dominant contribution to the viscous transport of momentum. For the heat source, the main near wall reduction occurs for the ejection mechanisms. Hence, we can observe that there is less viscous transport of momentum that is associated with ejection events in the near wall region. Similarly, there is a slight decrease in the contribution of sweep events in the immediate vicinity of the wall ($z/\delta < 0.01$). When chemical heat evolution is employed, we see the same increasing contribution of sweep events and further decreasing contribution of ejection events as was observed for the Reynolds shear stress decomposition. These results show that there is a close correlation in behaviour between the turbulent Reynolds shear stress and viscous transport of momentum when heat is added.

In a similar approach to quadrant decomposition, the turbulent Reynolds shear stress can be divided into eight octants based on the velocity fluctuations u' and w' and the temperature fluctuations T'. The eight octants are shown in figure 4.1-37. This process makes it possible to analyse how the turbulent Reynolds stress interacts with the thermal energy field across the boundary layer.

A key observation to make when heat is added through a source term is that for $z^+ < 100$, the ejection and sweep of cold fluid (octants II and IV) remains largely unchanged (figure 5.3-32). However, across nearly the entirety of the boundary layer ($z^+ < 1000$), there is a significant reduction in the contribution of the ejection of hot fluid (octant VI), compared to the unheated flow to almost negligible levels of Reynolds shear stress. This result indicates that the presence of a heated region severely impares the ejection of hot gas from the very near wall regions, a process that normally contributes significantly to the turbulent Reynolds shear stress. When heat is added through chemical evolution, we see largely the same behaviour in octant contributions. One notable difference is the now near suppresion of hot ejections (octant VI) for $z^+ < 1000$ from the turbulent Reynolds shear stress. As was observed for the quadrant analysis, there remains a significant increase in the contribution of sweeps of high momentum fluid to the wall. Here we can identify this as an increase in the sweep of cold fluid, which then ties in with the observation of decreased ejections of hot fluid. This increasing contribution of sweep events, however, does not match the decrease in hot ejection contribution that occurs and an overall decrease in shear stress still results.

The wall normal turbulent heat flux is also decomposed into eight contributing octants in figure 5.3-33. For both heat addition approaches, we observe an increasing contribution of cold turbulent transport half of the octants to the total wall normal turbulent heat flux. This increasing contribution of cold ejection and cold sweeps to the turbulent wall normal heat flux is a result of the fluid in the very near wall region and freestream flow circulating up and down, slowly permeating the heated regions and hence bringing cooler fluid with them. The increasing contribution of cold ejections can be thought of as a direct result of the increasing cold sweep contribution. Combining this observation with the increased contribution of cold sweeps to the Reynolds shear stress could suggest that there is a reduction in turbulent mixing to the near wall region, hence, retaining more cool fluid in these regions. Unlike the Reynolds shear stress, there is no alteration to the octants contributing to the wall normal heat flux near the wall ($z^+ < 100$). This demonstrates that, unlike the wall shear stress, we do not expect to see a decreasing wall heat transfer through reducing turbulent transport.

As has been discussed previously, the simulations presented here for combustion are that of premixed hydrogen and air and unlike the experimental configurations, where a jet of hydrogen is injected at the wall, there is a relatively low mass fraction of hydrogen at the surface. These low hydrogen mass fraction levels would occur experimentally quite far downstream of injection. As such, this would occur at a point where wall heat transfer is expected to rise from analytical

calculations (Stalker, 2005). Hence, the observation of no reduction in heat transfer to the wall is corroborated. However, were the combustion to occur further from the wall, at the interface of the hydrogen jet and mainstream air, as occurs in the experiments, it is possible that the increasing cold sweep contribution to the wall normal turbulent heat flux may lead to the reductions in wall heat transfer observed experimentally (Suraweera, 2006; Goyne, 1998).

5.4.6 Turbulent Stress Transport

Examination of the budgets of the turbulent Reynolds stress and turbulent kinetic energy is useful for developing an understanding of the transport of momentum through turbulent processes. The budgets provide a detailed description of how turbulent velocity fluctuations are produced, dissipated and transported between directional components within a boundary layer. The terms computed for the presented budgets are normalized by the nominal freestream components as described in section 4.1.8.

By analysing the turbulent kinetic energy transfer, it is expected that the viscous drag is reduced through two mechanisms: (a) a reduction in turbulent energy production which suggests that the heating process damps the transfer of energy from the mean flow into turbulent fluctuations, and/or (b) a reduction of the dissipation of turbulence (Gyr and Bewersdorff, 1995). McMurtry et al. (1989) observed that the most significant effect of heat release on the turbulent kinetic energy balance was manifested through a reduction in mean-flow production of turbulent kinetic energy. The turbulent kinetic energy redistribution and viscous dissipation terms are other key aspects of the flow, which are influenced by heat addition.

A lowering of the turbulent kinetic energy production is observed in figures 5.3-34 and 5.3-35. It is the production term that describes the exchange of energy between the mean flow and the fluctuating motions as it results from the interaction of the mean velocity gradient and turbulent stresses. The turbulence generation process is characterized physically by the ejection of low speed fluid created by streaks being ejected from the wall, inducing wall normal transport and wall shear stress, and finally interacting with the mean boundary layer velocity profile. In the preceding sections we have clearly observed a reduction in ejection processes through elongation of the near wall streaks, giving rise to lower turbulent production. In other words, lower turbulence production implies lower turbulent transport rates and thus lower exchange of mass, momentum and energy amongst fluid elements and the wall. The distribution of the turbulent kinetic energy

production remains essentially the same, marked only by a decrease in peak level. However, the production of turbulent kinetic energy does not completely account for the reductions in turbulent momentum transfer.

The production of turbulent shear stress (figures 5.3-36 and 5.3-37), like the turbulent kinetic energy production, is dominated by the mean velocity gradient and behaves in a similar manner. However, for the turbulent shear stress, the production arises from the interaction of the wall normal velocity fluctuations with the mean velocity gradient. A more significant reduction in the production is observed here. This indicates reduced wall normal velocity fluctuations, which correlates with profiles of the RMS wall normal velocity fluctuations indicated. Figures 5.3-38 and 5.3-39 plot the changes in the pressure-strain term associated with the transport of the Reynolds shear stress for the heat source and combustion process respectively. Under normal unheated conditions the pressure transport is largely responsible for balancing the production of Reynolds shear stress. Clearly there is an increasing contribution of the pressure transport to the production of Reynolds shear stress in the immediate vicinity of the wall. This increase, however, quickly diminishes and once again provides a contribution to the removal of Reynolds shear stress that decays to zero as the wall normal distance increases.

As stated earlier, there is no direct production of spanwise or wall-normal velocity fluctuations from the mean flow. These fluctuations are produced by the redistribution of energy from the streamwise component to the other normal stress components by the pressure-strain and turbulent diffusion. The pressure-strain, however, has no effect on the turbulent kinetic energy as the sum of the pressure-strain terms for each direction is zero. Instead, each component is plotted separately in figures 5.3-40 and 5.3-41. When heat is added to the flow, we see a suppresion of the pressure-strain curves in the streamwise and wall normal direction for case 1. The streamwise pressure-strain curve becomes less negative, indicating there is now less removal of streamwise velocity fluctuations and, correspondingly, there is now less of a source of velocity fluctuations in the wall normal direction through a reduction in the positive contribution of the wall-normal pressure-strain. This change in the pressure redistribution is a clear indication of how the heat addition process inhibits the formation of spanwise and wall normal velocity fluctuations. The behaviour of the pressure-strain profiles for the combustion chemical kinetics differs from that of the heat source term. For the $z \approx 3$mm in the middle of the boundary layer/reaction region, the streamwise component of the pressure-strain is seen to reduce rapidly and the wall normal component begins to act as a sink for the fluctuations, rather than the conventional source. There is also a movement of the pressure-strain profiles towards the wall that is not observed for the heat source approach.

This overall reduction in turbulence redistribution for both heat addition approaches leads to lower mixing rates and lower momentum transfer, as was observed through lower shear layer growth rates when heat was added to a shear layer by McMurtry et al. (1989).

The turbulent diffusion provides another description of the redistribution of turbulent kinetic energy by the fluctuating velocity field, but its contribution is smaller than the pressure-strain term. Near the wall there is still a reduction in turbulent diffusion to be observed giving further indication of the changes occurring in the turbulent transport process. The turbulent shear stress turbulent diffusion term appears to be less affected than the pressure-strain term by the heat release.

The terms of the transport of turbulent kinetic energy that are of smaller magnitude than the dominant terms still play an important role in the overall transport of momentum and are sensitive to the addition of heat. The pressure dilatation represents a transfer mechanism between internal energy and kinetic energy other than dissipation. The pressure dilatation forms a component of what is collectively termed the compressibility contributions. The low level of the pressure dilatation and, hence, compressibility effects observed under no heat addition conditions is maintained when heat is added through both means (figures 5.3-42 and 5.3-43). The fact that the pressure dilatation remains negligible compared to the loss of turbulent kinetic energy due to dissipation maintains agreement with the DNS results of Guarini et al. (2000), Maeder (2000) and Xu and Martin (2004). For $z/\delta < 0.1$ there is a decreasing negative contribution suggesting that when heat is added through a source term, there is less of a transfer of turbulent kinetic energy from turbulent kinetic energy to internal energy. Unlike the heat source approach, the combustion process simulations leads to increased transfer of turbulent kinetic energy to internal energy for $z/\delta > 0.25$. This increased transfer of turbulent kinetic energy to internal energy could represent another mechanism of reducing turbulent transport of momentum. The turbulence convection term, while negligible relative to other terms shows a large reduction in magnitude for $z/\delta < 0.1$ and a corresponding increasing magnitude for $z/\delta > 0.3$. This change in turbulent convection is presumed to be caused by the disturbance associated with the heat addition or combustion process. The mass flux variation remains zero.

From the presented results, it is seen that the most significant effects of the heat release are a reduction in the turbulent production term for the turbulent Reynolds shear stress and turbulent kinetic energy budgets and reduced redistribution of the produced streamwise turbulence, thus leading to lower turbulent transport.

5.4.7 Strong Reynolds Analogy

When heat is added to the boundary layer it is important to see if the momentum and thermal energy remain transported by the same mechanisms. The Strong Reynolds Analogy allows for assessment of any such changes. The large negative correlation of the velocity and temperature fluctuations inbuilt to the SRA is still not observed in the computational results in figure 5.3-44. When heat is added, results show some deviation from its conventional behaviour. There exists more of a large negative correlation across the mid regions of the boundary layer, approaching a minima of ≈ 0.75 at $z/\delta = 0.5$, but still suggesting good agreement with the SRA. However, close to the wall ($z/\delta < 0.2$), the addition of heat leads to greater decorrelation of the fluctuations than if no heat were added. Debieve et al. (1997) experimentally determined that the correlation coefficient ($R_{u'T'}$) was not significantly influenced by at step change increase in wall temperature with little deviation from the adiabatic value of 0.8-0.9 being observed. This similar type of behaviour demonstrates that overall we are observing a behaviour that has been identified through previous experiment.

The computations of turbulent Prandtl number are presented in figure 5.3-45. For heat addition through a source term, the results remain in relatively good agreement with the commonly accepted value. However, the heat addition appears to shift the curve down, taking on a mid boundary layer value of approximately 0.75. This reduction in turbulent Prandtl number implies that there is slightly greater turbulent transport of heat than momentum. For the results from combustion, the turbulent Prandtl number estimation suffers from the presence of locations of zero computed heat flux. At points of zero heat flux the turbulent Prandtl number becomes undefined causing the plotted profile to exhibit significant fluctuations. These effects have been noticed before by Calhoon et al. (2003) in studying heat release and compressibility effects on planar shear layer development. Consequently, the turbulent Prandtl number for combustion is not included in figure 5.3-45.

Examining the SRA revealed that the inclusion of the terms to account for significant heat transfer in equation 4.42 returned unrealistic results, particularly when the combustion case turbulent Prandtl number was used. This suggested that either the addition of heat violated assumptions in its derivation or the SRA in that form no longer applied. However, the conventional SRA (Eq 4.37) that does not account for significant heat transfer, is plotted in figure 5.3-46. The agreement of the results with theory demonstrates that the flow appears to still be adhering to the assumption of similarity between turbulent heat and mass transfer when heat is added through a source term.

The success of the conventional formulation of the SRA may be attributed to the added heat approximately balancing the heat transfer to the wall, removing the need to account for it. The combustion process leads to the general tendency to shift the SRA curve upwards. An upward shift implies that the combustion process introduces greater temperature fluctuations than the heat source approach. The same behaviour in the viscous sublayer is observed for both methods of heat addition with the denominator (velocity and its fluctuations) tending to zero faster than the numerator (temperature and its fluctuations).

5.4.8 Instantaneous Fields

Instantaneous flow field visualisations are used to further interpret the effects of heat release for case 1. The same phenomena are observed for case 2, but are not presented as the same changes occur. Figure 5.3-47 gives an instantaneous static temperature field snapshot showing the regions that are influenced by the introduction of heat to the boundary layer. The instantaneous static temperature fields give perspective for the heat addition regions relative to the contour plots presented in figures 5.3-48 and 5.3-49. The latter figures allow for examination of the vorticity dynamics of the flow and thus how the large scale structures of the flow are influenced. The three dimensional nature of the turbulent structure interactions mean that the vorticity alone is no longer a completely reliable representation of the fluid motion (McMurtry et al., 1989), for instance, in laminar shear flow there is vorticity without rotation (Bernard and Wallace, 2002). However, interpretations can still be made.

The instantaneous vorticity magnitude, which is dominated by the spanwise component of vorticity, given in figures 5.3-48 and 5.3-49 are for two time samples for case 1 without heat, with heat source and with combustion. The filled contours represent a greyscale of vorticity magnitude from zero to $1.5 \times 10^6\ s^{-1}$. The lines represent contours of spanwise baroclinic torque at uniform intervals from -5×10^{10} to $5 \times 10^{10}\ s^{-2}$. The baroclinic torque is defined as:

$$T_{bc} = \frac{(\nabla\rho \times \nabla p)}{\rho^2} \tag{5.14}$$

Baroclinic torque appears whenever surfaces of constant density and surfaces of constant pressure and their respective gradients are not aligned and makes a contribution to the rate of change of

vorticity. The baroclinic torques have been reasoned by Wallace (1981) (reference in McMurtry et al. (1989)) to act to reduce the entrainment velocities of a mixing layer.

The most apparent differences between the case of no heat addition and those where heat is added, is that when heat was added the baroclinic torque increases in the outer regions of the boundary layer. By combining this observation of increased baroclinic torque contribution in the outer region of the boundary layer with the identification of a reduction of the vorticity magnitude in the outer boundary layer, some links could be made. This phenomena was identified by examining the same points at the same spatial and temporal location with and without heat release. Some such points are clearly identified in the figures. This observation is similar to that of McMurtry et al. (1989), where the baroclinic torque was observed to decrease the vorticity near the upper and lower limits of the mixing layer. It appears that for the conditions studied there was a more diffuse vortex structure resulting from the increased baroclinic torque, decreasing the mass entrainment into the boundary layer. This reduction in entrainment of mass from the mainstream flow is entirely consistent with the previously made observations of reductions in turbulent transport of momentum. It stands to reason that any reduction in mass and hence momentum entrainment in the outer regions of the boundary layer results in a reduction in the momentum transported to the wall through turbulent means.

To find the structure within a turbulent boundary layer, however, we require a more sophisticated method of identification than the obvious choice of concentrated regions of vorticity. Instead, vortical structures are identified by following the approach developed by Chong et al. (1998) with extension to compressible flow by Pirozzoli and Grasso (2006). The resulting technique enables vortex structures to be identified in whatever form they have. To begin with, P, Q and R are defined as the first, second and third invariants of the strain rate tensor (S_{ij}, equation 3.16).

The first invariant of S_{ij} is defined;

$$P = -S_{ii} \tag{5.15}$$

the second invariant is defined;

$$Q = \frac{1}{2}\left(S_{ii}^2 - S_{ij}S_{ji}\right) \tag{5.16}$$

and finally, the third is defined:

$$\begin{aligned} R &= -\det(S_{ij}) \\ &= -(S_{11}S_{22}S_{33} + S_{13}S_{21}S_{32} + S_{12}S_{23}S_{31} - \\ &\quad S_{13}S_{22}S_{31} - S_{11}S_{23}S_{32} - S_{12}S_{21}S_{33}) \end{aligned} \tag{5.17}$$

From these invariants it is possible to construct a velocity gradient tensor discriminant, D. Even though the three-dimensional trajectories of particles can be extremely complex and confusing and, hence, give no real insight into turbulent eddy motions, isosurfaces of D enclose rather concentrated and well-ordered vortex lines (Chong et al., 1998). The discriminant is defined as:

$$D = \left(\frac{\Delta}{(U_\infty/\delta_2)^6} \right) \tag{5.18}$$

where:

$$\Delta = \frac{27}{4}R^2 + \left(P^3 - \frac{9}{2}PQ \right) R + \left(Q^3 - \frac{1}{4}P^2Q^2 \right) \tag{5.19}$$

The discriminant isosurface value is chosen with the stipulation that it must be small enough to capture an adequate number of structures, but large enough such that too many structures are not identified and interpretation becomes difficult. The threshold value of Pirozzoli and Grasso (2006) is applied:

$$\left(\frac{\Delta}{(U_\infty/\delta_2)^6} \right) > 3.61 \times 10^{-3} \tag{5.20}$$

The iso-contour visualization of the vortical structures near the wall in the $x - y$ and $x - z$ plane is given in figures 5.3-50 and 5.3-51 respectively. Visible in figure 5.3-50 are the quasi-streamwise vortices consistent with the observations from the two-point correlations of velocity and the generally accepted turbulent boundary layer coherent structure theory (Robinson, 1991) in the near wall region. While the two-point correlations of velocity fluctuations indicated an elongation of the streaks, the instantaneous visualizations of the vortex structures are not as clear. When heat is added, it can be argued that there is a decreasing occurrence of short streaks and those that remain are as long or longer than those present when no heat is added. However, given that these visualizations represent a discrete point in time for the flow, conclusions about the effects of heat addition are limited because a complete statistical picture is not presented. The correlations, on the other hand, provide the better illustration of the effects of heat addition on streak length. From figure 5.3-51 we see, above the near wall region ($z \approx 0.5\delta$), the vortex structures that

have lifted up from the wall through an ejection process when no heat is added. However, when heat is added through a source term, there is a clear reduction in the occurrence of these ejected vortices. The same observation is made when heat is added through combustion, but the effects are less striking. This decrease in ejected vortices is entirely consistent with the lower contribution of the ejection mechanism to the Reynolds shear stress identified through the quadrant analysis results of section 5.4.5. Similarly, there does appear to be agreement between the vortex structure and vorticity, with both quantities being more diffuse for $z \approx 0.5\delta$ when heat is added (see also figures 5.3-48 and 5.3-49).

Finally, instantaneous visualizations of the gradient of density ($\nabla\rho$) are presented in figure 5.3-52. These visualizations reinforce the observation of decreasing ejection mechanisms. For the case of no heat addition, structures reaching from the very near wall region towards the outer boundary layer are clearly visible. It is these structures that are the result of the lift-up (ejection) of the near wall streaks and the formation of hairpin/horseshoe vortices. When heat is added through a heat source term or combustion, the lift-up of the streaks is less noticeable, correlating with the observations made earlier.

5.5 Summary

The work of this chapter had two main goals. The first goal was to verify the numerical scheme employed and demonstrate its validity for describing the turbulent flow and transport within supersonic turbulent boundary layers. In doing so, grid independence was demonstrated while achieving good agreement with various experimental investigations. The grid resolutions and domains were shown to be sufficient to capture the relevant turbulent structures and scales and the observed turbulent transport mechanisms were in agreement with postulated theory for the coherent/organised motions within a turbulent compressible boundary layer. The second goal was to identify the changes that occurred in the turbulent transport mechanisms when heat was added to the boundary layer. Through the process of this investigation, it was observed that using a heat source term returned similar levels of drag reduction and changes in turbulent transport as using finite rate chemical kinetics to model pre-mixed hydrogen combustion. Hence, the heat source approach presents itself as being far more computationally efficient than including chemistry with no significantly detrimental results, thus, suggesting possible computational savings by using the heat source approach for future investigations. The investigation of the effects of heat addition confirmed that drag reduction, that agrees with theoretical predictions, occurs and extends the

understanding of the effects beyond changes to mainstream flow quantities. These changes were demonstrated by interpreting the changes in turbulent statistics, budgets of the resolved Reynolds stress transport equations and instantaneous visualizations of turbulent structure fields. The detailed conclusions from the observations of section 5.4 are discussed in the concluding chapter (Chapter 6).

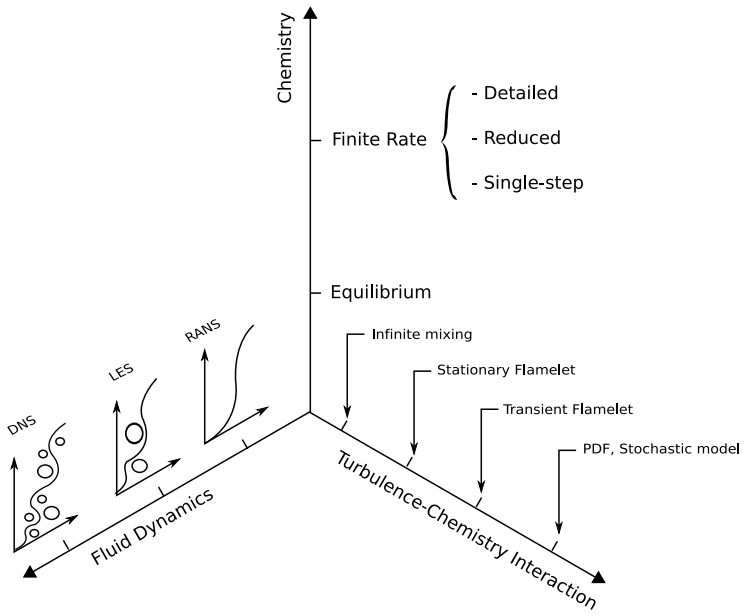

Figure 5.3-1: Various models for turbulent reacting flows for increasing computational demand. Adapted from Chen (2004)

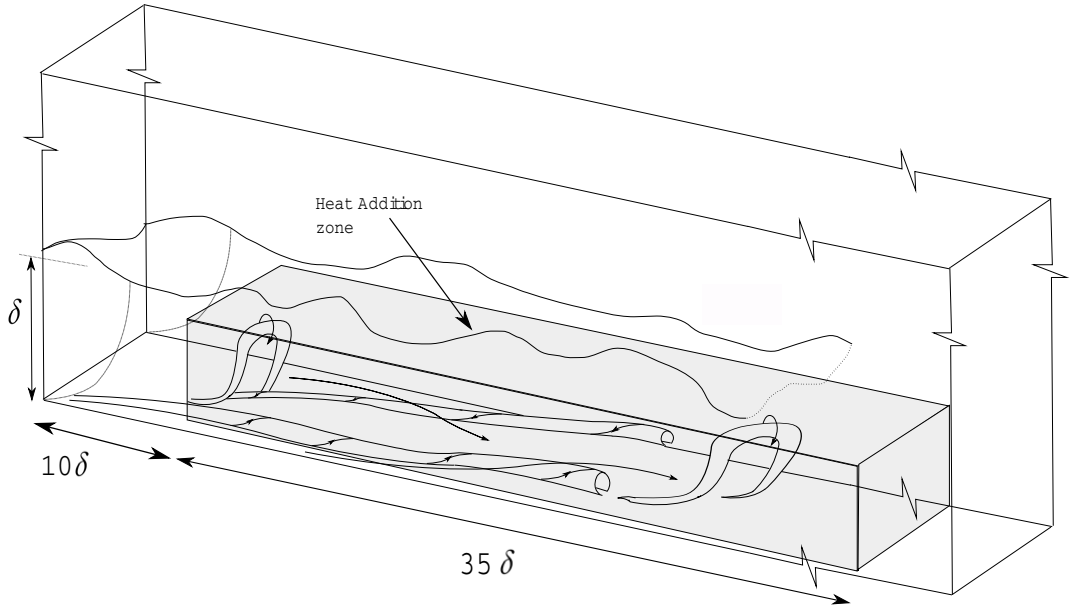

Figure 5.3-2: Region of heat addition through source term

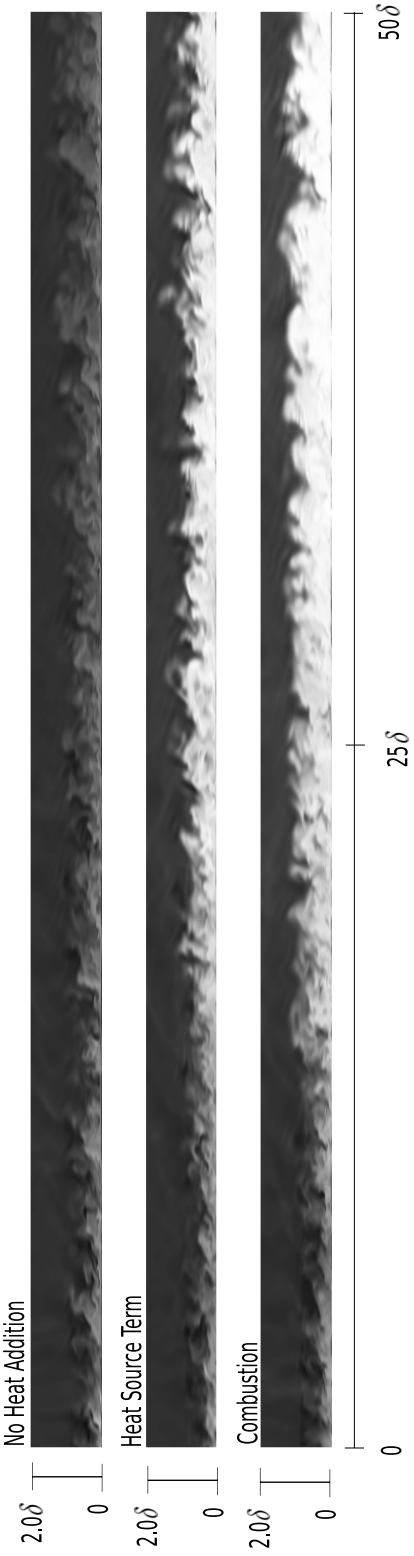

Figure 5.3-3: Instantaneous flow field of static temperature - Case 1. Flow is from left to right. The view of the domain is stretched in vertical direction for clarity.

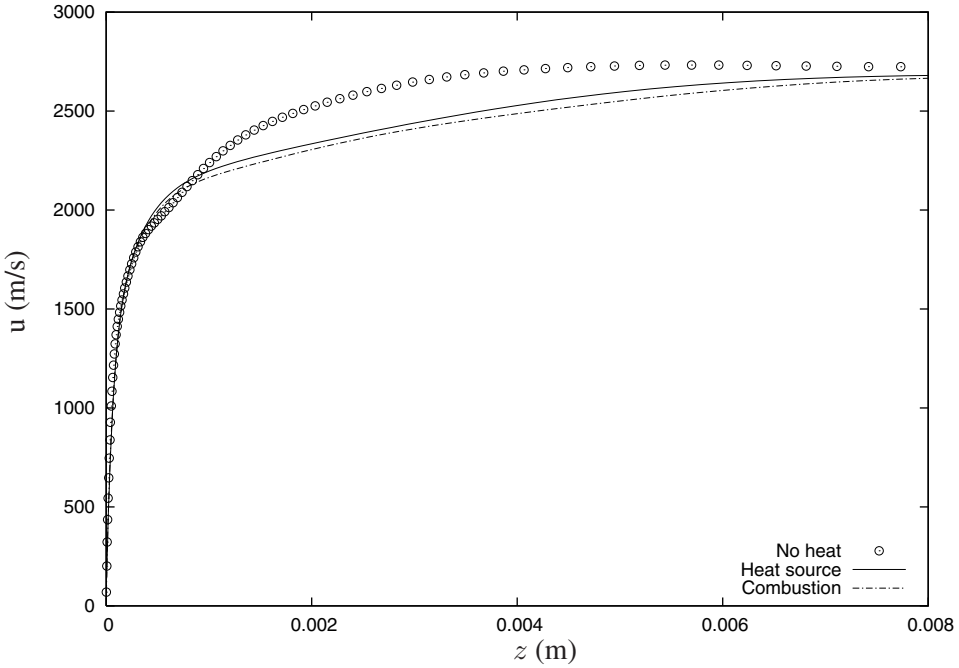

Figure 5.3-4: Effect of heat addition on mean streamwise velocity flow profiles - Case 1.

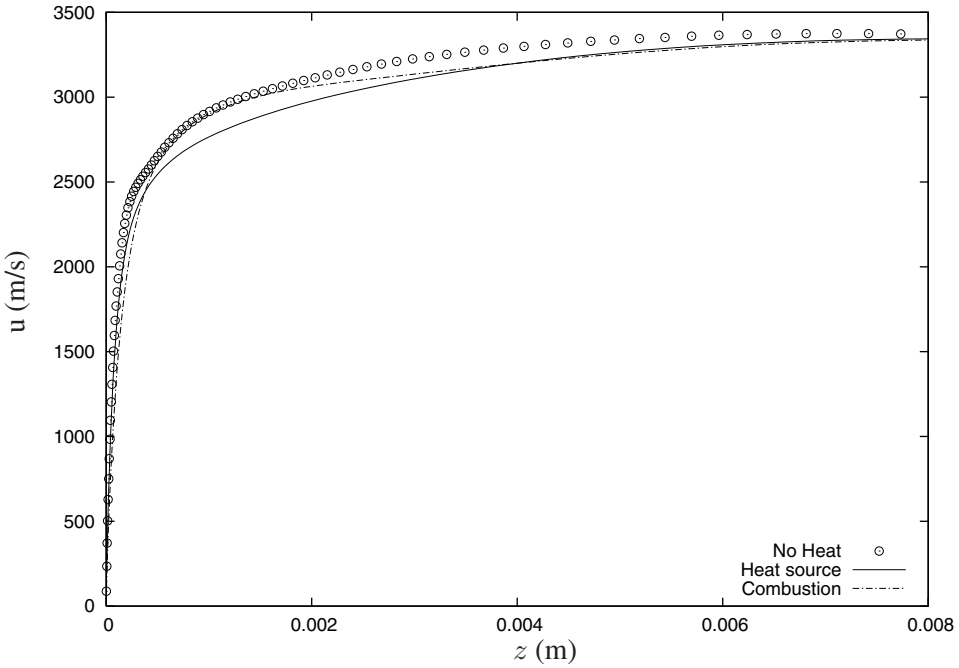

Figure 5.3-5: Effect of heat addition on mean streamwise velocity flow profiles - Case 2.

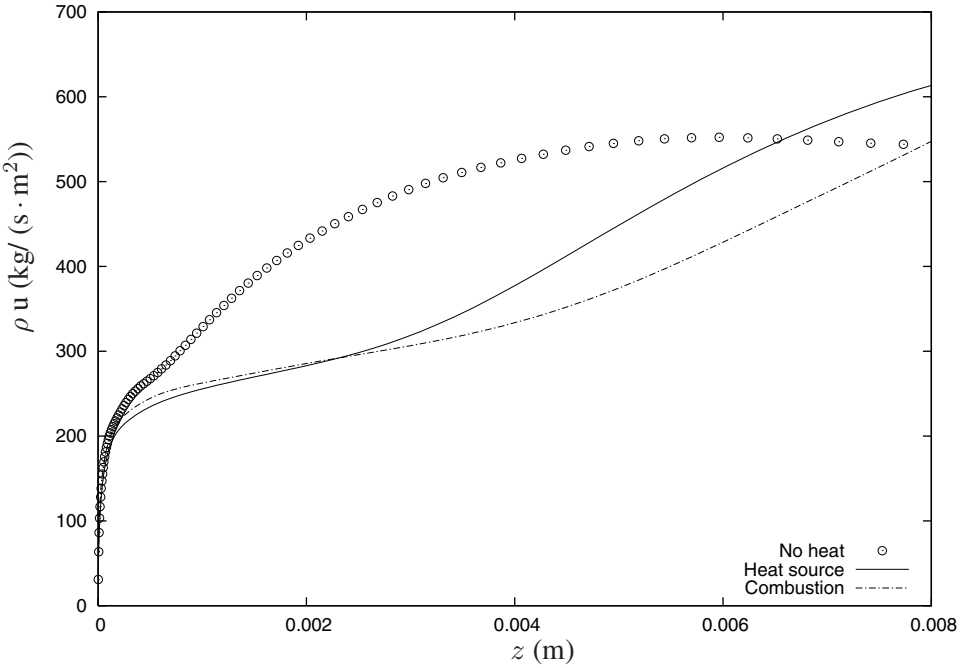

Figure 5.3-6: Effect of heat addition on mean streamwise momentum profiles - Case 1.

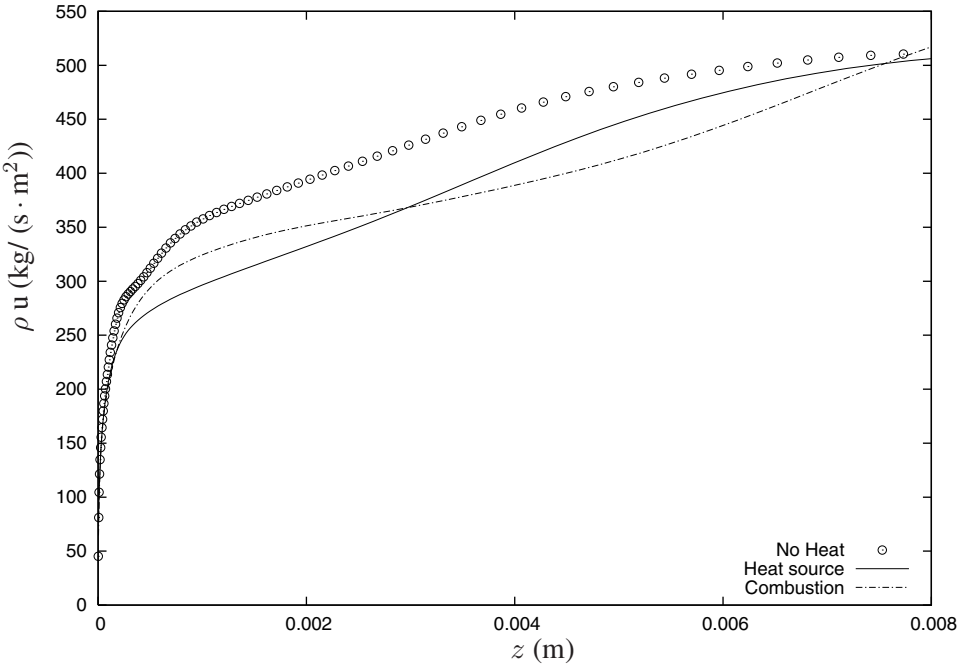

Figure 5.3-7: Effect of heat addition on mean streamwise momentum profiles - Case 2.

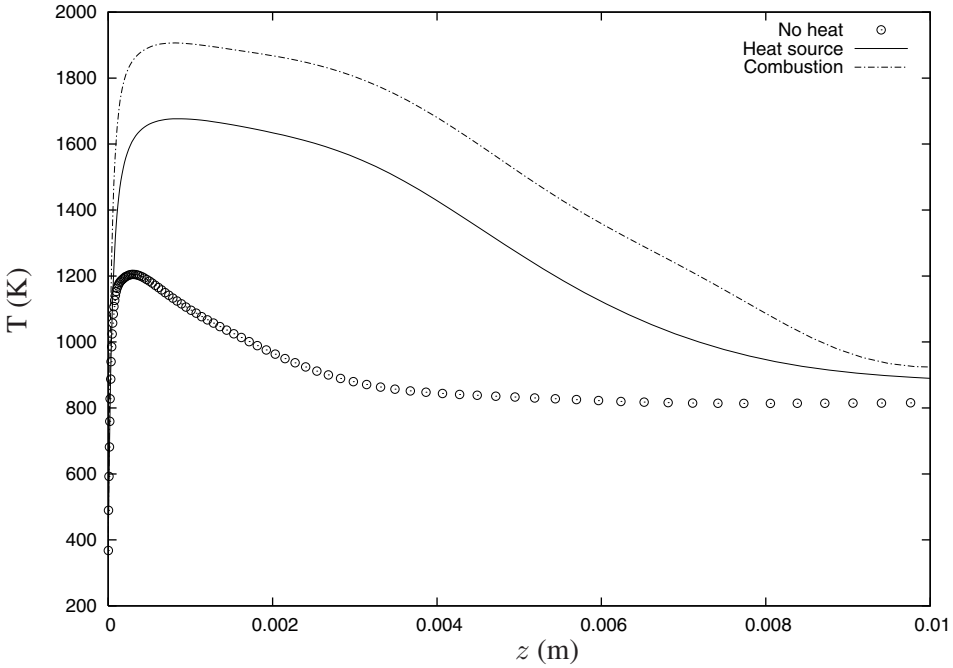

Figure 5.3-8: Effect of heat addition on mean static temperature profiles - Case 1.

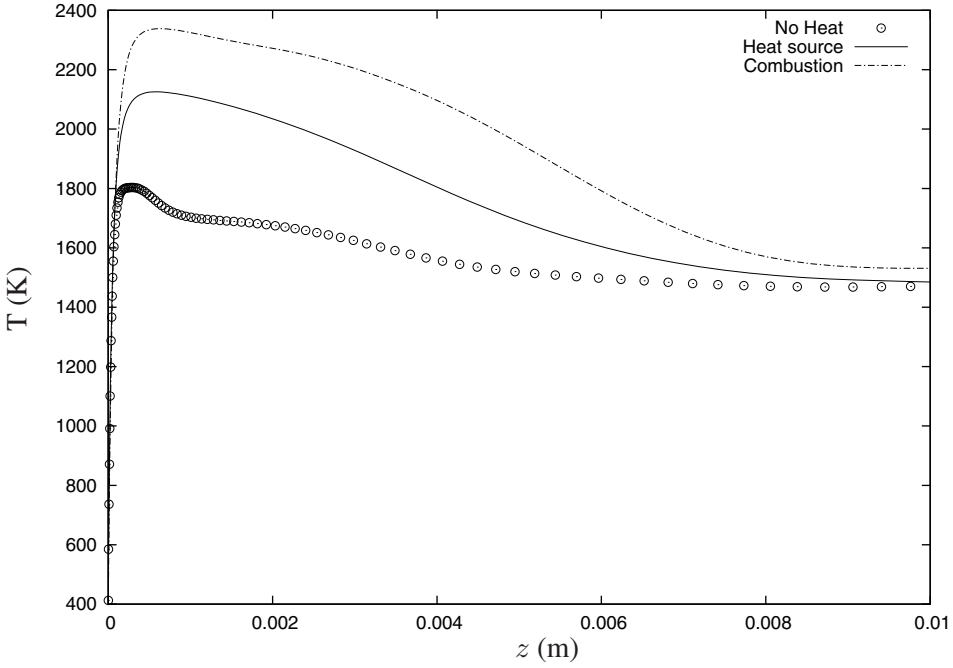

Figure 5.3-9: Effect of heat addition on mean static temperature profiles - Case 2.

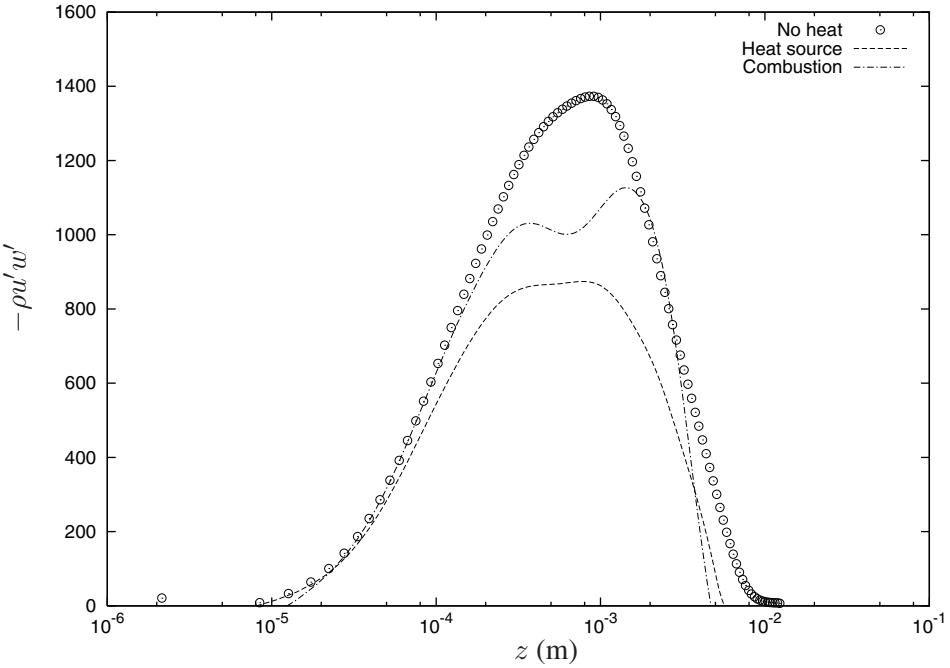

Figure 5.3-10: Effect of heat addition on Reynolds shear stress - Case 1.

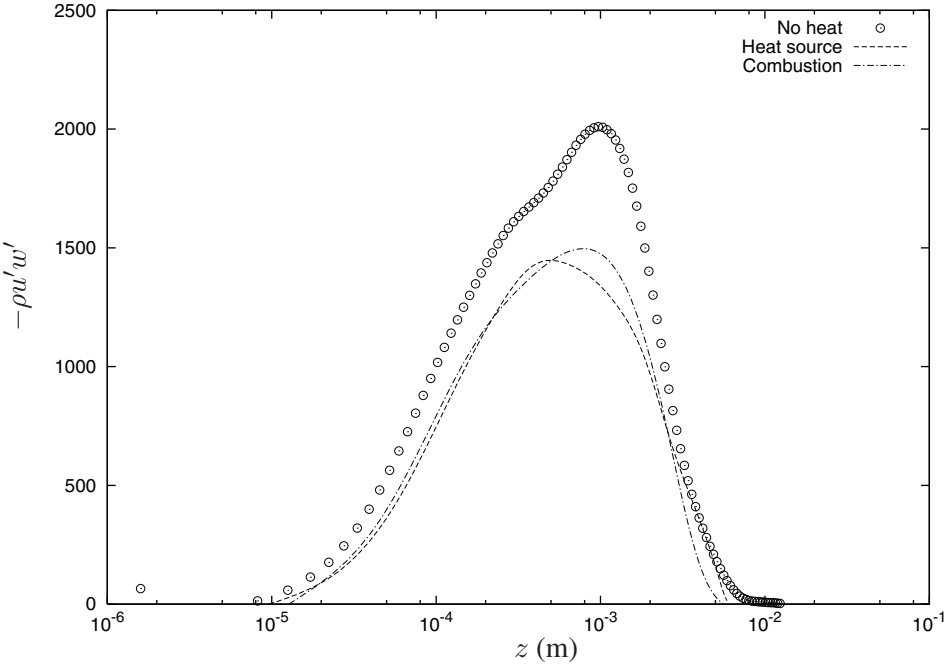

Figure 5.3-11: Effect of heat addition on Reynolds shear stress - Case 2.

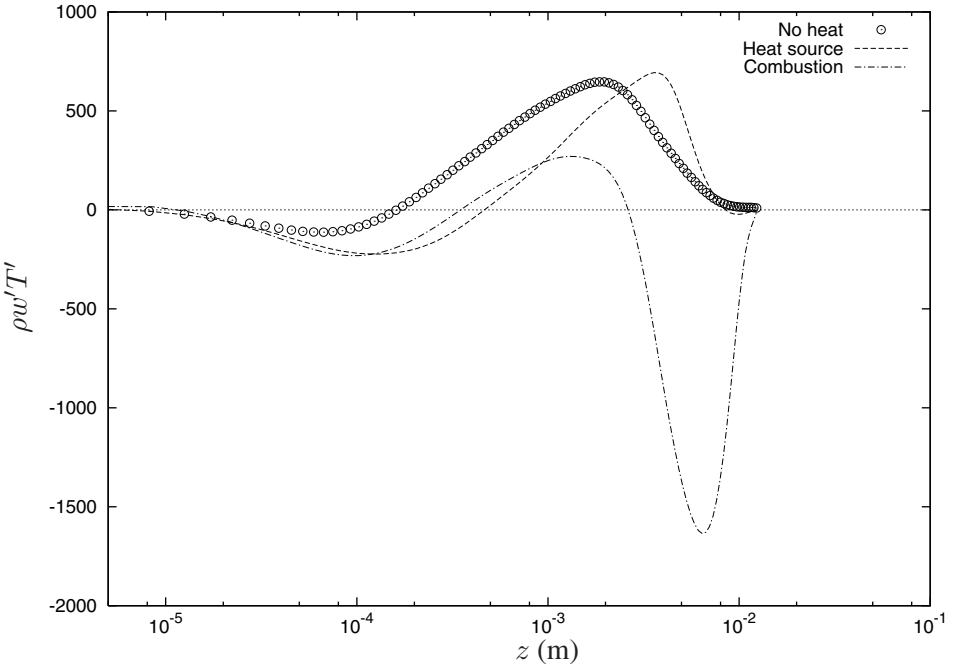

Figure 5.3-12: Effect of heat addition on Reynolds wall normal heat flux - Case 1.

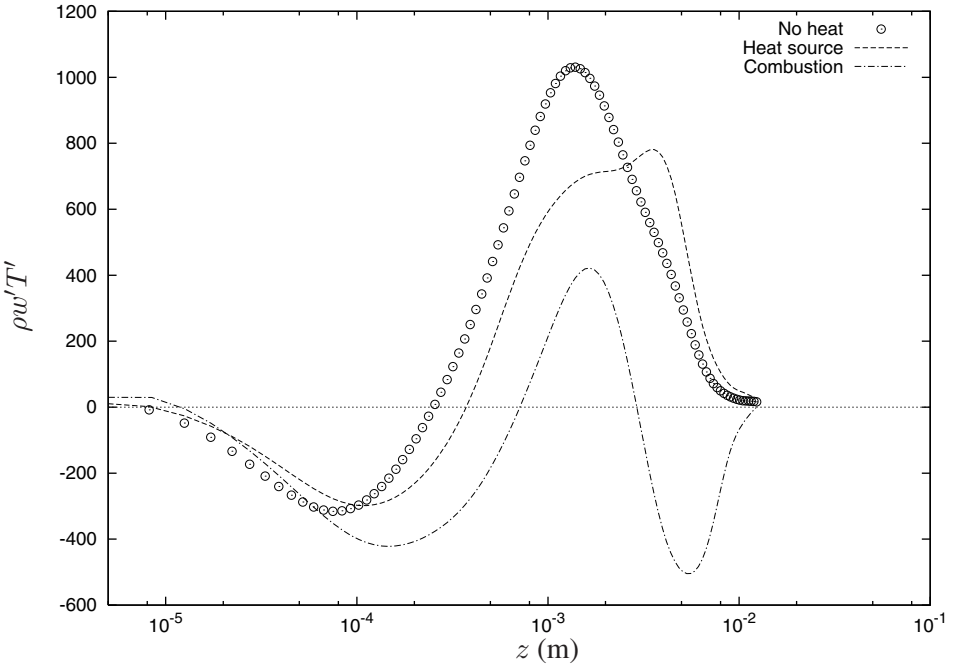

Figure 5.3-13: Effect of heat addition on Reynolds wall normal heat flux - Case 2.

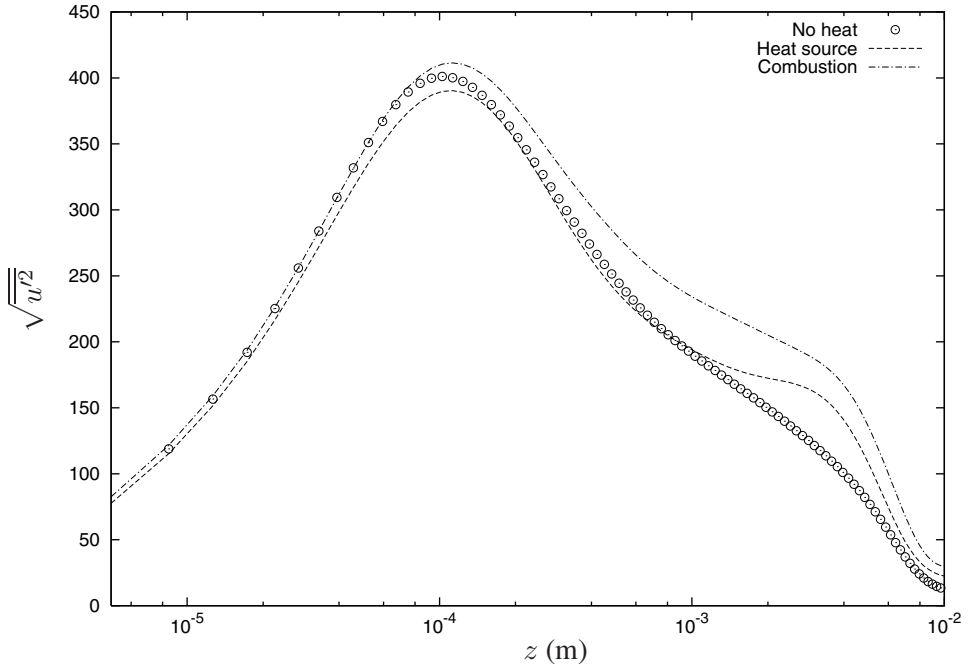

Figure 5.3-14: Effect of heat addition on RMS of streamwise velocity fluctuations - Case 1.

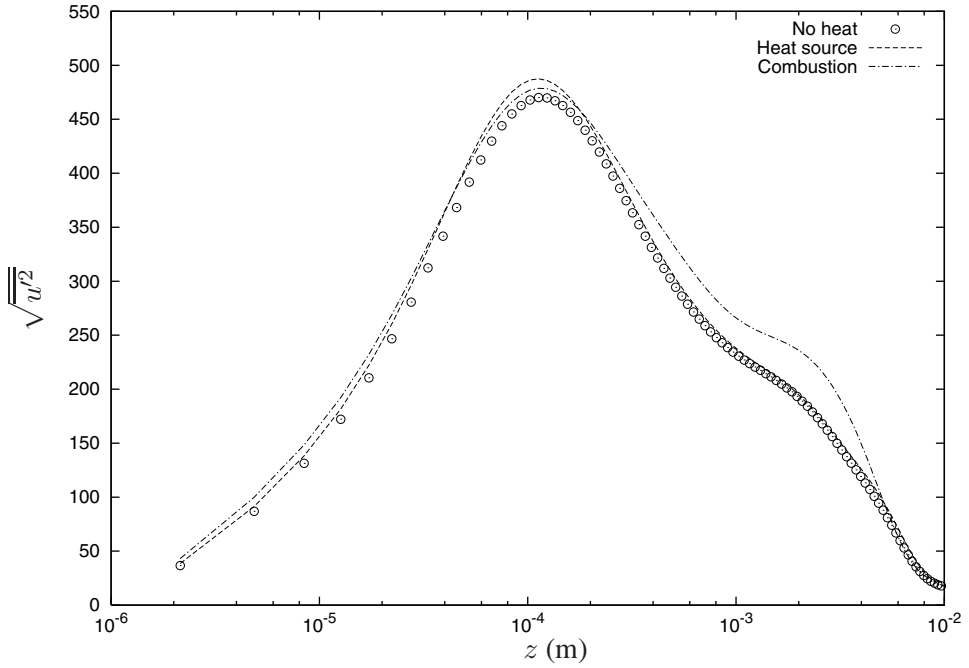

Figure 5.3-15: Effect of heat addition on RMS of streamwise velocity fluctuations - Case 2.

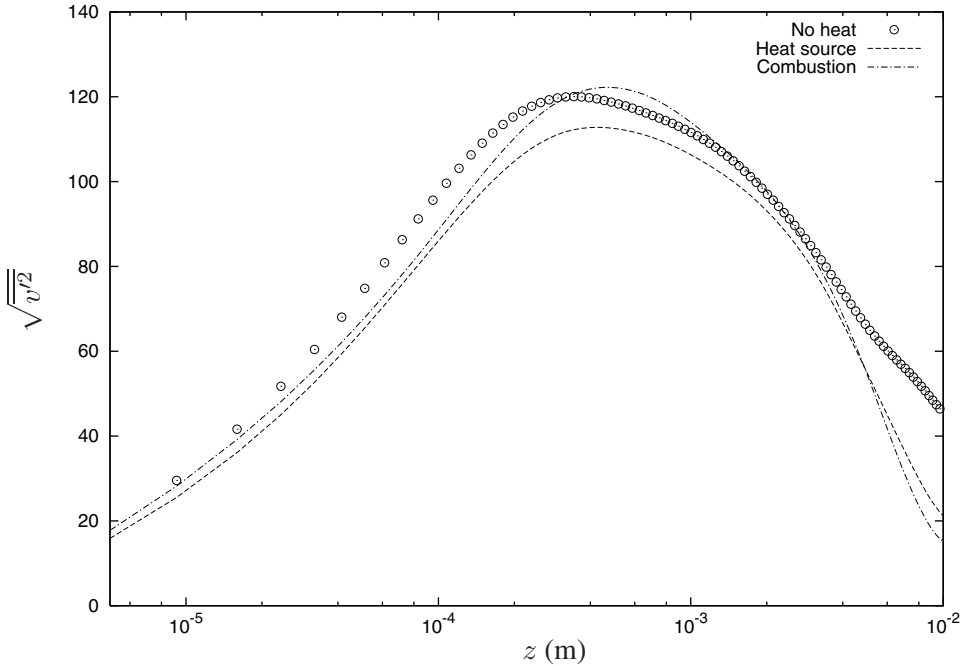

Figure 5.3-16: Effect of heat addition on RMS of spanwise velocity fluctuations - Case 1.

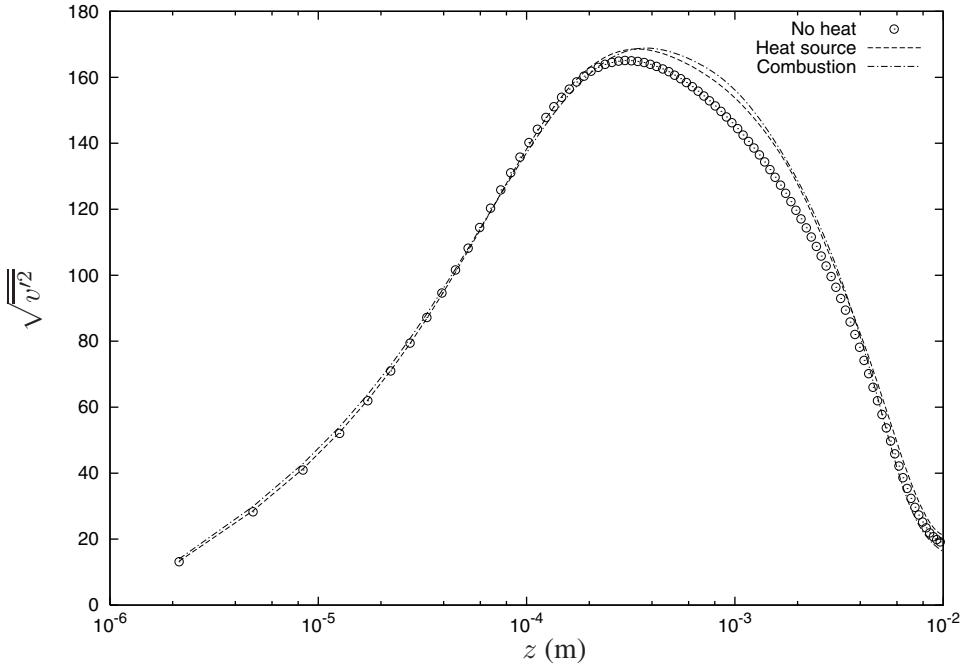

Figure 5.3-17: Effect of heat addition on RMS of spanwise velocity fluctuations - Case 2.

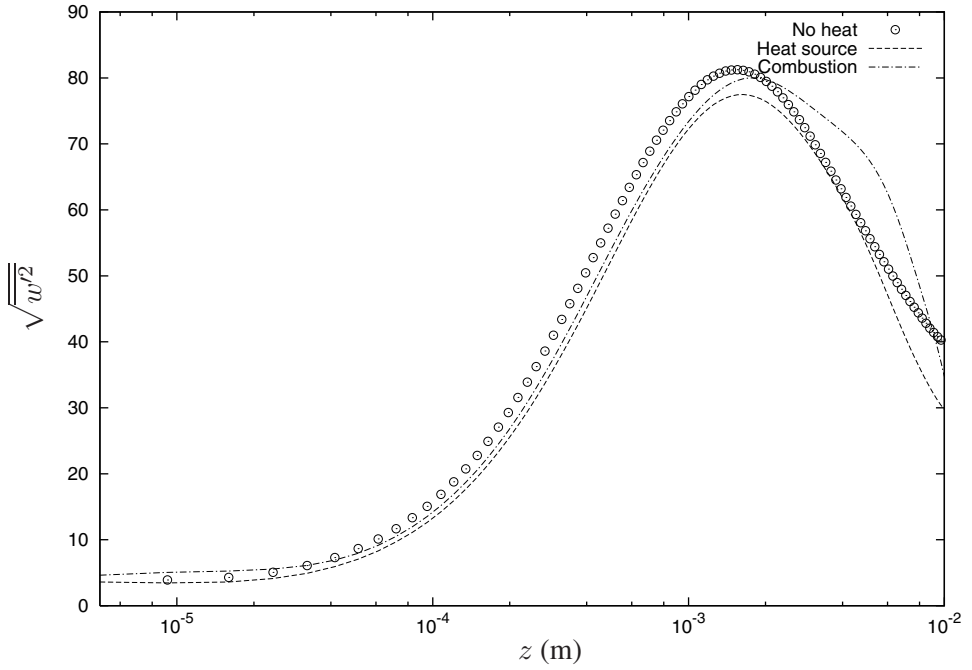

Figure 5.3-18: Effect of heat addition on RMS of wall normal velocity fluctuations - Case 1.

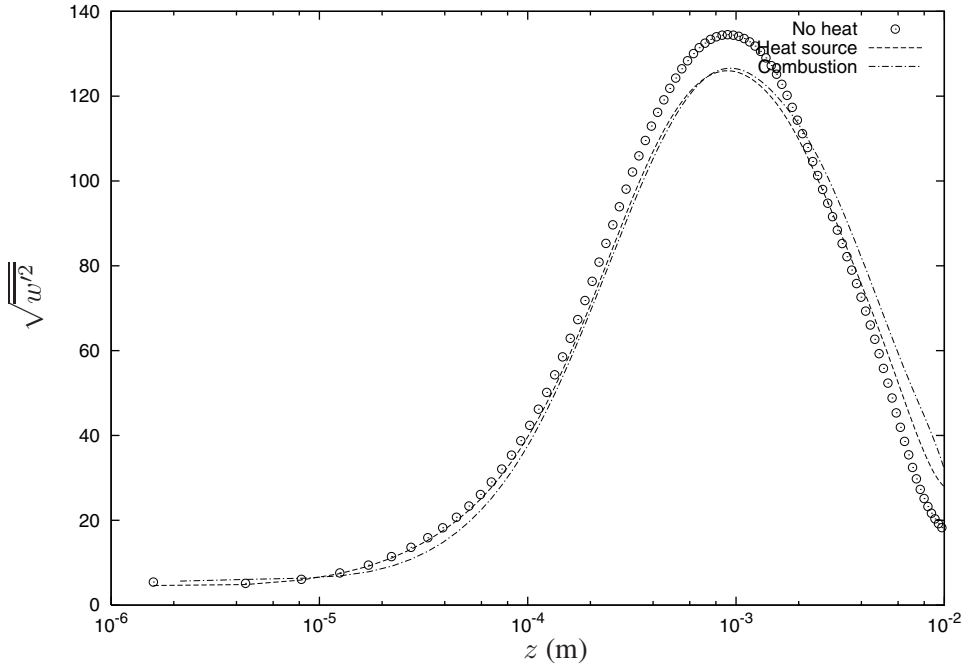

Figure 5.3-19: Effect of heat addition on RMS of wall normal velocity fluctuations - Case 2.

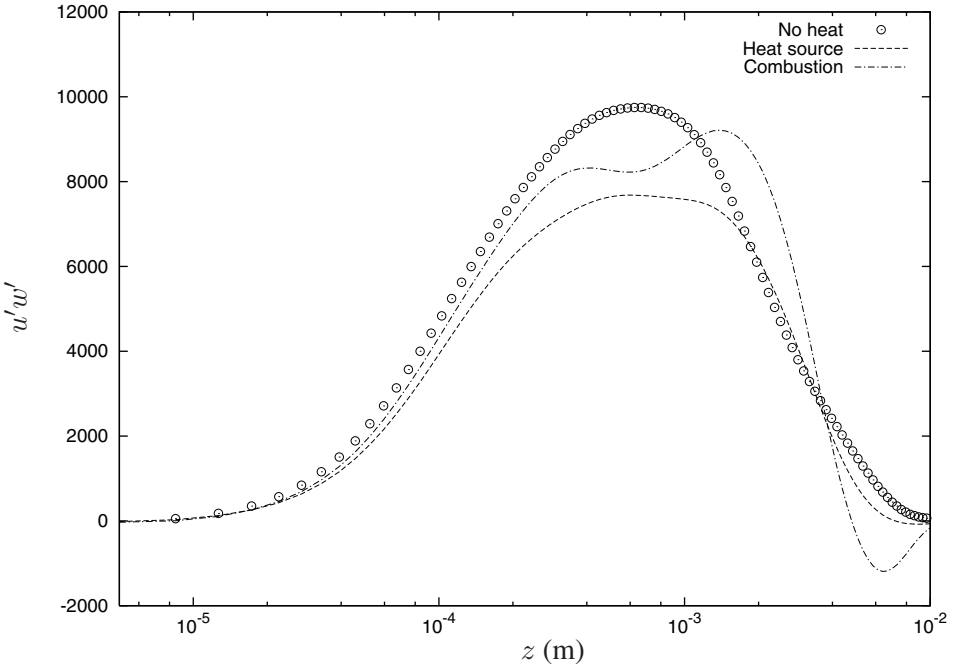

Figure 5.3-20: Effect of heat addition on Reynolds shear stress without density scaling - Case 1.

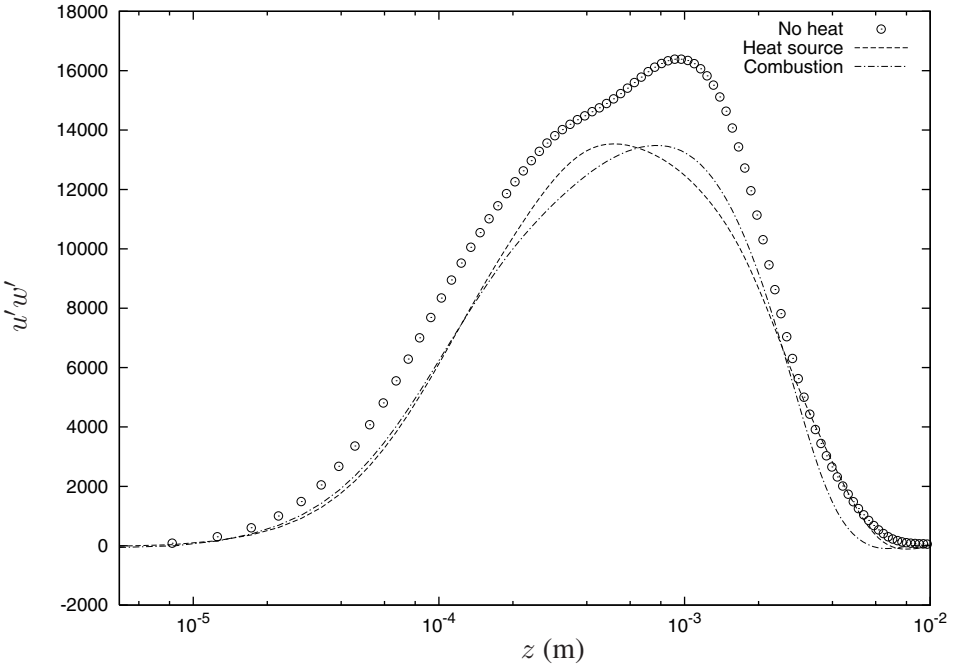

Figure 5.3-21: Effect of heat addition on Reynolds shear stress without density scaling - Case 2.

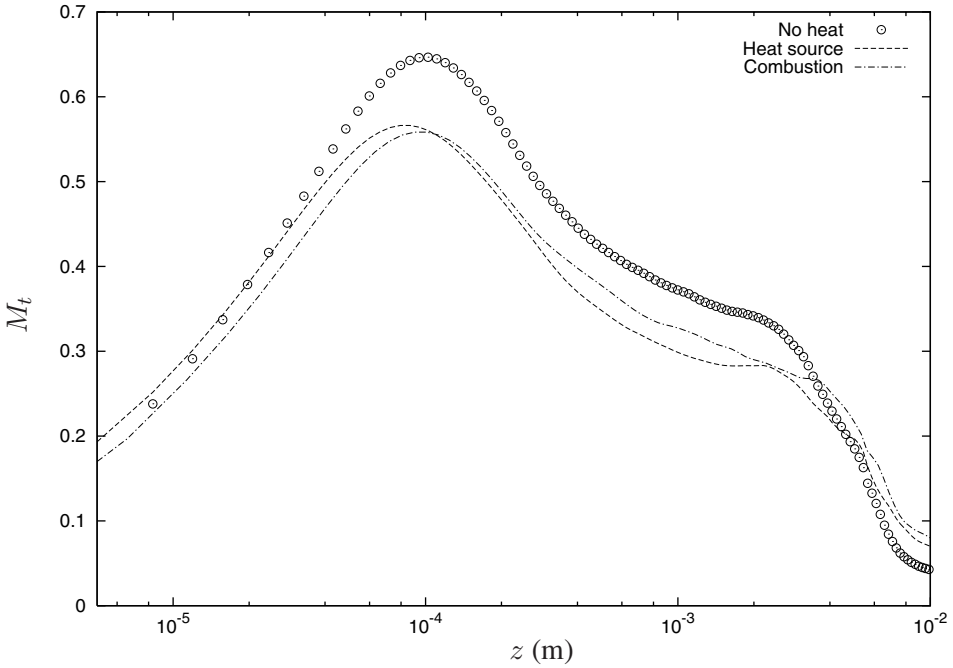

Figure 5.3-22: Effect of heat addition on Turbulent Mach number - Case 1.

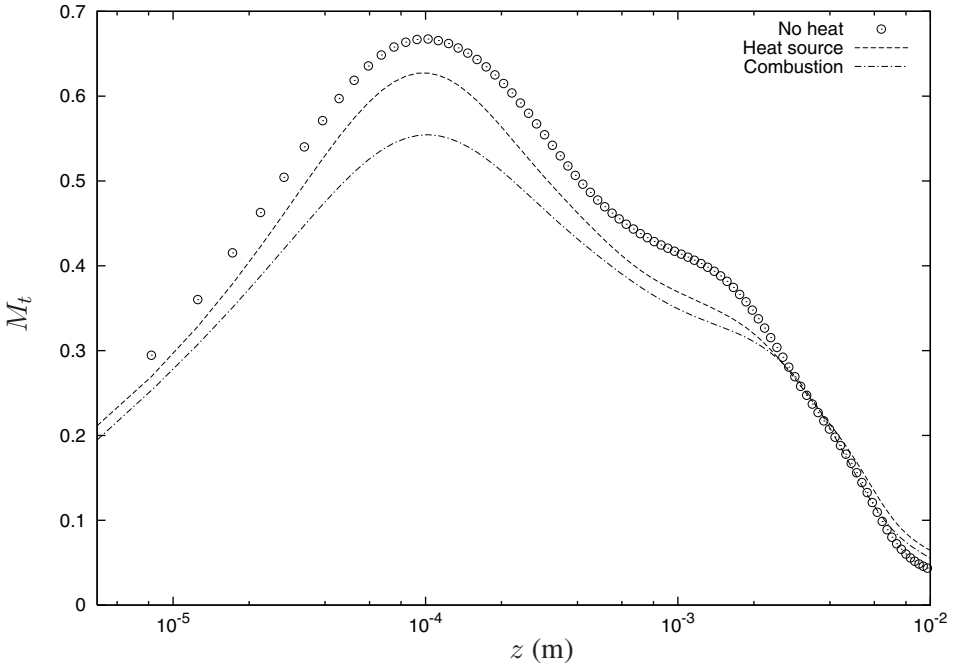

Figure 5.3-23: Effect of heat addition on Turbulent Mach number - Case 2.

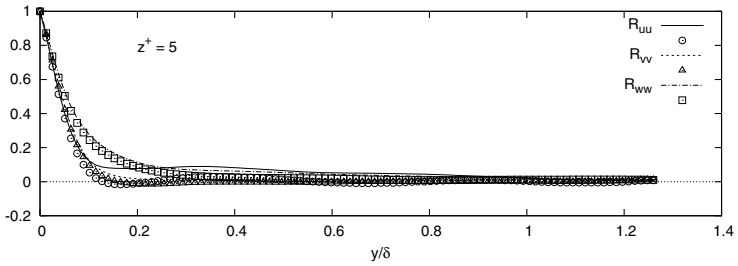

(a) Spanwise two-point autocorrelation - Case 1 heat source

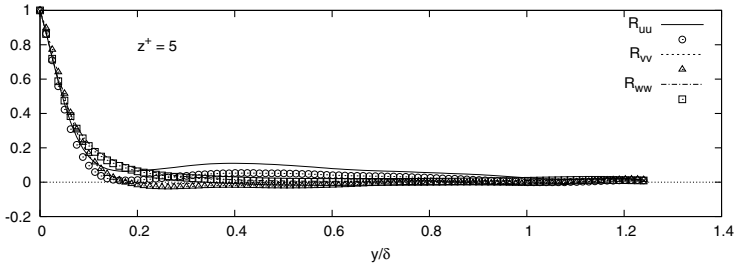

(b) Spanwise two-point autocorrelation - Case 2 heat source

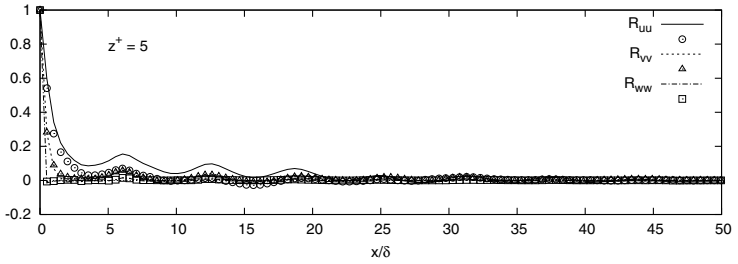

(c) Streamwise two-point autocorrelation - Case 1 heat source

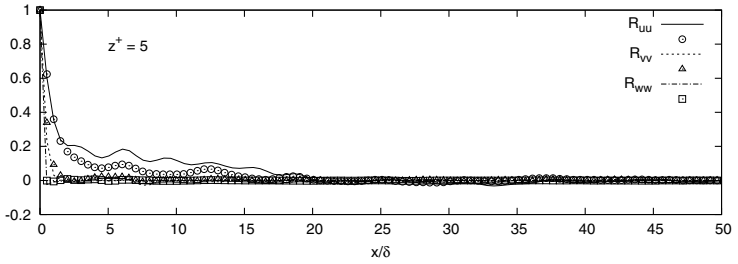

(d) Streamwise two-point autocorrelation - Case 2 heat source

Figure 5.3-24: Two-point velocity fluctuation autocorrelations. Points represent no heat addition

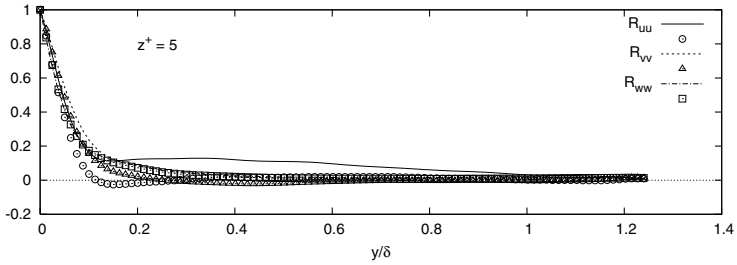

(a) Spanwise two-point autocorrelation - Case 1 combustion

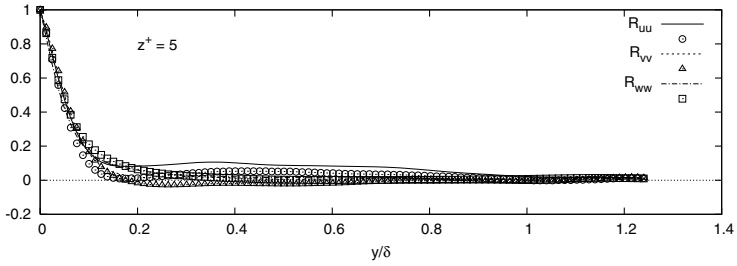

(b) Spanwise two-point autocorrelation - Case 2 combustion

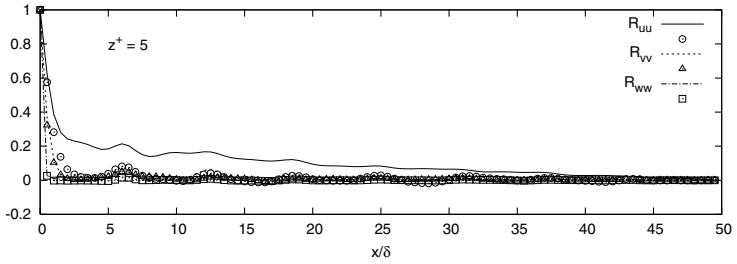

(c) Streamwise two-point autocorrelation - Case 1 combustion

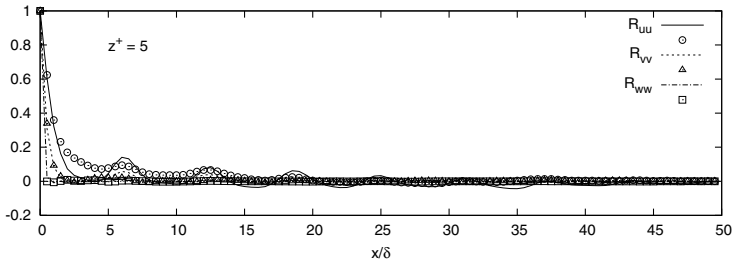

(d) Streamwise two-point autocorrelation - Case 2 combustion

Figure 5.3-25: Two-point velocity fluctuation autocorrelations. Points represent no heat addition

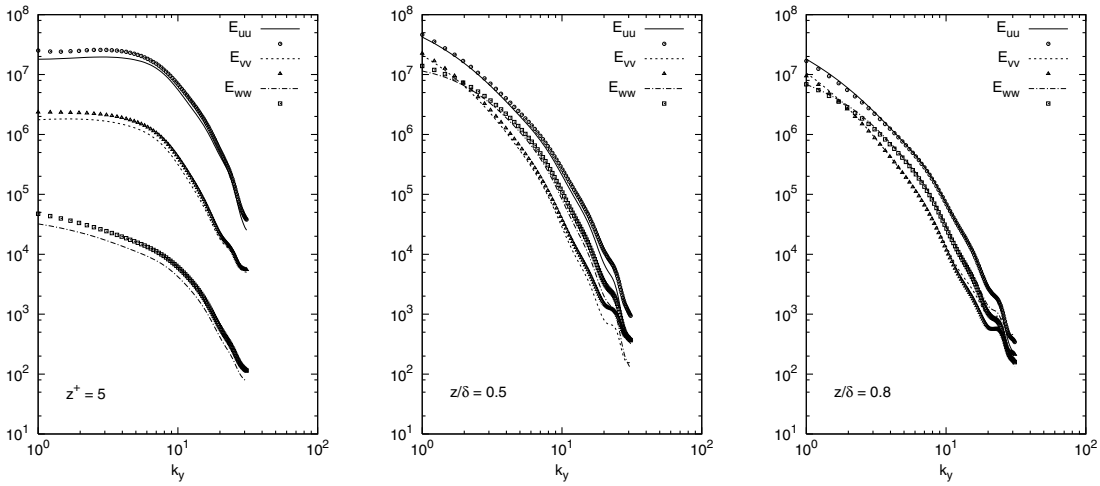

Figure 5.3-26: Spanwise energy spectra - Case 1 heat source. Points represent no heat addition

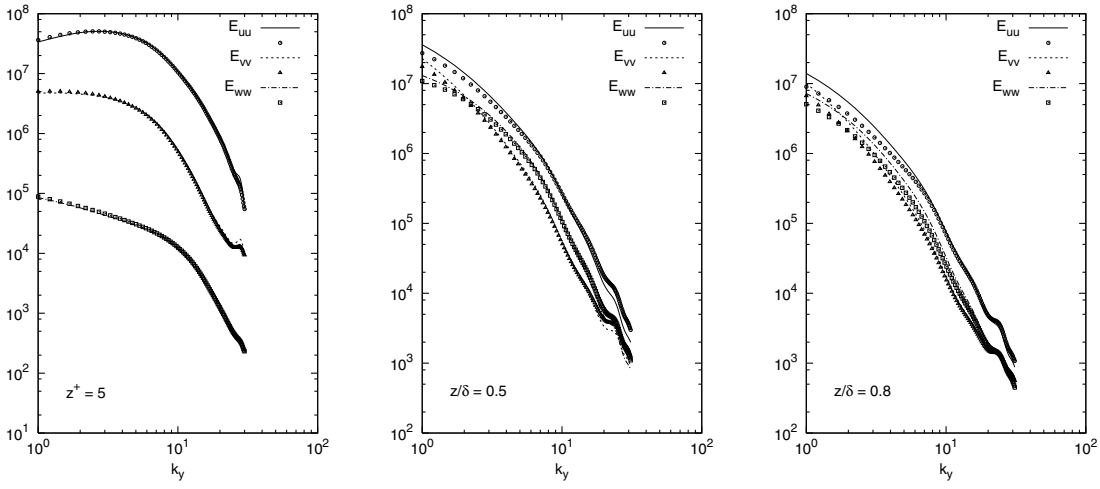

Figure 5.3-27: Spanwise energy spectra - Case 2 heat source. Points represent no heat addition

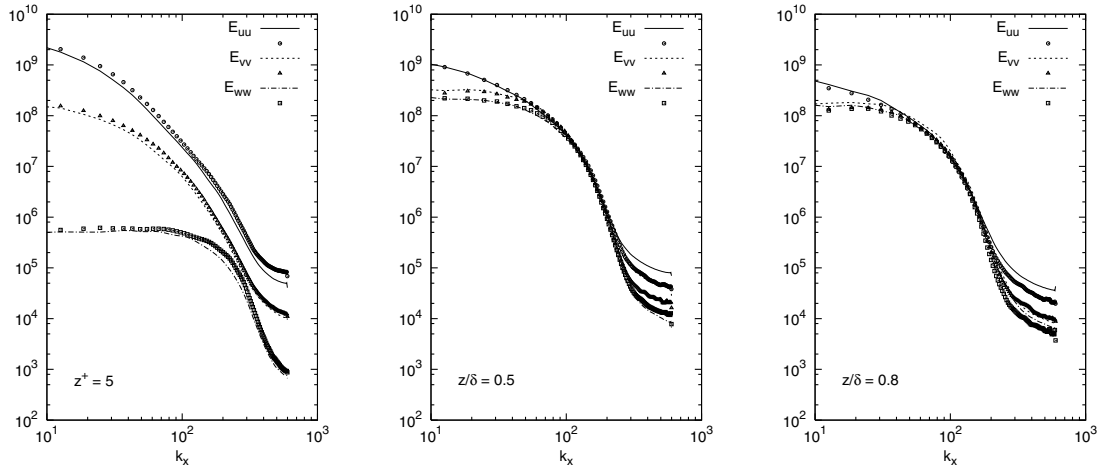

Figure 5.3-28: Streamwise energy spectra - Case 1 heat source. Points represent no heat addition

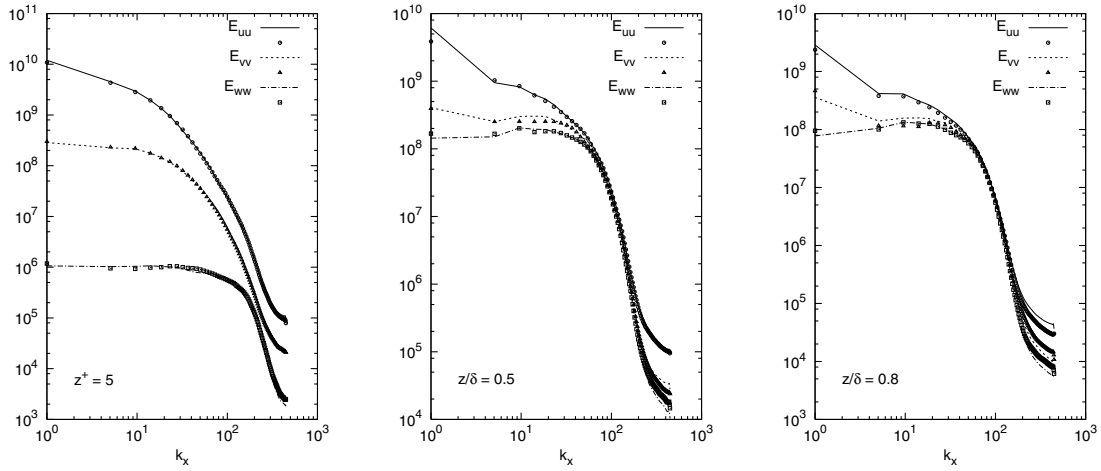

Figure 5.3-29: Streamwise energy spectra - Case 2 heat source. Points represent no heat addition

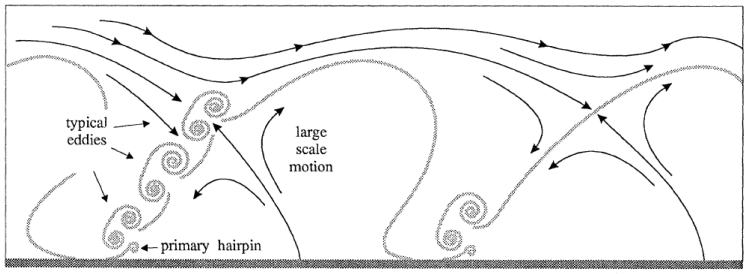

Figure 5.3-30: Schematic of typical eddies and large scale motion in a boundary layer (Falco (1991))

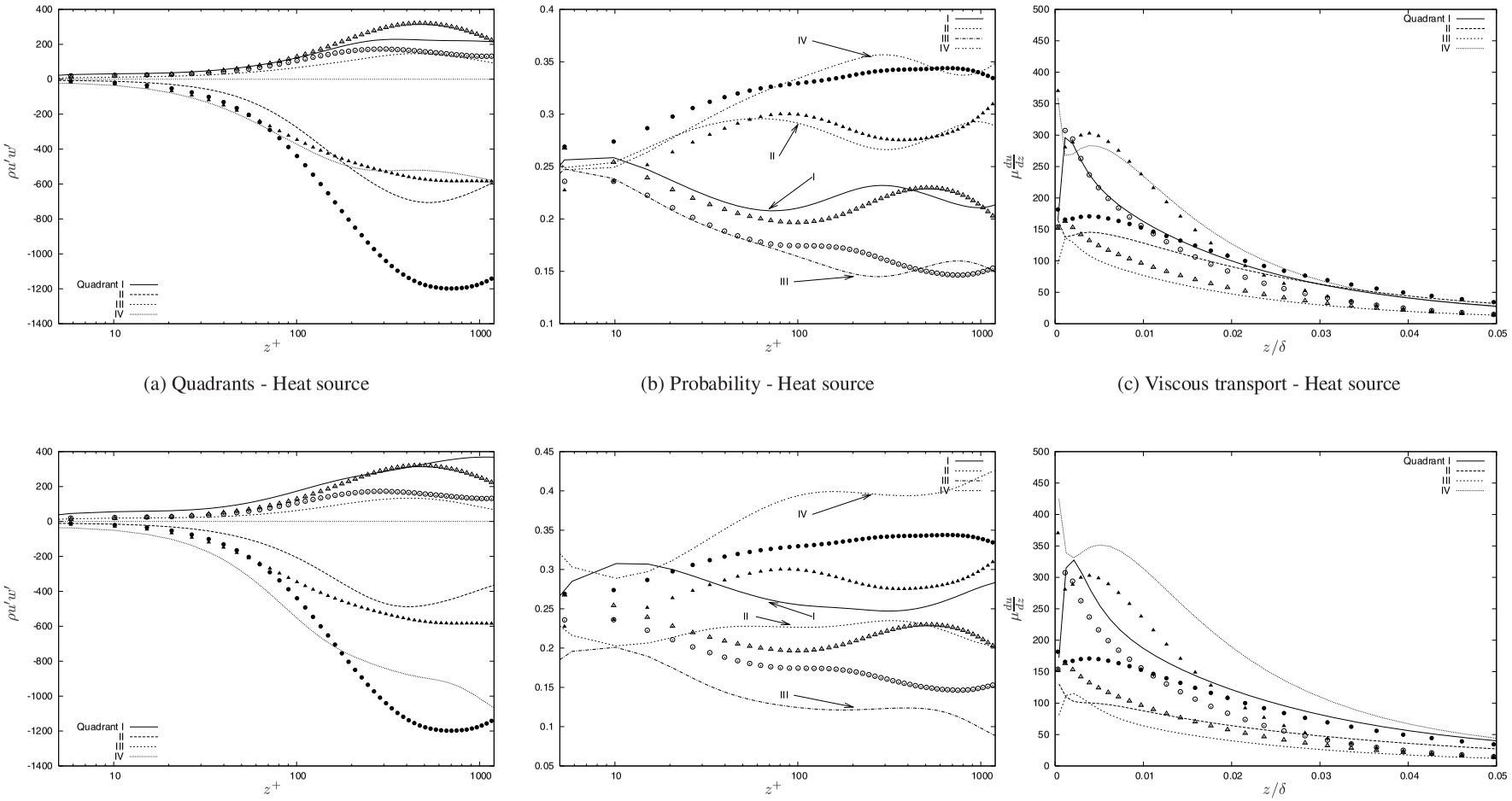

(a) Quadrants - Heat source

(b) Probability - Heat source

(c) Viscous transport - Heat source

(d) Quadrants - Combustion

(e) Probability - Combustion

(f) Viscous transport - Combustion

Figure 5.3-31: Case 1 - Classification of turbulent Reynolds shear stress and viscous transport into quadrants and probability of each mechanism occurring in a quadrant. The points represent the natural or no heat boundary layer condition. ○, I - outward interaction ; ●, II - ejection ; △, III - wallward interaction; ▲, IV - sweep.

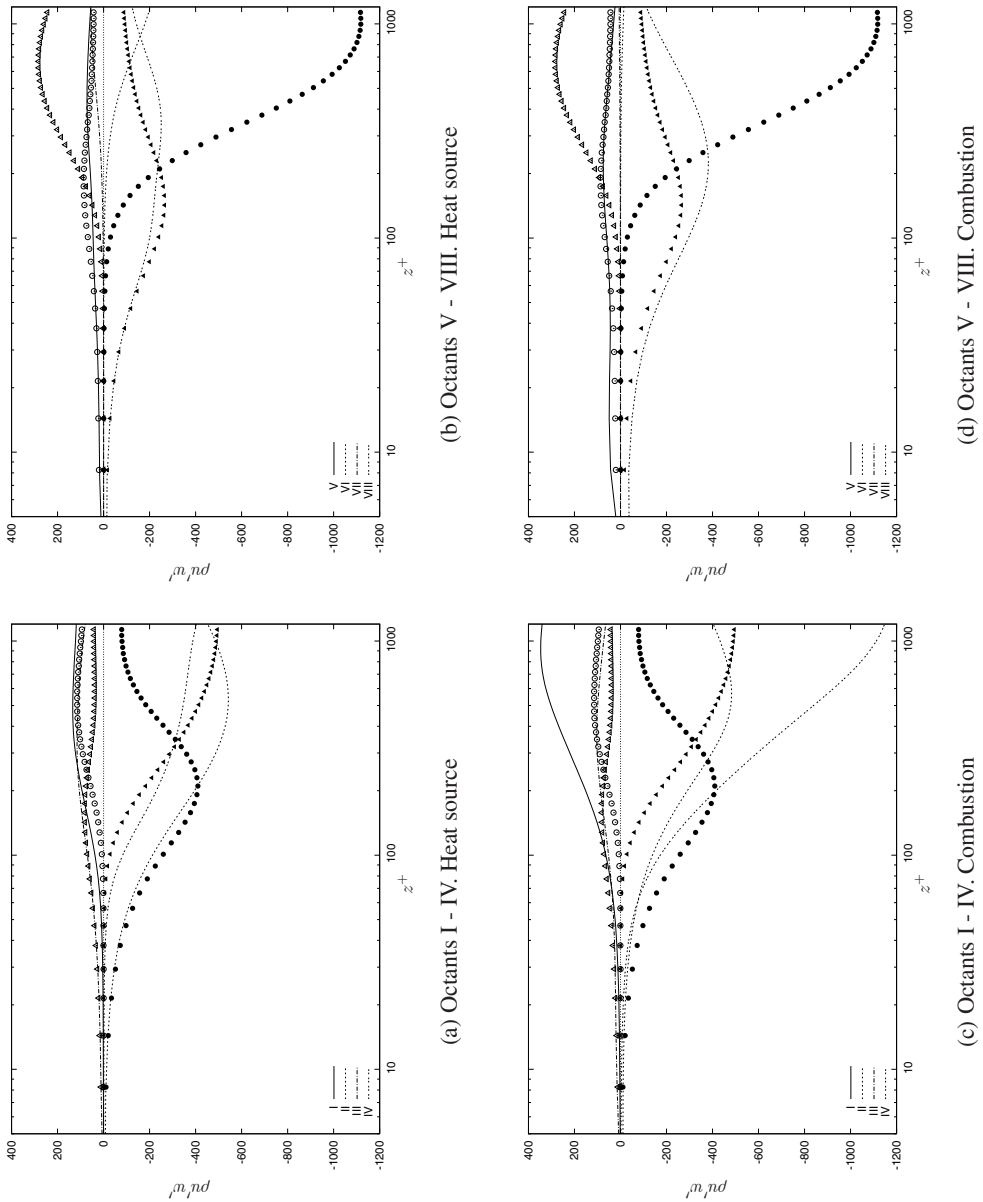

Figure 5.3-32: Case 1 - Classification of Reynolds shear stress into octants. The points represent the natural or no heat boundary layer condition. ○, I,V -outward interaction ; ●, II,VI - ejection ; △, III,VII - wallward interaction; ▲, IV, VIII - sweep.

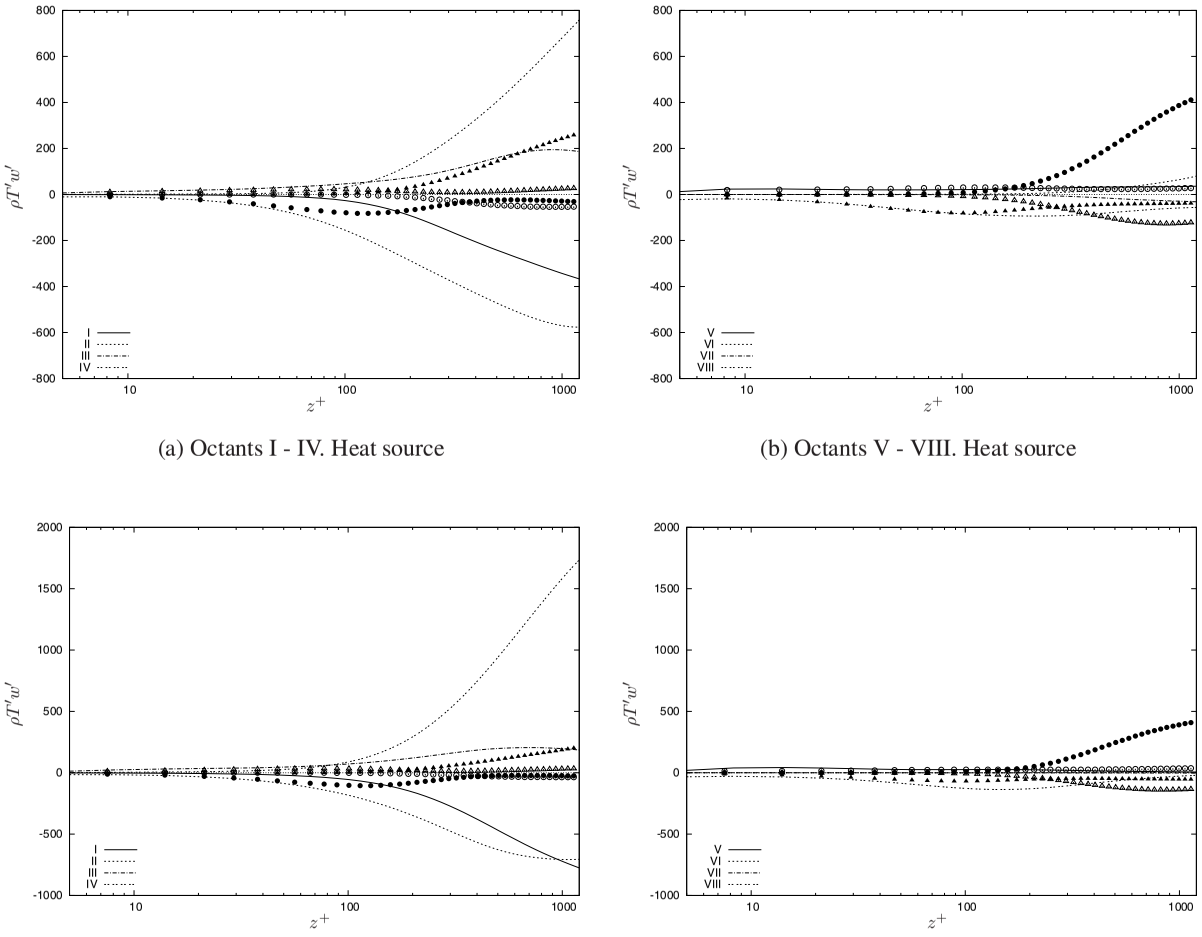

(a) Octants I - IV. Heat source

(b) Octants V - VIII. Heat source

(c) Octants I - IV. Combustion

(d) Octants V - VIII. Combustion

Figure 5.3-33: Case 1 - Classification of wall normal turbulent heat flux into octants. The points represent the natural or no heat boundary layer condition. ○, I,V -outward interaction ; ●, II,VI - ejection ; △, III,VII - wallward interaction; ▲, IV, VIII - sweep.

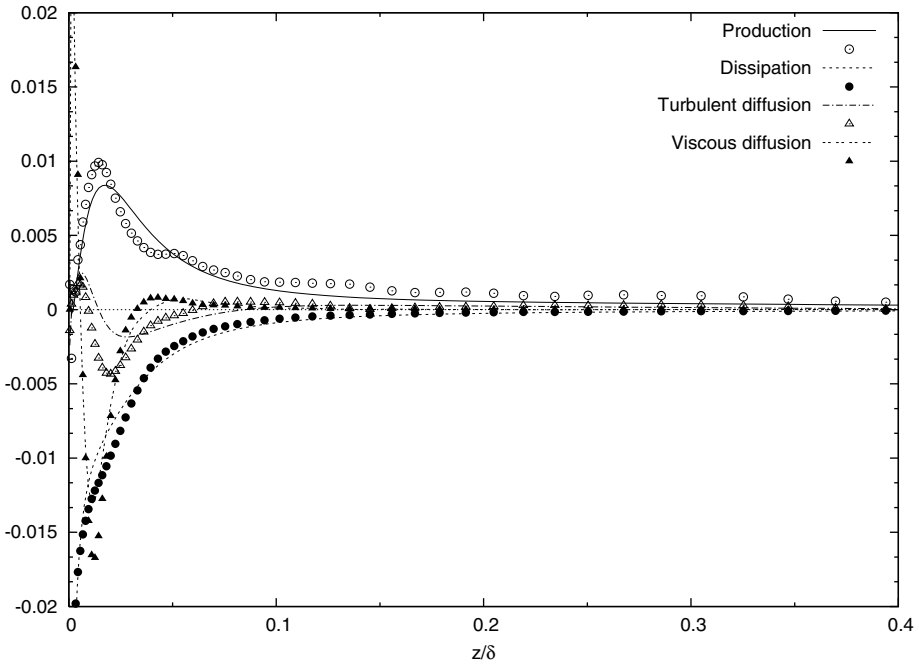

Figure 5.3-34: Effect of heat addition on the turbulent kinetic energy budget - Case 1 heat addition. The points represent the natural or no heat boundary layer condition.

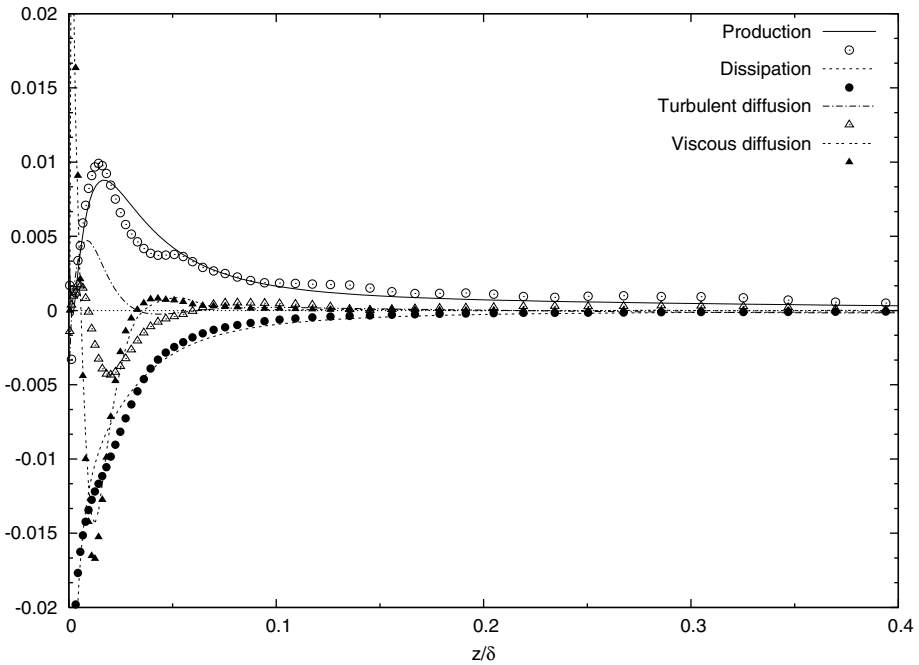

Figure 5.3-35: Effect of heat addition on the turbulent kinetic energy budget - Case 1 combustion. The points represent the natural or no heat boundary layer condition.

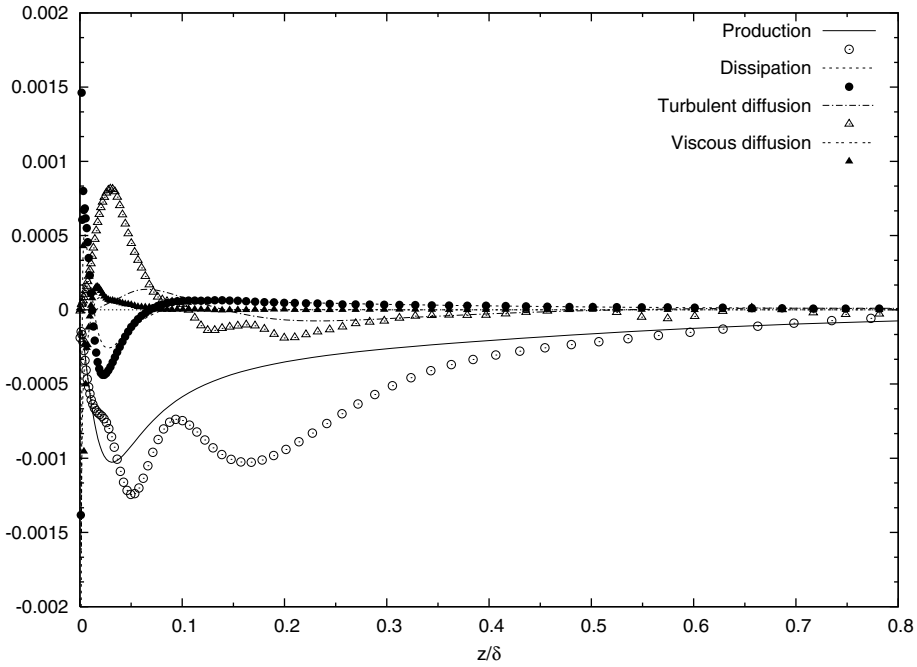

Figure 5.3-36: Effect of heat addition on the Reynolds shear stress budget - Case 1 heat addition. The points represent the natural or no heat boundary layer condition.

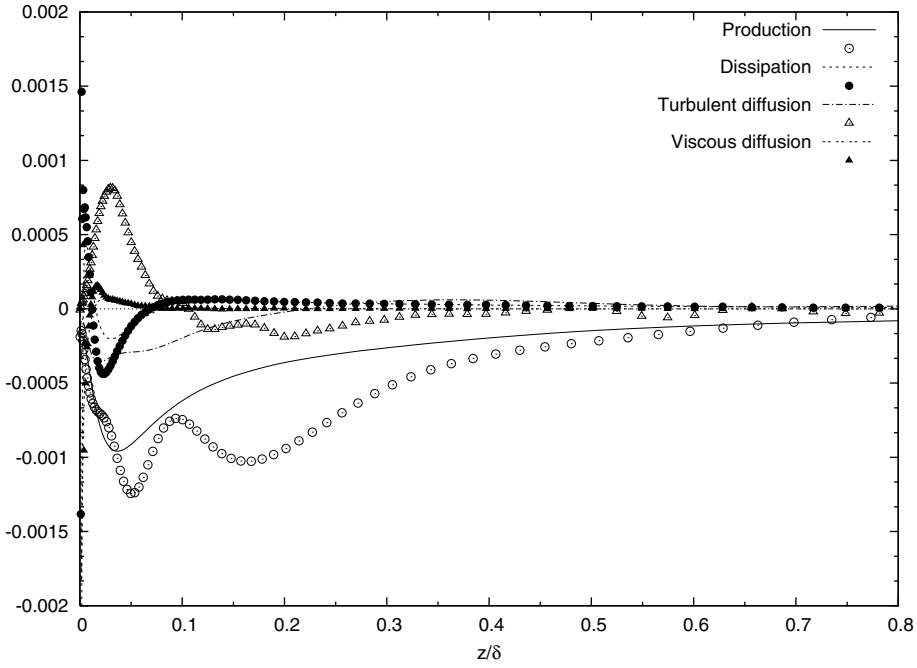

Figure 5.3-37: Effect of heat addition on the Reynolds shear stress budget - Case 1 combustion. The points represent the natural or no heat boundary layer condition.

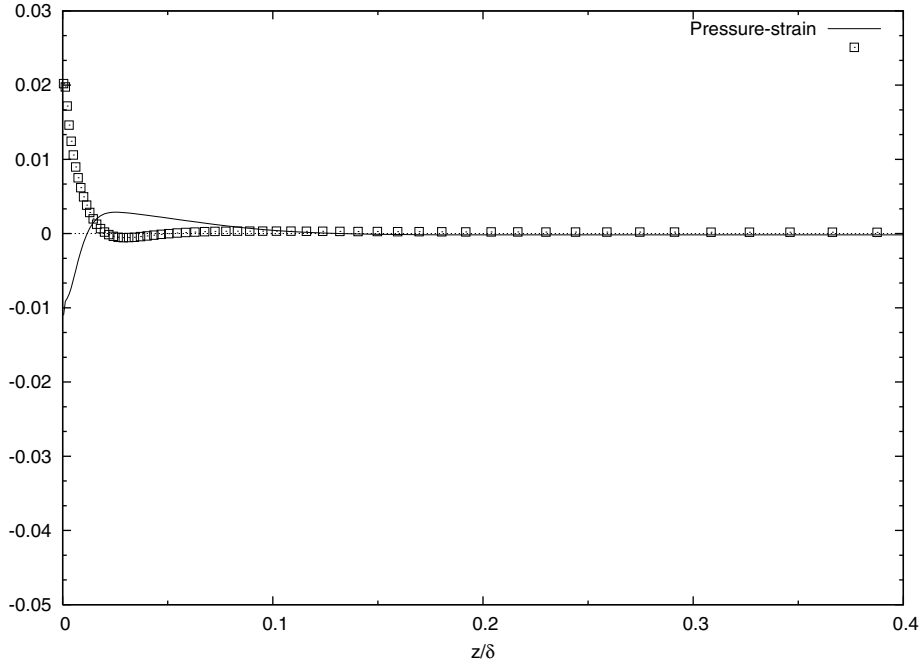

Figure 5.3-38: Effect of heat addition on the pressure-strain contribution to the Reynolds shear stress budget - Case 1 heat addition. The points represent the natural or no heat boundary layer condition.

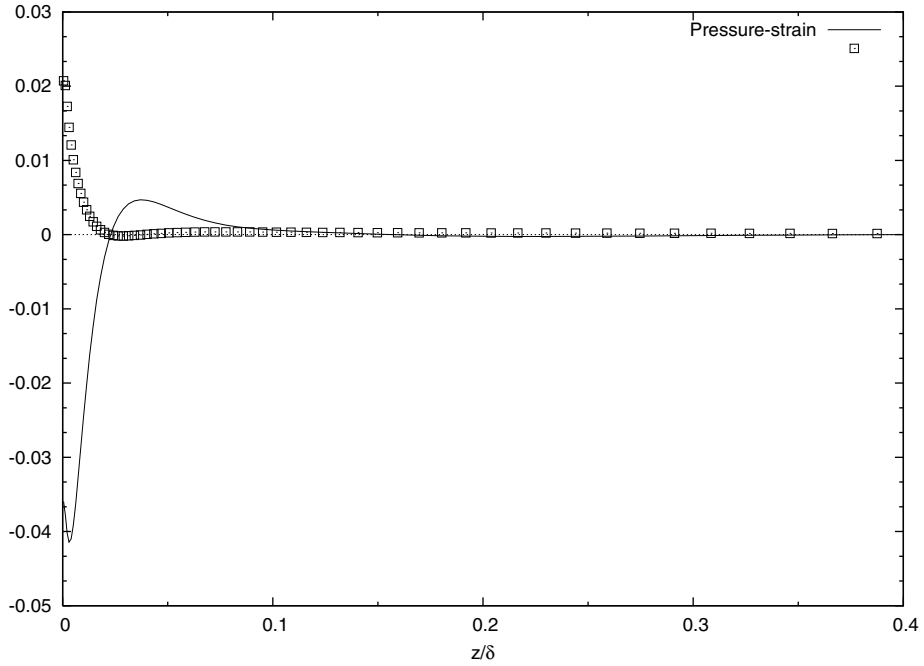

Figure 5.3-39: Effect of heat addition on the pressure-strain contribution to the Reynolds shear stress budget - Case 1 combustion. The points represent the natural or no heat boundary layer condition.

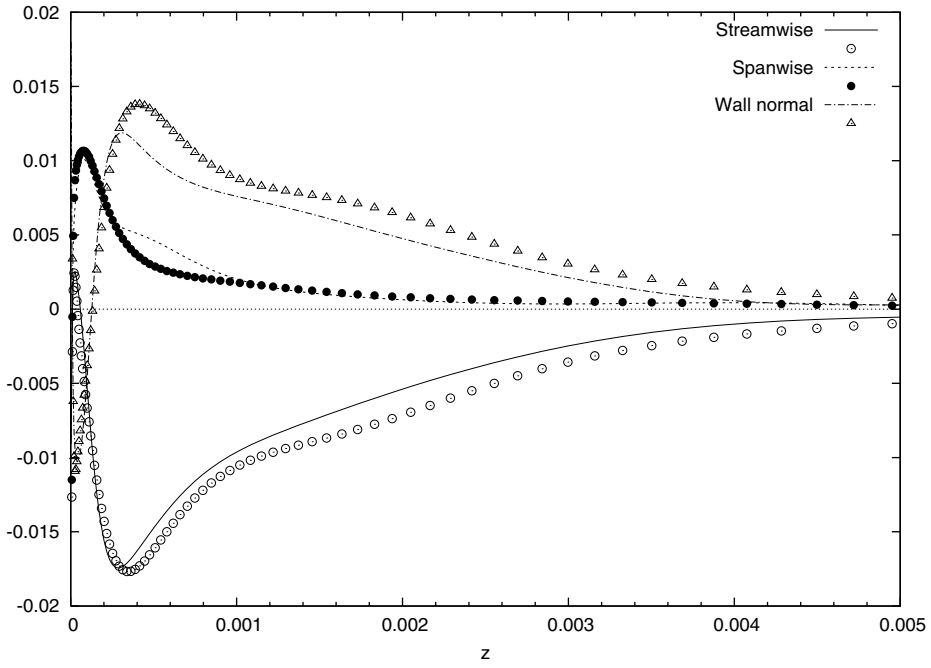

Figure 5.3-40: Effect of heat addition on the pressure-strain term of turbulent kinetic energy transport - Case 1 heat addition. The points represent the natural or no heat boundary layer condition.

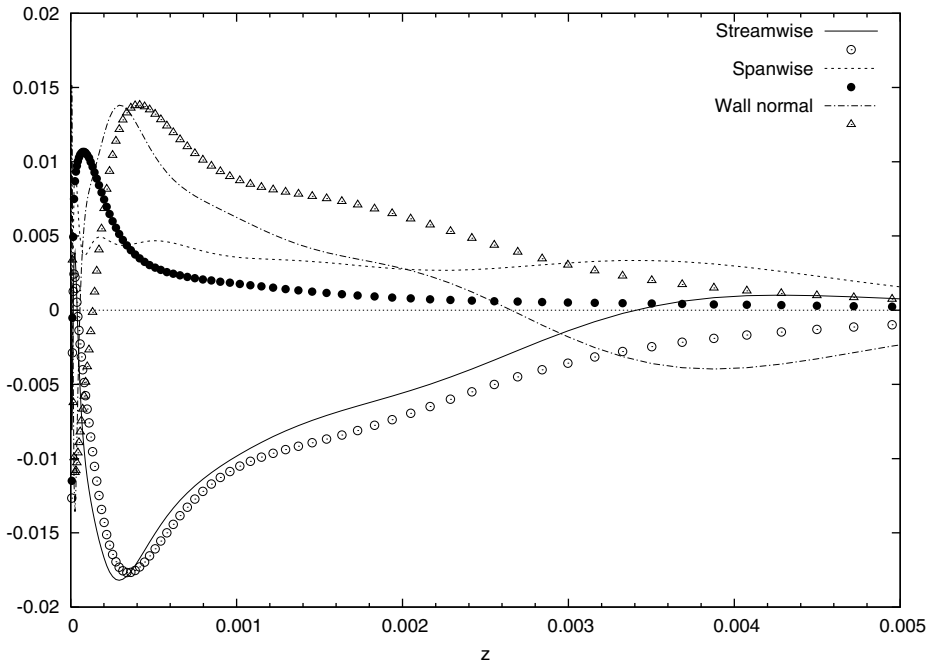

Figure 5.3-41: Effect of heat addition on the pressure-strain term of turbulent kinetic energy transport - Case 1 combustion. The points represent the natural or no heat boundary layer condition.

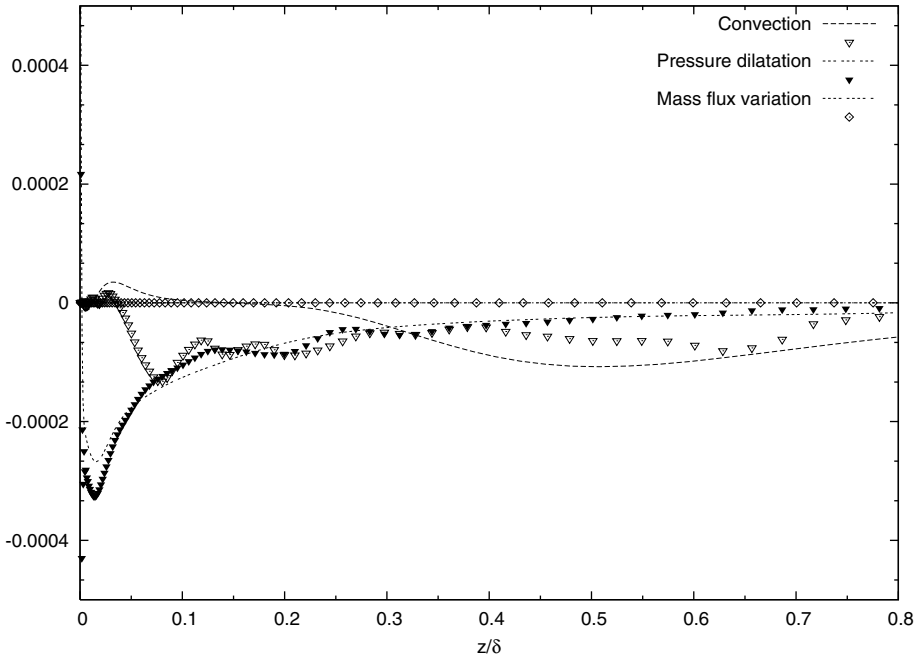

Figure 5.3-42: Effect of heat addition on the compressibility contribution to turbulent kinetic energy transport - Case 1 heat addition. The points represent the natural or no heat boundary layer condition.

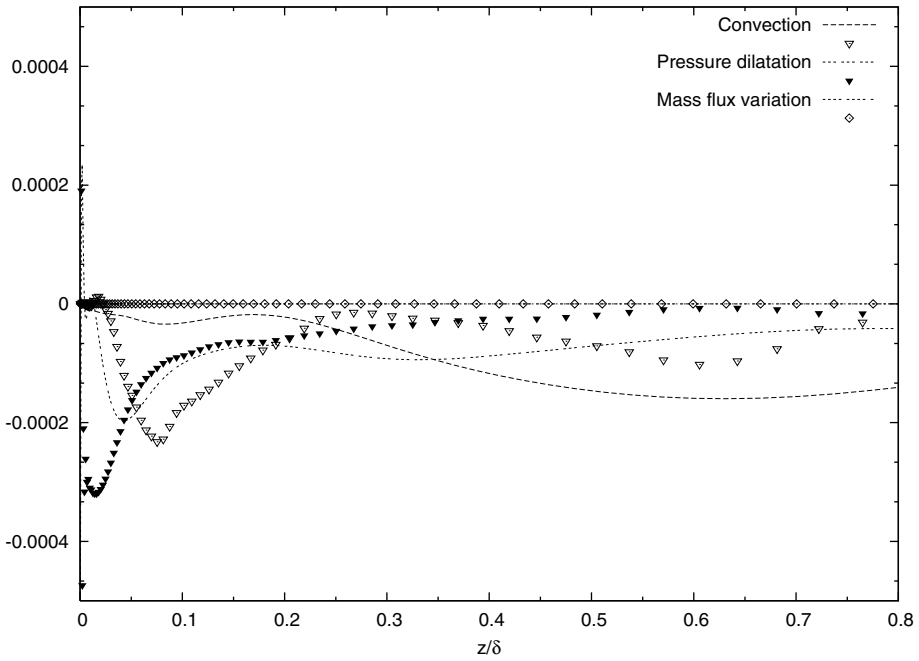

Figure 5.3-43: Effect of heat addition on the compressibility contribution to turbulent kinetic energy transport - Case 1 combustion. The points represent the natural or no heat boundary layer condition.

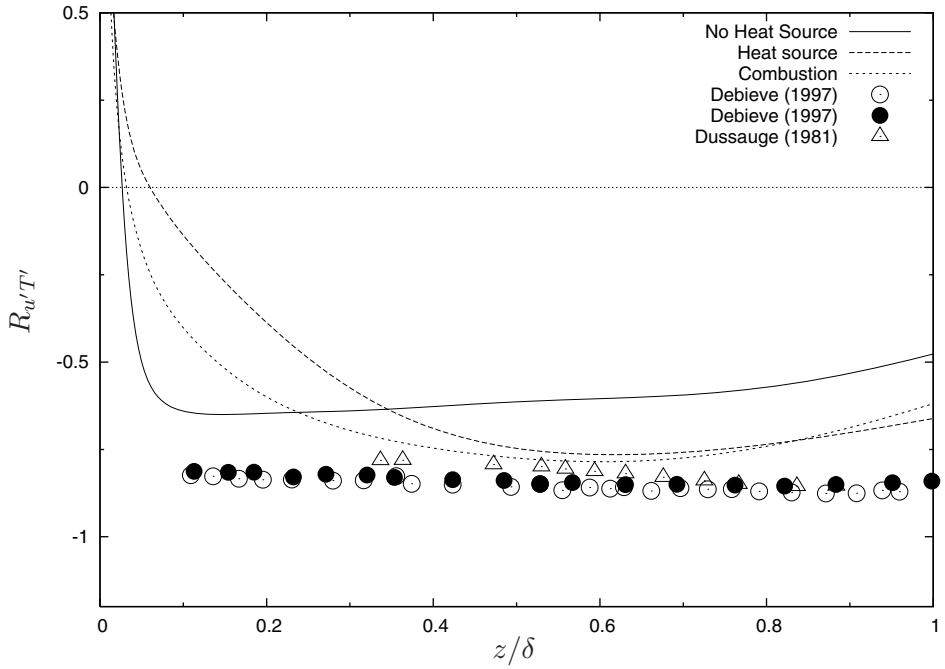

Figure 5.3-44: Effect of heat addition on correlation coefficient $R_{u'T'}$ with comparison to unheated experimental data.

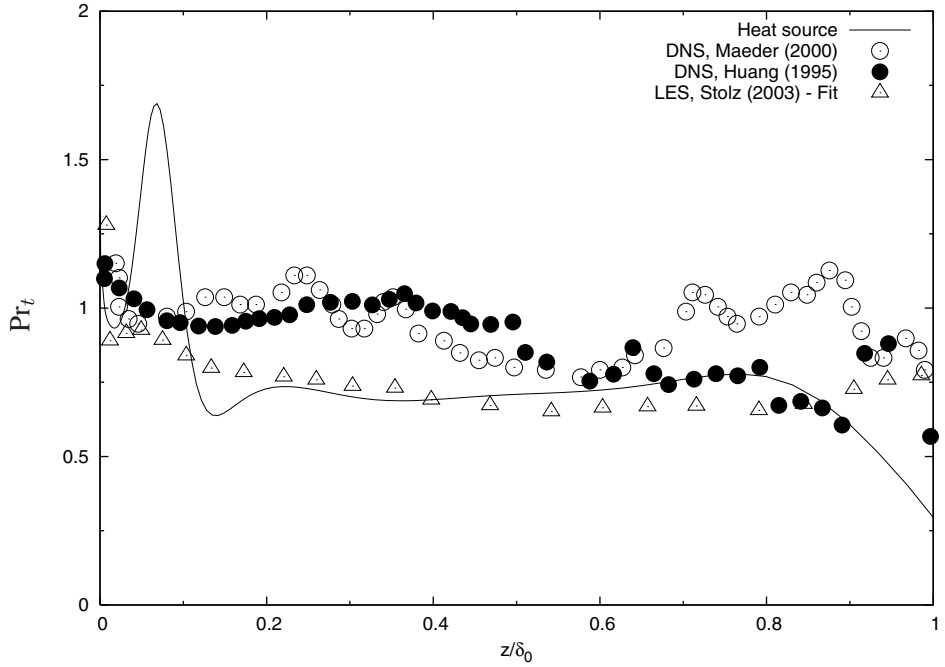

Figure 5.3-45: Effect of heat source addition on turbulent Prandtl number with comparison to unheated numerical data.

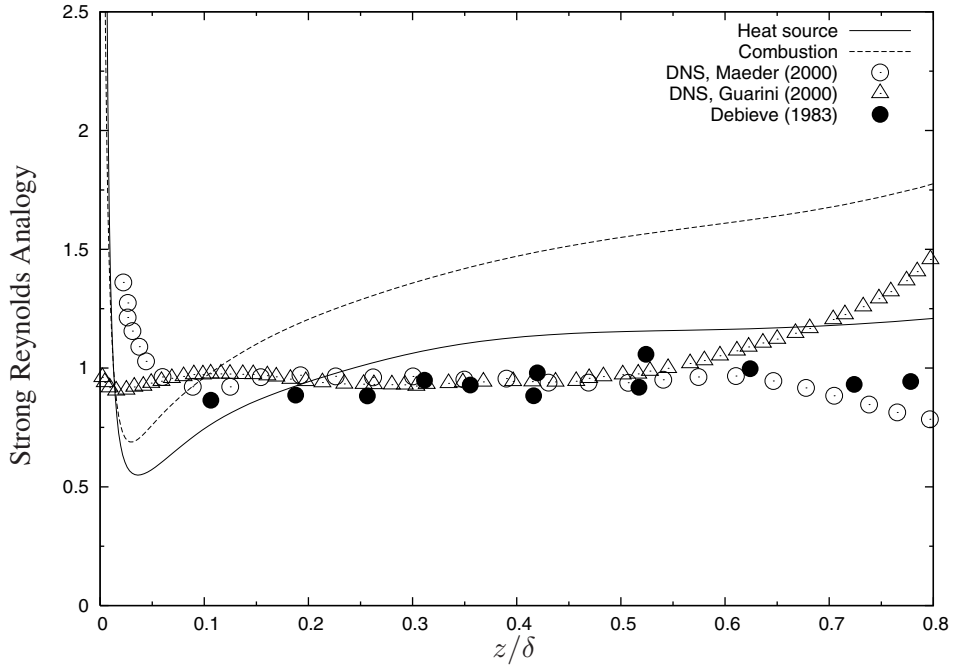

Figure 5.3-46: Effect of heat addition on Strong Reynolds Analogy (equation 4.37) with comparison to unheated numerical data. Experimental data from Gaviglio (1987), original data from Debiève (1983)

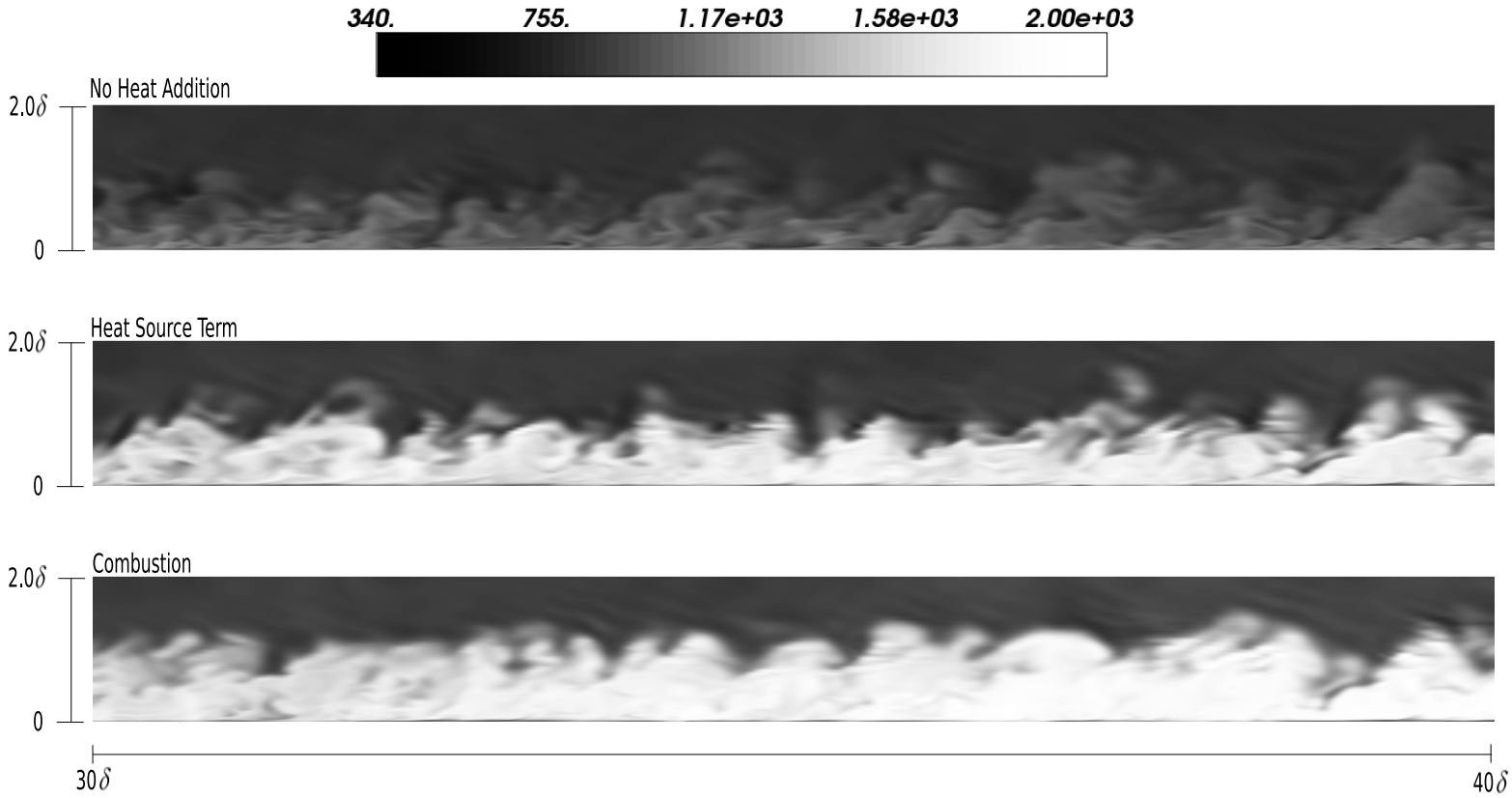

Figure 5.3-47: Instantaneous flow field of static temperature - Case 1. Flow is from left to right. Reduced domain length is shown for clarity.

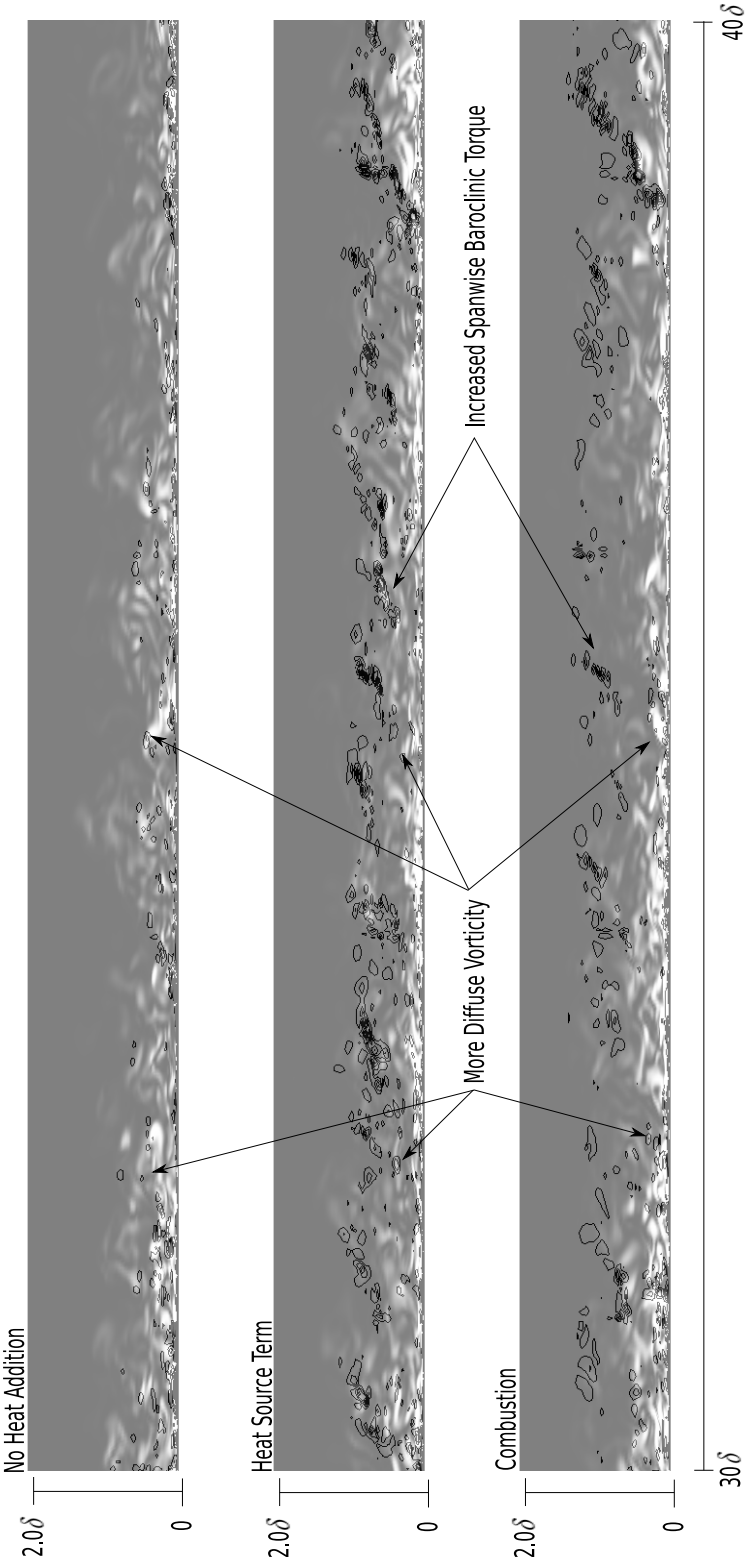

Figure 5.3-48: Instantaneous flow field of vorticity magnitude (filled contours) and spanwise baroclinic torque (lines) - Case 1. Flow is from left to right. Reduced domain length is shown for clarity.

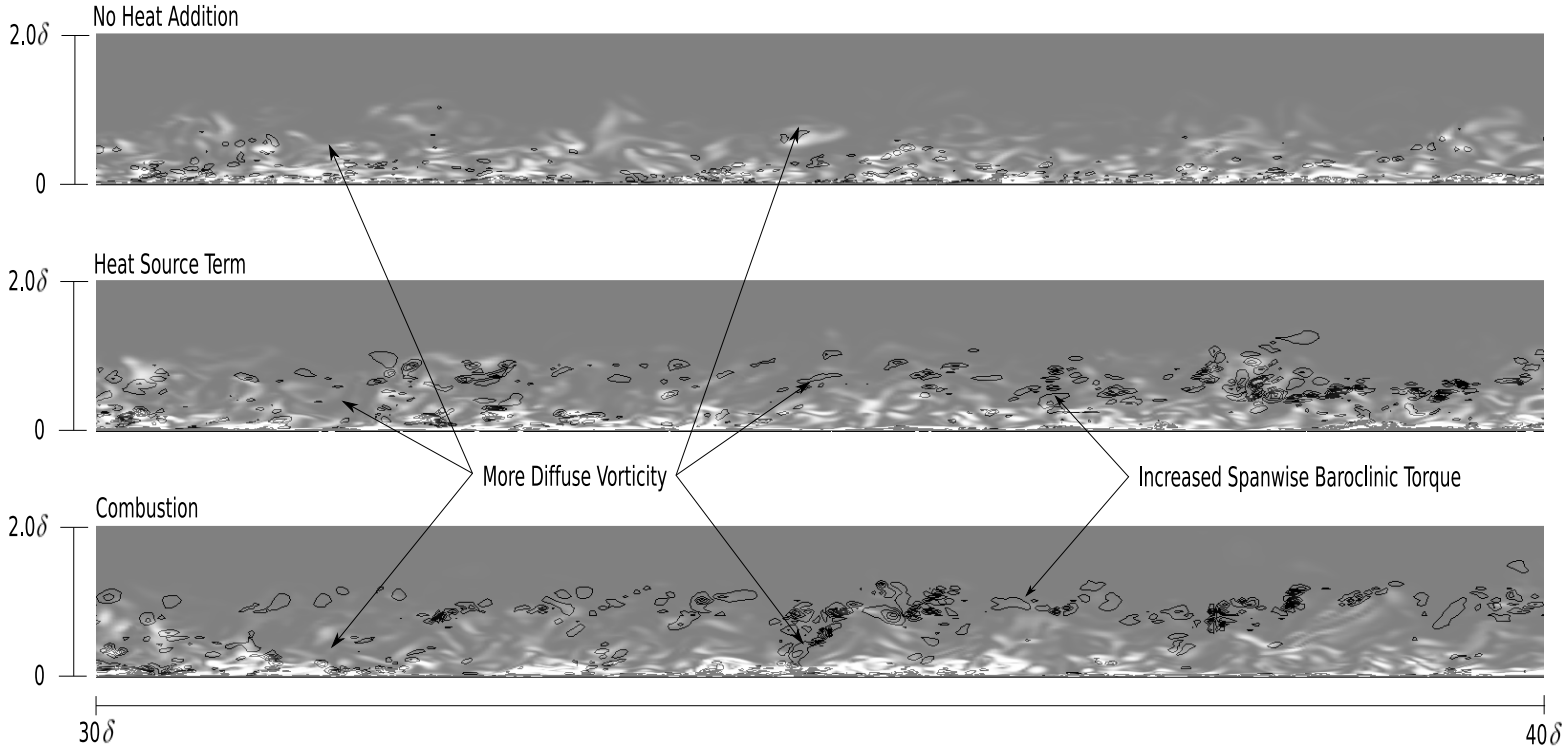

Figure 5.3-49: Instantaneous flow field of vorticity magnitude (filled contours) and spanwise baroclinic torque (lines) - Case 1. Flow is from left to right. Reduced domain length is shown for clarity.

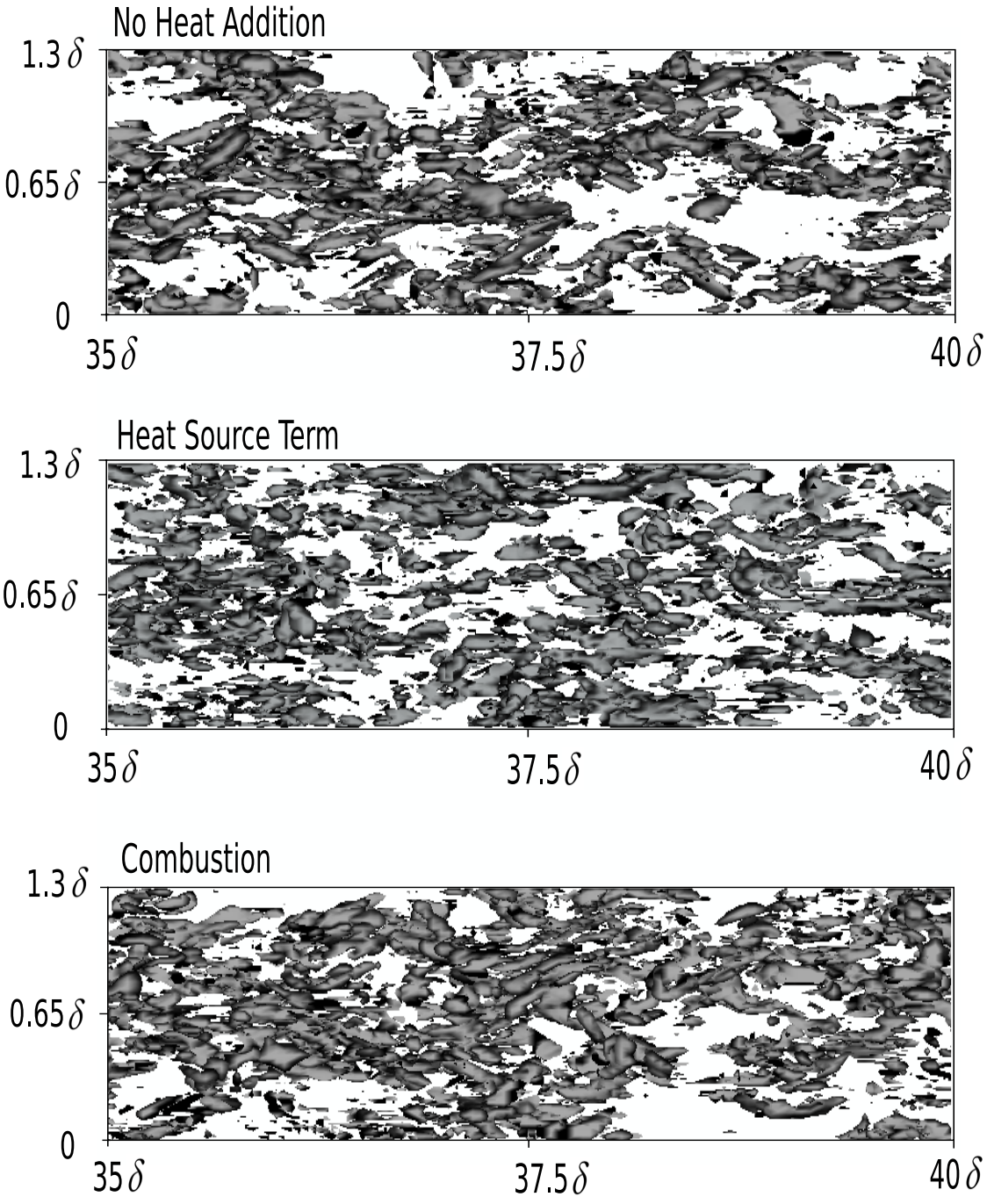

Figure 5.3-50: Projection of vortex structures on *x-y* plane - Case 1. Flow is from left to right. Reduced domain length is shown for clarity.

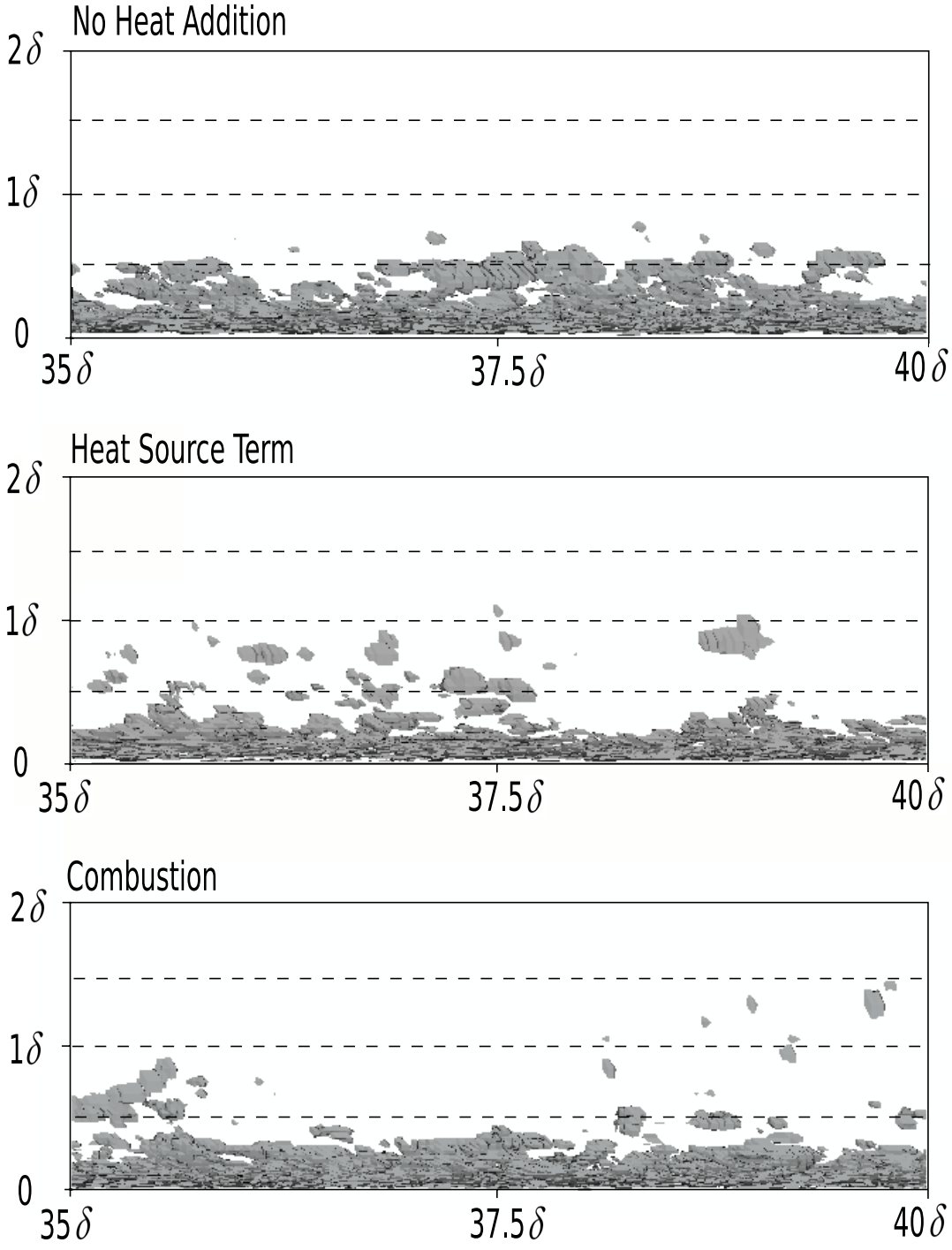

Figure 5.3-51: Projection of vortex structures on *x*-*z* plane - Case 1. Flow is from left to right. Reduced domain length is shown for clarity.

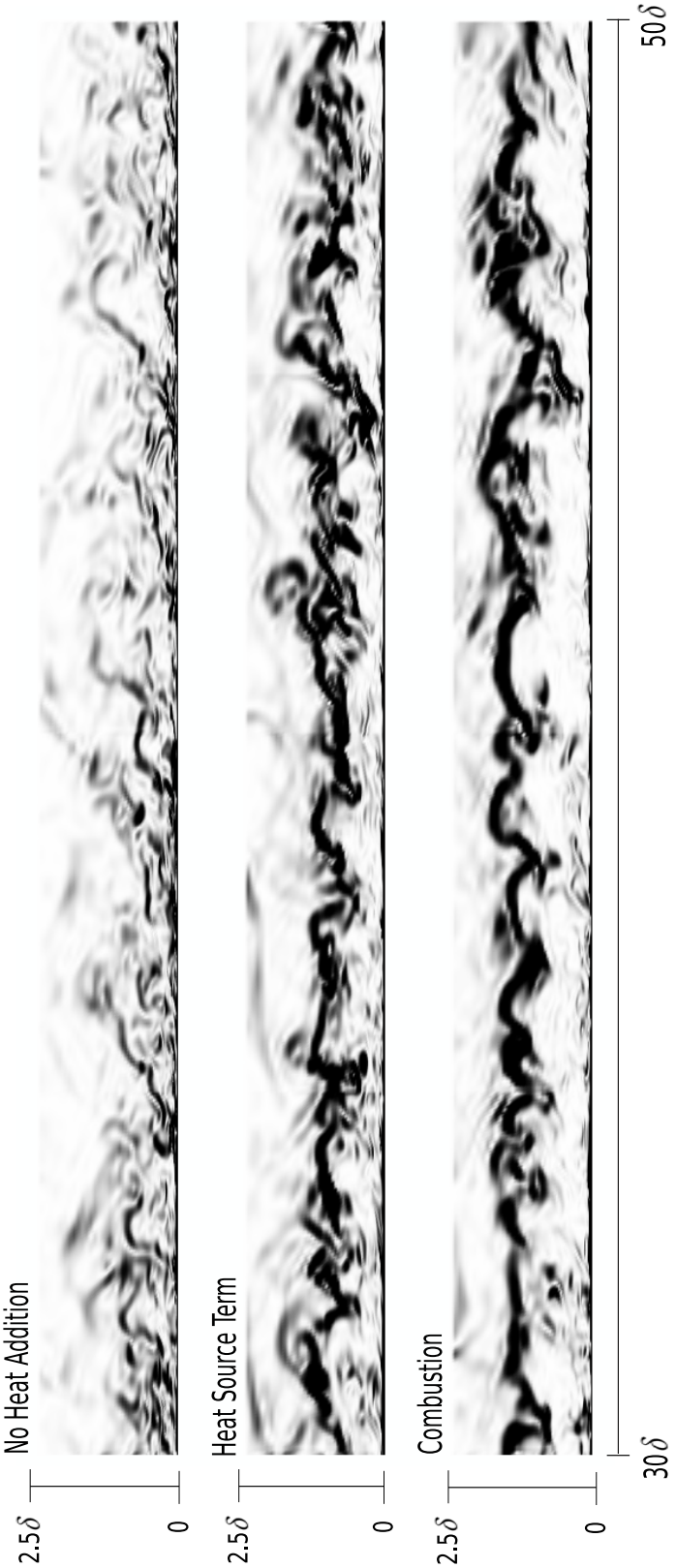

Figure 5.3-52: Flow visualization of boundary layer obtained by taking gradient of density field ($\nabla\rho$) - Case 1. Flow is from left to right. Reduced domain length is shown for clarity.

CHAPTER 6

CONCLUSIONS AND FUTURE WORK

6.1 Conclusions

The aim of this thesis was to evaluate the changes in mechanisms of momentum and energy transport within a turbulent boundary layer under conditions that would support the combustion of hydrogen. Motivation for this study was driven by the lack of a full description of the changes in the transport mechanisms that lead to an overall reduction of wall shear stress. The effects of combustion were included through two methods: Finite rate chemical kinetics and heat addition through a heat source term. The hypothesis was that both of these processes would lead to observable differences in wall shear stress and transport processes. LES was used to simulate the detailed turbulent flow behaviour undergoing heat addition to achieve the aim of this work. The comparisons of momentum and energy transport, with and without heat addition, were made through the use of mean flow state profiles, velocity fluctuation statistics, Reynolds stress budgets and instantaneous visualizations of the flow field.

The performance of three subgrid-scale models for the LES of supersonic turbulent boundary layers has been assessed. The approximate deconvolution model was found to be both accurate and efficient in terms of grid resolution requirements when compared to the eddy-viscosity/eddy-diffusivity models also implemented in this work. The validation of the numerical code contained in Chapter 4 allowed for comparison to both DNS and experimental work, demonstrating the validity of the numerical code used.

The LES results presented in Chapter 5 for supersonic turbulent boundary layers, with and without heat addition through a combustion and heat source approach, have been analysed to gain an understanding of the mechanisms of turbulent momentum transport and how they change under heat addition. To verify that the numerical procedure was working as desired and that a level of grid refinement that no longer influenced the results was being used, a number of numerical grids were trialled. The mean streamwise velocity and Reynolds stress profiles were shown to have little dependence on grid resolutions. Analysis of unheated supersonic boundary layers over cool walls demonstrated the importance of using a semi-local scaling to remove Reynolds number dependency, while permitting comparison of mean streamwise velocity profiles with the standard laws of the wall.

To date, there had remained uncertainty as to how the combustion process reduced the wall shear stress. Initially it was postulated that reductions in density yielded the desirable reductions in wall shear stress, however, this body of work has identified that it is not density alone. It has been demonstrated that the coherent turbulent structures within the boundary layer undergo changes. These changes were identified through both heat addition using combustion of pre-mixed hydrogen in the boundary layer through finite-rate chemical kinetics and a source term to mimic the combustion process. Calculated reductions in wall shear stress and skin friction coefficient that are in agreement with theoretical predictions were computed for the two flow conditions. This demonstrated that the heat addition techniques were producing the desired behaviour, via processes that can be further analysed.

The Reynolds shear stress ($\rho u'w'$) provides a dominant mechanism for the transport of momentum from the mainstream flow to the wall. Clear reductions in the Reynolds shear stress profile ($\rho u'w'$) were computed for both flow conditions and heat addition methods. To isolate the effects of density on the computed turbulent transport quantities, the Reynolds shear stress profile without density scaling ($u'w'$) were also presented. The reductions in this quantity demonstrated that the influence of the heat addition caused changes beyond those to the mean flow quantities.

The energy spectra of the turbulent velocity fluctuations indicated some changes in behaviour under heat addition. In the near wall region, the energy content was observed to shift slightly towards the larger scales or lower frequencies. The net effect of this process is a weakening of the typical eddies. These typical eddies, though being small and having minimal contribution to the resolved velocity fluctuations, make a significant contribution to the overall transport across the boundary layer.

The effect of heat addition on the budgets of the resolved Reynolds stress and turbulent kinetic energy transport equations was calculated. The production of streamwise turbulence through interaction of the mean velocity profile with the Reynolds shear stress was seen to reduce. Similarly, the production of Reynolds shear stress was also observed to decrease. Since these are the dominant mechanisms of turbulent production within the boundary layer, it can be reasoned that they influence the turbulent transport properties of the flow. Furthermore, the pressure-strain term, responsible for the redistribution of the streamwise turbulence to the spanwise and wall normal directions, appears to also reduce with the addition of heat. As a consequence, there is less of a source of wall normal turbulence leading to a lowering of turbulent transport to the wall.

Two-point spatial correlations for the streamwise velocity fluctuations indicated an increasing coherence length for the near wall streaks when heat was added. Along with this, the streaks were observed to increase their spanwise spacing somewhat. This enlarging of the near wall streaks represents itself as a means of reducing the turbulent transport of momentum to the wall by a net decrease in regions of momentum transport to and from the wall.

Quadrant analysis for the Reynolds shear stress revealed a significant reduction in the ejection mechanism. With the eventual lift up and termination of the near wall streaks corresponding to the ejection mechanism and the ejections making a large contribution to the generation of wall shear stress, the reduced contribution provided a clear mechanical explanation of the observed wall shear stress reduction. This result was also seen as confirmation of the elongation of the streaks observed from the two-point spatial correlations. Octant analysis was used to analyse the behaviour of both the Reynolds shear stress and turbulent wall normal heat flux. It was found that the addition of heat through both methods resulted in a large suppresion of the contribution of hot ejections to the Reynolds shear stress, a mechanism that under normal circumstances provides a significant contribution. The inclusion of the combustion process led to an increasing contribution of the sweep of cold fluid to the Reynolds shear stress, while for the heat source approach this was not observed. Interestingly, for combustion, the cold sweeps and ejections were identified to provide an increased contribution to the wall normal heat flux in the lower levels of the boundary layer ($z^+ < 1000$), suggesting that the cold fluid was being retained in the lower boundary layer levels. This fact, combined with the increasing cold sweep contribution to the Reynolds shear stress, provides another indication of an overall reduction in mixing within the boundary layer when heat is added.

Coherent structures were clearly identified within the flow domain by visual methods. Instanta-

neous visualizations of baroclinic torque revealed an increase in activity towards the boundary layer edge. This increasing activity is postulated to produce more diffuse vortex structures, hence reducing entrainment velocities and overall turbulent transport. Using a vortex identification technique that goes beyond just contouring vorticity, allowed for identification of flow regions undergoing significant rotation. This technique allowed for identification of the near wall streaks and visually demonstrated some arguable enlarging in the $x - y$ plane. More significantly, visualizations in the $x - z$ plane revealed a reduction in the ejection of the streaks. Such an observation is in clear agreement with the observations of the quadrant analysis, while providing another demonstration of a process where reduction in the ejection mechanism leads to a reduction in wall shear stress. Visualizations of density contours ($\nabla\rho$) reinforced this observation by clearly demonstrating a reduction in ejection of turbulent near wall structures.

6.2 Future Work

There remains several areas where the present research can be extended. Given that a deeper understanding of the effects of heat addition on the turbulent transport within the boundary layer has been achieved, it is desirable to extend this understanding to flow configurations that are a step closer to those studied in experiments.

To increase the similarity with the experimental conditions, it would be pertinent to include the injection of the hydrogen injection jet at the inflow plane. The main motivation of this extension is to gain an even greater understanding of the process of mixing between the injected hydrogen jet and the mainstream flow and the associated additional film cooling that accompanies it. Such an investigation would allow for the identification of the reductions in heat transfer observed experimentally when the near wall hydrogen jet combusted. Such a phenomena could not be seen in the current work. This task, however, must be approached with caution as it would require a significantly larger streamwise domain leading to futher increases in the already large computational demands.

Given that the heat source term approach has demonstrated its ability to mimic the broad combustion process, this approach can be coupled with high resolution DNS. A DNS study of this flow would provide a flow database free of the subgrid-scale effects and aliasing errors associated with the coarser LES grids. Such a database would prove to be highly useful as a reference point for further LES study of such flows.

Finally, the changes in turbulent transport identified by the present results can be used to develop or tune existing RANS turbulence models to properly account for the changes when heat is added.

APPENDIX A

SUPPLEMENTARY FIGURES

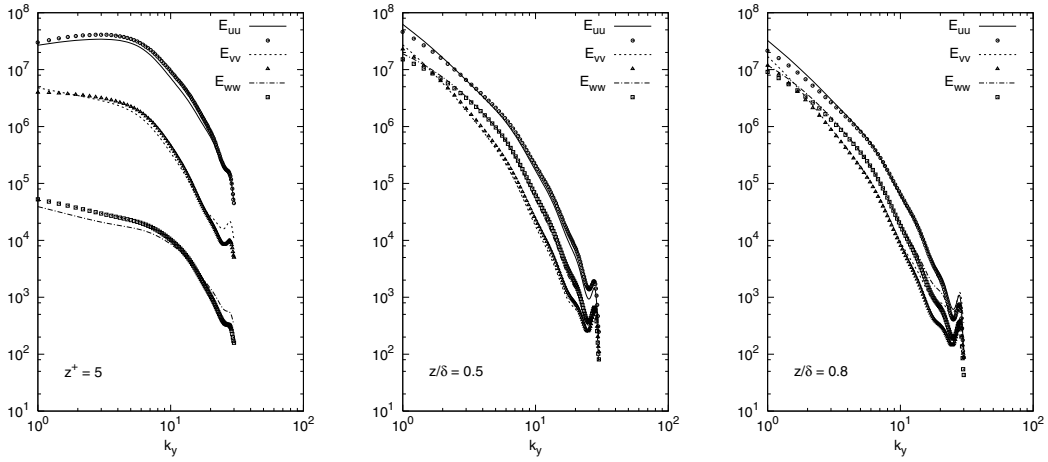

Figure A.1-1: Spanwise energy spectra - Case 1 combustion. Points represent no heat addition

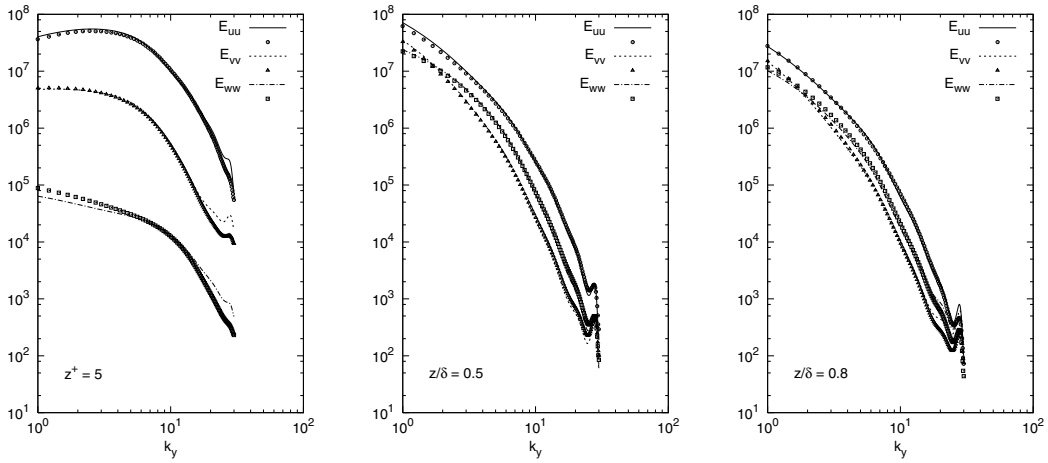

Figure A.1-2: Spanwise energy spectra - Case 2 combustion. Points represent no heat addition

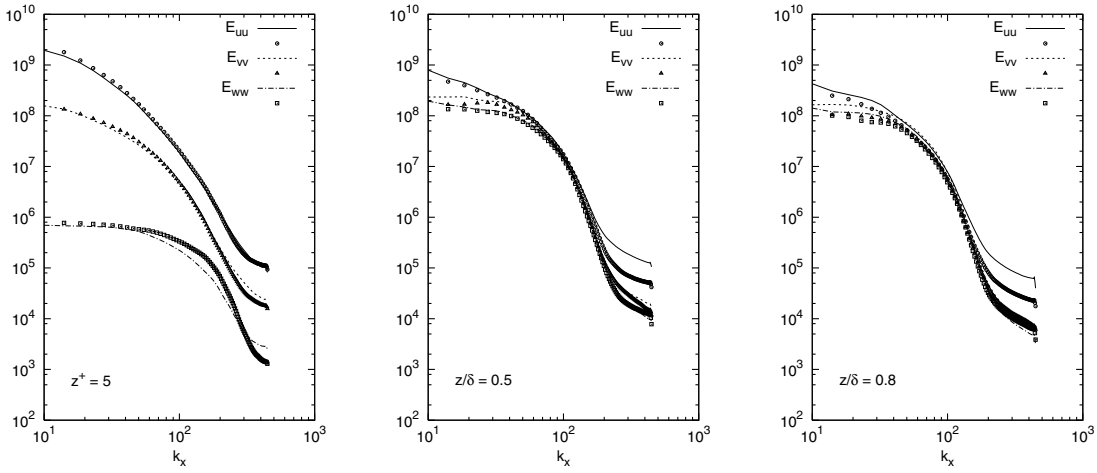

Figure A.1-3: Streamwise energy spectra - Case 1 combustion. Points represent no heat addition

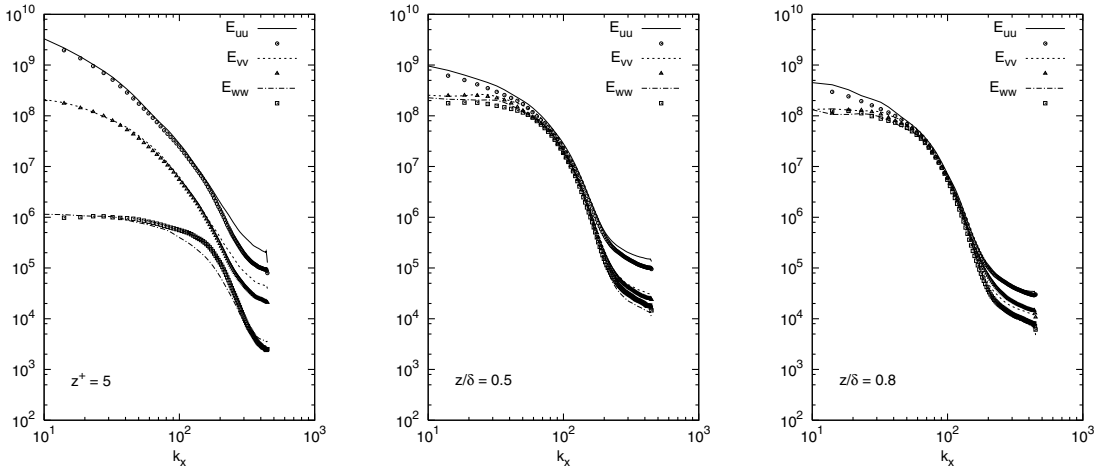

Figure A.1-4: Streamwise energy spectra - Case 2 combustion. Points represent no heat addition

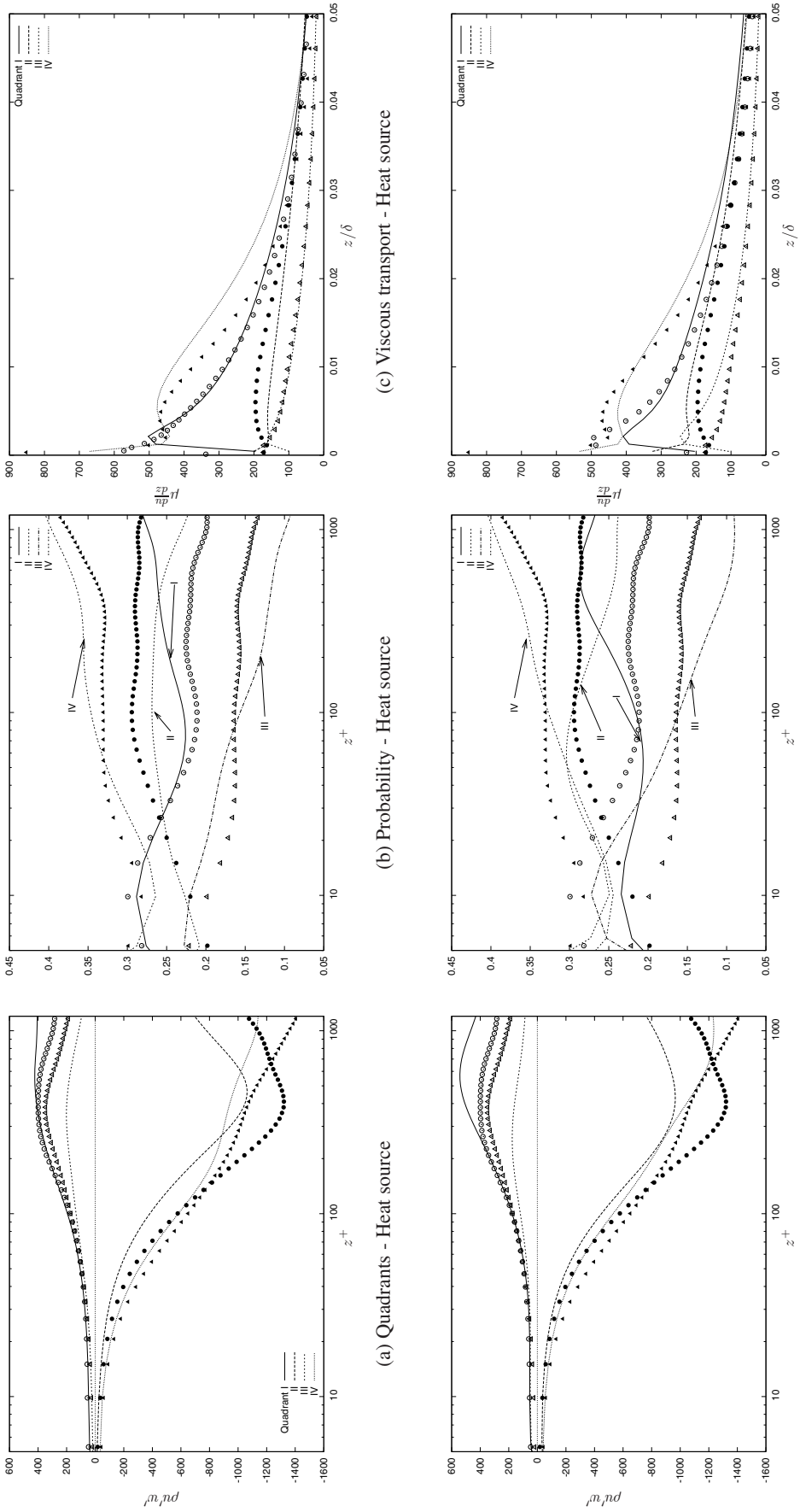

Figure A.1-5: Case 2 - Classification of turbulent Reynolds shear stress and viscous transport into quadrants and probability of each mechanism occurring in a quadrant. The points represent the natural or no heat boundary layer condition. ○, I - outward interaction ; ●, II - ejection ; △, III - wallward interaction; ▲, IV - sweep.

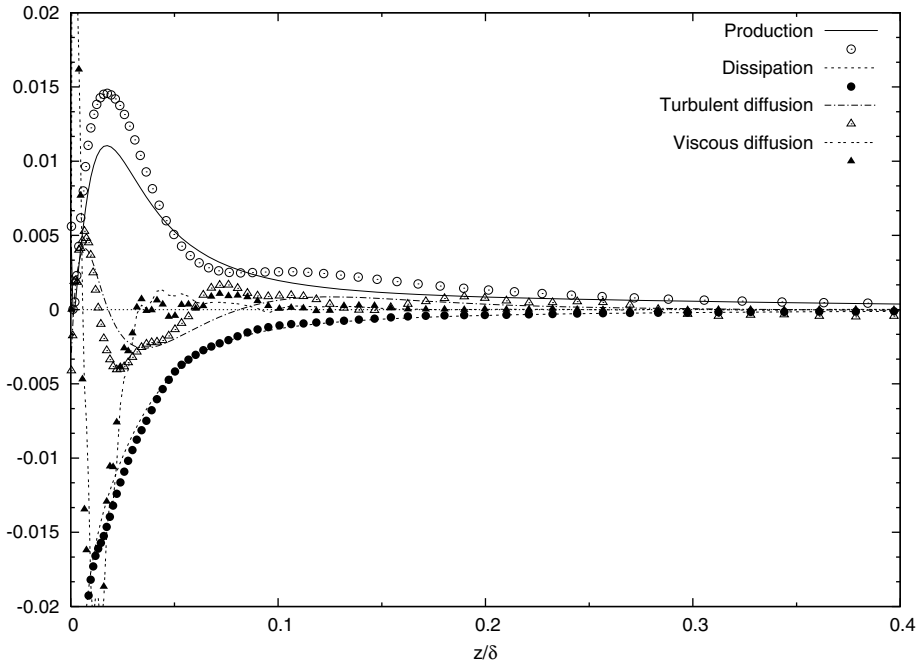

Figure A.1-6: Effect of heat addition on the turbulent kinetic energy budget - Case 2 heat addition. The points represent the natural or no heat boundary layer condition.

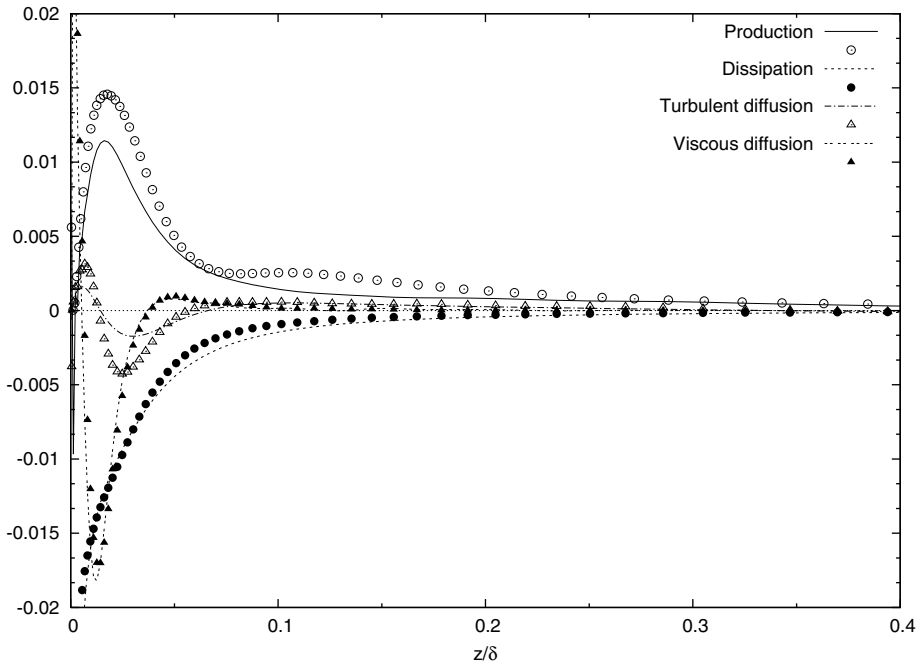

Figure A.1-7: Effect of heat addition on the turbulent kinetic energy budget - Case 2 combustion. The points represent the natural or no heat boundary layer condition.

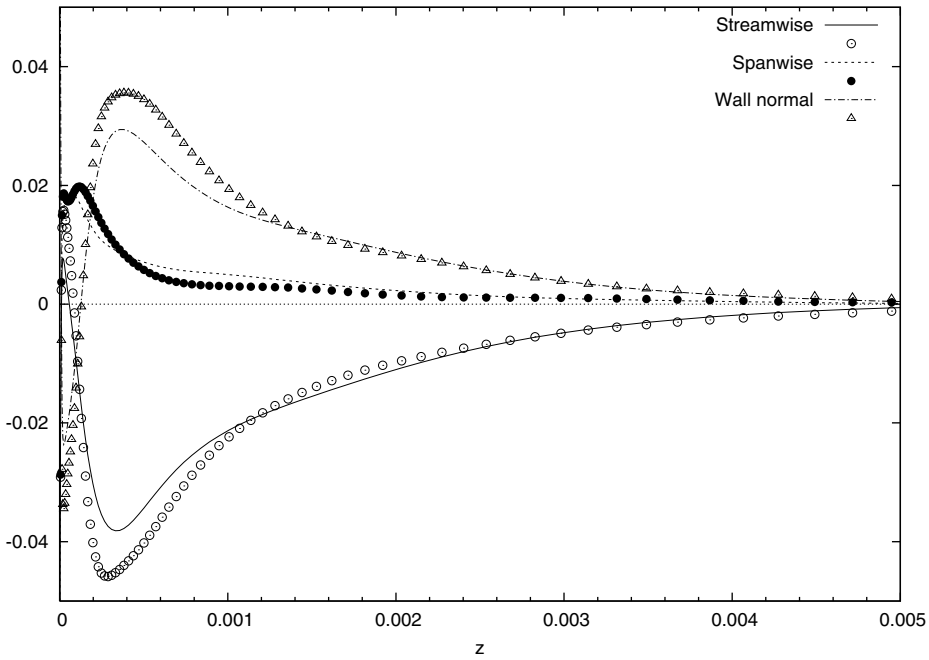

Figure A.1-8: Effect of heat addition on the pressure-strain term of turbulent kinetic energy transport - Case 2 heat addition. The points represent the natural or no heat boundary layer condition.

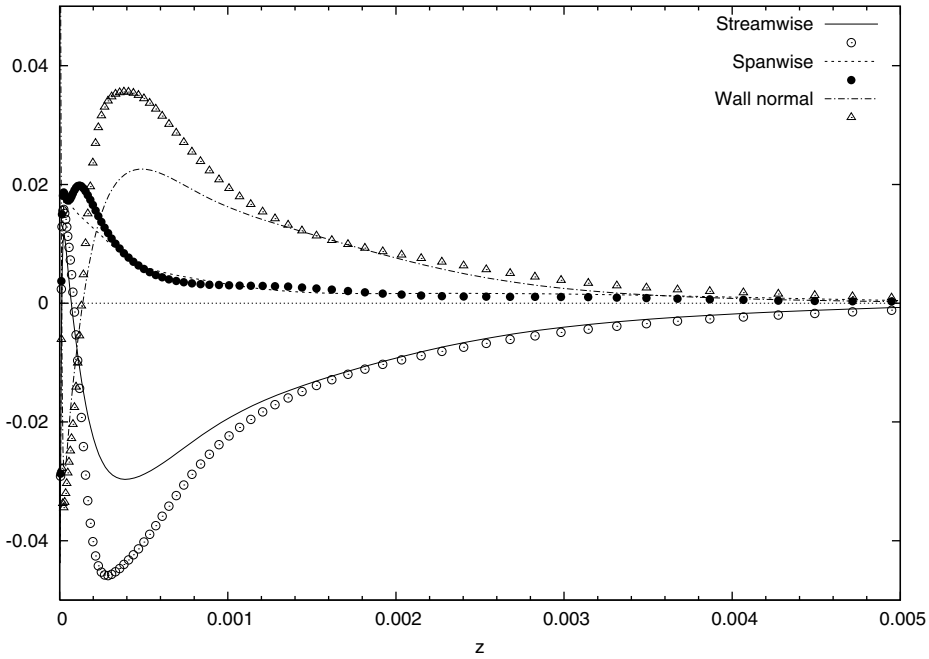

Figure A.1-9: Effect of heat addition on the pressure-strain term of turbulent kinetic energy transport - Case 2 combustion. The points represent the natural or no heat boundary layer condition.

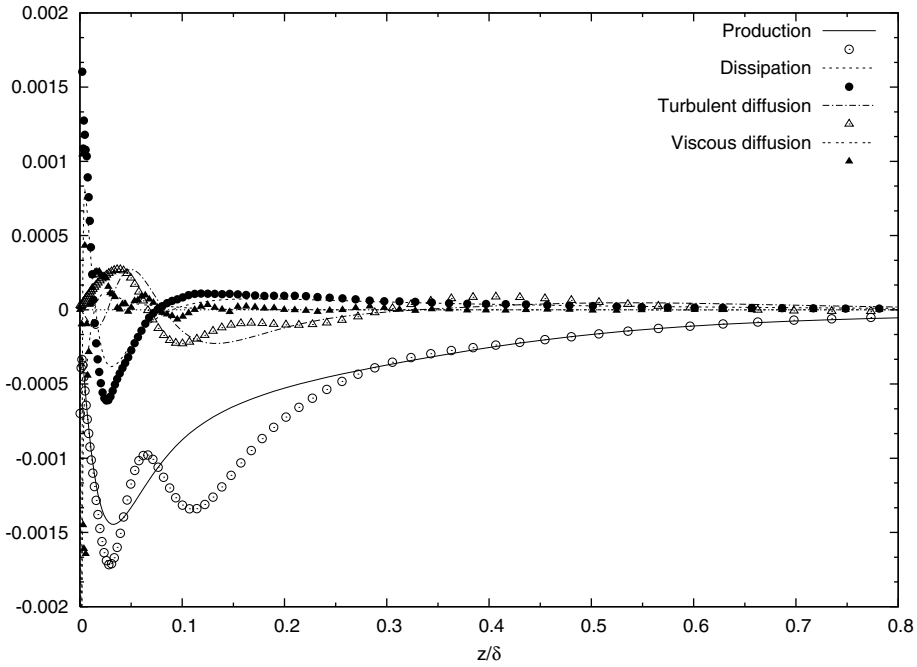

Figure A.1-10: Effect of heat addition on the Reynolds shear stress budget - Case 2 heat addition. The points represent the natural or no heat boundary layer condition.

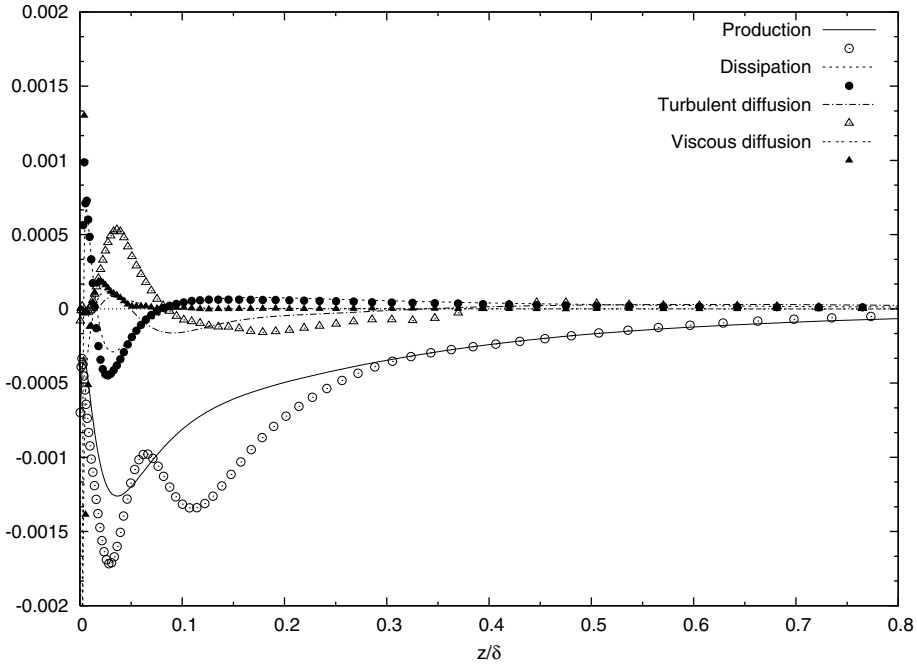

Figure A.1-11: Effect of heat addition on the Reynolds shear stress budget - Case 2 combustion. The points represent the natural or no heat boundary layer condition.

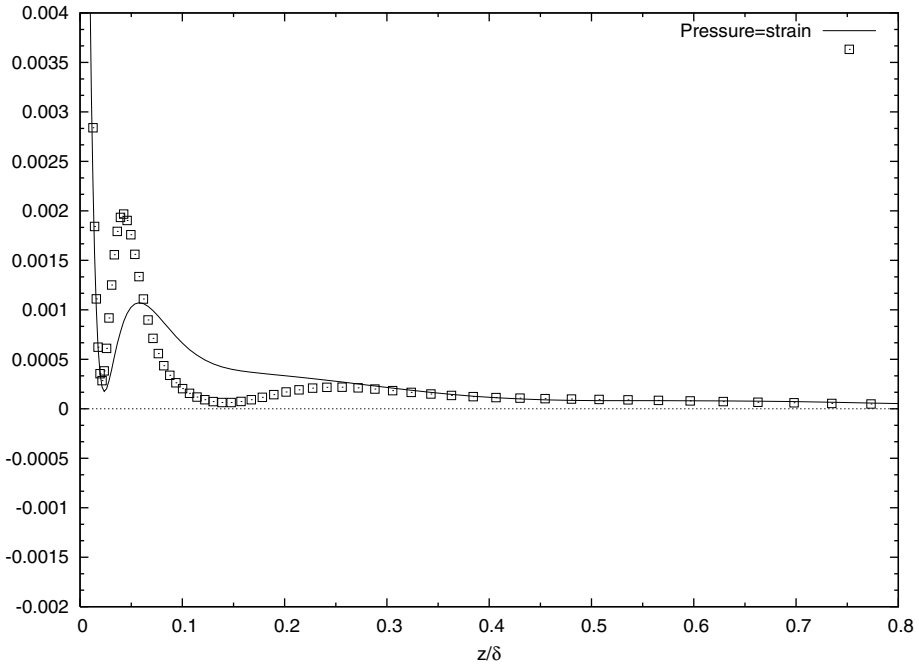

Figure A.1-12: Effect of heat addition on the pressure-strain contribution to the Reynolds shear stress budget - Case 2 heat addition. The points represent the natural or no heat boundary layer condition.

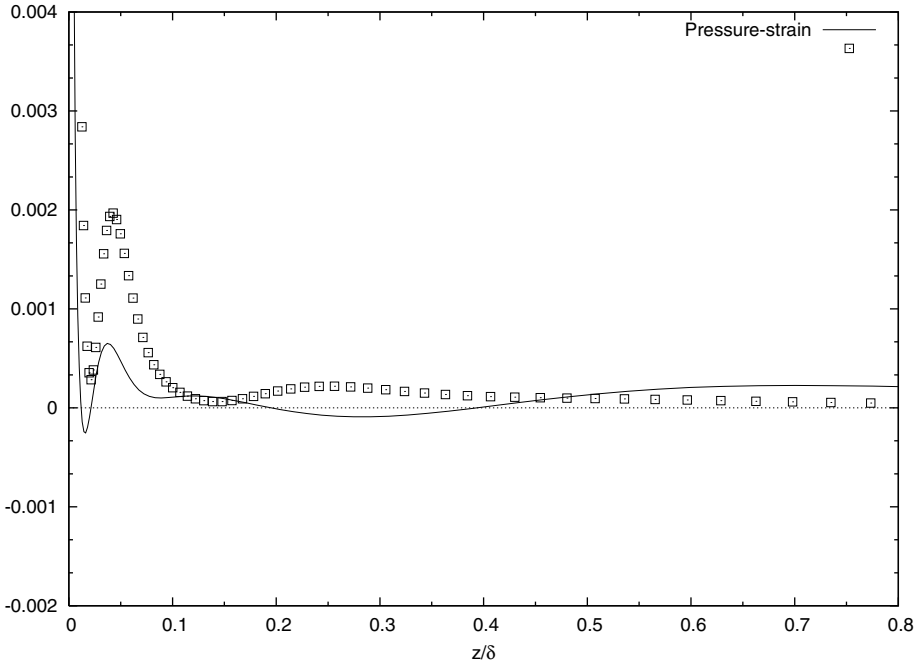

Figure A.1-13: Effect of heat addition on the pressure-strain contribution to the Reynolds shear stress budget - Case 2 combustion. The points represent the natural or no heat boundary layer condition.

Bibliography

Adams, N. (1998). Direct numerical simulation of turbulent compression ramp flow. *Theoretical and Computational Fluid Dynamics*, 12:109–129.

Adams, N. (2000). Direct numerical simulation of the turbulent boundary layer along a compression ramp. *Journal of Fluid Mechanics*, 420:47–83.

Adams, N. and Leonard, A. (1999). Deconvolution of subgrid-scales for the simulation of shock-turbulence interaction. CALTECH ASCII technical report 42, DOE/ASCII.

Alving, A. and Smits, A. (1990). Correlation measurements and structure angles in a turbulent boundary layer recovering from a convex curvature, In *Near-Wall Turbulence*. Kline, S. and Afgan, N. (editors). Hemisphere.

Anderson, J. (1989). *Hypersonic and High Temperature Gas Dynamics*. McGraw-Hill.

Antonia, R., Krishnamoorthy, L., and Fulachier, L. (1988). Correlation between the longitudinal velocity fluctuation and temperature fluctuation in the near-wall region of a turbulent boundary layer. *International Journal of Heat and Mass Transfer*, 31(4):723–730.

Baldwin, B. and Lomax, H. (1978). Thin layer approximation and algebraic model for separated turbulent flows. Paper Number 78-257, 16th Aerospace Sciences Meeting, Huntsville, Alabama. AIAA.

Bayless, J. and Brigham, E. (1970). Application of the Kalman filter to continuous signal restoration. *Geophysics*, 35(1):2–23.

Bernard, P. and Wallace, J. (2002). *Turbulent flow*. Wiley.

Bilson, M. (2004). *Momentum and scalar transport in the straight pipe and rotating cylinder - a comparison of transport mechanisms*. PhD thesis, Mechanical Engineering, University of Queensland.

Bodony, D. and Lele, S. (2003). Subgrid scale noise models for aeroacoustic prediction. In *Workshop on LES and SGS Modeling for turbulent Mixing and Reactive flows*. Caltech.

Brescianini, C. (1993). *An investigation of the wall-injected Scramjet: An experimental and numerical study of the wall-injected Scramjet at high-enthalpy conditions*. PhD thesis, Mechanical Engineering, University of Queensland.

Brown, G. and Thomas, A. (1977). Large structure in a turbulent boundary layer. *The Physics of Fluids*, 20(10):S243–S252.

Burrows, M. and Kurkov, A. (1973). Analytical and experimental study of supersonic combustion of hydrogen in a vitiated airstream. Technical Report TM X-2828, NASA.

Burtschell, Y. and Zeitoun, D. (2004). Numerical investigation of H_2 injection in Mach 5 air flow with a strong shock/boundary layer interaction. *Shock Waves*, 13:465–472.

Calhoon, W., Arunajatesan, S., and Dash, S. (2003). Heat release and compressibility effects on planar shear layer development. Paper Number 2003-1273, 41th Aerospace Sciences Meeting, Reno, Nevada. AIAA.

Cary, A. and Hefner, J. (1972). Film-cooling effectiveness and skin friction in hypersonic turbulent flow. *AIAA Journal*, 10(9):1188–1193.

Chen, J.-Y. (2004). Challenges in modelling of turbulence-chemistry interactions with large eddy simulations. *Progress in Computational Fluid Dynamics*, 4(3-5):155–161.

Choi, H., Moin, P., and Kim, J. (1994). Active turbulent control for drag reduction in wall bounded flows. *Journal of Fluid Mechanics*, 262:75–110.

Choi, J., Yang, V., Ma, F., Won, S., and Jeung, I. (2006). DES combustion modelling of a Scramjet combustor. Paper Number 2006-5097, 42nd AIAA/ASME/SAE/ASEE Joint Propulsion Conference and Exhibit, Sacramento, Ca. AIAA.

Chong, M., Soria, J., Perry, A., Chacin, J., Cantwell, B., and Na, Y. (1998). Turbulence structures of wall-bounded shear flows found using DNS data. *Journal of Fluid Mechanics*, 357:225–247.

Coleman, G., Kim, J., and Moser, R. (1995). A numerical study of turbulent supersonic isothermal-wall channel flow. *Journal of Fluid Mechanics*, 305:159–183.

Coles, D. (1953). Measurement of turbulent friction on a smooth flat plate in supersonic flow. *Journal of the Aeronautical Sciences*, 21:433–448.

Debieve, J., Dupont, P., Smith, D., and Smits, A. (1997). The response of a supersonic turbulent boundary layer to a step change in wall temperature. *AIAA Journal*, 35:51–57.

DeBonis, J. and Scott, J. (2002). Large-eddy simulation of turbulent compressible round jet. *AIAA Journal*, 40(7):1346–1354.

Delo, C., Kelso, R., and Smits, A. (2004). Three-dimensional structure of a low-Reynolds-number turbulent boundary layer. *Journal of Fluid Mechanics*, 512:47–83.

Dershin, J., Leonard, C., and Gallaher, W. (1967). Direct measurement of skin friction on a porous flat plate with mass injection. *AIAA Journal*, 5(11):1934–1939.

Domaradzki, J., Dubois, R., and Honein, A. (1998). A subgrid-scale estimation model applied to large eddy simulations of compressible turbulence. *Center for Turbulence Research, Proceedings of the Summer Program*, pages 351–366.

Domaradzki, J. and Saiki, E. (1997). A subgrid-scale estimation model based on the estimation of unresolved scales of turbulence. *Physics of Fluids*, 9(7):2148–2164.

Ducros, F., Comte, P., and Lesieur, M. (1996). Large-eddy simulation of transition to turbulence in a boundary layer developing spatially over a flat plate. *Journal of Fluid Mechanics*, 326:1–36.

Dussauge, J., Smith, R., Fernholz, H., Finley, P., Smits, A., and Spina, E. (1996). Turbulent boundary layers in subsonic and supersonic flow. Technical Report 335, AGARD.

El Baz, A. and Launder, B. (1993). Second-moment modelling of compressible mixing layers, In *Engineering Turbulent Modelling and Experiments*. Rodi, W. and Martelli, F. (editors). Elsevier.

El-Hady, N. (1994). Structure function dynamic subgrid-scale model, In *Transition, Turbulence and Combustion*. Hussaini, M., Gatski, T., and Jackson, T. (editors), volume I, pages 343–354. Kluwer Academic Publishers.

El-Hady, N. and Zang, T. (1995). Large-eddy simulation of non-linear evolution and breakdown to turbulence in high-speed boundary layers. *Theoretical and Computational Fluid Dynamics*, 7:217–240.

Elena, M. and Lacharme, J. (1988). Experimental study of a supersonic turbulent boundary layer using laser dopler anemometer. *Journal Mécanique Théorique et Appliquée*, 7:175–190.

Erlebacher, G., Hussaini, M., Speziale, C., and Zang, T. (1992). Toward the large-eddy simulation of compressible turbulent flows. *Journal of Fluid Mechanics*, 238:155–185.

Evans, J. and Schexnayder, C. (1980). Influence of chemical kinetics and unmixedness on burning in supersonic hydrogen flames. *AIAA Journal*, 18(2):188–193.

Falco, R. (1977). Coherent motions in the outer region of turbulent boundary layers. *The Physics of Fluids*, 20(10):S124–S132.

Falco, R. (1991). A coherent structure model of the turbulent boundary layer and its ability to predict Reynolds number dependence. *Philosophical Transactions: Physical Sciences and Engineering*, 336(1641):103–129.

Fernholz, H. and Finley, P. (1977). A critical compilation of compressible turbulent boundary layer data. Technical Report AG-223, AGARD.

Fernholz, H. and Finley, P. (1980). A critical commentary on mean flow data for two-dimensional compressible turbulent boundary layers. Technical Report AG-253, AGARD.

Fernholz, H. and Finley, P. (1981). A further compilation of compressible boundary layer data with a survey of turbulence data. Technical Report AG-263, AGARD.

Fernholz, H., Finley, P., Dussauge, J., and Smits, A. (1989). A survey of measurements and measuring techniques in rapdily distorted compressible turbulent boundary layers. Technical Report 315, AGARD.

Fukagata, K., Iwamoto, K., and Kasagi, N. (2002). Contribution of Reynolds stress distribution to the skin friction in wall-bounded flows. *Physics of Fluids*, 14:L73–L76.

Ganapathisubramani, B., Clemens, N., and Dolling, D. (2006). Large-scale motions in a supersonic turbulent boundary layer. *Journal of Fluid Mechanics*, 556:271–282.

Garnier, E., Mossi, M., Sagaut, P., Comte, P., and Deville, M. (1999). On the use of shock-capturing schemes for large-eddy simulation. *Journal of Computational Physics*, 153:273–511.

Gatski, T. (1997). Modeling compressibility effects on turbulence, In *New Tools in Turbulent Modelling*. Métais, O. and Ferziger, J. (editors), chapter 4, pages 73–104. Springer.

Gatski, T. and Erlebacher, G. (2002). Numerical simulation of a spatially evolving supersonic turbulent boundary layer. Technical Report 2002-211934, NASA.

Gaviglio, J. (1987). Reynolds analogies and experimental study of heat transfer in the supersonic boundary layer. *International Journal of Heat and Mass Transfer*, 30(5):911–926.

Gollan, R. (2003). Yet another finite-rate chemistry module for compressible flow codes. Division Report 9, Division of Mechanical Engineering, University of Queensland.

Goyne, C. (1998). *Skin Friction Measurements in High Enthalpy Flows at High Mach Number*. PhD thesis, Mechanical Engineering, University of Queensland.

Goyne, C., Stalker, R., and Paull, A. (1999). Shock-tunnel skin-friction measurement in a supersonic combustor. *Journal of Propulsion and Power*, 15(5):699–705.

Goyne, C., Stalker, R., Paull, A., and Brescianini, C. (2000). Hypervelocity skin-friction reduction by boundary-layer combustion of hydrogen. *Journal of Spacecraft and Rockets*, 37(6):740–746.

Grinstein, F. and Fureby, C. (2002). Recent progress on MILES for high Reynolds number flows. *Journal of Fluids Engineering*, 124:848–861.

Guarini, S., Moser, R., Shariff, K., and Wray, A. (2000). Direct numerical simulation of a supersonic boundary layer at Mach 2.5. *Journal of Fluid Mechanics*, 414:1–33.

Gyr, A. and Bewersdorff, H. (1995). *Drag reduction of turbulent flows by aditives*, chapter 4, pages 96–97. Kluwer Academic Publishers.

Head, M. and Bandyopdhyay, P. (1981). New aspects of turbulent boundary-layer structure. *Journal of Fluid Mechanics*, 107:297–338.

Hinze, J. (1975). *Turbulence*. McGraw Hill.

Hopkins, E., Keener, E., Polek, T., and Dwyer, H. (1972). Hypersonic turbulent skin-friction and boundary-layer profiles on nonadiabatic flat plates. *AIAA Journal*, 10:40–48.

Horstman, C. and Owen, F. (1972). Turbulent properties of a compressible boundary layer. *AIAA Journal*, 10:1418–1424.

Huang, P., Coleman, G., and Bradshaw, P. (1995). Compressible turbulent channel flows: DNS results and modelling. *Journal of Fluid Mechanics*, 305:185–218.

Huntley, M., Wu, P., Miles, R., and Smits, A. (2000). Mhz rate imaging of boundary layer transition on elliptic cones at Mach 8. Paper Number 2000-0379, 38th Aerospace Sciences Meeting, Reno, Nevada. AIAA.

Jacobs, P. and Craddock, C. (1999). Simulation and optimization of heated, inviscid flows in Scramjet ducts. *Journal of Propulsion and Power*, 15(1):73–81.

Jacobs, P., Denman, A., and Gollan, R. (2007a). The Elmer Code: Theory and implementation of a compressible flow solver. Division Report 2007/01, Division of Mechanical Engineering, University of Queensland.

Jacobs, P., Gollan, R., and Denman, A. (2007b). The Elmer Code: User guide and example book. Division Report 2007/02, Division of Mechanical Engineering, University of Queensland.

Johnson, D. and Rose, W. (1975). Laser velocimeter and hot-wire anemometer comparison in a supersonic boundary layer. *AIAA Journal*, 13:512–515.

Jones, J., Isaacson, L., and Vreeke, S. (1971). A turbulent boundary layer with mass addition, combustion, and pressure gradients. *AIAA Journal*, 9:1762–1768.

Keating, A. (2003). *Large-eddy simulation of heat transfer in turbulent channel flow and in the turbulent flow downstream of a backward-facing step*. PhD thesis, Mechanical Engineering, University of Queensland.

Kim, K. and Adrian, R. (1999). Very large-scale motion in the outer layer. *Physics of Fluids*, 11:417–422.

Kistler, A. (1959). Fluctuation measurements in a supersonic turbulent boundary layer. *Physics of Fluids*, 2:290–296.

Klebanoff, P. (1955). Characteristics of turbulence in a boundary layer with zero pressure gradient. Technical Report 1247, NACA.

Knight, D., Zhou, G., Okong'o, N., and Shukla, V. (1998). Compressible large eddy simulation using unstructured grids. Paper Number 98-0535, 36th Aerospace Sciences Meeting and Exhibit, Reno, Nevada. AIAA.

Konrad, W. and Smits, A. (1998). Turbulence measurements in a three-dimensional boundary layer in supersonic flow. *Journal of Fluid Mechanics*, 372:1–23.

Kosovic, B., Pullin, D., and Samtaney, R. (2002). Subgrid-scale modeling for large-eddy simulations of compressible turbulence. *Physics of Fluids*, 14(4):1511–1522.

Kravchenko, A., Choi, H., and Moin, P. (1993). On the relation of near-wall streamwise vortices to wall skin friction in turbulent buondary layers. *Physics of Fluids A*, 5(12):3307–3309.

Kuerten, J., Geurts, B., Vreman, A., and Germano, M. (1999). Dynamic inverse modeling and its testing in large-eddy simulations of the mixing layer. *Physics of Fluids*, 11(12):3778–3785.

Kulgein, N. (1962). Transport processes in a combustible turbulent boundary layer. *Journal of Fluid Mechanics*, 12:417–437.

Kussoy, M., Horstman, C., and Acharya, M. (1978). An experimental documentation of pressure gradient and Reynolds number effects on compressible turbulent boundary layers. Technical Report TM 78488, NASA.

Laderman, A. and Demetriades, A. (1974). Mean and fluctuating flow measurements in the hypersonic boundary layer over a cooled wall. *Journal of Fluid Mechanics*, 63:121–144.

Laderman, A. and Demetriades, A. (1979). Turbulent shear stresses in compressible boundary layers. *AIAA Journal*, 17(7):736–744.

Larin, O. and Levin, V. (1999). Flow in a turbulent supersonic boundary layer with a heat source. *Technical Physics Letters*, 25(4):265–266.

Lenormand, E., Sagaut, P., L., T. P., and Comte, P. (2000). Subgrid-scale models for large-eddy simulations of compressible wall bounded flows. *AIAA Journal*, 38(8):1340–1350.

Levin, V. and Larin, O. (2003). Skin-friction reduction by energy addition into a turbulent boundary layer. Paper Number 2003-0036, 41st Aerospace Sciences Meeting, Reno, Nevada. AIAA.

Ligrani, P. and Bradshaw, P. (1987). Spatial resolution and measurement of turbulence in the viscous sublayer using subminiature hot-wire probes. *Experiments in Fluids*, 5:407–417.

Liou, M. and Steffen, C. (1991). A new flux splitting scheme. Technical Memorandum 104404, NASA.

Lund, T., Wu, X., and Squires, K. (1998). Generation of turbulent inflow data for spatially-developing boundary layer simulations. *Journal of Computational Physics*, 140:233–258.

Mabey, D., Meier, H., and Sawyer, W. (1974). Experimental and theoretical studies of the boundary layer on a flat plate at Mach numbers from 2.5 to 4.5. Technical Report TR 74127, RAE.

Maeder, T. (2000). *Numerical Investigation of Supersonic Turbulent Boundary Layers*. PhD thesis, Swiss Federal Institute of Technology, Zurich.

Maeder, T., Adams, N., and Kleiser, L. (2001). Direct simulation of turbulent supersonic boundary layers by an extended temporal approach. *Journal of Fluid Mechanics*, 429:187–216.

Martín, M. (2000). Shock-capturing in LES of high-speed flows. *Center for Turbulence Research, Annual Research Briefs*, pages 193–198.

Martín, M. (2004). DNS of hypersonic turbulent boundary layers. Paper Number 2004-2337 in 34th Fluid Dynamics Conference and Exhibit. AIAA.

Martín, M. (2005). Preliminary study of the SGS time scales for compressible boundary layers using DNS data. Paper Number 2005-0665, 43rd Aerospace Sciences Meeting, Reno, Nevada. AIAA.

Martín, M. and Candler, G. (2000). DNS of a Mach 4 boundary layer with chemical reactions. Paper Number 2000-0399, 38th Aerospace Sciences Meeting, Reno, Nevada. AIAA.

Martín, M., Candler, G., and Piomelli, U. (2000). Subgrid-scale models for compressible large-eddy simulations. *Theoretical and Computational Fluid Dynamics*, 13:361–376.

Mathew, J., Lechner, R., Foysi, H., Sesterhenn, J., and Friedrich, R. (2003). An explicit filtering method for large eddy simulation of compressible flows. *Physics of Fluids*, 15(8):2297–2289.

McMurtry, P., Riley, J., and Metcalfe, R. (1989). Effects of heat release on the large-scale structure in turbulent mixing layers. *Journal of Fluid Mechanics*, 199:297–332.

Möbus, H., Gerlinger, P., and Brüggemann, D. (2003). Scalar and joint scalar-velocity-frequency Monte Carlo PDF simulation of supersonic combustion. *Combustion and Flame*, 132:3–24.

Moin, P., Squires, K., Cabot, W., and Lee, S. (1991). A dynamic subgrid-scale model for compressible turbulence and scalar transport. *Physics of Fluids A*, 3:2746–2757.

Morkovin, M. (1962). Effects of compressibility on turbulent flows, In *Mecanique de la Turbulence*. Favre, A. (editor). CNRS.

Morkovin, M. and Phinney, R. (1958). Extended applications of hot wire anemometry to high speed turbulent boundary layers. Technical Report ASTIA AD-158-279, Dept. Aeronautical Engineering, The Johns Hopkins University.

Nagarajan, S., Lele, S., and Ferziger, J. (2003). A robust high-order compact method for large eddy simulation. *Journal of Computational Physics*, 191:392–419.

Normand, X. and Lesieur, M. (1992). Direct and large-eddy simulations of transition in the compressible boundary layer. *Theoretical and Computational Fluid Dynamics*, 3:231–252.

Norris, J. and Edwards, J. (1997). Large-eddy simulation of high-speed, turbulent diffusion flames with detailed chemistry. Paper Number 97-0370, 35th Aerospace Sciences Meeting, Reno, Nevada. AIAA.

Oldaker, D. and Tiederman, W. (1977). Spatial structure of the viscous sublayer in drag-reducing channel flows. *The Phyiscs of Fluids*, 20(10):S133–S144.

Olsen, G. and Nowak, R. (1995). Hydrogen film cooling with incident and swept-shock interations in a Mach 6.4 nitrogen free stream. Technical Report 4603, NASA.

Oran, E. and Boris, J. (2001). *Numerical simulation of reactive flow*. Cambridge University Press.

Parthasarathy, K. and Zakkay, V. (1970). An experimental investigation of turbulent slot injection at Mach 6. *AIAA Journal*, 8(7):1302–1307.

Paull, A., Stalker, R., and Mee, D. (1995). Experiments on supersonic combustion ramjet propulsion in a shock tunnel. *Journal of Fluid Mechanics*, 296:159–183.

Perry, A., Smits, A., and Chong, M. (1979). The effects of certain low frequency phenomena on the calibration of hot wires. *Journal of Fluid Mechanics*, 90:415–431.

Piomelli, U. (1993). High Reynolds number calculations using the dynamic subgrid-scale stress model. *Physics of Fluids A*, 5(6):1484–1490.

Piomelli, U. (2001). Large-eddy and direct simulation of turbulent flows. In *2001 - A CFD Odyssey*, 9e Conférence Annuelle de la Société Canadienne de CFD.

Pirozzoli, S. and Grasso, F. (2006). Direct numerical simulation of impinging shock wave. *Physics of Fluids*, 18(6).

Pitsch, H. (2006). Large-eddy simulation of turbulent combustion. *Annual Review of Fluid Mechanics*, 38:453–482.

Richards, B. and Stollery, J. (1979). Film cooling experiments in hypersonic flow. *Journal of Aircraft*, 16(3):177–181.

Rizzetta, D. and Visbal, M. (2004). Large-eddy simulation of supersonic boundary layer flow by a high order method. *International Journal of Computational Fluid Dynamics*, 18(1):15–27.

Roache, P. (1998). Verification of codes and calculations. *AIAA Journal*, 36(5):696–702.

Robinson, S. (1991). Coherent motions in the turbulent boundary layer. *Annual Review of Fluid Mechanics*, 23:601–639.

Rowan, S. (2003). *Viscous drag reduction in a Scramjet combustor*. PhD thesis, Mechanical Engineering, University of Queensland.

Roy, C. (2003). Grid convergence error analysis for mixed-order numerical schemes. *AIAA Journal*, 41(4):595–604.

Rubesin, M. (1954). An analytical estimation of the efffect of transpiration cooling on the heat-transfer and skin friction characteristics of a compressible, turbulent boundary layer. Technical Report TN 3341, NACA.

Sagaut, P. and Grohens, R. (1999). Discrete filters for large-eddy simulation. *International Journal for Numerical Methods in Fluids*, 31(8):1195–1220.

Sandborn, V. (1974). A review of turbulence measurements in compressible flow. Technical Report TM X-62 337, NASA.

Schetz, J. and Van Overeem, J. (1975). Skin-friction reductions by injection through combinations of slots and porous sections. *AIAA Journal*, 13(8):971–972.

Shutts, W., Hartwig, W., and Weiler, J. (1955). Final report on turbulent boundary layer and skin friction measurements on a smooth thermally insulated flat plate at supersonic speeds. *Report No. DRL-366*, CM-823.

Smagorinsky, J. (1963). General circulation experiments with the primitive equations. I. The basic experiment. *Monthly Weather Review*, 91:99–164.

Smits, A. and Dussauge, J. (1996). *Turbulent shear layers in supersonic flow*. AIP.

Smits, A. and Dussauge, J. (2006). *Turbulent shear layers in supersonic flow, 2nd Ed.* AIP.

Smits, A., Spina, E., Alving, A., Smith, R., Fernando, E., and Donovan, J. (1989). A comparison of the turblence structure of subsonic and supersonic boundary layers. *Physics of Fluids A*, 1:1865–1875.

Spalart, P. (1988). Direct simulation of a turbulent boundary layer up to Re_θ = 1410. *Journal of Fluid Mechanics*, 187:61–98.

Spalart, P., Moser, R., and Rogers, M. (1991). Spectral Methods for the Navier-Stokes Equations with one infinite and two periodic directions. *Journal of Computational Physics*, 96:297–324.

Speziale, C., Erlebacher, G., Hussaini, M., and Zang, T. (1988). The subgrid-scale modeling of compressible turbulence. *Physics of Fluids A*, 31(4):940–942.

Spina, E., Donovan, J., and Smits, A. (1991). On the structure of high-Reynolds-number supersonic turbulent boundary layers. *Journal of Fluid Mechanics*, 222:293–327.

Spina, E. and Smits, A. (1987). Organised structures in a supersonic turbulent boundary layer. *Journal of Fluid Mechanics*, 182:85–109.

Stalker, R. (1989). Thermodynamics and wave processes in high Mach number propulsive ducts. Paper Number 89-0261, 27th Aerospace Sciences Meeting, Reno, Nevada. AIAA.

Stalker, R. (2005). Control of hypersonic turbulent skin friction by boundary-layer combustion of hydrogen. *Journal of Spacecraft and Rockets*, 42(4):577–587.

Stolz, S. (2000). *Large-eddy simulation of complex shear flows using an approximate deconvolution model*. PhD thesis, Swiss Federal Institute of Technology, Zürich.

Stolz, S. and Adams, N. (1999). An approximate deconvolution procedure for large-eddy simulation. *Physics of Fluids*, 11(7):1699–1701.

Stolz, S. and Adams, N. (2003). Large-eddy simulation of high-Reynolds-number supersonic boundary layers using the approximate deconvolution model and a rescaling and recycling technique. *Physics of fluids*, 15(8):2398–2412.

Stolz, S., Adams, N., and Kleiser, L. (2001a). An approximate deconvolution model for large-eddy simulation with application to incompressible wall-bounded flows. *Physics of Fluids*, 13(4):997–1015.

Stolz, S., Adams, N., and Kleiser, L. (2001b). The approximate deconvolution model for large-eddy simulations of compressible flows and its application to shock-turbulent-boundary-layer interaction. *Physics of Fluids*, 13(10):2985–3001.

Suraweera, M. (2006). *Reduction of skin friction drag in hypersonic flow by boundary layer combustion*. PhD thesis, Mechanical Engineering, University of Queensland.

Tanimizu, K., Mee, D., and Stalker, R. (2006). Measurement and prediction of the force of an unfuelled axisymmetric scramjet model. Paper Number 2006-8064, 14th AIAA/AHI Space Planes and Hypersonic Systems and Technologies Conference, Canberra, Australia. AIAA.

Thompson, K. (1990). Time-dependent boundary conditons for hyperbolic systems, II. *Journal of Computational Physics*, 89:1439–461.

Tromeur, E., Garner, E., Sagaut, P., and Basdevant, C. (2003). Large eddy simulations of aero-optical effects in a turbulent boundary layer. *Journal of Turbulence*, 4:1 – 22.

Urbin, G., Knight, D., and Zheltovodov, A. (1999). Compressible large eddy simulation using unstructured grid: Supersonic turbulent boundary layer and compression corner. Paper Number 99-0427, 37th Aerospace Sciences Meeting, Reno, Nevada. AIAA.

Vasilyev, O. (1999). High order finite difference schemes on non-uniform meshes with good conservation properties. *Journal of Computational Physics*, 157:746–761.

Veynante, D. and Poinsot, T. (1997). *Reynolds Averaged and Large Eddy simulation modeling for turbulent combustion*, chapter 5, pages 105–140. Springer.

Volino, R. and Simon, T. (1994). An application of octant analysis to turbulent and transitional flow data. *Journal of Turbomachinery*, 116:752–758.

von Kaenel, R., Adams, N., Kleiser, L., and Vos, J. (2002). The approximate deconvolution model for large-eddy simulation of compressible flows with finite volume schemes. *Journal of Fluids Engineering*, 124:829–835.

Vreman, B., Geurts, B., and Kuerten, H. (1995). A priori tests of large eddy simulation of the compressible plane mixing layer. *Journal of Engineering Mathematics*, 29:299–327.

Wada, Y. and Liou, M. (1994). A flux splitting scheme with high-resolution and robustness for discontinuities. Paper Number 94-0083, 32nd Aerospace Sciences Meeting, Reno, Nevada. AIAA.

Wallace, A. (1981). *Experimental investigation on the effects of chemical heat release on shear layer gorwth and entrainment*. PhD thesis, University of Adelaide.

Wallace, J., Eckelmann, H., and Brodkey, R. (1972). The wall region in turbulent shear flow. *Journal of Fluid Mechanics*, 339:357–390.

Walsh, M. and Weinstein, L. M. (1978). Drag and heat transfer on surfaces with small longitudinal fins. Paper Number 78-1161, 11th Fluid and Plasma Dynamics Conference, Seattle, Washington. AIAA.

Wilcox, D. (2002). *Turbulence Modlling for CFD*. Griffin Printing, California.

Wilmarth, W. and Lu, S. (1972). Structure of the Reynolds stress near the wall. *Journal of Fluid Mechanics*, 55:65–92.

Wooldridge, C. and Muzzy, R. (1962). Measurements in a turbulent boundary layer with porous wall inection and combustion. In *Proceedings of the Tenth International Symposium on Combustion*, pages 1351–1362. Combustion Institute.

Xu, S. and Martin, M. (2004). Assessment of inflow boundary conditions for compressible turbulent boundary layers. *Physics of Fluids*, 16(7):2623–2639.

Yan, H., Knight, D., and Zheltovodov, A. (2002). Large-eddy simulation of supersonic flat-plate boundary layers using the Monotonically Integrated Large-Eddy Simulation (MILES) Technique. *Journal of Fluids Engineering*, 124:868–875.

Zheltovodov, A. and Yakovlev, V. (1986). Stages of developments, gas dynamic structure and turbulence characteristics of turbulent compressible separated flows in the vicinity of 2-D obstacles. *USSR Acadamey of Sciences, Novosibirsk*. In Russian.